Research on Engineering Structures & Materials

P-ISSN: 2148-9807 E-ISSN: 2149-4088

Volume 7 Issue 2 June 2021

J R E S M

www.jresm.org

Research Group

The International Journal of **Research on Engineering Structures and Materials (RESM**) is a peer-reviewed open access journal (p-ISSN: 2148-9807; o-ISSN: 2149-4088) published by MIM Research Group. It is published in February, June, September, and December.

The main objective of RESM is to provide an International academic platform for researchers to share scientific results related to all aspects of mechanical, civil and material engineering areas.

RESM aims the publication of original research articles, reviews, short communications technical reports, and letters to the editor on the latest developments in the related fields.

All expenditures for the publication of the manuscripts are most kindly reimbursed by *MIM Research Group*. Thus, authors do not need to pay for publishing their studies in the journal.

The scope of the journal covers (but not limited to) behavior of structures, machines and mechanical systems, vibration, impact loadings and structural dynamics, mechanics of materials (elasticity, plasticity, fracture mechanics), material science (structure and properties of concrete, metals, ceramics, composites, plastics, wood, etc.,), nano-materials performances of new and existing buildings and other structural systems, design of buildings and other structural systems, seismic behavior of buildings and other structural systems, repair and strengthening of structural systems, case studies and failure of structural systems, safety and reliability in structural and material engineering, use of new and innovative materials and techniques in energy systems and mechanical aspects of biological systems (biomechanics and biomimetics).

The topics covered in JRESM include:

- Structural Engineering
- Mechanical Engineering
- Material Engineering
- Earthquake Engineering
- Nano-technology
- Energy Systems
- Biomechanics and Biomimetics

Abstracting and Indexing
Please visit http://www.jresm.org for more information.

Graphics and Design

Yunus Demirtaş ydemirtas@jresm.net

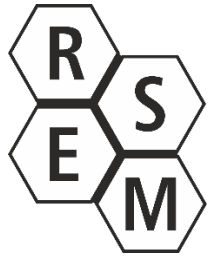

RESEARCH on ENGINEERING STRUCTURES & MATERIALS

Published by MIM Research Group

Editorial Board Members

Advisory Board Members

Yinusa Amoo Ahmed	University of Lagos	Nigeria
Erkin Akdoğan	Karamanoğlu Mehmetbey University	Turkey
Mustafa Akpolat	Munzur University	Turkey
Sevim Alışır	Ondokuz Mayis University	Turkey
Saber Alizadeh	Bu-Ali-Sina University	Iran
Danar Altalabani	University of Applied Sciences Karlsruhe	Germany
Mustafa Yasin Aslan	Usak University	Turkey
Huseyin Ersen Balcıoglu	Usak University	Turkey
Beyhan Bayhan	Bursa Technical University	Turkey
Emin Bayraktar	Supméca Institute of Mechanics of Paris	France
Mehmet Bulut	Hakkari University	Turkey
Hektor Cullufi	Polytechnic University of Tirana	Albania
Preeta Datta	North Carolina State University	USA
J. Paulo Davim	University of Aveiro	Portugal
Hakan Demir	Iskenderun Technic University	Turkey
Cengiz Görkem Dengiz	Ondokuz Mayıs Unıversity	Turkey
Akar Dogan	Munzur University	Turkey
Hany El-Hamshary	Tanta University	Egypt
Engin Emsen	Akdeniz University	Turkey
H. Murat Enginsoy	Usak University	Turkey
Ali Faghidian	Islamic Azad University	Iran
Mohamed Guenfoud	University Larbi Tébessi	Algeria
Mükrimin Şevket Güney	Giresun University	Turkey
Dulce Franco Henriques	Instituto Politécnico de Lisboa	Portugal
Halit Levent Hosgun	Bursa Technical University	Turkey
Mahdi Hosseini	Jawaharlal Nehru Technological University	India

Advisory Board Members

Ercan Isik	Bitlis Eren University	Turkey
Zafer Kaya	Dumlupınar University	Turkey
Ali Koçak	Yildiz Technical University	Turkey
Sedat Kömürcü	İstanbul Technical University	Turkey
Güven Kurtuldu	ETH Zurich	Switzerland
Charles Langston	University of Memphis	USA
Ahmet Meram	KTO Karatay University	Turkey
Süha Orçun Mert	İskenderun Technical University	Turkey
Masoomeh Mirrashid	Semnan University	Iran
Jinxu Mo	Yangtze University	China
Kim Hung Mo	University of Malaya	Malaysia
Arunima Nayak	Graphic Era University	India
Mehmet Palanci	Istanbul Arel University	Turkey
Amin Moslami Petrudi	University Amirkabir	Iran
Majid Pouraminian	Islamic Azad University	Iran
Alaa M. Rashad	Building Materials Research and Quality Control Institute	Egypt
Fabio Rizzo	University of Chieti-Pescara	Italy
Behnam Rosti	Shiraz University of Technology	Iran
Tamer Saracyakupoglu	Istanbul Gelisim University	Turkey
Rudimylla Septimio Azeredo	Federal University of Southern and Southeastern Pará	Brazil
Neritan Shkodrani	Polytechnic University of Tirana	Albania
Ramachandran Seshadri	Stony Brook University	USA
Adnan Sozen	Gazi University	Turkey
Brijesh Singh	National Council for Cement & Building Material	India
Hossein Taghipoor	Semnan University	Iran

Advisory Board Members

Anand B. Tapase	Karmaveer Bhaurao Patil College of Engineering	India
Faris Tarlochan	Qatar University	Qatar
Hamide Tekeli	Süleyman Demirel University	Turkey
Dilay Uncu	Manisa Celal Bayar University	Turkey
Abid Ustaoğlu	Bartin University	Turkey
Ümit Ünver	Yalova University	Turkey
Gustavo Bosel Wally	Federal University of Rio Grande do Sul	Brazil
Jhair Yacila	Pontificia Universidad Católica del Perú	Peru
Onder Yesil	Usak University	Turkey
Salih Hakan Yetgin	Dumlupınar University	Turkey
Ferhat Yıldırım	Çanakkale Onsekiz Mart University	Turkey
Recep Yurtseven	Pamukkale University	Turkey

In This Issue

Research on Engineering Structures & Materials
MIM Reseach Group Publications
P-ISSN: 2148-9807
E-ISSN: 2149-4088
http://www.jresm.org

ABSTRACTING / INDEXING

The international journal of Research on Engineering Structures and Materials (RESM) is currently Absracted/Indexed by Asos Indeks, CiteFactor, Cosmos, CrossRef, Directory of Research Journal Indexing, Engineering Journals (ProQuest), EZB Electronic Journal Library, Global Impact Factor, Google Scholar, International Institute of Organized Research (I2OR), International Scientific Indexing (ISI), Materials Science & Engineering Database (ProQuest), Open Academic Journals Index, Publication Forum, Research BibleScientific Indexing Service, Root Indexing, Scopus, Ulakbim TR Index (Tubitak), Universal Impact Factor and under evaluation by many other respected indexes.

Check web site for current indexing info.

Scopus®

DRJI

TÜBİTAK ULAKBİM

ProQuest

ASOS indeks

crossref

Google Scholar

Universal Impact Factor

Scientifically derived Journal Impact Factor

SIS Scientific Indexing Services

Journal Seeker Research Bible

CiteFactor Academic Scientific Journals

EZB Elektronische Zeitschriftenbibliothek

Open Academic Journals Index

GIF GLOBAL IMPACT FACTOR

ROOTINDEXING JOURNAL ABSTRACTING AND INDEXING SERVICE

Cosmos

Publication Forum

Research on Engineering Structures & Materials
journal homepage: http://jresm.org
Research Group

Research Article

Strength prediction of engineered cementitious composites with artificial neural networks

Seda Yeşilmen

Department of Civil Engineering, Cankaya University, Ankara, Turkey

Article Info

Article history:
Received 13 Oct 2020
Revised 15 Jan 2021
Accepted 21 Feb 2021

Keywords:
ECC; ANN; Strength prediction; Compressive Strength

Abstract

Engineered Cementitious composites (ECC) became widely popular in the last decade due to their superior mechanical and durability properties. Strength prediction of ECC remains an important subject since the variation of strength with age is more emphasized in these composites. In this study, mix design components and corresponding strengths of various ECC designs are obtained from the literature and ANN models were developed to predict compressive and flexural strength of ECCs. Error margins of both models were on the lower side of the reported error values in the available literature while using data with the highest variability and noise. As a result, both models claim considerable applicability in all ECC mixture types.

1. Introduction

Prediction of concrete strength has been a popular area among concrete technology topics [1,2]. Accuracy of the strength prediction is more critical for repair and retrofitting materials such as Engineered Cementitious Composites (ECC). ECC is a strong alternative for conventional materials for repair, retrofitting and infrastructural applications. They offer significant improvements on various mechanical and durability properties of concrete especially flexural strength. PVA fibers bridging microcracks prohibits formation of large cracks consequently ultimate tensile strain capacity and tensile strength values reported up to 4.7% and 6 MPa respectively in the literature [3-6].

The major factor determining the compressive strength of cementitious composites is mix design, the components of which widely used in strength prediction of cementitious composites. Artificial neural networks (ANN) is a widely used method for strength prediction of concrete and cementitious composites [7,8]. ANN is used to construct mapping functions for predicting strength and it is a powerful tool for solving very complex problems. Multilayer perceptron (MLP) neural networks are standard neural network models with an input layer representing cementitious composite mix design components, hidden layers with computation neurons, and an output layer containing one neuron representing strength prediction.

Previous studies on concrete mixtures are known to yield high accuracies especially when data is from a single batch or from a single production location [9]. However, when ANN models were trained with data from various sources, test errors increased even with a powerful tool such as ANN [10,11].

Predictive performance of ANN is dependent on various factors and can be quite different for various types of cementitious composites. There are lots of other contributing factors

Corresponding author: syesilmen@cankaya.edu.tr
orcid.org/0000-0002-2046-3841
DOI: http://dx.doi.org/10.17515/resm2020.222ma1013

other than mix design parameters when predicting strength, such as age, curing conditions, and handling practices, etc. Most of these factors are not included in the training data because they are categorical parameters and cannot be used in a regression problem directly. These categorical parameters considered to be one of the reasons for decreasing accuracies in strength prediction. Considering cementitious composites such as ECC, there are even more categorical parameters such as fiber type, mineral admixture type, etc. Individual ANN models were developed for different fiber types or different admixture types to be able to obtain acceptable accuracies when predicting ECC strength in the literature [12,13]. These models yield very high accuracies, but they are both specific to one type of ECC and the test results are obtained from a single batch of ECC which has very low noise and variability in the input data. [11-14]

This study aims to incorporate several categorical parameters for strength prediction of ECC mixtures, so a single ANN model can be developed for very different mixture characteristics. Additionally the models will be applicable to a range of different ECC mixes unlike previous studies. Compressive strength of any cementitious composite is the most important materials property since they are designed to mainly work in compression as a building material. In the literature compressive strengths in the range of 25 to 115 MPa were reported [3-6,15]. Considering ECC gained its popularity mostly due to its high flexural strength capacity, two strength categories namely flexural and compressive strength were predicted using the data obtained from literature. Two single ANN models were developed to predict compressive and flexural strengths of ECC with different chemical and mineral admixture types, fiber types, age, specimen geometry and dimensions.

2. Materials and Methods

Artificial neural networks (ANNs) use back-propagation (BP) algorithm, which adjusts connection weights (w) and bias values (b) during training. The forward propagation in ith output layer can be expressed as:

$$z_j^{[i]} = \sum_{k}^{n} w_{jk}^{[i]} x_k^{[i-1]} \tag{1}$$

$$a_j^{[i]} = f\left(z_j^{[i]}\right) \tag{2}$$

where i is the layer of the neuron, n is the number of neurons in the previous layer, wjk is the weight associated to jth neuron applied to the kth neuron from the previous layer, xk is the output of neuron k, zj is the output of neuron j for layer i, and aj activation function applied to zj for layer i. After initializing weights, an optimization method is used to minimize the selected cost function.

Two hidden layers were used in the ANN model for this study. ANN model was implemented using Tensorflow library in the medium of python. Activation function was selected to be sigmoid for all layers except output layer. Sigmoid function is often used in ANN to introduce nonlinearity in a model. It simply converts the output of the neuron to a value in the range of (0,1) so that activated output that will be fed to the next set of perceptrons will be 1 at most when the output is too large and 0 if output is too small [16].

Gradient descent-based algorithms are used commonly in ANN models. Adam Optimization algorithm was selected to be used in the ANN model since it showed better convergence compared to other gradient descend based algorithms in the literature. Adam optimization is based on the idea of adaptive moment estimation, learning rate decay is implemented using exponential moving average of the gradient. This algorithm is reported

to be efficient and convenient for a wide range of optimization problems in the field of machine learning [17].

Total dataset was divided into 80% and 20% to use as training and test data, respectively. Training and testing data were separated using train_test_split function of sklearn library. Train_test_split function splits arrays or matrices into random training and testing subsets. This function also shuffles the data before splitting which can be critical during training. Validation data was not used, instead cross validation was performed for hyper parameter tuning. Cross validation method is commonly used when training data is relatively small. In cross validation method, training data is split into 5 subsets, and 4 of those subsets are used to train the model with a specific hyperparameter combination, as one of the subsets kept as test data. For categorical features, one_hot encoding was applied using get_dummies function in pandas library.

A total of 214 different ECC mix designs for compressive strength and 147 for flexural strength are obtained from various sources [3,13,18-36]. A total of 13 parameters were incorporated which were readily available from the literature namely; age, cement content, cement type, fiber content, water content, aggregate content, and chemical admixture content, mineral admixture type and content, specimen geometry, specimen dimensions, Calcium and silica content of mineral admixtures. Since flexural specimens were always prismatic, specimen geometry parameter was not included which reduced the total parameters to 12 for flexural strength model. Categorical variables are given in Table 1. The categories for each categorical variable listed in this table shows the categories that are found in the database used. All the non-categorical parameters were defined for 1m3 of ECC. Minimum and maximum values of non-categorical parameters for the dataset used in this study are given in Table 2.

There is no specific standard that governs the specimen preparation for ECC. Typically mixtures were prepared following a typical ECC mixing procedure. The procedure involves mixing the dry ingredients first and adding liquid ingredients such as superplasticizers, water, admixtures etc. The mixing operation is performed at various speeds to ensure homogeneous fiber dispersion [18-36]. Following demolding after 24 hours, specimens usually cured sealed in plastic sheets until the testing date. Compressive and flexural strength testing followed related ASTM standards [37,38]

Table 1. Categorical Parameters

Parameters	Categories
Cement type	CEM I 52.5R, Type I OPC, CEM I 42.5N
Mineral admixture type	Limestone powder, Fly ash, Blast furnace slag, Silica fume, Natural pozzolan
Specimen geometry	Compression: Cylinder, Prism Flexure: Prism
Specimen dimensions	Compression: 40*40*40, 50*50*50, 75*150 Flexure: 40*40*160, 100*100*400, 75*50*360

Table 2. Dataset properties

Dataset for compressive strength of ECC			
Parameter	Unit	Min.	Max.
Age	Day	7	180
Cement content	kg/m^3	275	1000
Fiber content	% by volume	0.25	2
Water content	kg/m^3	74	638
Chemical admixture content	kg/m^3	1.8	30
Mineral admixture content	kg/m^3	0	2550
Calcium content of mineral admixture	% (by mass)	0	35.1
Silica content of mineral admixture	% (by mass)	0.3	78.1
Compressive strength	MPa	8.2	95.1
Flexural strength	MPa	0.3	23.75

3. Results and Discussion

A grid search algorithm was performed to establish learning rate and model architecture. Grid search algorithm was employed for both training and validation data. As mentioned in the previous chapter cross validation method is used to create validation data. Different node numbers were used in the range of 3 to 9 for each layer. Additionally, a learning rate range of 0.001-0.009 was also included in the search space. Range values for learning rates and node numbers were decided based on the literature [11-14]. ANN also known to be sensitive to weight initialization. The initial set of weights can cause the algorithm to be stuck in local minima eliminating the chance to find the global solution. Consequently, each architecture was run 10 times for each learning rate and the average values were recorded so the effect of weight initialization can be removed. In Table 3 learning rates are reported for the lowest RMSE yielding model after all values are applied in the learning rate range. As can be seen from this table increase in the node numbers did not always translate into a decrease in RMSE values. Final architecture was chosen to be 6 and 7 nodes at first and second hidden layers, respectively with a learning rate of 0.005. A similar grid search was performed for flexural strength model and the optimum architecture was selected to be 8 and 7 nodes in the first and second hidden layers, respectively.

Table 3. Grid Search for hyperparameters in compressive strength prediction model

Nodes	Nodes	LearningRate	RMSE Training	RMSE Validation	R2 Training	R2 Validation
4	3	0.005	5.953	5.193	0.93	0.92
	4	0.005	5.023	4.596	0.95	0.94
	5	0.004	5.248	4.748	0.94	0.93
	6	0.006	4.312	4.650	0.96	0.93
	7	0.006	4.805	4.524	0.94	0.94
	8	0.006	4.712	4.309	0.95	0.94
	9	0.007	4.250	4.271	0.96	0.95
5	3	0.007	4.337	4.329	0.96	0.94
	4	0.007	5.011	4.181	0.94	0.95
	5	0.007	4.147	4.250	0.97	0.95
	6	0.007	4.629	4.342	0.96	0.94
	7	0.007	4.629	4.342	0.96	0.94
	8	0.007	4.342	3.999	0.96	0.95
	9	0.007	4.776	4.227	0.95	0.94
6	3	0.004	4.322	4.566	0.99	0.95
	4	0.006	4.119	4.329	0.99	0.95
	5	0.007	3.721	4.137	0.97	0.94
	6	0.006	3.864	3.660	0.98	0.96
	7	0.005	2.881	3.899	0.99	0.96
	8	0.006	3.268	3.914	0.98	0.96
	9	0.005	3.041	3.838	0.99	0.96
7	3	0.007	3.666	3.591	0.98	0.97
	4	0.004	3.941	4.218	0.97	0.95
	5	0.004	4.376	4.209	0.98	0.95
	6	0.005	2.989	4.287	0.99	0.95
	7	0.006	3.992	3.846	0.97	0.96
	8	0.007	3.911	3.886	0.99	0.96
	9	0.007	3.971	3.769	0.98	0.96
8	3	0.005	4.005	4.209	0.98	0.95
	4	0.004	3.193	3.856	0.99	0.96
	5	0.007	3.625	3.927	0.98	0.96
	6	0.005	3.014	3.542	0.99	0.97
	7	0.006	3.158	3.406	0.99	0.98
	8	0.007	2.803	4.267	0.99	0.95
	9	0.006	4.064	4.067	0.98	0.96
9	3	0.007	3.495	3.679	0.98	0.96
	4	0.005	3.497	3.577	0.98	0.97
	5	0.007	2.694	3.438	0.99	0.97
	6	0.005	4.594	3.772	0.95	0.96
	7	0.004	3.938	3.671	0.97	0.98
	8	0.007	3.549	3.647	0.98	0.96
	9	0.007	3.890	3.843	0.98	0.96

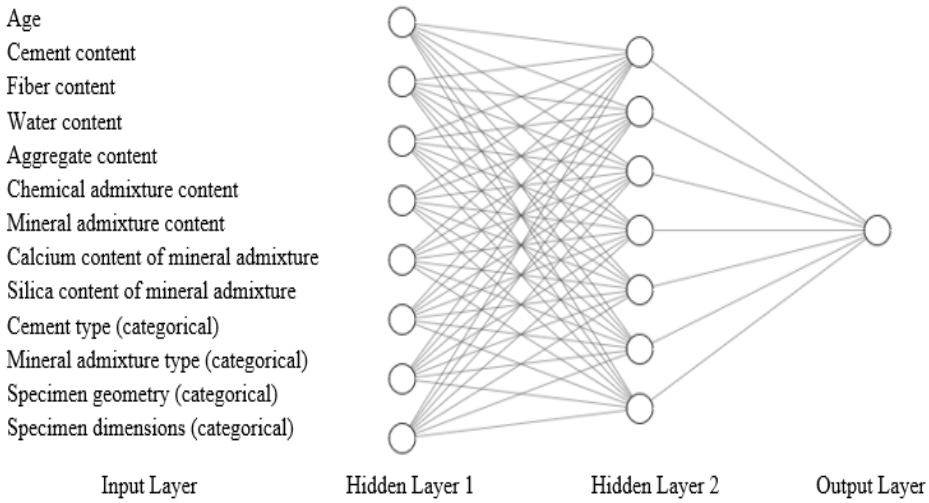

Fig. 1 ANN architecture

Architecture for flexural strength model is shown in the Fig 1. As for the Adam Optimizer, beta1 and beta 2 values were chosen as 0.9 and 0.999 which are already default values. Two prediction targets were defined in the output layer; compressive and flexural strength both in MPa as unit resulting in two different models. The average compressive and flexural strengths for the ECC mix designs used were 54.8 and 9.22 MPa. Predicted strength versus actual strength values for test data is presented in Figs 2 and 3. There are a couple of strength values that were both over and under predicted in compressive strength model however it can be seen from Fig 2 that majority of the predictions are within the close proximity (deviating around 1-1.5 MPa) of the actual strength value. The RMSE value for the test data is measured as 3.34 MPa, which is on the same range with reported values for ECC strength prediction in similar papers [12-14]. For flexural strength values it can be observed from Figure 3 the deviations from actual strength is much less compared to compressive strength. Accordingly, RMSE obtained from test data for flexural strength model is (0.35 MPa) much lower compared to that of compressive strength which is also similar in the reported literature.

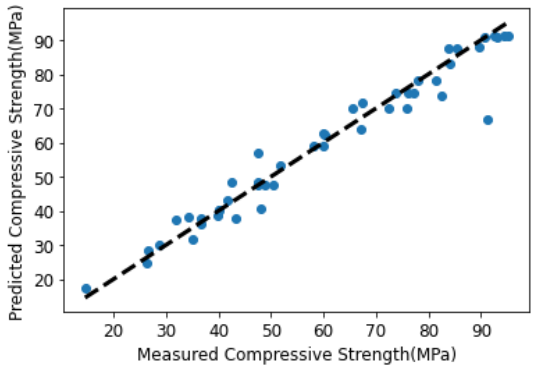

Fig. 2 Predicted compressive strength versus actual strength values for test data.

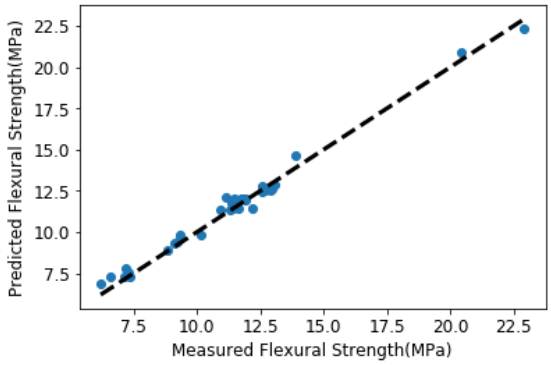

Fig.3 Predicted flexural strength versus actual strength values for test data.

Compared to literature available on strength prediction of ECC, accuracy of both compression and flexural strength models are either in the same range or superior. In addition to high accuracy, strength of a much wider range of ECC types and ages were predicted, mainly due to inclusion of categorical variables [1112,39]. An ANN model trained using data from a single batch of ECC offers very limited applicability. Additionally, high accuracy obtained from such model is most likely achievable by other predictive methods too because of the low variability in the training inputs. However, the literature available on ECC strength prediction is limited to models trained on ECC cast using a single batch with varying only ingredient quantities. Major difference of this work from limited literature works on ECC strength prediction is these ANN models predict strength of ECC with different components obtained from a wide range of data sources with the same accuracy as reported in single batch studies. Accuracy of the model is increased by inclusion of categorical parameters to the model unlike similar model trained in the literature. Predictive scores from test data and final hyperparameters of the ANN models for compressive and flexural strength is given in Table 4.

Table 4. ANN model results for compressive and flexural strength test data.

	Compressive Strength	Flexural Strength
MSE	11.120	0.121
RMSE	3.34	0.348
R2	0.958	0.967
Nodes	6 and 7	8 and 7
Learning rate	0.005	0.006

5. Conclusions

Strength prediction of ECC were performed in this study. Data from several papers with a wide range of mix design components were used. Different ECC types and mix designs from different sources in the literature were used which introduced a considerable variance to the dataset. Limited literature available on ECC strength prediction contained data from a single batch of concrete while only quantities of composite components are changing. Relative error values reported for the models trained using low variability data were around 2-10% for compressive strength and 3-5% for flexural strength. Two ANN models

were developed which predicted compressive and flexural strength of ECC. A grid search was also performed for selecting the model architecture and learning rate. Although architectures of the two models were different, a learning rate of 0.06 were proved to be optimal for both models. Number of layers were decided as two since most of the literature on cementitious composites and concrete materials proved to be 2-layer architecture was optimal for strength prediction. Relative errors for the models were 6.5% and 3% for compressive and flexural strengths, respectively. In addition, the models were able to predict strength of a wide range of ECC mixes with different specimen shape, specimen geometry, age, mineral and chemical admixture types with high accuracy.

The most important output of this study is the high accuracy obtained with a dataset created using data from various studies. Often when a dataset contains mixed data, accuracy reduces significantly due to increased noise in the data. This study used ECC mix design and strength values from 14 different sources and high accuracy in test data shows both models can be used for strength prediction. It must be noted that inclusion of categorical variables made it possible for the model to learn strength prediction for different ECC types and increased accuracy of the models.

Acknowledgement

The author wishes to thank Sinan Kefeli for helping with data preparation.

References

[1] Atici U. Prediction of the strength of mineral-addition concrete using regression analysis. Magazine of Concrete Research, 2010; 62: 585-92. https://doi.org/10.1680/macr.2010.62.8.585

[2] Bhanja S. Sengupta B. Investigations on the compressive strength of silica fume concrete using statistical methods. Cement and Concrete Research, 2002; 32: 1391-4. https://doi.org/10.1016/S0008-8846(02)00787-1

[3] Li VC, Wang S. Wu C. Tensile Strain-Hardening Behavior of Polyvinyl Alcohol Engineered Cementitious Composite (PVA-ECC). Materials Journal, 2001; 98: 483-492 https://doi.org/10.14359/10851

[4] Wang S, Li, VC. Engineered cementitious composites with high-volume fly ash. ACI Materials Journal, 2007; 104: 233-241. https://doi.org/10.14359/18668

[5] Pan Z, Wu C, Liu J, Wang W, Liu J. Study on mechanical properties of cost-effective polyvinyl alcohol engineered cementitious composites (PVA-ECC). ACI Materials Journal, 2015; 78: 397-404. https://doi.org/10.1016/j.conbuildmat.2014.12.071

[6] Yang EH, Yang Y, Li VC. Use of high volumes of fly ash to improve ECC mechanical properties and material greennes. ACI Materials Journal, 2017; 104: 620-628.

[7] Oztas A, Pala M, Ozbay E, Kanca E, Caglar N. Bhatti MA. Predicting the compressive strength and slump of high strength concrete using neural network. Construction and Building Materials, 2006; 20: 769-75. https://doi.org/10.1016/j.conbuildmat.2005.01.054

[8] Hong-Guang N, Ji-Zong W. Prediction of compress ive strength of concrete by neural networks. Cement and Concrete Research, 2000; 30: 1245-50. https://doi.org/10.1016/S0008-8846(00)00345-8

[9] Peng CH, Yeh IC, Lien LC. Building strength models for high-performance concrete at different ages using genetic operation trees, nonlinear regression, and neural networks. Engineering Composites, 2010; 26: 61-73. https://doi.org/10.1007/s00366-009-0142-5

[10] Yeh IC. Modeling of strength of high-performance concrete using artificial neural networks. Cement Concrete Research, 1998; 28: 1797-1808. https://doi.org/10.1016/S0008-8846(98)00165-3
[11] Shi L, Lin STK, Lu Y, Ye L, Zhang YX. Artificial Neural Network Based Mechanical and Electrical Property Prediction of Engineered Cementitious Composites. Construction and Building Materials, 2018;174: 667-74. https://doi.org/10.1016/j.conbuildmat.2018.04.127
[12] Hossain KMA, Anwar MS, Samani SG. Regression and artificial neural network models for strength properties of engineered cementitious composites. Neural Computing Applications, 2018; 29: 631-645. https://doi.org/10.1007/s00521-016-2602-3
[13] Altwair NM, Johari MAM, Hashim SFS. Influence of treated palm oil fuel ash on compressive properties and chloride resistance of engineered cementitious composites. Materials and Structures, 2014; 47: 667-682. https://doi.org/10.1617/s11527-013-0087-4
[14] Liu TY, Zhang P, Wang J, Ling YF. Compressive Strength Prediction of PVA Fiber-Reinforced Cementitious Composites Containing Nano-SiO2 Using BP Neural Network. Materials, 2020; 13: 1215-1229 https://doi.org/10.3390/ma13030521
[15] Ding, Y, Yu K, Mao W. Compressive performance of all-grade engineered cementitious composites: Experiment and theoretical model Construction and Building Materials, 2020; 24:1-11 https://doi.org/10.1016/j.conbuildmat.2020.118357
[16] Basheer IA, Hajmeer M. Artificial neural networks: fundamentals, computing, design, and application. Journal of Microbiological Methods, 2000; 43: 3-31. https://doi.org/10.1016/S0167-7012(00)00201-3
[17] Kingma D, Adam BJ. A Method for Stochastic Optimization. 3rd International Conference on Learning Representations, San Diego, CA, USA, May, 2015.
[18] Choucha S, Benyahia A, Ghrici M, Mansour MS. Effect of natural pozzolan content on the properties of engineered cementitious composites as repair material. Frontiers of Structural and Civil Engineering, 2018; 12: 261-269. https://doi.org/10.1007/s11709-017-0394-x
[19] Chung KL, Ghannam M, Zhang C. Effect of Specimen Shapes on Compressive Strength of Engineered Cementitious Composites (ECCs) with Different Values of Water-to-Binder Ratio and PVA Fiber. Arabian Journal for Science and Engineering, 2018; 43: 1825-1837. https://doi.org/10.1007/s13369-017-2776-8
[20] Yang EH, Yang Y, Li VC. Use of High Volumes of Fly Ash to Improve ECC Mechanical Properties and Material Greenness. Materials Journal, 2007, 104: 61-64 https://doi.org/10.14359/18966
[21] Li VC, Mishra DK, Wu HC. Matrix design for pseudo-strain-hardening fibre reinforced cementitious composites. Materials and Structures, 1995; 28: 586-595. https://doi.org/10.1007/BF02473191
[22] Sahmaran M, Yucel HE, Demirhan S, Arik MT, Li VC. Combined Effect of Aggregate and Mineral Admixtures on Tensile Ductility of Engineered Cementitious Composites. Materials Journal, 2012; 109: 115-124 https://doi.org/10.14359/51684160
[23] Noushini A, Vessalas K, Samali B. Static Mechanical Properties of Polyvinyl Alcohol Fibre Reinforced Concrete (PVA-FRC). Magazine of Concrete Research, 2014; 66: 122-31 https://doi.org/10.1680/macr.13.00320
[24] Pan J, Yuan F, Luo M, Leung K. Effect of composition on flexural behavior of engineered cementitious composites. China Technical Sciences Journal, 2012; 55: 3425-3433. https://doi.org/10.1007/s11431-012-4990-7
[25] Ramanathan P, Baskar I, Muthupriya P, Venkatasubramani R. Performance of self-compacting concrete containing different mineral admixtures. KSCE Journal of Civil Enginering, 2013; 17: 465-472. https://doi.org/10.1007/s12205-013-1882-8
[26] Şahmaran M, Al-Emam M, Yıldırım G, Şimşek YE, Erdem TK, Lachemi, M. High-early-strength ductile cementitious composites with characteristicsof low early-age

shrinkage for repair of infrastructures. Materials and Structures, 2015; 48: 1389-1403. https://doi.org/10.1617/s11527-013-0241-z
[27] Wang S, Li V. Engineered Cementitious Composites with High-volume Fly Ash. ACI Materials Journal, 2007; 104: 1-12 https://doi.org/10.14359/18668
[28] Yao Y, Zhu Y, Yang Y. Incorporation superabsorbent polymer (SAP) particles as controlling pre-existing flaws to improve the performance of engineered cementitious composites (ECC). Construction and Building Materials, 2012; 28: 139-145. https://doi.org/10.1016/j.conbuildmat.2011.08.032
[29] Zhou J, Qian S, Sierra Beltran MG, Ye G, van Breugel K, Li VC. Development of engineered cementitious composites with limestone powder and blast furnace slag. Materials and Structures, 2010; 43: 803-814. https://doi.org/10.1617/s11527-009-9549-0
[30] Ge WJ, Cai C, Ji X, Ashour AF, Cao DF. Experimental study of mechanical properties of PVA-ECC under freeze-thaw cycles. Journal of Testing and Evaluation, 2018, 46:1-8 https://doi.org/10.1520/JTE20160145
[31] Ji J, Zhang S, Jiang L, Zhou L, Xu Z, Liu Y, Yu D. Feasibility of developing engineered cementitious composite with high volumes of fly ash using cost-effective PVA fiber. Journal of Testing and Evaluation, 2018; 48: 1188-1205 https://doi.org/10.1520/JTE20170596
[32] Yıldırım G, Öztürk O, Al-Dahawi A, Afşın Ulu A, Şahmaran M. Self-sensing capability of Engineered Cementitious Composites: Effects of aging and loading conditions. Construction and Building Materials, 2020; 231: 1-16 https://doi.org/10.1016/j.conbuildmat.2019.117132
[33] Lee SW, Oh CL, Zain MRM, Yahya NA, Rahman AA. Mechanical performances of green engineered cementitious composites incorporating various types of sand. Key Engineering Materials, 2019, 821: 512-517 https://doi.org/10.4028/www.scientific.net/KEM.821.512
[34] Booya E, Gorospe K, Das S, Loh P. The influence of utilizing slag in lieu of fly ash on the performance of engineered cementitious composites, Construction and Building Materials, 2020, 256: 1-11 https://doi.org/10.1016/j.conbuildmat.2020.119412
[35] Chung KL, Xie S, Ghannam M, Guan M, Ning N, Li Y, Zhang C. Strength Prediction and Correlation of Cement Composites: A Cross-Disciplinary Approach. IEEE Access, 2019; 7: 41746-41756 https://doi.org/10.1109/ACCESS.2019.2908042
[36] Sherir MAA, Hossain KMA, Lachemi M. Fresh state, mechanical & durability properties of strain hardening cementitious composite produced with locally available aggregates and high volume of fly ash. Construction and Building Materials, 2018; 189: 253-264 https://doi.org/10.1016/j.conbuildmat.2018.08.204
[37] ASTM C109. Standard Test Method for Compressive Strength of Hydraulic Cement Mortars (Using 2-in. or [50-mm] Cube Specimens). Annual Book of ASTM Standards, PA, USA; 2012.
[38] ASTM C348 Standard Test Method for Flexural Strength of Hydraulic Cement Mortars Annual Book of ASTM Standards, PA, USA;2008.
[39] Samani SG, Yeganeh AE, Hossain KMA. Prediction of strength properties of engineered cementitious composites using artificial neural network. Proceedings of Annual Conference - Canadian Society for Civil Engineering, Canada, June, 2015.

Research on Engineering Structures & Materials
journal homepage: http://jresm.org
MIM Research Group

Research Article

Performance evaluation of geopolymer concrete using E-waste and M-sand

Pachaivannan Partheeban[*1,a], A. R. R. Kalaiyarrasi[2,b], Lakshmi Narayanan P. B[3,c]

[1]*Department of Civil Engineering, Chennai Institute of Technology, Chennai, Tamilnadu, India.*
[2]*Department of Civil Engineering, St. Peters' Institute of Higher Education, Chennai, Tamilnadu, India.*
[3]*Department of Civil Engineering, St. Peters' College of Engineering and Technology, Chennai, Tamilnadu, India.*

Article Info

Article history:
Received 02 Dec 2020
Revised 09 Mar 2021
Accepted 30 Mar 2021

Keywords:

Geopolymer Concrete;
E-Waste;
M-Sand;
GGBFS;
Aggregates;
Strength

Abstract

This study has been conducted to diminish the carbon footprint of concrete and to assess the performance of geopolymer concrete by completely replacing river sand with Manufactured sand (M-Sand) and Electronic Waste (E-waste). Fly ash and Ground Granulated Blast Furnace Slag (GGBFS) are used in various combinations as a cementitious material in geopolymer concrete. The characteristic strength of geopolymer concrete is obtained by completely replacing fine aggregate with E-waste and M-sand with different percentages. An optimum percentage replacement is arrived at by studying the physical, chemical, and mechanical characteristics. The sizes of the E-waste particles used in this research are between 0.3mm and 0.15 mm and it has a deep colour with a specific gravity of 2.68. Maximum compressive strength of 35.8 N/mm^2 on 28 days is achieved for the optimal mix proportion of 80% fly ash, 20% GGBFS, 80% M-sand, and 20% E-waste as fine aggregate. Maximum flexural strength obtained is 6.54 N/mm^2 for mix proportion 1 and split tensile strength is 4.75 N/mm^2 resulted in mix proportion 2. The use of fly ash, E-waste, and M-sand in geopolymer concrete reduce the environmental pollution and depletion of natural river sand. The results of this experimental study very well match with Indian standards of concrete.

1. Introduction

The most popular artificial construction material on earth is concrete. Concrete is used in construction to build structures for thousands of years. The invention of high-strength concrete is a breakthrough in the field of materials used for construction. Usually, conventional concrete is associated with Portland cement as the main constituent for making concrete. In the modern world, most structures are built using concrete which creates a huge demand for concrete.

The disposal of e-waste is another worldwide environmental problem and public health issue [1]. Direct disposal of E-waste is not possible since it contains composite materials. Impacts of river mining include changes in floodplains profile, river hydraulics, sediments, and the climate [2]. To analyze the nature of binding with fine and coarse aggregates different proportions of binding materials added to the geopolymer concrete.

Global warming and climate change pose a threat to our environment. About 65% of global warming is due to the emission of CO_2, one of the greenhouse gases. Cement factories are accountable for around 6% of all CO_2 emissions. Approximately one ton of Carbon-di-oxide

*Corresponding author: parthi011@yahoo.co.in
[a] orcid.org/0000-0003-4345-0741; [b] orcid.org/0000-0002-5408-9544; [c] orcid.org/0000-0001-7366-7402
DOI: http://dx.doi.org/10.17515/resm2020.234ma1202

is released when one ton of Portland cement is produced. The term 'geopolymer' was coined by Davidovits in 1978 [3]. Geopolymer is synthesized from silicon and aluminium rich material either of the geological origin or industrial by-products like fly ash. Zeolite and geopolymer have similar chemical compositions but geopolymers exhibit amorphous microstructure and hence stronger compared to zeolites. Alkaline solutions aid the dissolution of Si and Al in the source materials and form a gel. The polymerisation process is quickened by curing at elevated temperatures.

The Egyptian pyramids were built using geopolymer methods of construction as presented by Davidovits in his research**.** Davidovits has proved that geopolymer material has good mechanical properties, high resistance to acidic solutions, and no alkali-aggregate reaction even in the occurrence of high alkalinity. Geopolymers are beneficial in structures exposed to harsh environments such as marine locations and sewers. Precast railway sleepers and hazardous waste encapsulation are some of the immediate applications of geopolymer concrete.

The geopolymer research work carried out by Palomo et al [4] is related to binder paste or mortar in a small size sample. The form of activator, curing temperature, and curing time were found to be the controlling factors for the mechanical strength of a fly ash-based geopolymer binder in their research. The alkaline solution to fly ash ratio had no influence. An increase in curing temperature has exhibited an increased compressive strength. Alkaline activator, which contains soluble silicates, reacts faster than the solution containing hydroxide only.

While Van Jaarsveld et al [5] ensured the importance of curing at a superior temperature for FA-based geopolymer material, they also insisted that curing for a prolonged period at superior temperature weakens the microstructure. Barbosa et al [6] stated that the total water quantity influences the characteristics of geopolymer binders, besides the chemical composition of the oxides employed as activators.

Lenin Sundar et al [7] studied the Geopolymer concrete with E-Waste as a partial replacement of fine aggregate. Their research is to replace the sand with E-waste at 10%, 20%, and 30%. 12 M Sodium hydroxide (NaOH) solution and sodium silicate (Na_2SiO_3) solution are used as alkaline liquids. 90 % of fly ash and 10 % of GGBS are used as binders. He conducted the research to better understand the relationship between geopolymer concrete compressive and tensile strength and E-waste. It was discovered that substituting 20% E-Waste for standard geopolymer concrete of M40 grade resulted in a higher intensity. Mahaboob Basha et. al. [8], have studied the effect of E-waste and M-sand as a replacement for river sand and arrived at the optimum percentage level to improve the characteristic strength of geopolymer concrete, replaced with 10%, 20%, 30%, 40%, and 50 % of E-waste and M-sand as a fine aggregate, and find out the optimum percentage replacement.

Gayathri et al. [9] investigated the effect of e-waste in concrete on the mechanical properties of geopolymer concrete. In this study, e-waste was used to substitute sand in the following proportions: 0%, 10%, 20%, 30%, 40%, and 50%. Furthermore, the strength characteristics of geopolymer concrete cubes, beams, and cylinders with varying E-waste mix ratios were investigated. Balasubramanian et. al., [10], have studied the mechanical strength of cement concrete with E-Waste as coarse aggregate, partially replacing conventional coarse aggregate. Different forms of traditional concrete cubes were partially replaced with E-waste at a rate of 10%, 15%, 20%, 25%, and 30% to coarse aggregate with a water-cement ratio of 0.5.

The aim of Kale and Pathan [11] was to compare the strengths of concrete with fresh concrete, waste concrete, and E-waste concrete. Various mix ratios are adopted by varying

Cement, sand, and aggregates for a design mix M25. Krishna Prasanna [12] looked into the output of concrete that included E-waste as part of the coarse aggregate. In an experiment, specimens were prepared using E-waste as coarse aggregates in concrete up to 20% of the amount of traditional coarse aggregate. Sourav Kr. Das et al., [13], gave an overall view of the process and parameters which affected the geo-polymer concrete. It was found that geopolymer concrete made of fly ash as the binder or GGBS and fly ash as the binder, resulted in an 80% reduction in CO_2 emission compared to OPC, even though the alkaline solution pollutes the environment to some extent. Ganapati Naidu [14] studied the mechanical properties of geopolymer concrete using Class F fly ash and slag in different percentages. Sodium silicate and sodium hydroxide solutions were used as activators. With 28.57% replacement of slag, maximum compressive strength of 57MPa in 28 days in ambient curing and 43.56 MPa when cured in 500°C for 2 hours was attained.

The performance of geopolymer concrete with steel slag as coarse aggregate was investigated by Palankar and Ravi Shankar [15]. GGBFS-FA geopolymer concrete with steel slag coarse aggregates was made by substituting natural granite aggregates for 0%, 25%, 50%, 75%, and 100% of the time, and the mechanical properties of the concrete were investigated. Mechanical intensity had decreased slightly as a result of the experiment. The water absorption and volume of permeable voids of Geopolymer concrete with FA-GGBS as binder and steel slag as coarse aggregate had a little higher value but within permissible limits. Steel slag as coarse aggregate was satisfactory for structural and pavement applications. Felixkala and Partheeban [16] carried out an experimental study on high-performance concrete made using granite powder as fine aggregate. They have achieved the highest compressive strength that contains 25% granite powder.

Smit and Kearsley [17] studied the influence of paste content on the properties of HSC used in UTCRCP. Two pieces of concrete were tested. The paste quality of the first package was from 23 percent to 37 percent by quantity, using Multivariate Analysis in combination with a superplasticiser (SP) dosage. The paste quality of the second package was from 25 percent to 60 percent by bulk, with only differing SP dosage to monitor workability. It could be seen from the findings that the rise in the paste content of HSC usually has a negative effect. The paste content of HSC used in UTCRCP should be reduced while preserving reasonable workability. Kessy et al., [18] suggested the means of redrafting and incorporating the reliability requirements of every revamped edition of SANS 10100-2, taking into consideration both the prescriptive and the performance alternatives. Besides, a framework for designing sustainable standards suitable for the South African concrete industry is suggested and proposals for potential improvements are made.

Assaggaf et al. [19] proposed an experimental study to assess the effect of Accelerated Carbonation Curing (ACC) on the performance of two concrete mixtures of identical proportions but different cement materials (plain-cement and fly-ash-blended-cement). When ACC-treated specimens were exposed to sunlight, the intensity increased significantly, lasting up to seven days for plain concrete and up to 28 days for fly ash-blended concrete. ACC-treated concrete was found to have a slightly lower long-term strength than moist-cured concrete (15 percent for plain cement and 5 percent for fly ash-concrete). Nonetheless, the ACC-treated concrete mixtures' average output was comparable to that of the corresponding moist-cured concrete mixtures.

Kannan and Ganesan [20] investigated the fresh condition and mechanical properties of self-compacting concrete (SCC) made with binary and ternary cement mixtures of metakaolin (MK) and fly ash (FA), as well as the interrelationships between them. For this reason, various mixtures were prepared with different amounts of MK and fly ash by substituting 5 to 40 percent of ordinary Portland cement (OPC) for MK or FA. As a result of the increase in the proportion of MK, FA, and MK+FA, the mechanical properties of SCC

increased considerably. It was observed that the specimen containing the ternary mixture of cement with 15 percent MK and 15 percent FA exhibited greater workability and mechanical properties than that of the standard SCC specimen without MK or FA.

Shinde et al. studied the mechanical properties of geopolymer concrete made from fly ash [21]. For preparing geopolymer concrete with fine fly ash, they used a 13 molar concentration solution. They also performed compression, split tensile, and flexural strength tests on specimens that had been cured in an oven at 110°C for 7 hours and tested after 7 and 28 days.

Ahmet Emin Kurtoglu et al. [22] performed a report on the mechanical and toughness properties of fly ash and slag-based geopolymer concrete. The study's aim was to equate geopolymer concrete to traditional Portland cement concrete. Because of its more robust and strong cross-linked alumina silicate polymer structure, slag-based Portland cement concrete is found to be stronger and more reliable than fly ash-based geopolymer concrete in this report.

The review of the literature indicates that the construction sector will gain more importance soon due to economic and industrial development. Based on the literature review the following objectives are framed:

- To assess the mechanical properties of geopolymer concrete by replacing fine aggregate with M-Sand and E-waste and using different binders such as fly-ash and GGBFS.
- To investigate the durability of fly ash, GGBFS-based geopolymer concrete containing M sand and E-waste.
- To assess the maximum amount of E-waste that can be replaced without compromising strength.

The hypothesis of the research is to find out the relationship between various mix proportions of the concrete and the strength of the geopolymer concrete. The use of fly ash and GGBFS in geo-polymer concrete and replacing M-sand and E-waste in the place of fine aggregates drastically reduces the energy involved in producing the construction materials. Molarity of sodium hydroxide (NaOH) solution was chosen in the range of 14M. The ratio of activator solution-to-fly ash is used in this study is 0.40. Ambient curing is adopted. The aim of this research is to investigate the use of M-sand and E-Waste as a complete substitute for fine aggregate in Geopolymer concrete in order to reduce contamination, reduce natural river sand depletion, and allow use of non-biodegradable waste.

The use of M-sand and E-waste in place of fine aggregate, as well as fly ash, is the subject of an extensive experimental investigation on eco-friendly geopolymer concrete. In this experimental study, the alternative binders, fly ash, and GGBFS in the combination of (90:10), (80:20), (70:30), (60:40), and (50:50) percent are used. Fine aggregate is replaced by crushed granite called Manufactured sand **(** M-sand) and Electronic Waste (E-waste), which is almost impossible to dispose of and hazardous to the environment, in combinations of (90:10), (80:20), (70:30), (60:40) and (50:50) percent respectively. The general alkaline liquid used in geo polymerisation is a 2.5:1 mixture of sodium silicate (Na2SiO3) and sodium hydroxide (NaOH).

2. Properties of Materials

2.1. Properties of Fly ash and M-sand

Depending on the type of fly ash and its degree of reactivity, it is used in concrete. Fly ash is divided into two types: Class F (low calcium) and Class C (high calcium). Class F fly ash is used in this study, as described by IS 3812 (Part 1) [23], and the properties are mentioned in Table 1.

Table 1. Physical Properties of Fly Ash

Sl. No.	Test	Results	Requirements as per IS 3812
1	Normal consistency (%)	31.98	Not specified
2	Initial Settings time (min)	326	-
3	Final settings time (min)	513	-
4	Soundness (%)	0.6	0.8
5	Comparative compressive strength at 28 days (min) %	81.56	Not less than 80% of the strength corresponding to plain cement mortar cubes
6	Residue on 45-micron (max) %	25.56	34 and 50 (IS 3812(Part2)-2013

GGBFS may be used to make a strong concrete foundation when combined with ordinary Portland cement and/or other pozzolanic materials. GGBFS may be replaced with cement varying from 30 % to 85 %. The GGBFS used in this research is as per the BS: 6699-1992. Coarse aggregates used in this research are 20 mm and 12 mm and their properties are within the range as per IS 2386 (part 3 and part 4) [24 and 25]. Crushing granite stones to fine aggregate size results in Manufactured sand, which can replace the conventional one. Fine aggregate within the size of 4.75 mm to 0.075 mm is used in this investigation. Properties of M- sand are arrived at in confirmation to relevant code and tabulated in Table 2.

Table 2. Properties of M Sand

SI. No.	Properties	Values	Code used
1	Specific Gravity	2.72	IS:2386(Part 3)
2	Water Absorption	2.18 %	IS:2386(Part 3)
3	1.Bulk Density (Loose)	15561856Kg/m^3	IS:2386(Part 3)
	2.Bulk Density (Rodded)	17421856Kg/m^3	IS:2386(Part 3)
4	Silt Content by Volume	3.16 %	IS:2386(Part 2)
5	Bulkage	2.0 %	IS:2386(Part 1)
6	Moisture Content	1.41 Ton	IS:2386(Part 4)
7	Organic Impurities	Nil	IS:2386(Part 4)
8	Deleterious Materials		
	a) Clay Lumps	Nil	IS:2386(Part 2)
	b) Materials Finer than 75µ	Nil	IS:2386(Part 2)
9	Chloride	0.016 %	IS:2386(Part 1)
10	Sulphate	0.22 %	IS:2386(Part 1)

2.2. Properties of E-waste

Electronic wastes are generated from circuit boards of discarded electronic devices and toughened glass from display units. These waste materials, mostly printed circuit boards

and glass in the pulverised form, are used in concrete to decrease environmental pollution. The sizes of the particle are in the range between 0.3 mm and 0.15 mm and have a dark colour. The most important process in this research is the collection and grinding of E-Waste into the required size. In this study, E-Waste replaces fine aggregate. E-waste products used in this investigation are outlined in Table 3.

Table 3. Properties of E-Waste

Sl. No.	Properties	Values
1.	Specific gravity	2.68
2.	Water absorption	0.121%
3.	Fineness modulus	2.507
4.	Bulk density (loose) Bulk density (rodded)	1856Kg/m^3 2089Kg/m^3
5.	Lead content	4.28
6.	Type	Crushed
7.	Grade	III

2.3. Properties of Alkaline Solution and Superplasticisers

For their consistency, sodium silicate and sodium hydroxide (NaOH) solutions are favoured over potassium silicate and a mixture of potassium hydroxide (KOH). 14M Sodium hydroxide (NaOH) solution is employed in this research. Auramix 500 is a polycarboxylic ether polymer-based superplasticiser, with long lateral chains. Upon mixing with concrete, the occurrence of electrostatic dispersion allows cement particles to separate each other. The above procedure reduces the water demand in making flowable concrete. It helps with high workability in manufacturing high-performance concrete. Auramix 500 complies with IS: 9103-1999 [26]. It also meets Type F and G of ASMT C494 [27], depending on the dosage used. The standard dose range is from 0.3 to 2.0 kg/100 kg of cemented material (see Table 4).

Table 4. Properties of Superplasticisers (Auramix 500)

Description	Parameter
Appearance	Light yellow coloured liquid
pH	Minimum 6.0*
Volumetric mass @ 200 C	1.100 ± 0.02 kg/litre
Alkali content	Typically, less than 1.5 g Na2O equivalent/litre of admixture.

2.4. Experimental Investigation

Davidovits [28] proposed combining the sodium silicate and sodium hydroxide solutions a day ahead of time. Table 5 shows the proportions of the blend used in fly ash replacement and GGBFS. The different mix quantities used to prepare geopolymer concrete are shown in Table 6. Fly ash and GGBFS are used in varying amounts as binding materials, while manufactured sand and electronic waste are used as fine aggregate.

Table 5. Mix Proportion Adopted for Various Design Mix

Sl. No.	Mix	Fly ash (%)	GGBFS (%)	M-sand	E-waste
1	M1	90	10	90	10
2	M2	80	20	80	20
3	M3	70	30	70	30
4	M4	60	40	60	40
5	M5	50	50	50	50

Table 6. Mix Quantity for $1M^3$ for Concrete

Sl. No.	Materials	Mix1 (kg)	Mix2 (kg)	Mix3 (kg)	Mix4 (kg)	Mix5 (kg)
1	Fly ash	150	130	120	100	85
2	GGBFS	20	40	50	70	85
3	Coarse aggregate 20mm	280	280	280	280	280
4	Coarse aggregate 12mm	190	190	190	190	190
5	M-sand	271	247	214	185	152
6	E- waste	33	57	90	119	152

Dry mix with fly ash, GGBFS, and aggregates blended in a mixer machine for around 5 minutes. The alkaline solution is mixed with the dry mix for another 5 minutes. The cube and cylinder specimens are compacted by tamping each layer 35 times into three layers. Further specimens are compacted for 10 seconds using a vibrating table. Specimens such as cubes, cylinders, and prisms are cast and tested. After casting the concrete, a mix could be settled down in the moulds for 30 minutes.

Two forms of curing are used in this study, namely, curing at room temperature and curing for laboratory ovens at an elevated 60^oC temperature. The concrete is kept in the mould for 30 minutes. The specimens are permitted to cool in air, demoulded, and kept open until the day of testing. The specimens are kept at 60°C in the hot air to be cured; the geopolymer concrete experiences polymerisation processes when the specimens keep curing. The specimens are cured at elevated temperature and due to that, the concrete attains 70% of its strength within 3 to 4 hrs of curing. GPC's compressive strength depends on both curing time and temperature. Having a curing temperature in the range of 60°C to 90°C for 24 to 72 hours, the concrete's compressive strength can be obtained from about 400 to 500 kg.

2.5. Preparation of Tests Specimens

Specimens were cast in three layers, giving proper compaction. The specimens were demoulded and held at room temperature for 7, 14, and 28 days after casting. The test specimens such as a cube, cylinder, and prism are cast for studying the mechanical and chemical properties. Table 7 lists the measurements of the different specimens used in the current study. Specimens were designed according to the following testing conditions:

- Mix ratios used: M1, M2, M3, M4, M5.
- Curing duration: 7, 14, and 28 days.
- Concentration NaOH used: 14M.
- Curing: at room temperature.
- The ratio of alkaline activator solution-to-FA, by mass: 0.40.
- Mix Ratio: The trial ratio used 1: 1.84: 3.02.
- The ratio of sodium silicate -to-sodium hydroxide solution used: 1:2.5.

Table 7. Details of Specimen

Material Properties	Shape	Dimensions of the Specimens (mm)
Compressive Strength	Cube	150 × 150 × 150
Flexural Strength	Prism	100 × 100 × 500
Split Tensile Strength	Cylinder	100 × 150

2.6. Mechanical Properties of Concrete

A detailed experimental study on eco-friendly concrete that replaces fine aggregate with M-sand and E-waste was conducted. This investigation is performed with FA and GGBFS as binders in the combination of (90:10), (80:20), (70:30), (60:40) and (50:50) percent, respectively, and similarly fine aggregates are replaced in the same proportion by M-sand and E-waste. The strength of Geopolymer concrete in compression, tension, and flexure is found as per IS 516-1959 [29].

Compressive strength checks are carried out at 7, 14, and 28 days of age. Concrete resists compression and offers much less resistance to tension. Concrete roads subjected to flexural loading experience high tensile stresses. Flexural strength testing in the laboratory was carried out by beam test. According to IS 516-1959 [29], if the aggregate's largest nominal size does not exceed 20 mm, a prism of about 100 mm /100 mm /500 mm may be employed. Third point loading is used in a flexural strength test to replicate pure bending conditions. In the third point loading method, a crack may appear somewhere in the middle third of the span where the bending moment is maximum.

To determine split tensile strength of concrete, a Universal Testing Machine (UTM) with a capacity of 1000 kN, 100 mm diameter, and 150 mm height cylinder sample is used. Four-cylinder test specimens are averaged for split tensile power.

2.7 Durability Tests on Concrete

The durability of concrete is tested to ascertain its performance over time and in harsh climatic conditions. The following experiments were carried out to determine concrete's durability.

- Water Absorption
- The resistance of GPC blocks in 3% sulphuric acid.
- Residual Compressive Strength
- Residual Split Tensile Strength
- Change in Weight
- pH value of the solution

The water absorption test was carried out on 100 mm cubes according to ASTM C 642 [30] to determine the permeability characteristics of the geopolymer concrete over a span of 7, 14, and 28 days. Both the specimens which are cured at room temperature and 60°C are tested for the criteria for water absorption. The absorption percentage was calculated using equation (1). Table 8 shows the recommendations given by the Concrete Society Board.

$$\text{Absorption Percentage} = \frac{W_2 - W_1}{W_1} \times 100 \quad (1)$$

where

W1 = Weight of specimen after complete drying at 105°C (kg).

W2 = Final weight of the surface dry sample after immersion in water (kg).

Table 8. Assessment Criteria for Absorption

Absorption (%)	Absorption Rating	Concrete Quality
<3.0	0	Low Good
3.0 to 5.0	Average	Average
>5.0	High	Poor

The durability of e-waste and M-sand geopolymer concrete under severe exposure conditions was tested by immersing 28 days ambient temperature and elevated temperature cured 15 cm concrete cubes in 3% H_2SO_4 solution. In-room temperature conditions, the acid immersion test was conducted, and the acid solution was regularly stirred to ensure consistency. To maintain a constant concentration at regular intervals, the acidic solution was substituted. The cubes were separated from the solution after 7, 14, and 28 days of immersion. The surface is dressed in a nylon brush to remove any loose material and allow the surface to dry. The weights of the cubes were compared to the weights of respective concrete geopolymer cubes before immersion. After 7, 14, and 28 days of acid immersion, the cubes were tested for residual compressive and tensile strength.

Hardened concrete ought to be alkaline. Reduction in alkalinity caused damage to concrete and therefore a pH of 28 days cured Geopolymer concrete was tested. The mortar portion of the hardened concrete was crushed to ≤ 4 mm size. 20 grams of crushed mortar sample was diluted in 200 ml demineralized water or distilled water (15°C). The liquid is stirred for ±10 min before measurement of pH using a pH meter.

3. Results and Discussion

Geopolymer concrete workability with fly ash and GGBFS as binders has been studied and the slump values for four mixes are given in Table 9. With the increase in concrete grade, the water-to-geopolymer solids ratio decreases, and hence the workability decreases. With the NaOH solution's increased molarity, the water content decreases, and hence the geopolymer concrete's workability is good. From Table 9, the mix of M1 is a higher slump value and gradually decreases the slump values with other mix proportions. This is due to adding a higher percentage of GGBFS, the binding is good.

Table 9. Slump Values for Different Grades

Sl. No.	Mix Designation	Slump(mm)
1	CM	120
2	M_1	112
3	M_2	110
4	M_3	104
5	M_4	100
6	M_5	98

4. Mechanical Properties

Strength of ambient cured GPC in compression, tension and flexure were evaluated at 7, 14, and 28 days of age using appropriate specimens and tested as per IS 516-1959 [29].

4.1. Compressive Strength

The side cube of 150 mm is used to check geopolymer concrete compression, and the specimens are filled before failure. The results were obtained from the tests conducted and presented in Fig. 1.

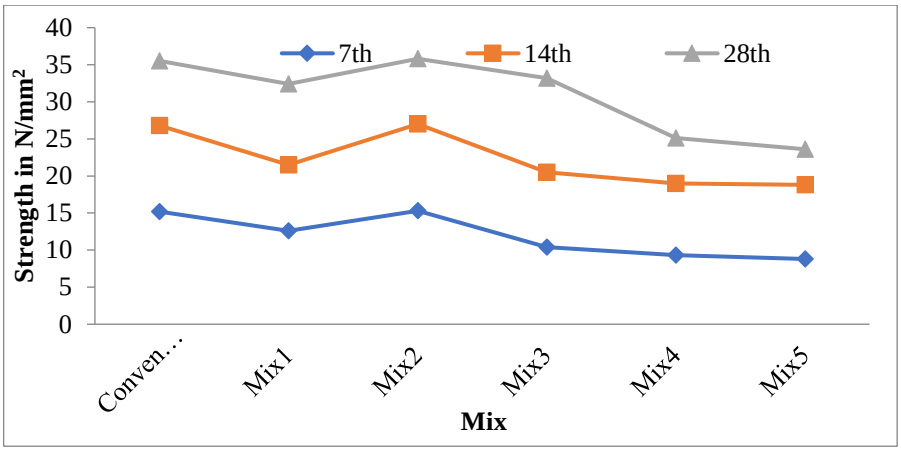

Fig. 1 Compressive Strength of Concrete

Mix 2 is more compressive than the other blends. At 28 days, the GPC compression power of Mix 2 is equivalent to standard concrete. For mix proportion 2, Figure 1 indicates that the compressive strength of the concrete increases as the concrete ages. The remaining amounts of the blend will be reversed. The maximum compressive strength of the E-waste and M-sand-based geopolymer concrete is 12.5 % less than the study results of Nagajothi Subramanian and Elavenil Solaiyan [31 and 32]. The low compressive strength is due to the addition of electronics waste in concrete.

4.2. Flexural Strength

Strength of GPC in flexure is tested using 500 x 100 x 100 mm prism specimen. The prism is then loaded at its centre point until failure. The flexural strength values obtained from the test are presented in Fig. 2.

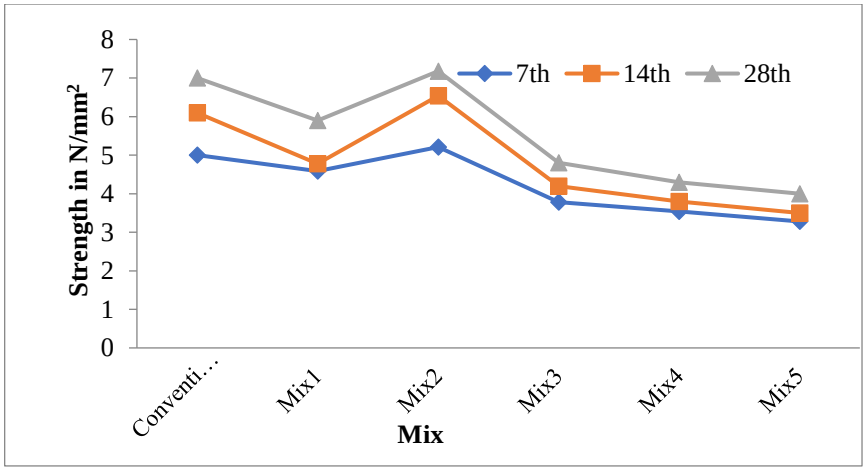

Fig. 2 Flexural Strength of Concrete

Mix 2 shows better flexural Strength than other mixes. Mix 2 and conventional concrete mix shows similar Flexural Strength of about 5 N/mm^2. Mix 1 too, yields better flexural strength approx. 5 N/mm^2 (on 7th day). The mix 2 proportion is achieved maximum flexural strength concerning the age of the concrete as like conventional concrete. The flexural strength of concrete results very well matches with results of [31, 32].

4.3. Split Tensile Strength

A 150 mm diameter and 300 mm height cylindrical concrete specimen is used to determine the split tensile strength. The cylinder is then subjected to a tensile load until failure. The Split tensile strength of all the blends was depicted in Figure 3. Split tensile strength is higher in Mix 2 than in the other blends. Mixes 3, 4, and 5 have low break tensile strength. Mix1, Mix2, and conventional concrete mix show similar split tensile strength of 3 – 3.5 N/mm^2 on the 7th day. Split tension test results are slightly higher than test results of [31, 32].

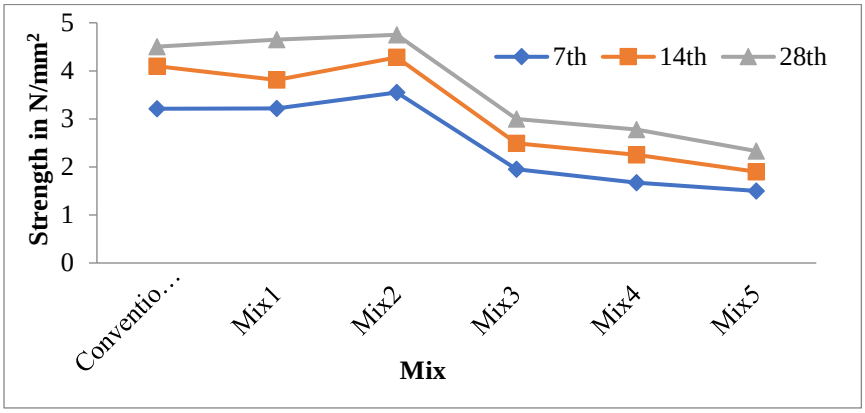

Fig. 3 Split Tensile Strength

5. Durability Properties

5.1. Water Absorption Test

The concrete cubes are immersed in water for 24 hrs and then the cubes are taken out and wiped, then weighed, again. The percentage of water absorption decreases with a rise in NaOH concentration from M1 to M4 as seen in Table 10.

Table 10. Percentage of Water Absorption of Concrete

Sl.No.	Mix	Weight of concrete before immersing water	Weight of concrete after immersed in water for 28 days	% of water absorption
1	Conventional Mix	8.82	8.90	4.50
2	Mix 1	8.70	8.79	4.24
3	Mix 2	8.48	8.60	4.15
4	Mix 3	7.81	7.80	3.85
5	Mix 4	7.66	7.79	3.74
6	Mix 5	6.79	6.96	3.44

5.2. Residual Compressive Strength

Cubes specimen are tested for residual compressive strength on the 7th, 14th, and 28th day of immersion in 3 % H2SO4 solution. The residual compressive strength of concrete with various mix ratios is depicted in Figure 4. The compressive residual strength of Mix 2 is higher than that of the other blends. Since E-waste combines slowly with an alkaline solution and reduces mortar binding strength, Mix 3, Mix 4, and Mix 5 have low residual compressive strength. Mix 2, which had the same compressive strength as traditional concrete at 28 days, had less residual compressive strength at 28 days than conventional concrete.

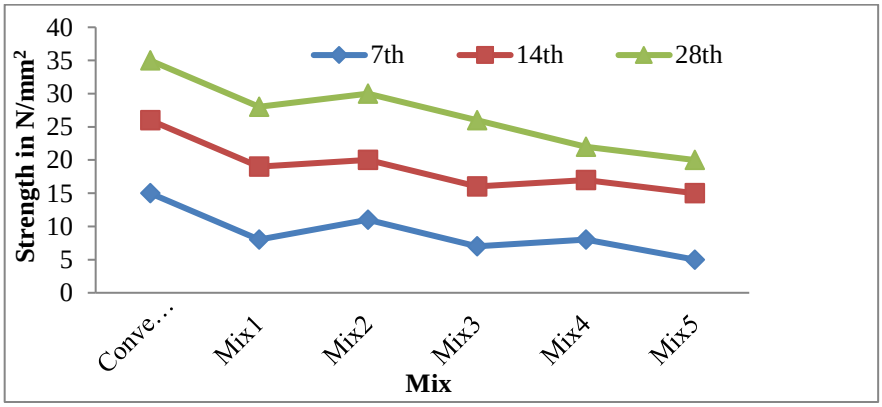

Fig. 4 Residual Compressive Strength

5.3. Residual Split Tensile Strength

The residual split tensile strength of a cylindrical concrete specimen with a diameter of 150 mm and a height of 300 mm is determined after immersion in acid for 7 days, 14 days, and 28 days. The cylinder is then subjected to tensile load until it fails. From the tests conducted, the results obtained are presented in Fig. 5.

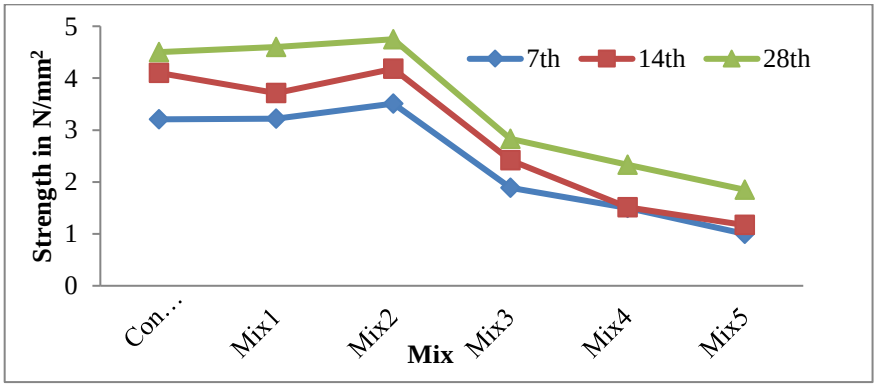

Fig. 5 Residual Split Tensile Strength

Mix 2 shows better split tensile strength than the other mixes. Mix 3, mix 4 and mix 5 show poor residual split tensile strength. Mix 1 and Mix 2 show similar split tensile strength of 3 – 3.5 N/mm² (on the 7th day).

5.4. Change in Weight and pH Value

The concrete cubes of various mixes are weighed in a weighing machine and compared with one another. pH measurements on the 28 days hardened mortar samples were measured, by diluting 20 grams of crushed ≤ 4 mm mortar sample in 200 ml demineralized water or distilled water (15°C). The total liquid is stirred for ±10 min before pH measurement and a pH meter is used for measuring pH values. Table 11 shows the change in weight and pH values of the specimen.

Table 11. Change in Weight of Concrete

Sl. No.	Mix	Mean Weight of Concrete in Kg	pH value
1	Conventional mix	8.88	12.80
2	Mix 1	8.74	12.62
3	Mix 2	8.5	12.58
4	Mix 3	7.33	12.46
5	Mix 4	7.68	12.41
6	Mix 5	6.86	12.37

The strength of the concrete is 35 N/mm^2 is above the standards of nominal concrete.

6. Conclusions

Eco-friendly concrete based on GGBFS and fly ash has gained strength at ambient temperature with an earlier period. High-temperature curing is eliminated due to adding GGBFS. Workability of E-waste and M-sand based geopolymer concrete is in the range 98 mm to 112 mm and it is less than the conventional concrete 120 mm when Geopolymer concrete's strength was more due to the higher percentage of GGBFS in the mix. Mix 1 had a higher compressive strength at first. Mix 2 was found to have a maximum compressive force of 35 N/mm^2 after 28 days. Furthermore, as the mix proportion is increased, the compressive strength of concrete reduces. The findings of the compressive strength test are consistent with those of other related tests. The results of the flexural and split stress tests were 7 N/mm^2 and 5 N/mm^2, respectively, and they were in fair agreement with other trials. Water absorption test results range from 3.44 % to 4.24 %, which is better than standard concrete water absorption.

Mix proportion 3, 4 and 5 show poor performance in all its experimental properties as E-waste steadily reacts with the alkaline solution and changes the colour of the concrete and does not allow the cementitious material to bind with one another. Thus, it results in lower strength of the hardened mortar. As a result, mix 2, consisting of 80 percent fly ash, 20 percent GGBFS, 80 percent M-sand, and 20 percent E-waste, is found to be the optimum mix proportion for eco-friendly concrete that provides outstanding strength and properties. Furthermore, geopolymer concrete made with GGBFS and fly ash has high compressive strength and is suitable for structural applications. Fine aggregates and binding materials are important in concrete but utilising many natural resources and polluting the environment. There are both environmental and economic benefits of using fly ash and GGBS. At this optimum ratio, the electronic waste used to create the binding device in concrete has environmental benefits. However, the use of E-waste is ecologically advantageous but economically fails. This study will be useful in many ways namely, reduces the carbon footprints, reduces the use of river sand, maximum use of fly ash, and environmentally friendly construction material. Hence this research can be highly useful

to society to the large extent. Finally, E-waste, M-sand, and fly ash used in the concrete will bring better living conditions.

Nomenclatures

Al;	Aluminium
CO_2;	Carbon Dioxide
H_2SO_4;	Sulphuric Acid
KOH;	Potassium Hydroxide
NaOH;	Sodium Hydroxide
Na_2SiO_3;	Sodium Silicate
Si;	Silicon

Abbreviations

E-waste;	Electronic Waste
FA;	Fly ash
GC/GPC;	Geopolymer Concrete
GGBFS/GGBS;	Ground Granulated Blast Furnace Slag
M-Sand;	Manufactured Sand
OPC;	Ordinary Portland Cement
UTM;	Universal Testing Machine

Acknowledgement

The authors acknowledge that this study is supported by Institution of Engineers (India) under students' project scheme.

References

[1] Dahl R. Who pays for e-junk? Environ Health Perspect. 2002;110:A196-9. [PMCID: PMC1240811] [PubMed: 11940446] https://doi.org/10.1289/ehp.110-a196
[2] Koehnken L, Rintoul MS, Goichot M, Tickner D, Loftus AC, Acreman MC. Impacts of riverine sand mining on freshwater ecosystems: A review of the scientific evidence and guidance for future research, River Res Applic. 2020;36:362-370. https://doi.org/10.1002/rra.3586
[3] Davidovits J. Le Livre de la Pierre - Que le Dieu Khnoum Protégé Kheops, Consteur de Pyramide. Saint-Quentin, 1978.
[4] Palomo A, Grutzeck MW, Blanco M.T. Alkali-activated fly ashes-A cement for the future. Cement and Concrete Research, 29, 1999, pp. 1323-1329. https://doi.org/10.1016/S0008-8846(98)00243-9
[5] Van Jaarsveld, JGS, Van Deventer JSJ, Lukey GC The characterisation of source materials in fly ash-based geopolymers, Materials Letters, 57, 2003, pp. 1272- 1280. https://doi.org/10.1016/S0167-577X(02)00971-0
[6] Barbosa, VFF, Mackenzie KJF, Thaumaturgo C. Synthesis and Characterisation of Materials Based on Inorganic Polymers of Alumina and Silica: Sodium Polyciliate Polymers, International Journal of Inorganic Materials, 2(4), 2000, pp. 309-317. https://doi.org/10.1016/S1466-6049(00)00041-6
[7] Lenin Sundar M, Raj S, Vadivel M. Experimental Investigation of Geopolymer Concrete with E-Waste, International Journal of Emerging Science and Engineering, 9(3), 2016, pp. 491-496.

[8] Basha M, Reddy B, Vasugi K. Research on Strength behaviour of geopolymer concrete replacing fine aggregates by M- sand and E-waste, International Journal of Engineering Research & Technology, 40(7), 2016, pp. 401-407. https://doi.org/10.14445/22315381/IJETT-V40P265
[9] Gayathri G, Ramya VS, Yasotha T. Experimental Investigation on Geopolymer Concrete with E-Waste, International Journal of Recent Research and Applied Studies, 8(2), 2016, pp. 280-291.
[10] Balasubramanian B, Gopal Krishna GVT, Saraswathy V. Investigation on Partial Replacement of Coarse Aggregate using E-Waste in Concrete, International Journal of Emerging Science and Engineering, 9(3), 2016, pp. 285-288.
[11] Kale SP, Pathan HI. Recycling of Demolished Concrete and E-waste, International Journal of Science and Research, 4(1), 2015, pp. 789-792.
[12] Krishna Prasanna P, Kanta Rao M. Strength. Variations in Concrete by Using E-Waste as Coarse Aggregate, International Journal of Education and Applied Research, 4(spl2), 2014, pp. 82-84.
[13] Kr. Das S, Kr. Mohapatra A, Rath AK. Geo-polymer Concrete-Green Concrete for the Future-A Review, International Journal of Computational Engineering Research, Volume 5, Number 1, 2014, pp. 21-28.
[14] Naidu. P G, Prasad ASSN, Adiseshu S, Satyanarayana PVV. A Study on Strength Properties of Geopolymer Concrete with Addition of G.G.B.S, International Journal of Engineering Research and Development, 2(4), 2012, pp. 19-28.
[15] Palankar NAU, Shankar R, Mithun BM. Studies on Eco-friendly Concrete Incorporating Industrial Waste as Aggregates. International Journal of Sustainable Built Environment, 4(2), 2015, pp. 378-390. https://doi.org/10.1016/j.ijsbe.2015.05.002
[16] Felix Kala T, Partheeban P. Study on the effect of granite powder on concrete properties, Proceedings of Institution of Civil Engineers: Construction Materials 163(2), 2010, pp. 63-70. https://doi.org/10.1680/coma.2010.163.2.63
[17] Smit MS, Kearsley EP. Effect of paste content on the properties of high-strength concrete pavements, Journal of the South African Institution of Civil Engineering, 57(4), 2015, pp. 20-29. https://doi.org/10.17159/2309-8775/2015/v57n4a3
[18] Kessy JG, Alexander MG, Beushausen H. Concrete durability standards: International trends and the South African context, Journal of the South African Institution of Civil Engineering, 57(1), 2015, pp. 47-58. https://doi.org/10.17159/2309-8775/2015/v57n1a5
[19] Assaggaf RA, Adekunle SK, Ahmad S, Maslehuddin M, Al-Amoudi OSB, Ali SI. Mechanical properties, durability characteristics and shrinkage of plain cement and fly ash concretes subjected to accelerated carbonation curing. Journal of the South African Institution of Civil Engineering, 61, 2019, pp. 73-81. https://doi.org/10.17159/2309-8775/2019/v61n4a7
[20] Kannan V, Ganesan K. Mechanical properties of cementitious blends of with binary and ternary self-compacting concrete metakaolin and fly ash, Journal of the South African Institution of Civil Engineering, 56(2), 2017, pp. 97-105.
[21] Shinde P, Patankar S, Sayyad A. Investigation on effects of fineness of fly ash and alkaline ratio on mechanical properties of geopolymer concrete. Res. Eng. Struct. Mat., 2018; 4(1): 61-71.
[22] Kurtoglu AE, Alzeebaree R, Aljumaili O, Niş A, Gülşan ME, Humur G, Çevik A. Mechanical and durability properties of fly ash and slag based geopolymer concrete, Advances in Concrete Construction, Vol. 6, No. 4 (2018) 345-362.
[23] IS 3812-1 2013. Specification for Pulverized Fuel Ash, Part 1: for Use as Pozzolana in Cement, Cement Mortar and Concrete. Bureau of Indian Standards New Delhi 110002ASTM C 642: 2006, Standard Test Method for Density, Absorption, and Voids in Hardened Concrete, ASTM International, USA.

[24] IS: 2386 (Part III) - 1963. Indian Standard Methods of Test for Aggregates for Concrete Part Ill Specific Gravity, Density, Voids, Absorption and Bulking. Bureau of Indian Standards New Delhi 110002.
[25] IS: 2386 (Part IV) - 1963. Methods of test for aggregates for concrete, Part 4: Mechanical properties [CED 2: Cement and Concrete]. Bureau of Indian Standards New Delhi 110002.
[26] IS 9103: 1999 2007. Concrete Admixtures - Specification, Bureau of Indian Standards New Delhi 110002.
[27] ASTM C494/C494M-05 2005. Standard Specification for Chemical Admixtures for Concrete. ASTM International, USA.
[28] Davidovits, J. Chemistry of Geopolymeric Systems, Terminology. In: Joseph Davidovits, R. Davidovits and C. James (Editors). Geopolymer '99 International Conference, France, 1999, pp. 9-40.
[29] IS: 516 - 1959 2007. Indian Standard Methods of Tests for Strength of Concrete. Bureau of Indian Standards New Delhi 110002.
[30] ASTM C 642: 2006, Standard Test Method for Density, Absorption, and Voids in Hardened Concrete, ASTM International, USA.
[31] Subramanian N, Solaiyan E. GGBFS & M-sand impact on workability and strength properties of fly-ash based geopolymer concrete, Indian Journal of Engineering & Materials Sciences Vol. 27, February 2020, pp. 67-76.
[32] Ganesh C, Muthukannan M. Investigation on the glass fiber reinforced geopolymer concrete made of M-sand, Journal of Materials and Engineering Structures 6 (2019) 501-512.

Research on Engineering Structures & Materials
journal homepage: http://jresm.org
Research Group

Research Article

Effects of metakaolin and treated rice husk ash on the compressive strength of concrete

Rasheed Abdulwahab*[a], Samson Olalekan Odeyemi[b], Habeeb Temitope Alao[c], Toyyib Adeyinka Salaudeen[d]

Department of Civil Engineering, Kwara State University, Malete, Nigeria.

Article Info

Article history:
Received 14 Oct 2020
Revised 15 Dec 2020
Accepted 11 Jan 2021

Keywords:
Concrete;
Metakaolin;
Treated Rice Husk Ash;
Workability;
Compressive Strength

Abstract

Cement industry being source of emission of carbon dioxide (CO2) causing global warming; it is necessary to source for alternative binder in concrete. The problem of longer age strength attainment by pozzolanic blended concrete calls for introduction of treated pozzolans. This paper investigates the influence of co-addition Metakaolin (MK) and Treated Rice Husk Ash (TRHA) in the production of concrete. The kaolin was calcined at a temperature of 650°C for 2 hours and thereafter, characterized. Furthermore, the rice husk (RH) was roasted to temperature of 700°C and thereafter, treated with H2SO4. MK was replaced in varying percentages of 0%, 5%, and 10%. Thereafter, TRHA was added by weight of the cement in varying percentages of 1%, 2%, and 3% to the optimum MK replacement (5%). From the results, it was found that concrete with 5% MK and 2% TRHA had enhanced compressive strength as against the control. Hence, it can be inferred that 5% MK and 2% TRHA concrete could be used in the construction industry. The increase in the strength properties of the concrete could be as a result of additional binding tendency exhibited by MK and TRHA.

1. Introduction

In pursuit of urbanizing the environment, there is need to provide basic amenities amongst are: buildings, roads, adequate and portable water supply system for the citizenry. The rate of development of infrastructures is on the very high side and one of the mostly used construction materials that is very relevant in the highlighted amenities is concrete. Concrete comprises of cement, sand, stone (aggregate) and water. Its fast advancement in this century has made it one of the most widely used construction materials all over the globe [1]. Cement being one of the primary ingredients of concrete is the point of attention most especially the marginal increase in its price and the environmental threat it poses to the atmosphere via emission of CO_2 and other greenhouse gases (GHG). Currently, the interest in Portland cement as a binder in concrete is growing in developing countries with a global production rate of approximately 1.2 billion tons/year. This increase in demand for cement could be complemented for by adding either fully or partly supplementary cementitious materials (SCM) that when in contact to lime released from hydration of cement and in the presence of water exhibit binding property, thus adding more strength to the composites [2, 3].

The call for addition SCM of in concrete technology had resulted into searching for industrial and agricultural wastes that have tendency of exhibiting the binding property.

*Corresponding author: abdulwahab.rasheed@kwasu.edu.ng
[a] orcid.org/0000-0003-4371-2019; [b] orcid.org/0000-0001-5217-3403; [c] orcid.org/0000-0001-6083-9359; [d] orcid.org/0000-0002-6312-7661
DOI: http://dx.doi.org/10.17515/resm2020.223ma1014

In other words, most industrial wastes are source of agricultural as most industrial raw materials are agro-based. The available waste in countries differs which in turn is subject to types of agricultural produce available in their various domain. Agricultural wastes are by-product obtained at the end of processing and consumption of farm produce and are so enormous amongst are: wheat, corn cob, guinea corn, need seed, groundnut shell and rice husk [4]. The rate of cultivation and consumption of rice is very high and consequently, the availability of its husk. The high silica content of the soil had in turn made the silica content of plants to be high and this has positive influence on the pozzolanic tendency of most agricultural products. Hence, enhance its SCM in concrete composite [5].

Pozzolans are either natural or artificial. Natural pozzolans (NP) being sourced from volcanic eruption could either be volcanic ash or volcanic pumice. The artificial ones are obtained as a result of heat treatment of industrial wastes or clay materials and some examples of this class includes: MK, fly ash (FA), silica fume (SF), Rice Husk Ash (RHA), and Ground granulated blast furnace Slag (GGBFS) [6]. The technical benefits of pozzolans in concreting could be attributed to the presence of abundant quantity of alumina or silica which have tendency of enhancing the hydration process of cement and consequently, better strength enhancement with remarkable microstructural development [7]. Although, MK is quite different from other artificial pozzolans as it is sourced from the heat treatment process involving removal of water and phase changing of hydroxyl present in china clay called kaolin [8][9].

Clay minerals are so enormous but kaolin clay distinct itself amongst other due to high level of purity and consequently, the presence of quartz, rutile, pyrite, siderite, feldspar [10]. In addition, MK could be gotten from calcination of paper sludge [11]. It is more of pure clay with some other minerals but not limited to: halloysite, dickite, anauxite and nacrite [8]. The uniqueness of MK as compared to other pozzolans could be affiliated to the following benefits: Dilution effect, filling ability, lubrication of very coarse cement particles and consequently, enhanced acceleration of the hydration of cement [9]. Furthermore, MK had performed very satisfactorily compared to other pozzolans in terms of strength development at early stage of curing in particular silica fume. This has been attributed to its enhanced rate of hydration of cement [12].

MK is obtained by the thermal activation (dehydroxylation) of kaolin clay in a temperature of between 600°C to 850°C for at most 12 hours [13]. The calcination process has the tendency of breaking the crystalline nature of the MK thereby changing it to amorphous phase and consequently, improving on the pozzolanic tendency [14]. The process has the potential of unbounding water molecules in the pores of the clay as well as deformation of the crystalline nature. MK is quite distinct from other forms of pozzolans in that it could be purified to enhance its colour and sizes of the particles thus improving tremendously the reactivity [15]. MK when used as a partial replacement substance for cement in concrete, reacts with calcium hydroxide $Ca(OH)_2$, one of the by-products of hydration of cement and results in additional C-H-S gel which result in increased strength. Naresh [16] concluded 10% Mk replacement of cement enhanced the mechanical properties of concrete when incorporated with silica fume in the production of concrete. Malagavelli [17] opined 10% MK infused in concrete enhanced the splitting tensile, flexural and compressive strength of concrete as compared to the control specimen.

Furthermore, the work of Ramezanianpour [18] showed that MK performed satisfactorily well in terms of compressive strength enhancement and durability. Asides from MK having significant effects in terms of strength enhancement, it surpasses silica fume on the aspect of pull out performance of steel fibers incorporated in cement paste [19]. A parameter in determining the reactivity of pozzolan in concrete is to compute the Strength Activity Index (SAI). According to BS 3892 [20] the value of SAI greater than 0.80 at 28 days of curing

show high pozzolanic tendency. also, ASTM C618 [21] stated that a SAI greater than 0.75 is an indication of reactive NP. The influence of MK on the properties of concrete is not limited to the hardened state as it plays important role in the fresh properties of concrete. In particular, the consistency and setting of the concrete; the high surface area of MK makes the hydration of MK blended cement to require more water and hence, as the percentage of MK increases, the consistency reduces [22], [23]. The incorporation of moderate MK in concrete has good influence on the workability compared to other pozzolans where the addition of superplasticizer is required in order to achieve relatively good consistency [24]. Both the initial and final setting times of metakaolin blended concrete were observed to increase with increase in MK replacement [25].

Rice Husk (RH) has been found to have varying qualities in terms of purity due to the presence of some carbon content and other impurities like oxides of sodium and potassium which in turn could impair the reactivity went burnt to form RHA [26]. The recommended calcination temperature to give a reactive substance should not be more than 700 °C and any temperate above that could result into the transformation of amorphous silica into crystalline thereby leading to an unreactive material [27]. According to Prasad [28] the calcination temperature to give RHA with satisfactory pozzolanic properties should be in the range of 500 to 600°C. The pretreatment of RHA using some acids amongst are: hydrochloric and nitric have been found to significantly enhanced its purification [29]. This research is aimed at investigating the effect of addition of MK and RHA treated with sulfuric acid and base on the properties of concrete. With specific objectives of determining the chemical properties of MK as well as investigating its incorporation and purified RHA on the compressive of concrete

2. Materials and Method

In this research, the following materials were used: Ordinary Portland cement (OPC), fine aggregates (River sand), coarse aggregates (granite), MK, TRHA, Super-plasticizer and water. The kaolin clay was obtained from a mining site at Osin-Aremu, Ilorin South Local Government Area with coordinates 8.4519°N and 4.5378°E and the Rice Husk from a rice milling shop at Oja-gboro area in Ilorin, Kwara State. Ordinary Portland cement (OPC), Dangote cement brands of 32.5R which conforms to NIS 444-1[30] was purchased from a vendor in Ilorin, granite conforming to BS 882 [31] with nominal size of 20mm was used as coarse aggregate and river sand also conforming to BS 882 specification was used as fine aggregate in the concrete with the duo sourced from Malete, Kwara State, Nigeria.

Firstly, the kaolin clay was calcined at a temperature of 650 ˚C for one (1) hour and the RH was burnt at a temperature of 700 ˚C for a duration of three (3) hours using a furnace in the Department of Mechanical Engineering, Kwara State Polytechnic, Ilorin Kwara State. Thereafter, the sample was taken to the laboratory of the National Agency for Science and Engineering (NASENI), Akure, Ondo State, Nigeria for EDXRF analysis using SKYRAY instrument model EDX3600B. Also, the physical properties of the aggregates were determined and batching of concrete was done by weight with proportioning details as contained in Table 1. A concrete with target strength of 40N/mm^2 (M40) was designed for in accordance with the specification of Council for the Regulation of Engineering in Nigeria (COREN) Concrete Mix Design Manual. Mixing was done manually; the fine aggregate was spread on a non-absorbent surface and thereafter, mixed thoroughly with cement for homogeneity and consequently mixed with coarse aggregates. A water-binder ratio of 0.37 was used in the batching of concrete with the addition of superplasticizer.

Table 1. Quantity of concrete constituent per cubic meter

Concrete	Cement (kg)	MK (kg)	Treated Rice Husk Ash	Water (kg)	Super plasticizer (ml)	Fine Aggregate (kg)	Coarse Aggregate (kg)
Control	27.98	0	0	10.47	150	23.97	44.55
MK 5%	26.58	1.40	0	10.47	150	23.97	44.55
MK 10%	25.18	2.80	0	10.47	150	23.97	44.55
MK 5%+ TRHS 1%	26.3	1.40	0.28	10.47	150	23.97	44.55
MK 5% + TRHA 2%	26.02	1.40	0.56	10.47	150	23.97	44.55
MK 5% + TRHA 3%	25.74	1.40	0.84	10.47	150	23.97	44.55

Thereafter, required quantity of water was then added; mixed again thoroughly to achieve the final uniformity as shown in Figure 3. The control experiment was first batched with 0% replacement and thereafter, the cement was replaced with 5% and 10% Metakaolin respectively. To obtain the TRHA, 10 grams of Rice Husk Ash (RHA) samples were stirred in 80 ml sodium hydroxide solutions. RHA was boiled in a covered 250 ml Erlenmeyer flask for 3 hours. The solution was filtered, and the residue was washed with 20 ml boiling water. The filtrate was allowed to cool to room temperature and added H_2SO_4 until pH 2. Thereafter, NH_4OH was added at room temperature until pH 8.5 was obtained. The filtrate was then dried at 120 ˚C for 12 hours. The chemical composition of the TRHA was determined and thereafter, added in varying percentages of 1%, 2%, and 3% by weight of the binder to the 5% Metakaolin (being optimum) replacement. As soon as uniformity was achieved, slump test was carried out to determine the properties of the concrete in fresh state. A slump cone of high 300mm with diameters 100mm and 200mm at the top and bottom was placed on a non-absorbent plane surface. The fresh concrete was poured to fill up the cone in three layers with a tamping of 25 strokes for each layer. After filling, excess concrete at the top was carefully scraped using a trowel. Thereafter, the cone was lifted and concrete subsides, the corresponding height of fall was measured to read the slump values. Concrete cubes specimens of size 150mm x 150mm x 150mm were cast and cured in water for 7, 21, 28, and 56days respectively. The compressive strength of the cubes was determined at different ages of curing and the cubes were placed in the machine as shown in Figure 1 and allowed to compressed between the platens of a compression machine with gradual application of load. At a point in time, cracks were observed on the cubes and load readings in (kN) read on the gauge. This was performed three times and the average load was calculated. The compressive strength was computed by finding the ratio of the load to the corresponding area of the cubes. Hence, the Strength Activity Index (SAI) of the specimen was obtained using equation 1 in order to compare the strength of the control specimens relative to the test experiment.

$$SAI = \frac{A}{B} * 100 = \left(\frac{45.86}{30}\right) * 100 = 1.52 \quad (1)$$

Where:

A= Unconfined Compressive Strength Test of pozzolan specimen

B = Unconfined Compressive Strength Control concrete (0% pozzolan) Table 1 Drill pipe dimensions and properties [6]

Fig. 1Compressive strength test of concrete cube

3. Results and Discussion

3.1 Chemical Composition of Metakaolin, RHA and TRHA

The result of chemical analysis is as shown in Table 2, the predominant oxide was found to be silicon dioxide and the sum of SiO_2, Al_2O_3, Fe_2O_3 of the metakaolin clay is 71.04% less than 95.22% as obtained in other work [32] but greater than 70%. Hence, the calcined clay can be classified as class N pozzolan [21], [33]. Furthermore, the relative abundance of Sulphate is 0.96% less than 4%, also affirmed the metakaolin belongs to the class N pozzolan [21]. Tables 3 and 4 show the chemical composition of oxides present in both RHA and TRHA. From the tables, the silica content was found to increase with corresponding in both sodium and potassium oxides. These results show an enhancement in purification of the RHA and the result is in agreement when compared with the work of some researchers [34]

Table 2. Results of Chemical Analysis of Metakaolin

Chemical Compounds	SiO_2	Al_2O_3	Fe_2O_3	CaO	MgO	SO_3
Percentage Composition (%)	50.10	19.20	1.74	4.415	4.61	0.96

Table 3. Results of Chemical Analysis of RHA

Chemical Compounds	SiO_2	Al_2O_3	Fe_2O_3	CaO	MgO	Na_2O	K_2O
Percentage Composition	83.62	1.43	0.78	1.24	0.09	0.04	0.08

Table 4. Results of Chemical Analysis of TRHA

Chemical Compounds	SiO_2	Al_2O_3	Fe_2O_3	CaO	MgO	Na_2O	K_2O
Percentage Composition	89.70	1.01	0.29	0.83	0.04	0.02	0.03

3.2 Physical Properties of Aggregates

Table 5 indicates the result of the specific gravity and water absorption test carried out on fine aggregate and coarse aggregate used in this research. The range of specific gravity of aggregates specified by ACI Education Bulletin [35] ranges from 2.30 to 2.90. Thus, the results of specific gravity of fine and coarse aggregates are within the acceptable limits for aggregates.

Table 5. Properties of Coarse Aggregate and Fine Aggregate

Property	Fine Aggregate	Coarse aggregate
Specific Gravity	2.56	2.64
Water Absorption (%)	1.10	0.25

3.3 Workability

The slump height of the test experiment was found to be greater than the control. This implies that the addition of MK and TRHA increased the consistency of the concrete as compared to the control (0% replacement). It is indicative of higher workability. The 5% MK + 2% TRHA had the greatest height of subsidence and consequently, the most workable proportion see Figure 2.

Table 6. Statistical Analysis of Metakaolin Blended Concrete with TRHA

Metakaolin/ TRHA	N	Mean	Standard Deviation	Standard Error Mean
MK 0%				
MK 5% + 1% TRHA	12	40.2258	4.67782	1.35037
MK 5% + 2% TRHA	12	42.4443	3.83125	1.10599
MK 5% + 3% TRHA	12	31.7112	3.29439	0.95101

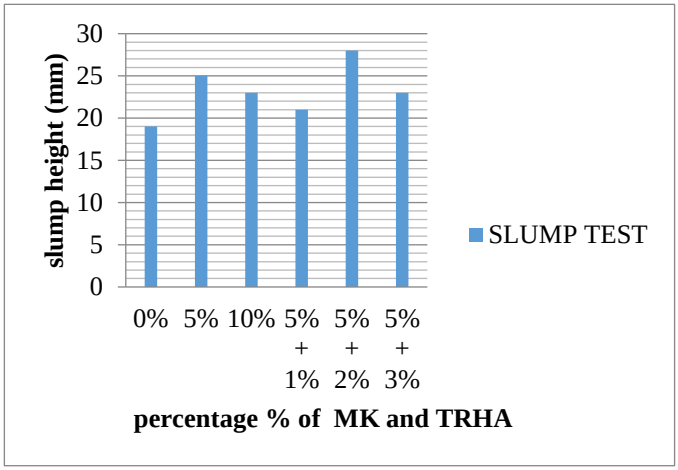

Fig. 2 Graph showing slump height against percentage replacement of MK and TRHA

Table 7. T-Test for Average Compressive Strength of Metakaolin Blended Concrete with TRHA

Metakaolin	T	Degree of Freedom	P-Value	Mean Difference	Correlation
MK 5% + 1% TRHA	20.16	11	0.000	15.05411	0.871
MK 5% + 2% TRHA	24.84	11	0.000	17.19010	0.869
MK 5% + 3% TRHA	5.363	11	0.000	7.13383	0.681

3.4 Compressive Strength Test

Figure 3 revealed the incorporation of metakaolin at both 5 and 10 % was found to increase compressive strength of concrete as compared to the control with 5% MK being optimum at all curing ages. Figure 4 shows early compressive strength enhancement when TRHA was added to the concrete. The compressive strength of 5% MK and 2% TRHA at 28 days of curing was 45.867 N/mm^2 as compared to the strength of 5% MK at 56 days of curing (43.141N/mm^2), which implies that strength of 5% MK+ 2% TRHA at 28 days of curing was higher than the strength of 5% MK at 56 days of curing. The result is in agreement as compared to the work of Kwan [26], [29] where acid treated RHA have been found to increase strength. The statistical analysis further explained the result as contained in Tables 6 and 7. Since the significance level of 0.05, a two-tailed test allots half of your alpha to testing the statistical significance in one direction and half of your alpha to testing statistical significance in the other direction. The mean is considered significantly different from *x* if the test statistic is in the top 2.5% or bottom 2.5% of its probability distribution, resulting in a p-value less than 0.05. because the p-value is Zero (< alpha level), you reject the null hypothesis and conclude that there's a statistically significant difference. In addition, the strength of the duo was found to be greater than the control specimen (30.100N/mm^2). Furthermore, the result of the SAI was found to be 1.52 greater than the minimum value of 0.8 specified by [20].

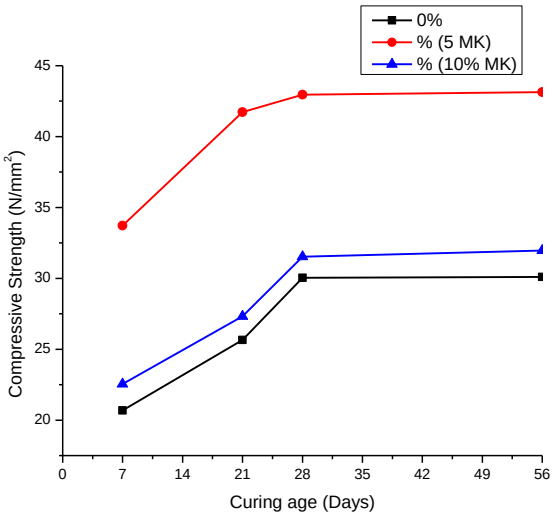

Fig. 3 Graph showing Compressive Strength of Concrete Incorporated with Metakaolin

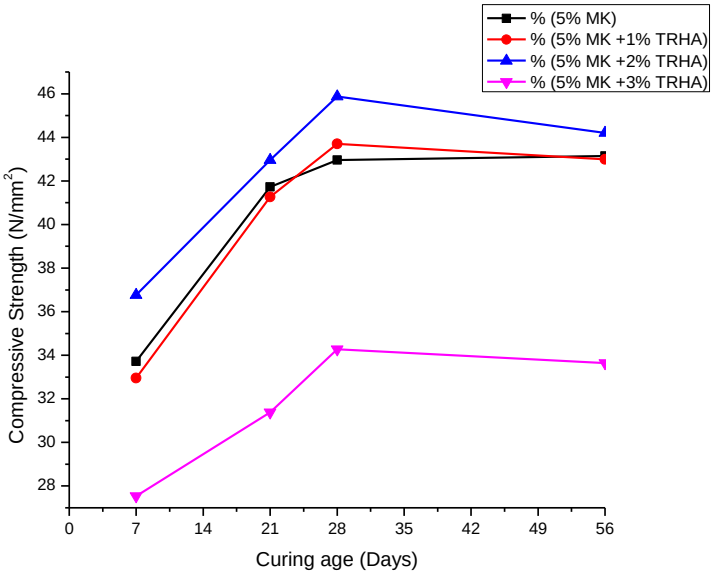

Fig. 4 Compressive Strength of Metakaolin concrete with Treated Rice Husk Ash

5. Conclusions

From the research, it could be inferred that:

- The sourced MK having the addition of silica, ferric and Aluminium oxides greater than 70% as specified by ASTM C 618. Hence, the material exhibits supplementary cementitous tendency and classified as Class N pozzolan.

- Also, it can be concluded that the compressive strength of concrete attained its maximum with optimum 5% MK replacement.
- Furthermore, 5% Mk and 2% TRHA gave better compressive strength at shorter age of curing than 5% Mk only with prolonged period of curing with a percentage strength increment of 5.94%. However, the results of compressive strength of both test experiments (5% Mk +2% TRHA) gave strength increment of 34.38% and 30.22% respectively.

Acknowledgement

The Authors acknowledge the teaching and non-teaching staff in the Department of Civil and Environmental Engineering, Kwara State University, Malete, Kwara State, Nigeria, for their contributions towards the successful completion of this research.

References

[1] ANIFOWOSE MA, ADEBARA SA, ODEYEMI SO, OLAHAN AB, ALIYU T. Density, Workability and Compressive Strength Assessment of Steel Slag in Concrete. ACTA Tech CORVINIENSIS - Bull Eng. 2017;10(4):63-7.
[2] Couthino JS. The combined benefits of CPF and RHA in improving the durability of concrete structures. Cem Concr Compos. 2003;25:51-9. https://doi.org/10.1016/S0958-9465(01)00055-5
[3] Siddique R, Klaus J. Influence of Metakaolin on the Properties of Mortar and Concrete - A Review. Appl Clay Sci. 2009;43:392-400. https://doi.org/10.1016/j.clay.2008.11.007
[4] Raheem AA, Ikotun BD. Incorporation of Agricultural Residues as Partial Substitution for Cement in Concrete and Mortar. J Build Eng. 2020;31(101428). https://doi.org/10.1016/j.jobe.2020.101428
[5] Birick H, Akoz F, Berktay I, Tuglar AN. Study of Pozzolanic Properties of Wheat Straw Ash. Cem Concr Res. 1999;29:637-43. https://doi.org/10.1016/S0008-8846(98)00249-X
[6] Raheem KA., Abdulwahab, R, Kareem MA. Incorporation of metakaolin and Nanosilica in Blended Cement Mortar and Concrete- A Review. J Clean Prod. 2021;1-12. https://doi.org/10.1016/j.jclepro.2021.125852
[7] Sidek MN, Johari MA, Arshad MF, Jaafar MF. Behaviour of Metakaolin Concrete in Different Curing Condition. Int J Civ Eng Geo- Environ. 2013;4:1-7.
[8] Chandak MA, Pawade PY. Influence of Metakaolin in Concrete Mixture - A Review. Int J Eng Sci. 2018;37-41.
[9] Moodi F, Ramezanioanpour AA, Safavizadeh AS. Evaluation of the Optimal Process for the Thermal Activation of Kaolins. Sci Iran. 2011;18(4):906-12. https://doi.org/10.1016/j.scient.2011.07.011
[10] Yanguati H, Tobon J, Ramirez J. Pozzolanic Reactivity of Kaolin Clays - A Review. Rev Ing Constr. 2017;32(2):13-24. https://doi.org/10.4067/S0718-50732017000200002
[11] Garcia R, Vigil RD, Vegas I, Frias M, Sanchez de Rojas MI. The Pozzolanic properties of paper sludge waste. Constr Build Mater. 2008;22(4):1484-90. https://doi.org/10.1016/j.conbuildmat.2007.03.033
[12] Moghaddam, F K Ravindrarajah RS, Sirivivatnanon V. Properties of Metakaolin Concrete. Int Conf Sustain Struct Concr. 2015;1-11.
[13] Rashad AM. Metakaolin- Fresh Properties and Optimum Content for Mechanical Strength in Traditional Cementitious Materials - A Comprehensive Overview. Rev. Adv. Mater. 2015;40;15-44
[14] Ambroise J, Maximilien S, Pera J. Properties of Metakaolin Blended Cement. Adv Cem Based Mater. 1994;1:161-8. https://doi.org/10.1016/1065-7355(94)90007-8
[15] Ding JT, Li Z. Effect of Metakaolin and Silica Fume on Properties of Concrete. Am Concr Inst Mater J. 2002;99(4):393-8. https://doi.org/10.14359/12222

[16] Naresh KA. Study of Metakaolin and Silica Fume used in Various Cement Concrete Designs. Int J Enhanc Res Sci Technol Eng. 2014;3(6):176-81.
[17] Malagavelli V, Angadi S, Prasad JS. Influence of Metakaolin in Concrete as Partial Replacement of Cement. Cem Compos Int J Civ Eng Technol. 2018;9(7):105-11.
[18] Ramezanianpour AA, Jovein HB. Influence of Metakaolin as supplementary cementing material on strength durability of concrete. Constr Build Mater. 2012;470-9. https://doi.org/10.1016/j.conbuildmat.2011.12.050
[19] Bathia N, Yan C. Bond Slip Characteristics of Steel Fibers in High Reactivity Metakaolin Modified Cement based Matrices. Cem Concr Res. 1996;26(5):657-62. https://doi.org/10.1016/S0008-8846(96)85000-9
[20] BS EN 450-1:2012. Fly ash for concrete. Definition, specifications and conformity criteria. 2012 p. 1-36.
[21] ASTM C-618. Standard specification for testing Pozzolanas. American Society for Testing and Materials. 2001.
[22] Bai J, Wild S, Sabir BB, Kinuthia JM. Workability of Concrete Incorporating Pulverized Fuel Ash and Metakaolin. Mag Concr Res. 1999;51(3):207-16. https://doi.org/10.1680/macr.1999.51.3.207
[23] Johari M, Brooks J, Kabir S, Rivard P. Influence of Supplementary Cementitious Materials on Engineering Properties of High Strength Concrete. Constr Build Mater. 2011;25:2639-48. https://doi.org/10.1016/j.conbuildmat.2010.12.013
[24] Caldarone MA, Gruber KA. High Reactivity Metakaolin- A Mineral Admixture for High Performance Concrete, Concrete Under Severe Condition: Environment and Loading. In: Proceedings of International Conference of Concrete Under Severe Loading. 1995. p. 1015-24.
[25] Brooks JJ, Johari MM. Effect of Metakaolin on Creep and Shrinkage of Concrete. Cem Concr Compos. 2001;23(6):495-502. https://doi.org/10.1016/S0958-9465(00)00095-0
[26] Kwan WH, Wong YS. Acid Leached Rice Husk Ash in Concrete - A Review. Mater Sci Enegry Technol. 2020;3:501-7. https://doi.org/10.1016/j.mset.2020.05.001
[27] Setyawan N, Hoerudin, Wulanawati A. Simple Extraction of Silica Nanoparticles from Rice Husk using Technical Grade Solvent: Effect of Volume and Concentration. IOP Conf. Series: Earth and Envir Sci. 2019; 309,1-9. https://doi.org/10.1088/1755-1315/309/1/012032
[28] Prasad R, Pandey M. Rice Husk Ash as a Renewable Source for the production of Value Added Silica Gel and its Application - An Overview. Bull Chem React Eng Catal. 2012;7(1):1-25.
[29] Feng Q, Yamamichi H, Shoya M, Sugita S. Study on Pozzolanic Properties of Rice Husk Ash by Hydrochloric Acid Pretreatment. Cem Concr Res. 2004;34(3):521-6. https://doi.org/10.1016/j.cemconres.2003.09.005
[30] NIS 444-1:2003. Composition, Specifications and Conformity Criteria for Common Cements. Nigerian Industrial Standard, Standard Organisation of Nigeria, Lagos, Nigeria. 2003.
[31] BS EN 12620:2002+A1:2008. Specification for Aggregates from natural sources for concrete. British Standards, BSI Group Headquarters 389 Chiswick High Road, London, W4 4AL, UK, Standards Policy and Strategy Committee. 2008.
[32] Ayininuola GM, Adekitan OA. Characterization of Ajebo Kaolinite Clay for Production of Natural Pozzolan. Int J Civ Environ Eng. 2016;10(9):1233-40.
[33] Siddique R. Performance Characteristics of High-Volume Class F Fly Ash Concrete. Cem Concr Res. 2004;34:487-93. https://doi.org/10.1016/j.cemconres.2003.09.002
[34] Ghosh R. A Review Study on Precipitated Silica and Activated Carbon from Rice Husk. J Chem Eng Process Technol. 2013;4(4). https://doi.org/10.4172/2157-7048.1000156

[35] ACI Education Bulletin. Aggregates for Concrete-Materials for Concrete Construction. Developed by Committee E-701, American Concrete Institute, 38800 Country Club Dr, Farmington Hills, Michigan, United States. 2007.

Research on Engineering Structures & Materials
journal homepage: http://jresm.org
Research Group

Research Article

Evaluation of fresh and hardened properties of blended silica fume self-compacting concrete (SCC)

Olatokunbo M. Ofuyatan[1,a]*, Adewale George Adeniyi[2,b], Joshua O. Ighalo[2,c]

[1]*Department of Civil Engineering, College of Engineering, Covenant University Ota, Lagos, Nigeria*
[2]*Department of Chemical Engineering, Faculty of Engineering and Technology, University of Ilorin, Ilorin, P. M. B. 1515, Nigeria*

Article Info

Article history:
Received 23 Oct 2020
Revised 24 Feb 2021
Accepted 03 Mar 2021

Keywords:
Self Compacting Concrete;
Silica Fume;
Cement;
Concrete;
Partial Replacement

Abstract

Recent technologies now investigate the use of materials that can serve as partial cement replacement and also impact on self-compacting ability in concrete mixtures. In this study, fresh and hardened properties of self-compacting concrete containing silica fumes as partial replacement for cement were evaluated. Cement was replaced by silica fume in the extent of 15%, 25% and 35% by volume alongside the control mix (0%). The flow test, V-funnel test and L-box test were conducted on the fresh concrete. The compressive strength, flexural strength, water absorption property and microstructural properties of the hardened concrete were determined. Utilization of silica fume as partial cement replacement improved the fresh state properties of the concrete in the domain of the flow-ability. Higher partial replacement led to lesser compressive and flexural strength due to weak interfacial transition zone, the porosity of the mortar during adhesion to the fine and coarse aggregates. Rapid water absorption was observed after the first day of the concrete preparation which gradually tailed off with time.

1. Introduction

Concrete is the most popularly material used for construction in the world [1]. One of the most important innovations in the construction industry is the development of self-compacting concrete [2] also known as self-consolidating concrete [3]. Self-compacting concrete (SCC) is a flowing concrete mixture which compacts or is consolidated under its own self weight [4]. This type of concrete can fill form-works without any external mechanical compaction required [1, 5]. SSC provides a better process in terms of economics of manpower and finance [6]. SSC allows for the recycling of recycled aggregates in concrete without any significance deterioration of the mechanical properties in the short and long term [7, 8].

Cement utilization leads to much release of green-house gases [9]. Partial cement replacement is an important aspect in achieving sustainability in the cement industry [10]. Recent technologies now investigate the use of materials that can serve as partial cement replacement and also impact a self-compacting ability in concrete mixtures [8]. Several studies have utilized materials such as pumice powder [6], nano-silica [11, 12], fly ash [2, 6, 13], metakaolin [14], slag [6, 13], rice husk ash [15] and palm oil fuel ash [16] as partial replacement of cement in self-compacting concrete (SSC).

*Corresponding author: adeniyi.ag@unilorin.edu.ng , olatokunbo.ofuyatan@covenantuniversity.edu.ng
[a] http://orcid.org/0000-0001-9052-2758; [b] http://orcid.org/0000-0001-6615-5361;
[c]http://orcid.org/0000-0002-8709-100X;
DOI: http://dx.doi.org/10.17515/resm2020.228ma1023
Res. Eng. Struct. Mat. Vol. 7 Iss. 2 (2021) 211-223

Silica fume, also known as micro silica, is a collection of soot that escapes with exhaust gas during the process of melting industrial silicon and ferrosilicon at high temperature using an industrial electric furnace [17]. Silica fume and superplasticizer are reciprocal materials to produce self-levelling cements with incredible attachment of the crisp blend [18]. Superplasticizers are admixtures for concrete, which are incorporated to reduce the water content in a mix or to direct the setting rate of the strong while holding the spilling properties of a mix. One of the best points of interest of utilizing silica fume in SCC is due to its small size which makes self compaction possible. The expansion of silica smoulder augments the size conveyance of the cementitious particles in cement, permitting progressively effective molecule pressing, densifying the interfacial change zone and changing over CH into C– S– H, therefore expanding quality and toughness.

In recent times, silica fumes have gained popularity as a partial replacement for cement to achieve sustainable building and formwork. Ardalan, Joshaghani [6] utilized silica fume in a blend with pumice in SSC. They observed that the addendum improved the compressive strength and workability of the SSC. Bernal, Reyes [11] observed that a ternary mixture of nano-silica and silica fumes gave the best mechanical properties together (in contrast with the binary blends). Ghoddousi and Saadabadi [14] studied the use of electrical resistivity of SSC to determine the amount of calcium hydroxide. The study investigated SSC containing silica fumes and metakaolin. Leung, Kim [19] studied the moisture absorption properties of SSC obtained using flay ash and silica fumes as partial cement replacement. Moisture absorption decreased with partial replacement but compressive strength was improved. No relationship was observed between moisture absorption and compressive strength. Sasanipour, Aslani [20] observed that silica fumes in SSC (developed with waste concrete aggregates) has less moisture absorption and porosity. In terms of the pore properties, an optimum of 5% silica fume in SSC was observed by Zarnaghi, Fouroghi-Asl [21].

Although there are much benefits of SSC, it has not yet gained widespread use in Nigeria. The aim of this study is to evaluate the fresh and hardened properties of self-compacting concrete obtained using silica fumes as partial replacement for cement. The flow test, V-funnel test and L-box test were conducted on the fresh concrete. The compressive strength, flexural strength, water absorption property and microstructural properties of the hardened concrete were determined. Alongside the microstructural analysis the compositional elements of the concrete was investigated using Scanning Electron Microscope with Energy Dispersive Spectroscopy (SEM-EDS).

2. Methodology

2.1 Materials

The cement type used in carrying out this experiment is Ordinary Portland Cement (OPC); Dangote cement of grade 42.5R, Nigeria. The fine aggregate used was natural sharp river sand obtained from river Ogun, Nigeria. It was free of silt deleterious materials and did not exceed 5 mm size. Most common type of course aggregates used for construction work is 19 mm size. Crushed, angular, graded granite having maximum size of 19 mm was therefore used as coarse aggregate. Conplast SP430 was used in the study. It is a brown chloride free liquid which instantly disperses in water. The properties of the superplasticizer used are given in Table 1. The other materials used in this study are fine silica fume and water (ASTM C1602 standard).

Table 1. Properties of Conplast SP430

Property	Description
Appearance	Brown Liquid
Specific Gravity	1.175 @ 30°C
Chloride Content	Nil BS 5075
Alkaline Content	Less than 50g. Na_2O equivalent/liter of admixture

2.2 Concrete mix design

For the investigation, four mixes of cubes (150 mm X 150 mm X 150 mm) were cast. Cement was replaced by silica fume in the extent of 15%, 25% and 35% by volume alongside the control mix (0%). After principal blend outline, the trial blend was planned and evaluated for the initial properties of SCC as indicated by EFNARC [22] rules. The fine aggregate, coarse aggregate, water content ratio and superplasticizer were kept constant for different mixes while cement and silica fume were varied based on gradual replacements. The details of the 4 mix proportions used in the study are presented in Table 2.

Table 2. Mix proportions

Constituents (kg/m³)	Mix 1	Mix 2	Mix 3	Mix 4
Portland Cement (kg/m³)	417.15	375.44	333.72	292
Fine Aggregates (kg/m³)	952	952	952	952
Coarse Aggregate (kg/m³)	653.54	653.54	653.54	653.54
Silica Fume (kg/m³)	0	41.72	83.43	125.15
Water Cement Ratio (%)	0.45	0.45	0.45	0.45
Superplasticizer (kg/m³)	4.17	4.17	4.17	4.17

2.3 Fresh state properties

2.3.1 Flow/slump test

This is the mean width of the spread of new solid utilizing a customary slump cone. It is utilized to gauge the consistency of cement. The standard (BS EN 12350-8) [23] was utilized to survey the flow-ability [24]. The cone was placed on the steel plate at 210 mm distance across checking. The concrete was put into the cone. The excess was removed within 30 seconds whilst moving it upward within 1-3 seconds. The time from lift to the 300 mm mark is noted. The biggest distance across is measured in two ways at 90° to the closest 10 mm. The normal from the point was taken to get the flow to the closest 10 mm.

2.3.2 V-funnel test

The V funnel test was used to evaluate the ability of the concrete to fill the form in its weight. A moist towel was used to wet the inner surface of the V-funnel. The opening of the V-funnel was cleaned and kept horizontal. The concrete was placed in the funnel and a straight edge plank was used to level the top. The gates were opened after 10 seconds and a stopwatch was started immediately. Once a visible space was observed through the funnel opening, the time was stopped and reading recorded.

2.3.3 L-Box test

The L-Box test was used to determine the ability of SCC to move through small checks with no separation or holding. The container was filled and left to stand for 60 ±10 seconds. The entryway was opened and monitored until flow stopped. The passing

capacity proportion (PL) was computed by the ratio of the profundity of the level (H2) and the vertical profundity (H1).

2.4 Hardened state properties

2.4.1 Determination of compressive strength

Compressive strength of the hardened concrete was determined after curing period of 7, 14, and 21 days. Compressive strength of the developed SCC was determined according to ASTM C39 [25] by means of a compression testing machine (Model YES-2000, England) shown in Figure 1. The dimension of the cube was 150 mm in length, breadth and height. The sample was placed on the machine in proper order. Care was taken to ensure the idle was on the base plate. The load was increased at 140 kg/cm^2 until failure. The highest load was observed and recorded.

Fig. 1 Test sample in the compression testing machine

2.4.2 Determination of flexural strength

Flexural strength of the hardened concrete was determined after curing period of 7, 14 and 21 days. Flexural strength of the developed SCC was determined according to ASTM standards [25, 26] by means of a three-point bending test (Impact engineering, Australia) shown in Figure 2. 100 mm by 450 mm samples were used for this test. The test ought to be dome on the sample following removal from the storage conditions in order to avoid surface drying which decreases flexural quality. The sample was placed on the stacking focuses. The hand completed surface of the example ought not to be in contact with stacking focuses. This will guarantee a worthy contact between the example and stacking focuses. The stacking framework was centered in connection to the connected power.

Employing 0.10 mm and 0.38 mm leaf-type sensor gauges, care was to taken to avoid spaces between the samples. Any hole more than 0.10 mm was eliminated utilizing calfskin shims (6.4 mm thick and 25 to 50 mm long). Capping or pounding were considered to evacuate holes in abundance of 0.38 mm. The sample was loaded consistently without stun till failure was achieved. Indian standard determined stacking rate of 400 kg/min for 150 mm sample and 180 kg/min for 100 mm sample was used at a stress increment rate 0.06 ±0.04 N/mm^2.s as per British standard.

Fig. 2 Three-point bending test

2.4.3 Water absorption test

The value of the water absorption capacity of the hardened SSC sample was evaluated in percentage (%) by weight (ASTM C642 standard) [27] . Each cube was immersed in water for 30 mins, 1 day, 2 days and 4 days. The surface was cleaned properly before weighing. The moisture absorption was calculated using the expression in Eqn. 1. Where Wi is the dry weight of the sample (g) and Wt is the weight of the sample (g) at particular time interval (t).

$$Water\ absorbed\ (wt\%) = \frac{Wt - Wi}{Wi} \times 100 \quad (1)$$

2.4.4 Microstructural characterization

The microstructural analysis show the composition of the hardened sample was investigated using Scanning Electron Microscope with Energy Dispersive Spectroscopy (SEM-EDS). The SEM-EDS (SEM, Phenom proX, Phenom-World BV, The Netherlands) was used at microspore acceleration voltage of 15 kV and magnification of ×1500 Adeniyi, Ighalo [28].

3. Results and Discussion

3.1 Fresh state properties

In this section, the fresh state properties of SCC obtained using silica fume as partial cement replacement was discussed. The tests considered were the flow test, V-funnel test and the L-box test. The results of the flow test are shown in Table 3. It can be observed that that partial cement replacement with silica fume improved the flow properties of the SCC. The flow properties were increased by a factor of about 6.64 with 35 vol% partial replacement of cement in the SCC. The results of the V-funnel test are shown in Table 4. The positive effect of silica fume partial replacement on the flow-ability in SCC is also emphasized from these results as less time is required before a visible space was observed through the funnel opening. The time decreased from 7 seconds to 4.3 seconds with 35 vol% partial cement replacement. The results of the L-box test are shown in Table 5. It can be observed from the results of the study that ability of SCC to move through small checks with no separation or holding was improved by partial replacement (except for 25 vol%). Rantung, Supit [2] observed that the flow properties of SSC were improved when fly ash was used as partial cement replacement which is in agreement with the observations of this study. Similar observations were also made by Ardalan, Joshaghani [6] for pumice, fly ash and slag as partial cement replacement.

Table 3. Results for flow test

Extent of cement replacement (vol %)	Flow (mm)	T_{50} (Sec)
0	70	4.00
15	400	4.30
25	450	4.08
35	465	4.00

Table 4. Results for V-funnel test

Extent of cement replacement (vol %)	T (Sec)
0	7.00
15	6.00
25	5.00
35	4.30

Table 5. Results for L-box test

Extent of cement replacement (vol %)	H2/H1
0	0.22
15	0.42
25	0.20
35	0.44

3.2 Hardened state properties

In this section, the mechanical, microstructural and compositional properties of the developed SCC was discussed.

3.2.1 Compressive strength

The results of the compressive strength are shown in Table 6. It can be observed that partial replacement of cement with silica fume reduced the compressive strength of the SSC over the entire domain of the curing time. Higher partial replacement led to

lesser compressive strength. It was also observed that curing improved the compressive strength with time (with an optimum obtained at 21 days curing time). This is because the partial replacement material was not able to improve the void filing ability of the composite concrete [21]. Further reasons for the decrease in compressive strength with partial cement replacement of silica fumes is due to weak interfacial transition zone, the porosity of the mortar during adhesion to the fine and coarse aggregates and the formation of cracks in the aggregates [29, 30]. Others studies have made similar observations to those noticed in this investigation. Sasanipour, Aslani [20] also observed a decrease in compressive strength in SSC with silica fumes partial cement replacement. Rantung, Supit [2] observed a decrease in compressive strength in SSC with fly ash partial cement replacement. Similar observations was also made by Ofuyatan and Edeki [31], Ranjbar, Behnia [16] and Ofuyatan and Edeki [32] for SSC with palm oil fuel ash partial cement replacement and by Raisi, Amiri [15] for rice husk ash partial cement replacement.

Table 6. Results for compressive strength

Extent of cement replacement (vol %)	7 Days (kN/mm^2)	14 Days (kN/mm^2)	21 Days (kN/mm^2)
0	19.70	30.70	39.24
15	20.30	27.80	34.42
25	13.30	20.50	25.10
35	9.50	16.10	20.60

3.2.2 Flexural strength

The results of the flexural strength are shown in Table 7. It can be observed that partial replacement of cement with silica fume reduced the flexural strength of the SCC over the entire domain of the curing time. This is due to the poor structure of SCC with partial replacement leading to stress concentration and the weakening of the interfacial bond between mortar and aggregates [16]. Ranjbar, Behnia [16] observed a decrease in flexural strength in SCC with palm oil fuel ash partial cement replacement which is in agreement with the observations of this study.

Table 7. Results for flexural strength

Extent of cement replacement (vol %)	7 Days (kN/mm^2)	14 Days (kN/mm^2)	21 Days (kN/mm^2)
15	4.6	2.5	5.0
25	2.0	1.0	2.0
35	1.0	3.0	1.5

3.2.3 Water absorption

The results of the water absorption of the hardened SCC are shown in Table 7. Partial cement replacement with 35 vol% silica fumes led to the highest water absorption. A rapid water absorption was observed after the first day of the concrete preparation which gradually tailed off with time. Water absorption in concrete is increased due to the presence of porous structures [33, 34]. A high partial replacement leading to more water absorption has been observed in other studies. Sasanipour, Aslani [20] and Xuan, Zhan [35] made similar observations whilst using recycled aggregates.

Table 8. Results for water absorption

Extent of cement replacement (vol %)	4 days (wt %)	2 days (wt %)	1 day (wt %)	30 minutes (wt %)
15%	2.2	1.5	1.8	0.0
25%	1.4	2.8	0.2	0.0
35%	3.0	3.9	7.9	0.0

3.2.4 Microstructural analysis

SEM micrographs of the hardened SSC at 15 vol% (a), 25 vol% (b) and 35 vol% (c) partial replacement are shown in Figure 3. On the surface of the sample with 15 vol% partial cement replacement, micro-clusters can be observed but there are no deep voids on the surface. On the surface of the sample with 25 vol% partial cement replacement, bigger micro-clusters (lumps) can be observed and there is the presence of some deep voids after curing. These lumps are as a result of the coarse aggregate composition of the concrete. For the surface of the sample with 35 vol% partial cement replacement, there are no observable lumps or micro-clusters on the concrete but a deep void can be observed. Voids are formed when the irregular shape of the coarse aggregate combines with a poor interfacial effect with the cementitious material and lead to interstitials during curing.

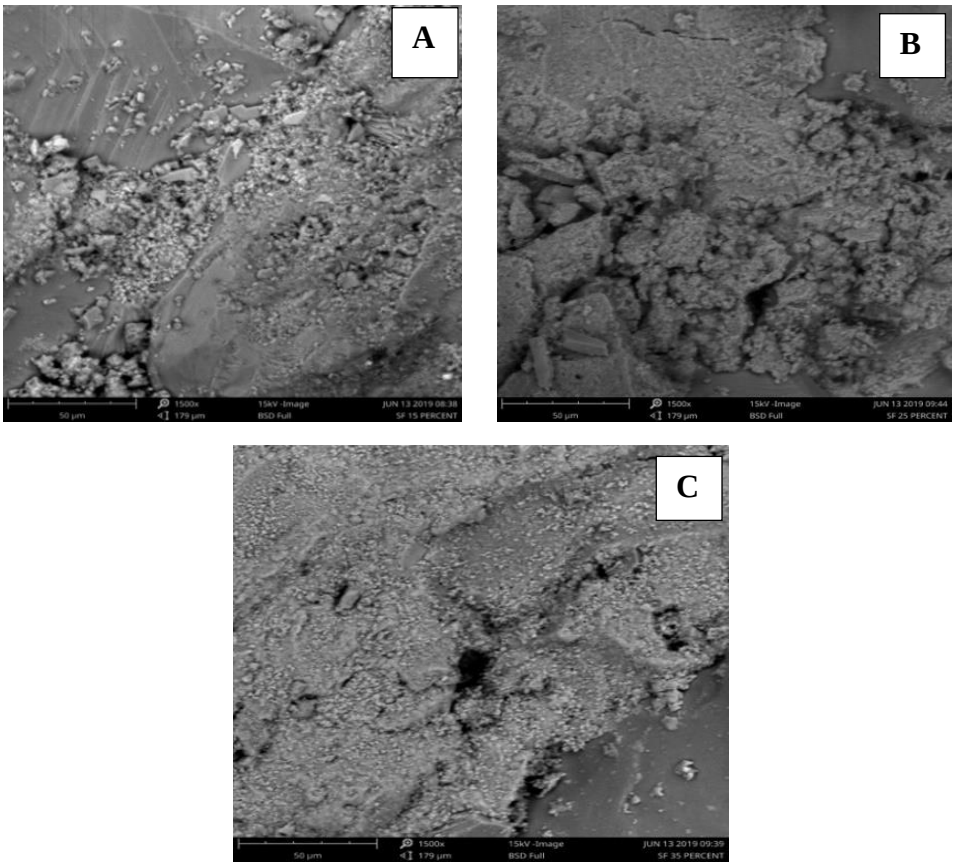

Fig. 3 SEM of the SSC at 15 vol% (a), 25 vol% (b) and 35 vol% (c) partial replacement (×1500 magnification)

3.2.5 SSC composition

The summary of the SSC composition is given in Table 9 and the associated EDS spectrum is given in Figure 4. The results are presented with the exception of oxygen and hydrogen. The major constituent of the SSC with partial replacement is carbon, calcium and silicon. The silicon content is due to the presence of SiO_2 in the coarse and fine aggregates. Furthermore, silica fume partial replacement is also a major contributor to the silica content of the SSC. There is no observable variation/relationship between SSC composition and increasing partial replacement. Calcium is a major constituent of cement (from lime and gypsum) hence it large presence in the SSC. The high carbon content is due to the high amount of soot in the silica fume. The iron and aluminum form oxides which are also major constituents in the cement hence their large amount in the concrete. The trace elements (most of which are earth and rare earth metals) in the concrete is due to the impurities in the cement and the other constituents within the crystalline structure of the coarse and fine aggregates. These trace elements usually exist as oxides [36]. Though this composition is good for comparison it is in itself no holistic due to it being on an oxygen and hydrogen free basis.

Table 9. Summary SSC composition

Element	Weight Conc. (15 vol %)	Weight Conc. (25 vol %)	Weight Conc. (35 vol %)
C	29.88	23.14	32.98
Ca	29.44	31.89	31.42
Si	23.91	16.81	17.62
N	-	17.47	10.76
Al	9.12	2.08	2.35
Na	3.25	0.81	1.07
Zr	2.26	-	1.26
Fe	1.88	3.10	0.97
Zn	-	1.56	-
S	-	1.25	0.67
Ti	0.25	-	0.20
Mg	-	0.97	0.70
P	-	0.93	-

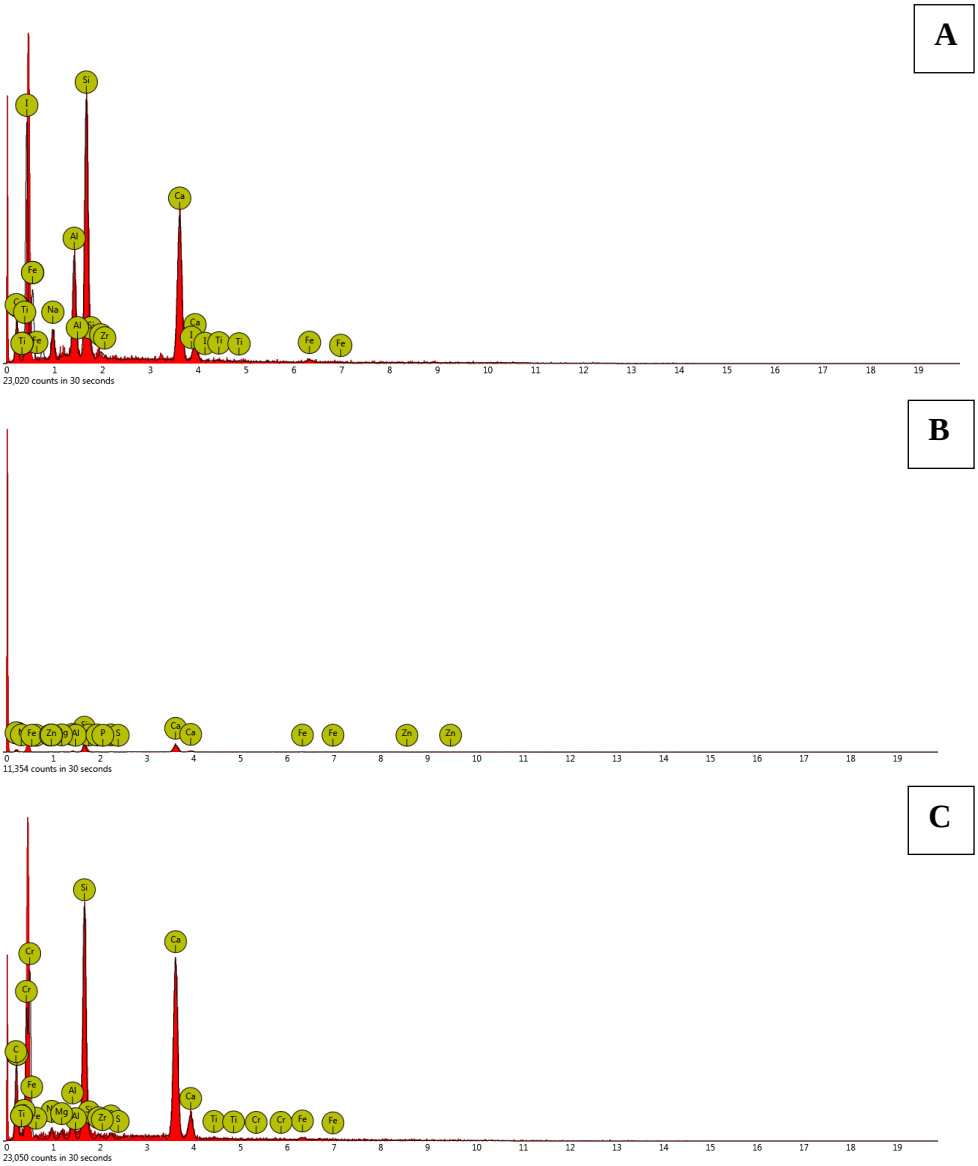

Fig. 4. EDS spectra for the SSC at 15 vol% (a), 25 vol% (b) and 35 vol% (c) partial replacement

4. Conclusion

In this study, fresh and hardened properties of self-compacting concrete obtained using silica fumes as partial replacement for cement was successfully evaluated for arrays of properties applicable to concrete development. Several key conclusions were drawn from the study.

Based on the results of the study, it is obtained that the utilization of silica fume as partial cement replacement gave a traceable improvement over the fresh state properties of the concrete in the domain of the flow-ability. This is confirmation of its usability in place of

cement in building industry. At the same time, the flow properties of SSC were improved when fly ash was used as partial cement replacement.

On the mechanical energy consideration, it is confirmed that the higher partial replacement led to lesser compressive strength due to weak interfacial transition zone. Partial replacement of cement with silica fume reduced the flexural strength of the SSC over the entire domain of the curing time. The decrease in compressive strength with partial cement replacement of silica fumes is due to weak interfacial transition zone. The weak transition zone associated with the silica fume application is negatively impacting the mechanical properties on curing. Moreover, the porosity of the mortar during adhesion to the fine and coarse aggregates and the formation of cracks in the aggregates are equally controllable.

Furthermore, it is equally deduced that the porosity of the mortar during adhesion to the fine and coarse aggregates. Voids were found formed when the irregular shape of the coarse aggregate combines with a poor interfacial effect with the cementitious material and lead to interstitials during curing. A high partial replacement leads to more water absorption. Moreover, the rapid water absorption was observed after the first day of the concrete preparation which gradually tailed off with time.

There is no observable variation/relationship between SSC composition and increasing partial replacement.

References

[1] Aslani F, Ma G, Wan DLY, Muselin G. Development of high-performance self-compacting concrete using waste recycled concrete aggregates and rubber granules. Journal of Cleaner Production. 2018;182:553-66. https://doi.org/10.1016/j.jclepro.2018.02.074

[2] Rantung D, Supit SW, Nicolaas S. Effects of different size of fly ash as cement replacement on self-compacting concrete properties. Journal of Sustainable Engineering: Proceedings Series. 2019;1:180-6. https://doi.org/10.35793/joseps.v1i2.25

[3] Brouwers H, Radix H. Self-compacting concrete: theoretical and experimental study. Cement and Concrete Research. 2005;35:2116-36. https://doi.org/10.1016/j.cemconres.2005.06.002

[4] Okamura H, Ouchi M. Self-compacting concrete. Journal of advanced concrete technology. 2003;1:5-15. https://doi.org/10.3151/jact.1.5

[5] Ofuyatan O, Olowofoyeku A, Edeki S, Oluwafemi J, Ajao A, David O. Incorporation of Silica Fume and Metakaolin on Self Compacting Concrete. Journal of Physics: Conference Series: IOP Publishing; 2019. p. 042089. https://doi.org/10.1088/1742-6596/1378/4/042089

[6] Ardalan RB, Joshaghani A, Hooton RD. Workability retention and compressive strength of self-compacting concrete incorporating pumice powder and silica fume. Construction and Building Materials. 2017;134:116-22. https://doi.org/10.1016/j.conbuildmat.2016.12.090

[7] Manzi S, Mazzotti C, Bignozzi MC. Self-compacting concrete with recycled concrete aggregate: Study of the long-term properties. Construction and Building Materials. 2017;157:582-90. https://doi.org/10.1016/j.conbuildmat.2017.09.129

[8] Mastali M, Dalvand A. Use of silica fume and recycled steel fibers in self-compacting concrete (SCC). Construction and Building Materials. 2016;125:196-209. https://doi.org/10.1016/j.conbuildmat.2016.08.046

[9] Arachchige US, amakm A, Balasuriya B, Chathumini K, Dassanayake N, Devasurendra J. Environmental Pollution by Cement Industry. International Journal of Research. 2019;6.
[10] Dewald U, Achternbosch M. Why more sustainable cements failed so far? Disruptive innovations and their barriers in a basic industry. Environmental Innovation and Societal Transitions. 2016;19:15-30. https://doi.org/10.1016/j.eist.2015.10.001
[11] Bernal J, Reyes E, Massana J, León N, Sánchez E. Fresh and mechanical behavior of a self-compacting concrete with additions of nano-silica, silica fume and ternary mixtures. Construction and building materials. 2018;160:196-210. https://doi.org/10.1016/j.conbuildmat.2017.11.048
[12] Mastali M, Dalvand A. The impact resistance and mechanical properties of fiber reinforced self-compacting concrete (SCC) containing nano-SiO2 and silica fume. European Journal of Environmental and Civil Engineering. 2018;22:1-27. https://doi.org/10.1080/19648189.2016.1177604
[13] Guo Z, Jiang T, Zhang J, Kong X, Chen C, Lehman DE. Mechanical and durability properties of sustainable self-compacting concrete with recycled concrete aggregate and fly ash, slag and silica fume. Construction and Building Materials. 2020;231:117115. https://doi.org/10.1016/j.conbuildmat.2019.117115
[14] Ghoddousi P, Saadabadi LA. Study on hydration products by electrical resistivity for self-compacting concrete with silica fume and metakaolin. Construction and Building Materials. 2017;154:219-28. https://doi.org/10.1016/j.conbuildmat.2017.07.178
[15] Raisi EM, Amiri JV, Davoodi MR. Mechanical performance of self-compacting concrete incorporating rice husk ash. Construction and Building Materials. 2018;177:148-57. https://doi.org/10.1016/j.conbuildmat.2018.05.053
[16] Ranjbar N, Behnia A, Alsubari B, Birgani PM, Jumaat MZ. Durability and mechanical properties of self-compacting concrete incorporating palm oil fuel ash. Journal of Cleaner Production. 2016;112:723-30. https://doi.org/10.1016/j.jclepro.2015.07.033
[17] Khan MI, Siddique R. Utilization of silica fume in concrete: Review of durability properties. Resources, Conservation and Recycling. 2011;57:30-5. https://doi.org/10.1016/j.resconrec.2011.09.016
[18] Bubshait AA, Tahir BM, Jannadi M. Use of microsilica in concrete construction: Reviews state-of-the-art silica fume concrete and discusses the influence silica fume has on the various properties of concrete and the effect on the bond between parent concrete and new concrete. Building research and information. 1996;24:41-9. https://doi.org/10.1080/09613219608727497
[19] Leung HY, Kim J, Nadeem A, Jaganathan J, Anwar M. Sorptivity of self-compacting concrete containing fly ash and silica fume. Construction and Building Materials. 2016;113:369-75. https://doi.org/10.1016/j.conbuildmat.2016.03.071
[20] Sasanipour H, Aslani F, Taherinezhad J. Effect of silica fume on durability of self-compacting concrete made with waste recycled concrete aggregates. Construction and Building Materials. 2019;227:116598. https://doi.org/10.1016/j.conbuildmat.2019.07.324
[21] Zarnaghi VN, Fouroghi-Asl A, Nourani V, Ma H. On the pore structures of lightweight self-compacting concrete containing silica fume. Construction and Building Materials. 2018;193:557-64. https://doi.org/10.1016/j.conbuildmat.2018.09.080
[22] EFNARC S. Guidelines for self-compacting concrete. London, UK: Association House. 2002;32:34.
[23] EN B. 12350-8: 2010. Testing fresh concrete.
[24] EN 12350-8 B. 12350-8. Testing fresh concrete. 2010.
[25] Standard A. Standard test method for compressive strength of cylindrical concrete specimens. ASTM C39. 2010.

[26] ASTM. ASTM C1602/C1602M-12: Standard specific cation for mixing water used in the production of hydraulic cement concrete. ASTM International West Conshohocken, PA, USA; 2012.
[27] C642-13 A. Standard test method for density, absorption, and voids in hardened concrete. West Conshohocken, PA: ASTM International. 2013.
[28] Adeniyi AG, Ighalo JO, Onifade DV. Biochar from the Thermochemical Conversion of Orange (Citrus sinensis) Peel and Albedo: Product Quality and Potential Applications. Chemistry Africa. 2020. https://doi.org/10.1007/s42250-020-00119-6
[29] Grdic ZJ, Toplicic-Curcic GA, Despotovic IM, Ristic NS. Properties of self-compacting concrete prepared with coarse recycled concrete aggregate. Construction and Building Materials. 2010;24:1129-33. https://doi.org/10.1016/j.conbuildmat.2009.12.029
[30] Silva YF, Robayo RA, Mattey PE, Delvasto S. Properties of self-compacting concrete on fresh and hardened with residue of masonry and recycled concrete. Construction and Building Materials. 2016;124:639-44. https://doi.org/10.1016/j.conbuildmat.2016.07.057
[31] Ofuyatan O, Edeki S. Dataset on the durability behavior of palm oil fuel ash self compacting concrete. Data in brief. 2018;19:853-8. https://doi.org/10.1016/j.dib.2018.05.121
[32] Ofuyatan O, Edeki S. Dataset on predictive compressive strength model for self-compacting concrete. Data in brief. 2018;17:801-6. https://doi.org/10.1016/j.dib.2018.02.008
[33] Khoshkenari AG, Shafigh P, Moghimi M, Mahmud HB. The role of 0-2 mm fine recycled concrete aggregate on the compressive and splitting tensile strengths of recycled concrete aggregate concrete. Materials & Design. 2014;64:345-54. https://doi.org/10.1016/j.matdes.2014.07.048
[34] Modani PO, Mohitkar VM. Self-compacting concrete with recycled aggregate: A solution for sustainable development. International Journal of Civil & Structural Engineering. 2014;4:430-40.
[35] Xuan D, Zhan B, Poon CS. Durability of recycled aggregate concrete prepared with carbonated recycled concrete aggregates. Cement and Concrete Composites. 2017;84:214-21. https://doi.org/10.1016/j.cemconcomp.2017.09.015
[36] Limbachiya M, Marrocchino E, Koulouris A. Chemical-mineralogical characterisation of coarse recycled concrete aggregate. Waste Management. 2007;27:201-8. https://doi.org/10.1016/j.wasman.2006.01.00

Research on Engineering Structures & Materials
journal homepage: http://jresm.org
Research Group

Research Article

Experimental investigation on use of ferrochrome slag as an alternative to natural aggregates in concrete structures

Parmanand N. Ojha[a], Abhishek Singh[b], Brijesh Singh[*c], Vikas Patel[d]

National Council for Cement and Building Materials, India

Article Info

Article history:
Received 02 Feb 2021
Revised 18 Mar 2021
Accepted 20 Mar 2021

Keywords:

Ferrochrome slag;
Aggregates;
Petrography;
Mortar Bar Test;
Durability;
Leaching

Abstract

In view of reducing the cost of concrete and to meet the demand of conventional raw materials used in concrete, various industrial and solid wastes are being studied for their utilization in concrete without affecting its fresh, hardened and durability properties. Ferrochrome slag is waste material obtained from manufacturing of high carbon ferrochromium alloy. Depending upon cooling process, two types of ferrochrome slag are produced i.e. air cooled by letting molten slag cooled down under normal temperature and water cooled ferrochrome slag by quenching molten slag. Presence of chromium in Cr+3 and Cr+6 state in ferrochrome slag is an area of concern towards its feasibility to be used as a constituent material in concrete. In this study, physical and chemical properties of both types of slags were evaluated to check the feasibility of replacing natural fine aggregates with water cooled ferrochrome slag and natural coarse aggregates with air cooled ferrochrome slag. In concrete mix designs, natural aggregates were replaced with ferrochrome slag at replacement levels of 30%, 60% and 100%. Mixes were prepared at two w/c ratios and were evaluated for different fresh, hardened and durability properties of concrete. It was concluded that 60% replacement of natural coarse aggregate with air cooled ferrochrome slag and 60% replacement of natural fine aggregate with water cooled ferrochrome slag in concrete is feasible.

1. Introduction

Concrete is the most commonly used structural material for majority of construction work taking place across the globe. Out of its total volume, aggregate (both coarse and fine combined) makes up for the 70% of its volume and thereby making them the principal component materials in concrete production. Rapid growth in population, urbanization and industrialization has led to huge increase in demand of housing, transportation and other infrastructural amenities which will require large amount of concrete. This has resulted in scarcity of conventional fine and coarse aggregates which are required for producing concrete. In view of reducing the cost of concrete and to meet the demand of conventional raw materials used in concrete, various industrial and solid wastes are being studied for their utilization in concrete without affecting its fresh, hardened and durability properties. The use of industrial solid waste as a partial replacement of conventional raw materials for preparation of concrete is a favorable way to reduce the environmental impact from the construction industry along with compensating the lack of natural resources and thereby reducing the demand for extraction of natural raw materials [1].

*Corresponding author: brijeshsehwagiitr96@gmail.com
[a] orcid.org/0000-0003-1754-4488; [b] orcid.org/0000-0002-2343-5934; [c] orcid.org/0000-0002-6512-1968; [d] orcid.org/0000-0002-2251-3849
DOI: http://dx.doi.org/10.17515/resm2021.255ma0202

The Ferrochrome slag is an important byproduct of ferrochromium industries and generated during the manufacturing of ferrochrome alloy. Ferrochrome alloy is manufactured in a submerged electric arc furnace by physiochemical process at the temperature of 1700ºC. The main constituents of ferrochrome slag are SiO2, Al2O3 and MgO with minor traces of ferrous/ferric oxides and CaO. Chromium is generally present in the form of partial altered chromite and entrapped alloy. Quartzite is added as fluxing material to reduce the melting temperature of slag. The slag production is 1.1-1.6 t / t Ferrochrome alloy depending on feed materials.

Depending upon the cooling process, two types of ferrochrome slag are produced i.e. air cooled by letting the molten slag cool under normal temperature and water cooled ferrochrome slag by quenching the molten slag. Since, the particle size of air cooled ferrochrome slag is in coarser range, it can potentially be used as replacement of natural coarse aggregate in concrete. Whereas, since the particle size of water cooled ferrochrome slag lies in finer range, it can potentially be used as replacement of natural fine aggregate in concrete. However, presence of chromium as Cr+3 which is not soluble in water (when oxidized turns into Cr+6) and Cr+6 which is soluble in water (hazardous), makes ferrochrome slag a potent threat to environment.

The Ferrochrome slag possesses physical properties similar to natural aggregates which makes it a suitable material for application in concrete as a replacement of natural aggregates. However, very limited research work and studies have been conducted to investigate presence of different forms of Chromium in ferrochrome slag and possibility of utilization of ferrochrome slag as replacement of conventional aggregates in concrete (especially reinforced cement concrete). In both water cooled and air cooled ferrochrome slag as determined by Nilamadhaba et.al [2], chromium is present in stable spinel phase and in the form of entrapped metallic granules. In molten slag, Cr is mainly in Cr+2, which is not stable at room temperature and therefore solidifies in most stable oxide i.e. Cr2O3 or Cr+3 which is insoluble in water and also not expected to oxidize at atmospheric temperature to highly soluble and carcinogenic Cr+6 form. The Chromium present in entrapped metallic granules is in dispersed state and therefore not expected to leach out when in contact with water. However, many researchers addressed the oxidation of Cr+3 to Cr+6 in the presence of strong oxidants which results in the possibility of slowly releasing Cr+6 to the environment in the long run. Leachability of heavy metals is the main environmental concern due to possible impacts on human health and environmental pacts.

Lind et. al [3] investigated that "leaching tests with salt seawater and pH adjusted water reveal low leachability from the slag for most elements. It was also reported that in road construction, there was a low migration of particles from the slag to the underlying soil and that the leaching from the Ferrochrome slag to the groundwater was low for the elements analyzed, with the exception of potassium. Al Jabri et al. [4] investigated the combined effects of fly ash as cement replacement and ferrochrome slag as a substitute of natural aggregate. Cement was replaced with fly ash at the ratio of 10, 20, and 30% whereas coarse limestone aggregates were replaced with coarse ferrochromium aggregate at replacement levels of 25, 50, and 75%. The results from the study revealed that inclusion of ferrochromium aggregates led to increase in the strength of concrete and also the abrasive wear resistance while it has negligible influence on the porosity and water absorption of concrete.

Panda et.al [5] investigated the environmental and mechanical properties of concrete containing ferrochrome slag. The concrete showed increased strength in comparison to control sample. The standard leaching experimental results showed that the leachable chromium remains well immobilized in the cement and concrete matrix with very low to non-detectable level of chromium leaching. Sathwik et. al [6] investigated the utilization of

ferrochrome slag as replacement of coarse aggregate in concrete. They conducted the study on M50 grade of concrete. Their studies revealed that in concrete made with up to 75% replacement of natural aggregates with ferrochrome slag, the compressive and flexural strength was found comparable with that of the control sample. Zyranov et. al [7] investigated the possibility of low carbon ferrochrome slag into a dry slag and further recycling it into commercial product. Their study concluded that the strength of concrete under normal condition is less than the strength of concrete under steam curing as high temperature activates the process of slag hydration.

In view of the above mentioned studies, it becomes imperative to conduct studies and evaluate the performance of concrete mixes containing water and air cooled ferrochrome slag as replacement of natural aggregates in concrete and compare their performance with corresponding control concrete mixes made with 100% natural aggregates in terms of different fresh, hardened and especially durability properties of concrete, as very limited studies has been conducted on the durability parameters of concrete made with ferrochrome slag as a replacement of natural aggregates.

2. The Effect of Factors on Shear Force

In this study, Ferrochrome slag (both water cooled and air cooled) aggregates were evaluated for different physical characteristics as per IS: 2386 [8] (as applicable for manufactured sand and manufactured coarse aggregates). Both water and air cooled ferrochrome slag samples were subjected to chemical analysis as per IS 4032 [9] for evaluation of loss on Ignition, major constituents (Cr_2O_3, Al_2O_3, Fe_2O_3, CaO, SiO_2, reactive silica and MgO) and minor constituents (Na_2O, K_2O, SO_3, Cl^-, TiO_2 etc.). Total alkali content as Na_2O equivalent, total sulphate content as SO_3, acid and water soluble chloride content and total sulphur as S. Elemental analysis and leaching study as per Toxicity characteristic leaching procedure (TCLP) as per ASTM D5233 [10] for heavy metals was carried out for both ferrochrome slag samples. Both air and water cooled ferrochrome slag aggregates were evaluated for Alkali Silica reactivity using accelerated and long term mortar bar test. Other concrete making materials such as cement, natural aggregate and admixture were meeting the criteria as mentioned in relevant Indian Standards.

Two control concrete mixes were prepared using Ordinary Portland Cement (OPC) along with 100% natural fine aggregates and 100% natural coarse aggregates at two different water-cement ratios of 0.65 and 0.40. Then, mixes were prepared by replacing natural fine aggregates with water cooled ferrochrome slag at 30, 60 and 100% along with 100% natural coarse aggregates at both the water cement ratios. Further, mixes were prepared by replacing natural coarse aggregate with air cooled ferrochrome slag at 30, 60 and 100% along with 100% natural fine aggregates at both the water cement ratios. Thus, a total number of 14 concrete mixes were prepared. All the mixes were studied for fresh properties of concrete such as workability (in terms of slump at 30, 60, 90 and 120 minutes) and air content of concrete as per IS: 1199 [11]. Further, mixes were evaluated for different mechanical properties such as compressive strength, flexural strength, split tensile strength, density, drying shrinkage of concrete and modulus of elasticity of concrete at various ages. Mixes were also studied for different durability properties of concrete tests such as Rapid Chloride ion penetrability test (RCPT), Sulphate expansion test, Chloride migration test, accelerated carbonation test and sorptivity test.

3. Properties of Air Cooled Ferrochrome Slag and Water Cooled Ferrochrome Slag

3.1. Physical Properties of Ferrochrome Slag

Sieve analysis of water cooled ferrochrome slag (< 4.75mm) and air Cooled Ferrochrome slag (20 mm and 10 mm) samples were carried out as per IS 383:2016 [12] and the results are given in Table 1.

Table 1. Sieve analysis of ferrochrome slag samples

IS Sieve Size	Water Cooled Ferrochrome slag (<4.75mm) % Passing	Air Cooled Ferrochrome slag, 20mm, % Passing	Air Cooled Ferrochrome slag, 10mm, % Passing
40 mm	-	100	-
20 mm	-	100	-
12.5 mm	-	-	100
10 mm	100	28	100
4.75 mm	100	1	23
2.36 mm	98	-	5
1.18 mm	79	-	-
600 µm	46	-	-
300 µm	28	-	-
150 µm	15	-	-

The physical properties of Ferrochrome slag samples are given in Table 2 below. The physical properties of water cooled and air cooled ferrochrome slag meets the various requirements of IS: 383-2016. The specific gravity of slag samples was observed to be higher than that of natural aggregates. Water absorption and material finer than 75 µm were found to be comparable with natural aggregates. The water cooled ferrochrome slag lies in zone 2 of grading as per IS: 383-2016. The low values of abrasion, crushing and impact reflects the stronger nature of air cooled ferrochrome slag.

Table 2. Physical properties of ferrochrome slag samples

Test Carried out	Water Cooled Ferrochrome slag (<4.75mm)	Air Cooled Ferrochrome slag, 20mm	Air Cooled Ferrochrome slag, 10mm
Specific gravity	2.87	2.99	2.98
Water absorption, %	0.74	0.33	0.31
Material finer than 75 µm % (wet sieving)	3.97	0.10	0.1
Soundness , $MgSO_4$ %	2.68	1.28	1.91
Organic impurities %	Nil	Nil	Nil
Clay Lumps %	Nil	Nil	Nil
Total deleterious material, % (excluding coal & lignite)	Nil	Nil	Nil
Loose Bulk Density, Kg/lit	1.09	1.61	1.43
Compacted Bulk Density, Kg/lit	1.21	1.71	1.56
Abrasion value	-	14	-
Crushing Value	-	19	-
Impact Value	-	15	-

3.2. Chemical Properties of Ferrochrome Slag Samples

Both type of ferrochrome slag samples (water cooled and air cooled) were studied for several chemical parameters as per IS 4032. The chemical properties of ferrochrome slag samples are tabulated in Table 3 below.

Table 3. Chemical properties of ferrochrome slag samples

Test Carried out	Water Cooled Ferrochrome slag (<4.75mm), %	Air Cooled Ferrochrome slag, (>4.75mm), %
Gain on Ignition, %	+1.51	+0.93
Silica	25.73	31.54
Iron Oxide	3.59	5.23
Alumina	35.3	28.67
Calcium Oxide	2.8	3.68
Magnesium Oxide	22.36	19.22
Sulphuric Anhydride	0.12	0.06
Chloride	0.015	0.01
Alkalis (as Na2Oeq)	0.23	0.55
Titanium Dioxide	1.06	1.44
Total Sulphur	0.25	0.44

As per IS 383: 2016, the prescribed limit of total alkali content is 0.3%. The observed value of alkalis equivalent is 0.23% in case of water cooled ferrochrome slag which lies within the limit specified. However, the value obtained in case of air cooled ferrochrome slag is higher than the prescribed limit. The observed values of chloride content, calcium oxide, iron oxide and total Sulphur are well within the limits specified in IS 383: 2016.

3.3. Elemental Analysis of Ferrochrome Slag Samples

Both water cooled and air cooled ferrochrome slag samples were subjected to elemental analysis. The results of elemental analysis of ferrochrome slag samples are tabulated in Table 4 below.

Table 11 of IS: 383-2016 quotes limits for environmental safety and quality standards for using iron, steel and copper slag aggregates. The values obtained for cadmium, lead, selenium and hexavalent chromium are within limits.

Table 4. Results of elemental analysis of ferrochrome slag samples

Element	Water Cooled Ferrochrome slag (<4.75mm), %	Air Cooled Ferrochrome slag, (>4.75mm), %
Barium	0.027	0.098
Beryllium	0.001	0.0005
Bismuth	Below detection Limit	Below detection Limit
Cadmium	0.002	0.001
Cobalt	0.012	0.012
Chromium	8	8.86
Copper	0.175	0.42
Gallium	Below Detection Limit	Below Detection Limit
Manganese	0.219	0.185
Molybednum	0.011	0.008
Nickel	0.032	0.04
Lead	0.013	0.008
Selenium	Below Detection Limit	Below Detection Limit
Strontium	0.088	0.008
Tellurium	Below Detection Limit	Below Detection Limit
Thallium	Below Detection Limit	Below Detection Limit
Zinc	0.029	0.061
Vanadium	0.012	0.013
Chromium, Cr+3	-	-
Chromium, Cr+6	0.0002	0.0003

3.4. Leaching Study for Heavy Metals on Ferrochrome Slag Samples

Leaching study on air and water cooled ferrochrome slag was conducted as per TCLP procedure. The results of concentration of heavy metals in slag sample is tabulated in Table 5 below.

Table 5. Results of leaching study on ferrochrome slag and natural aggregates

Sl No.	Constituents	Water cooled FS Slag FA	Air-cooled FS Slag CA	Limits as per TCLP procedure
1	Chromium	0.486	0.727	5
2	Copper	0.005	*BDL	25
3	Manganese	1.298	1.215	10
4	Nickel	0.831	0.774	20
5	Lead	0.020	BDL	5
6	Zinc	0.208	0.209	250
7	Iron	45.37	53.93	-
8	Titanium	0.012	0.011	-

As per the leachable concentration limits given in ministry of environment [13], forest and climate change guidelines, the observed values are lower than the prescribed limits.

3.5. Petrographic Examination of Ferrochrome slag Sample

Air cooled and water cooled ferrochrome slag samples were subjected to petrographic examination and their results are as mentioned below in sub sections 3.5.1 and 3.5.2.

3.5.1. Petrographic Examination of Air Cooled Ferrochrome Slag

This is a medium grained textured partially weathered random sample of the coarse aggregate. The major mineral constituents are spinel, olivine and clinopyroxene. Accessory minerals are quartz and iron oxide. Micro globular glass grains with corroded margins present as clusters are uniformly distributed in the sample. Majority of glass grains are in the size range of 7µm to 53µm. Subhedral to euhedral spinel grains with sharp grain margins are also uniformly distributed in the aggregate. Euhedral olivine grains with sharp grain margins are partially fractured and shattered. Grain size of olivine varies from 55 µm to 1052 µm with an average of 502 µm. Subhedral to anhedral clinopyroxene grains with corroded margins are fractured and shattered. Subhedral quartz grains with sharp grain margins are randomly distributed in the sample. Anhedral iron oxide grains are also randomly distributed in the sample. Microphotographs are given in Fig 1.

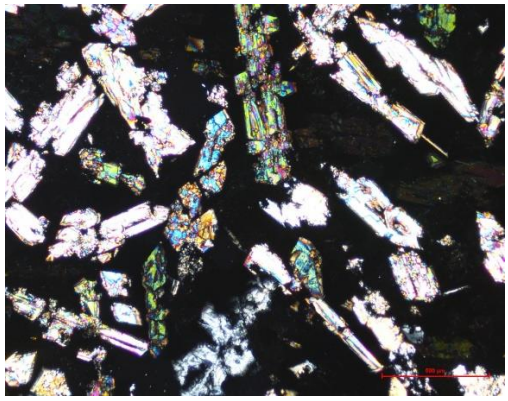

Fig. 1 Micrograph of air cooled Ferrochrome slag using optical microscope showing distribution of mineral grains in the sample (5x, x-nicols)

3.5.2. Petrographic Examination of Water Cooled Ferrochrome Slag

This is a fine grained textured partially weathered random sample of the fine aggregate. The predominant phase in the sample is glass. Subhedral to anhedral glass grains with sharp grain margins are uniformly distributed in the sample. Few elongated shaped glass grains are also observed in the fine aggregate. Grain size of glass varies from 15 µm to 408 µm with an average of 167 µm. Majority of glass grains are in the size range of 150µm to 170µm. Other mineral phases are quartz, orthoclase-feldspar, muscovite and iron oxide. Subhedral quartz grains with sharp grain margins are randomly distributed in the sample. Majority of quartz grains are in the size range of 100µm to 140µm. Subhedral orthoclase grains with rounded grain margins are also randomly distributed in the sample. Needle to lath shaped muscovite grains are mostly fresh in nature. Anhedral to subhedral iron oxide grains with corroded margins are uniformly distributed in the sample. Microphotographs are given in Fig 2.

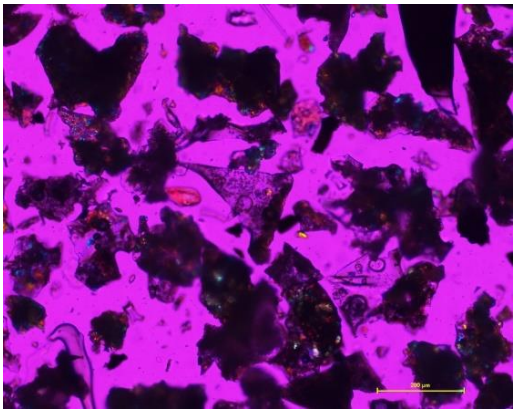

Fig. 2 Micrograph of water cooled ferrochrome slag using optical microscope showing distribution of mineral grains in the sample (5x, x-nicols)

3.6. Accelerated Mortar Bar Test

Accelerated mortar bar test was conducted on both water and air cooled ferrochrome slag aggregates as per ASTM C-1260 [14] for following compositions:

- 0% replacement of natural aggregates with ferrochrome slag
- 100% replacement of natural sand with water cooled ferrochrome slag samples.
- 100% replacement of natural coarse aggregate with air cooled ferrochrome slag samples.

The accelerated mortar-bar test as per ASTM 1260 consists of preparing mortar-bar in the same way as for conventional tests as per IS: 2386 i.e., by proportioning one part of Ordinary Portland Cement (OPC) to 2.25 parts of graded aggregates by mass, a fixed water to cement ratio of 0.47. The sample after 24-hours was de-moulded and then cured in hot water at 80ºC for 24-hours. Finally, the specimen was stored in 1N NaOH solutions at 80ºC for 14 days. The length change observations were taken in hot condition i.e., within 15+5 seconds after taking out from the solution. The samples were stored in plastic containers. As per ASTM criteria, the aggregate showing expansions less than 0.10% at 16 days after casting are classified as innocuous, whereas the aggregates showing more than 0.20% expansion are classified as potentially reactive. For aggregates showing expansion between 0.10% and 0.20%, the results are to be supported by other tests. Test results are given in Table 6. For all types of compositions, aggregates showed innocuous behaviour as expansion in all the cases were reported below 0.10%.

Table 6. Accelerated mortar bar test (ASTM C1260)

S.No.	Sample Type	1N NaOH 800C 14 Day Expansion %	Remarks
1	Fine Aggregate (0% replacement)	0.07	innocuous
2	Fine Aggregate (100% replacement)	0.03	innocuous
3	Coarse Aggregate (100% replacement)	0.09	innocuous

3.7. Mortar-Bar Test

Mortar-bar test was conducted at normal regime of 380 C and accelerated regime of 600 C as per IS: 2386. The test at 380 C was conducted to bring out the effect of metastable silica minerals present in aggregates, if any, and tests at 600 C was conducted to bring out the effect of slowly reactive strained quartz type of aggregates. The test was conducted using two reference OPC samples i.e. OPC-1 having alkali content (Na2O eq.) of 1.56% and OPC-2 having alkali content of 0.59%. The results of the mortar-bar tests are presented in Fig. 3 and 4. On perusal of mortar bar test results in Fig. 3 and 4, it can be seen that the expansions are within the permissible limits of 0.05% at 90 days and 0.06% at 180 days with all combinations. Therefore, ferrochrome aggregate samples were classified as innocuous as per IS: 2386.

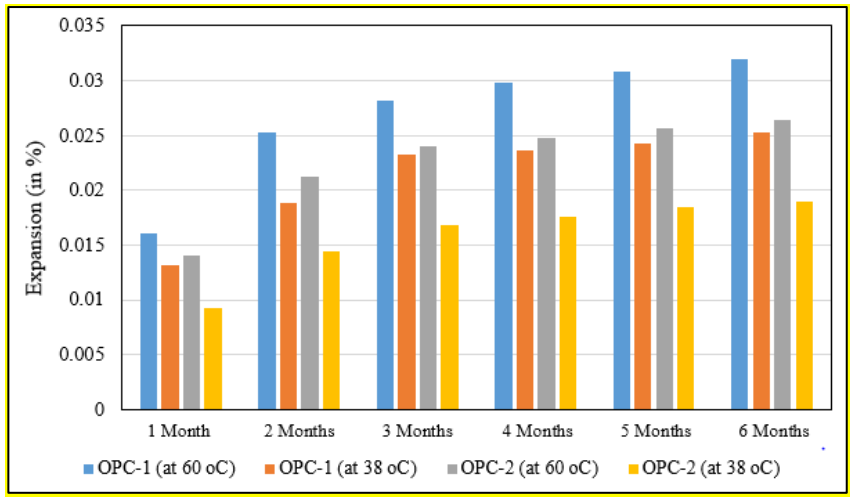

Fig. 3 Alkali aggregate reactivity as per IS: 2386 part VII for water cooled ferrochrome slag as 100% replacement of natural sand

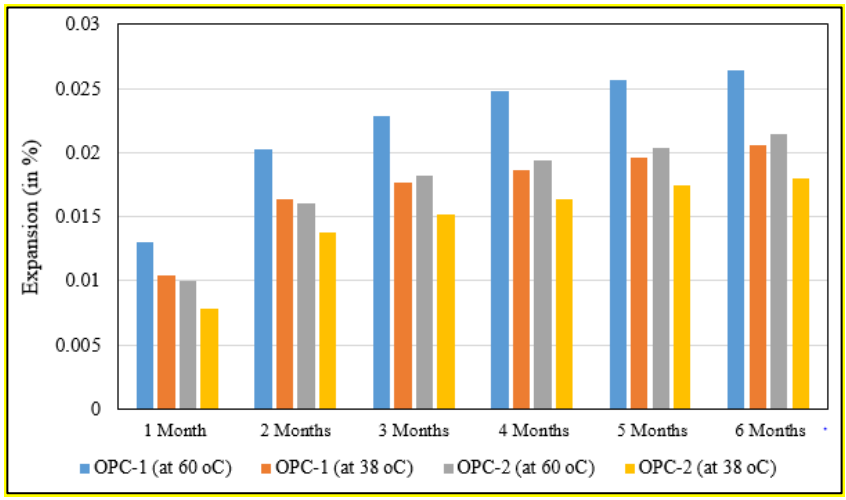

Fig. 4 Alkali aggregate reactivity as per IS: 2386 part VII for air cooled ferrochrome slag as 100% replacement of natural coarse aggregate.

4. Studies on Fresh, Hardened and Durability Properties of Concrete Mixes

4.1. Concrete Mixes Containing Water Cooled Ferrochrome Slag as Replacement of Natural Fine Aggregate

Two control concrete mixes (M4 and M0) were prepared using OPC along with 100% natural fine aggregates and 100% natural coarse aggregates at two water-cement ratios of 0.65 and 0.40. Then, mixes were prepared by replacing natural fine aggregate with water cooled ferrochrome slag at 30, 60 and 100% along with 100% natural coarse aggregates at both the water cement ratios

Therefore, a total of 8 mix designs (2 no. of control mixes + 3 x 2 = 6 number of mixes containing water cooled ferrochrome slag as fine aggregate) were carried out. The concrete mixes were designed for initial slump value of about 150 mm. Mix design details of concrete mixes are tabulated in Table 7.

Table 7. Concrete mix design details of mixes containing water cooled ferrochrome slag as replacement of natural fine aggregate

S. No.	Mix	Ferrochrome slag as fine Aggregates (%)	Cement (Kg/m3)	Water (Kg/m3)	Ferrochrome slag as fine aggregates (Kg/m3)
1	M0	0	300	195	0
2	M1	30	300	195	287
3	M2	60	300	195	573
4	M3	100	300	195	957
5	M4	0	425	170	0
6	M5	30	425	170	254
7	M6	60	425	170	507
8	M7	100	425	170	847

Table 7. (Con.) Concrete mix design details of mixes containing water cooled ferrochrome slag as replacement of natural fine aggregate

S. No.	Natural Fine Aggregate (Kg/m3)	Natural Coarse Aggregate (10 mm) (Kg/m3)	Natural Coarse Aggregate (20 mm) (Kg/m3)	Admix (%)
1	874	414	623	0
2	611	413	622	0.2
3	349	413	621	0.7
4	0	413	622	0.2
5	773	439	661	0.2
6	541	439	661	0.3
7	309	439	660	0.5
8	0	439	661	0.2

4.1.1. Fresh Concrete Properties

Fresh concrete properties such as workability (in terms of slump at 0 minutes, 30 minutes, 60 minutes and 120 minutes after preparation of mix) and air content were evaluated for all the 8 mixes and test results are given in Table 8.

Table 8. Fresh concrete properties of mixes containing water cooled Ferrochrome slag as replacement of natural fine aggregate

S. No	W/c Ratio	Mix ID	Ferrochrome slag as fine Aggregates (%)	Natural Sand
1	0.65	M0	0	100
2	0.65	M1	30	70
3	0.65	M2	60	40
4	0.65	M3	100	0
5	0.4	M4	0	100
6	0.4	M5	30	70
7	0.4	M6	60	40
8	0.4	M7	100	0

Table 8. (Con.) Fresh concrete properties of mixes containing water cooled ferrochrome slag as replacement of natural fine aggregate

S. No	Workability of concrete (mm):				Air Content, %	Remarks
	0 Min	30 Min	60 Min	120 Min		
1	145	135	125	100	1.8	Homogeneous mix
2	150	120	100	55	1.9	
3	160	110	85	30	2	
4	140	120	90	40	2.1	Segregation and bleeding
5	150	140	120	90	1.7	Homogeneous mix
6	150	110	80	40	1.9	
7	145	100	60	30	2.1	
8	150	110	80	40	2.4	Segregation and bleeding

Concrete mixes containing Ferrochrome slag showed significantly higher slump loss after 60 and 120 minutes in comparison to the control concrete mixes. Air content of all 8 mixes were similar and comparable (around 2%). It was observed that when replacement of natural coarse aggregate with air cooled ferrochrome slag goes beyond 60%, mixes showed signs of segregation and bleeding due to high specific gravity of ferrochrome slag.

4.1.2. Hardened Concrete Properties

Hardened concrete properties were evaluated for the eight concrete mixes. Compressive strength test was conducted on concrete cubes (150 mm × 150 mm × 150 mm) as per IS: 516 [15]. Flexural strength test was conducted on concrete beam (size 500mm x 100mm x 100mm) as per IS: 516. Split strength test and Modulus of Elasticity were conducted on concrete cylinder (150mm diameter and 300mm height) as per IS:5816 [16] and IS:516 respectively. Drying shrinkage test was conducted on concrete beam (75 x 75 x 300 mm) as per IS:1199. The test results are in Table 9.

Table 9. Hardened concrete properties containing of mixes containing water cooled ferrochrome slag as replacement of natural fine aggregate

W/c	Mix ID	Ferrochrome slag as fine Aggregates (%)	Compressive Strength, MPa				Flexural Strength, MPa	
			1 Day	3 Day	7 Day	28 Day	7 Day	28 Day
0.65	M0	0	4.54	12.5	18.1	26.22	4.07	5.05
0.65	M1	30	6.33	14.5	20.2	30.14	4.4	5.3
0.65	M2	60	7.38	16.5	22.95	38.05	5.07	5.37
0.65	M3	100	8.67	18.8	24.46	41.89	5.45	6.01
0.4	M4	0	15.95	32	41.86	49.79	6.4	8.07
0.4	M5	30	19.05	27.2	43.01	46.75	6.37	9.77
0.4	M6	60	20.84	29.3	42.89	53.08	7.17	10.3
0.4	M7	100	23.76	27.8	44.78	56.89	8.5	11.4

Table 9. (Con.) Hardened concrete properties containing of mixes containing water cooled ferrochrome slag as replacement of n atural fine aggregate

W/c	Mix ID	Split Tensile Strength, MPa	Dry Density Kg/m3	Drying Shrinkage	MOE (N/mm2)
		28 Day	28 Day	28 Day	28 Day
0.65	M0	2.42	2450	0.0171	28204
0.65	M1	2.67	2470	0.0168	30651
0.65	M2	2.72	2550	0.0164	32982
0.65	M3	3.21	2502	0.0179	34876
0.4	M4	4.51	2478	0.0191	37144
0.4	M5	4.75	2494	0.018	38013
0.4	M6	5.1	2520	0.0175	38885
0.4	M7	5.26	2560	0.0173	40016

Compressive, flexural and split tensile strength at age of 28 days for experimental mixes (containing water cooled ferrochrome slag as replacement of fine aggregates) at both w/c were found to be either higher or comparable to their control mix. Due to higher specific gravity of ferrochrome slag, dry density of the concrete mixes containing water cooled ferrochrome slag were higher than control mixes. The drying shrinkage values for all the concrete mixes were found satisfactory and comparable with their corresponding control mixes. Modulus of Elasticity (MOE) of the concrete mixes containing ferrochrome slag as

replacement of natural fine aggregates were found to be either higher or comparable to corresponding control mixes.

4.1.3. Durability Properties of Concrete mixes

Durability parameters of concrete such as Rapid Chloride ion penetrability test (RCPT) as per ASTM C-1202 [17], Sulphate expansion test as per ASTM C-1012 [18], Chloride migration test as per NT Build 492 [19], accelerated carbonation test as per ISO 1920 part 12 [20] and sorptivity test as per ASTM 1585 [21] were evaluated for all the eight concrete mixes. Test results are presented in Table 10.

Table 10. Durability properties of concrete mixes containing water cooled ferrochrome slag as replacement of natural fine aggregate

W/c	Mix ID	Ferrochrome slag as fine Aggregates (%)	RCPT, Coulomb	Chloride Migration, NT Build Diffusion coefficient (x 10-12 m2/s)		
			28 Day	28 Day	56 Day	90 Day
0.65	M0	0	3542	8.31	6.99	3.34
0.65	M1	30	3133	7.49	5.42	3.21
0.65	M2	60	3268	6.61	4.76	3.05
0.65	M3	100	2255	3.44	4.12	2.68
0.4	M4	0	1525	7.49	5.56	3.65
0.4	M5	30	1862	8.13	4.73	3.55
0.4	M6	60	1375	6.78	4.1	3.21
0.4	M7	100	1378	4.64	3.56	2.87

Table 10. (Con.) Durability properties of concrete mixes containing water cooled ferrochrome slag as replacement of natural fine aggregate

W/c	Mix ID	Sulphate expansion (%)			Carbonation Depth, mm	Sorptivity	
		28 Day	56 Day	90 Day		Initial	Secondary
0.65	M0	0.002	0.006	0.008	8.74	0.0057	0.0024
0.65	M1	0.003	0.005	0.007	7.33	0.0080	0.0028
0.65	M2	0.003	0.006	0.007	7.50	0.0062	0.0030
0.65	M3	0.002	0.005	0.009	7.10	0.0070	0.0038
0.4	M4	0.003	0.006	0.009	Nil	0.0032	0.0008
0.4	M5	0.003	0.005	0.007	Nil	0.0038	0.0009
0.4	M6	0.002	0.007	0.009	Nil	0.0005	0.0002
0.4	M7	0.004	0.006	0.008	Nil	0.0010	0.0006

In case of RCPT, it was observed that experimental mixes containing water cooled ferrochrome slag as replacement of natural sand show comparable performance to corresponding control concrete mixes. All the mixes having w/c of 0.65 fall under the permeability class “moderate” and mixes having w/c ratio of 0.40 fall under permeability class “low” as defined in ASTM 1260.

Similarly, performance of experimental mixes (containing water cooled ferrochrome slag as replacement of natural sand) in case of chloride migration test as per NT build 492 is similar and comparable to their corresponding control mixes. In case of accelerated carbonation test, mixes prepared at water to cement ratio of 0.65 (both experimental and control mix) showed similar carbonation depth (of around 8 mm) and mixes prepared at water to cement ratio of 0.40 (both experimental and control mix) showed nil carbonation depth. Sulphate expansion results for all the concrete mixes are well within the maximum

limits prescribed by ASTM C 1012. Sorptivity test results of experimental mixes containing water cooled ferrochrome slag as replacement of natural sand are similar and comparable to their corresponding control mixes.

This shows that replacement of natural fine aggregates with water cooled ferrochrome slag aggregates in a concrete mix does not have any negative or detrimental effect on the durability properties of concrete.

4.2. Concrete Mixes Containing Air Cooled Ferrochrome Slag as Replacement of Natural Coarse Aggregate

Along with two control concrete mixes (M4 and M0), mixes were prepared by replacing natural coarse aggregate with air cooled ferrochrome slag at 30, 60 and 100% along with 100% natural fine aggregates at both the water cement. Thus, six experimental mixes (containing air cooled Ferrochrome slag) were prepared along with two control mixes (M0 and M4). All the concrete mixes were designed for initial slump value of around 150 mm. Mix design details of concrete mixes are tabulated in Table 11.

Table 11. Concrete mix design details of mixes containing air cooled ferrochrome slag as replacement of natural coarse aggregate

Mix	Ferrochrome slag as coarse Aggregates (%)	Cement (Kg/m3)	Water Kg/m3	Natural Fine aggregate (Kg/m3)	Ferrochrome slag as coarse Aggregate (10mm) (Kg/m3)
M0	0	300	195	874	0
M8	30	300	195	863	116
M9	60	300	195	863	233
M10	100	300	195	862	387
M4	0	425	170	773	0
M11	30	425	170	759	123
M12	60	425	170	759	245
M13	100	425	170	759	409

Table 11. (Con.) Concrete mix design details of mixes containing air cooled ferrochrome slag as replacement of natural coarse aggregate

Mix	Ferrochrome slag as coarse aggregates (20mm) (Kg/m3)	Natural Coarse Aggregate (10 mm) (Kg/m3)	Natural Coarse Aggregate (20 mm) (Kg/m3)	Admix (%)
M0	0	414	623	0
M8	217	286	431	0
M9	433	164	246	0
M10	721	0	0	0.6
M4	0	439	661	0.2
M11	229	302	454	0.3
M12	457	172	260	0.3
M13	762	0	0	0.3

4.2.1. Fresh Concrete Properties

Fresh concrete properties such as workability and air content were evaluated for all the 8 mixes. Test results are given in Table 12.

Table 12. Fresh Concrete properties of mixes containing air cooled ferrochrome slag as replacement of natural coarse aggregate

S. No	W/c Ratio	Mix ID	Ferrochrome slag as coarse Aggregates (%)	Natural coarse aggregates
1	0.65	M0	0	100
2	0.65	M8	30	70
3	0.65	M9	60	40
4	0.65	M10	100	0
5	0.40	M4	0	100
6	0.4	M11	30	70
7	0.4	M12	60	40
8	0.4	M13	100	0

Table 12. (Con.) Fresh Concrete properties of mixes containing air cooled ferrochrome slag as replacement of natural coarse aggregate

S. No	Workability of concrete (mm):				Air Content, %	Remarks
	0 Min	30 Min	60 Min	120 Min		
1	145	135	125	100	1.8	Homogeneous mix
2	150	140	120	80	1.7	
3	150	130	110	50	1.8	
4	150	120	70	50	2	Segregation and bleeding
5	150	140	120	90	1.7	Homogeneous mix
6	150	135	110	70	1.6	
7	140	125	90	40	1.9	
8	145	90	60	50	2.1	Segregation and bleeding

Concrete mixes containing air cooled ferrochrome slag showed significantly higher slump loss after 60 and 120 minutes in comparison to the control concrete mixes. Air content of all 8 mixes were similar and comparable (around 2%). It was observed that when replacement of natural coarse aggregate with air cooled ferrochrome slag goes beyond 60%, mixes showed signs of segregation and bleeding due to high specific gravity of ferrochrome slag.

4.2.2. Hardened Concrete Properties

Hardened concrete properties were evaluated for all the six concrete mixes (M8 to M13) along with the control mixes (M4 and M0). Specimen size, test method and age of testing for all the tests were kept same as discussed in 4.1.2. Test results have been tabulated in Table 13.

Table 13. Hardened concrete properties of mixes containing air cooled ferrochrome slag as replacement of natural coarse aggregate

W/c	Mix ID	Ferrochrome slag as coarse Aggregates (%)	Compressive Strength, MPa				Flex Strength, MPa	
			1 Day	3 Day	7 Day	28 Day	7 Day	28 Day
0.65	M0	0	4.54	12.5	18.1	26.22	4.07	5.05
0.65	M8	30	4.91	16.7	19.11	27.96	4	4.83
0.65	M9	60	3.61	9.93	16.01	24.69	3.87	4.73
0.65	M10	100	6.57	16.4	21.68	28.55	3.89	4.97
0.4	M4	0	15.95	32	41.86	49.79	6.4	8.07
0.4	M11	30	14.42	30.9	33.04	47.44	5.67	7.03
0.4	M12	60	9.58	29.6	38.19	45.44	5.87	7.7
0.4	M13	100	11.92	29.9	37.18	45.39	4.73	6.93

Table 13. (Con.) Hardened concrete properties of mixes containing air cooled ferrochrome slag as replacement of natural coarse aggregate

W/c	Mix ID	Split Tensile Strength, MPa	Dry Density Kg/m3	Drying Shrinkage	MOE (N/mm2)
		28 Day	28 days	28 days	28 Days
0.65	M0	2.42	2450	0.0171	28204
0.65	M8	2.41	2470	0.0175	28508
0.65	M9	2.17	2460	0.0159	26588
0.65	M10	2.54	2580	0.0170	28486
0.4	M4	4.51	2478	0.0191	37144
0.4	M11	3.46	2490	0.0174	34140
0.4	M12	3.57	2515	0.0171	34395
0.4	M13	3.87	2560	0.0167	33854

Compressive, flexural and split tensile strength at age of 28 days for experimental mixes (containing air cooled ferrochrome slag as replacement of coarse aggregates) at both w/c were found to be similar and comparable to their control mix. Due to higher specific gravity of ferrochrome slag, dry density of the concrete mixes containing air cooled ferrochrome slag were higher than control mixes. The drying shrinkage values for all the concrete mixes were found satisfactory and comparable with their corresponding control mixes. Modulus of Elasticity (MOE) of the concrete mixes containing ferrochrome slag as replacement of natural coarse aggregates were found to be similar and comparable to corresponding control mixes.

4.1.3. Durability Properties of Concrete Mixes

Durability parameters of concrete such as Rapid Chloride ion penetrability test (RCPT) as per ASTM C-1202, Sulphate expansion test as per ASTM C-1012, Chloride migration test as per NT Build 492, accelerated carbonation test as per ISO 1920 part 12 and sorptivity test as per ASTM 1585 were evaluated for all the eight concrete mixes. Test results have been presented in Table 14.

Table 14. Durability properties of concrete mixes containing air cooled ferrochrome slag as replacement of natural coarse aggregate

W/c	Mix ID	Ferrochrome slag as coarse Aggregates (%)	RCPT, Coulomb	Chloride Migration, NT Build Diffusion coefficient (x 10-12 m2/s)		
			28 Day	28 Day	56 Day	90 Day
0.65	M0	0	3542	8.31	6.99	3.34
0.65	M8	30	2331	9.03	5.88	4.27
0.65	M9	60	3574	8.54	6.24	2.6
0.65	M10	100	4259	6.48	3.98	3.12
0.4	M4	0	1525	7.49	5.56	3.65
0.4	M11	30	2189	6.81	5.29	3.68
0.4	M12	60	3490	9	5.44	3.71
0.4	M13	100	2876	8.52	5.90	3.58

Table 14. (Con.) Durability properties of concrete mixes containing air cooled ferrochrome slag as replacement of natural coarse aggregate

W/c	Mix ID	Sulphate expansion (%)			Carbonation Depth, mm	Sorptivity	
		28 Day	56 Day	90 Day		Initial	Secondary
0.65	M0	0.002	0.006	0.008	8.74	0.0057	0.0024
0.65	M8	0.001	0.004	0.007	7.65	0.0021	0.0010
0.65	M9	0.002	0.005	0.008	12.55	0.0033	0.0017
0.65	M10	0.003	0.005	0.009	10.55	0.0023	0.0013
0.4	M4	0.003	0.006	0.009	Nil	0.0032	0.0008
0.4	M11	0.004	0.006	0.008	Nil	0.0011	0.0004
0.4	M12	0.003	0.005	0.008	Nil	0.0010	0.0003
0.4	M13	0.005	0.007	0.009	Nil	0.0013	0.0004

In case of RCPT results, it was observed that experimental mixes containing water cooled ferrochrome slag as replacement of natural sand show comparable performance to corresponding control concrete mixes. Similarly, performance of experimental mixes (containing air cooled ferrochrome slag as replacement of natural coarse aggregates) in case of chloride migration test as per NT build 492 is similar and comparable to their corresponding control mixes. In case of accelerated carbonation test, mixes prepared at water to cement ratio of 0.65 (both experimental and control mix) showed similar carbonation depth (of around 8 to 12 mm) and mixes prepared at water to cement ratio of 0.40 (both experimental and control mix) showed nil carbonation depth. Sulphate expansion results for all the concrete mixes are well within the maximum limits prescribed by ASTM C 1012. Sorptivity test results of experimental mixes containing air cooled ferrochrome slag as replacement of natural coarse aggregates are similar and comparable to their corresponding control mixes.

This shows that replacement of natural coarse aggregates with air cooled ferrochrome slag aggregates in a concrete mix does not have any negative or detrimental effect on the durability properties of concrete.

4.3. Leaching Studies on Selected Concrete Mixes

Leaching study was also conducted on few selected concrete samples made with replacement of natural aggregates with corresponding ferrochrome slag aggregates, as per Toxicity Characteristic Leaching Procedure (TCLP) to detect the presence of different

heavy metals constituents. The results of concentration of heavy metals ions leached out from concrete samples are given in Table 15.

Table 15. Results of Leaching study on concrete samples

Sl No.	Constituents	M0	M4	M1	M5	M6	Limits as per TCLP procedure
1	Chromium (Cr)	0.1341	0.010	0.119	0.169	0.187	5
2	Copper (Cu)	0.009	0.006	0.047	0.12	0.007	25
3	Manganese (Mn)	0.002	0.002	0.025	0.002	0.002	10
4	Nickel (Ni)	0.013	BDL	0.023	0.007	BDL	20
5	Lead (Pb)	BDL	BDL	BDL	BDL	BDL	5
6	Zinc (Zn)	0.039	0.035	0.053	0.028	0.034	250
7	(Fe) Iron	BDL	0.048	0.032	0.010	0.001	-
8	Titanium (Ti)	0.054	0.003	0.92	0.028	0.053	-

As per the leachable concentration limits given by ministry of environment, forest and climate change guidelines, the observed values of heavy metal ions are lower than the prescribed limits.

5. Conclusions

Based on the results and observations of above mentioned studies following conclusions are drawn:

- Physical properties of water and air cooled ferrochrome slag meets the various requirements of IS: 383-2016. Specific gravity of slag samples was observed to be higher than that of natural aggregates. Water absorption and material finer than 75 μm were found to be comparable with natural aggregates. The low values of abrasion, crushing and impact reflects the stronger nature of air cooled ferrochrome slag.
- The results of elemental analysis of ferrochrome slag samples showed that concentrations of elements are within limits.
- Concrete mixes were prepared at two w/c ratios by replacing natural fine aggregates with water cooled ferrochrome slag and natural coarse aggregates with air cooled ferrochrome slag. Concrete mixes containing Ferrochrome slag showed significantly higher slump loss after 60 and 120 minutes in comparison to the control mixes. It was observed that when replacement of natural aggregates with ferrochrome slag goes beyond 60%, mixes showed signs of segregation and bleeding due to high specific gravity of ferrochrome slag. Hardened properties of concrete mixes containing ferrochrome slag were found to be higher or comparable to their corresponding control mixes at the age of 28 days. In terms of different durability related parameters, experimental mixes containing ferrochrome slag aggregates showed comparable performance in comparison to their corresponding control concrete mixes containing 100 % natural aggregates.
- Leaching study was conducted on water and air cooled Ferrochrome slag as per Toxicity Characteristic Leaching Procedure (TCLP) to detect the presence of different heavy metals constituents such as Cr, Fe, Zn, Cu, Mn, Ni, Pb and Ti. The observed values of heavy metal ions are lower than the prescribed limits. Leaching study was also conducted on few selected concrete samples made with replacement of natural aggregates with corresponding ferrochrome slag aggregates and the observed values of heavy metal ions are lower than the prescribed limits.

Based on the above conclusions, following recommendations are being made:

Water cooled Ferrochrome slag can be used as replacement of natural fine aggregate up to 60% by weight along with 100 % with natural coarse aggregates for making concrete. Air cooled Ferrochrome slag can be used as replacement of natural coarse aggregate up to 60% by weight along 100 % with natural fine aggregates for making concrete.

References

[1] Panda CR, Mishra KK, Panda KC, Nayak BD, Nayak BB. 'Environmental and technical assessment of ferrochrome slag as concrete aggregate material, Construction and Building Materials, 49, 2013. https://doi.org/10.1016/j.conbuildmat.2013.08.002
[2] Sahu N, Biswas A, Kapure GU, A short review on utilization of ferrochromium slag, Mineral Processing and Extractive Metallurgy Review, 2016. https://doi.org/10.1080/08827508.2016.1168415
[3] Lind BB, Fallman AM, Larsson LB. Environmental impact of ferrochrome slag in road construction, International Conference on the Science and Engineering of Recycling for Environmental Protection, 2001. https://doi.org/10.1016/S0956-053X(00)00098-2
[4] Khalifa J, "Research on the use of Ferro-Chrome slag in civil engineering applications." MATEC Web of Conferences, 2018.
[5] Panda CR, Mishra KK, Panda KC, Nayak BD, Nayak BB. Environmental and technical assessment of ferrochrome slag as concrete aggregate material, Construction and Building Materials, 2013. https://doi.org/10.1016/j.conbuildmat.2013.08.002
[6] Sathwik SR, Sanjith J, Sudhakar GN. Development of high strength concrete using ferrochrome slag aggregate as replacement to coarse aggregate, American Journal of Engineering Research, 2016.
[7] Zyranov FA, Bukreev AB, Zyranova OO. Heavy Concrete on Cement with slag of low carbon ferrochrome. Electric Journal of Structural Engineering, 2016,
[8] IS: 2386 - 1963 (Reaffirmed 2002). "Methods of Test for Aggregates for Concrete". BIS, New Delhi
[9] IS 4032 -1995. "Method of chemical analysis of hydraulic cement". BIS, New Delhi
[10] ASTM D5233 – 92 (2009). "Standard Test Method for Single Batch Extraction Method for Wastes". ASTM International, West Conshohocken, PA
[11] IS: 1199 -1959 (Reaffirmed 2004). "Methods of Sampling and Analysis of Concrete". BIS, New Delhi
[12] IS: 383-2016. "Coarse and Fine Aggregate for Concrete – Specification (Third Revision)". BIS, New Delhi
[13] Government of India, Ministry of Environment, Forest and Climate Change, published in the gazette of India, extraordinary, part II, section 3, sub-section (i)
[14] ASTM C1260-14. "Standard Test Method for Potential Alkali Reactivity of Aggregates (Mortar-Bar Method)". ASTM International, West Conshohocken, PA
[15] IS: 516 - 1959 (Reaffirmed 2004). "Methods of test of strength of concrete". BIS, New Delhi
[16] IS: 5816 - 1999 (Reaffirmed 2004), Splitting Tensile Strength of Concrete - Method of Test". BIS, New Delhi.
[17] ASTM C1202-19. "Standard Test Method for Electrical Indication of Concrete's Ability to Resist Chloride Ion Penetration" ASTM International, West Conshohocken, PA
[18] ASTM C1012. "Standard Test Method for Length Change of Hydraulic-Cement Mortars Exposed to a Sulfate Solution". ASTM International, West Conshohocken, PA
[19] NT BUILD 492 (1999). "Concrete, mortar and cement based repair materials: Chloride migration coefficient from non-steady-state migration experiments". Published by Nordtest, ISSN 0283-7153
[20] ISO 1920 Part 12 (2015). "Determination of Carbonation resistance of concrete".

[21] ASTM C1585-13. “Standard Test method for mesurement of rate of absorption of water by hydraulic cement concrete”. ASTM International, West Conshohocken, PA.

Research on Engineering Structures & Materials
journal homepage: http://jresm.org
Research Group

Research Article

The effect of hemp fiber usage on the mechanical and physical properties of cement based mortars

Gökhan Kaplan*[1,a], Oğuzhan Yavuz Bayraktar[2,b]

[1]*Atatürk University, Faculty of Engineering, Department of Civil Engineering, Erzurum, Turkey.*
[2]*Kastamonu University, Faculty of Engineering and Architecture, Department of Civil Engineering, Kastamonu, Turkey*

Article Info

Article history:
Received 22 Dec 2020
Revised 18 Jan 2021
Accepted 28 Jan 2021

Keywords:

Hemp fiber;
Mortar;
Compressive strength;
Capillarity;
Apparent porosity

Abstract

In this study, the impact of hemp fibers used in different lengths and ratios on the physical and mechanical properties of mortars has been examined. In this context, the flow diameters, dry unit weight, porosity, bending and compressive strength and capillarity properties of the mortars have been determined. Hemp fiber was used in the lengths of 0.5, 1 and 2 cm and was added to the mixtures in ratios of 1, 2 and 3%. The increase in fiber length and ratio decreased the flow diameter of the mortars and increased the porosity values. In the case of using 3% fiber, the dry unit weight values of the mortars fell below 2100 kg/m^3. It is understood from the flexural strength results that the curing process is very important for the improvement of the fiber-matrix interface when hemp fiber is used. As a result, as the fiber ratio increased, the flexural strength increased in both 7 and 28 days. But the increase in fiber ratio decreased the 7 and 28 days compressive strength values. According to the capillary test results, it was observed that the optimum fiber ratio was 1%. As the fiber ratio increased, the capillarity coefficients of the mixtures also increased. Compressive strengths of 50 MPa and above were obtained in mixtures having 1% fiber with a capillarity coefficient of less than 0.10 mm/min$^{0.5}$. As a result, it was determined that the most suitable fiber length is 1 cm. It has been determined that 1 or 2% fiber content is more suitable in the production of mortars.

1. Introduction

Nowadays, concrete ranks at the top among building materials that are mostly used in the world. Concrete is a brittle building material with very low tensile strength, energy absorption capacity and flexural toughness [1]. In order to eliminate this disadvantage of concrete, steel or synthetic fibers are added into it. [1]. Extensive research continues today to evaluate and determine the advantages of fiber-reinforced concrete. Various fiber types such as steel, carbon, glass, polypropylene, polyolefin are used in concrete production. The use of steel or synthetic fiber is expensive and environmentally harmful with respect to production [1]. For this reason, researches have been made in relation to the use of natural fibers in concrete production in recent years. Use of natural fiber goes back to about 5,000 years ago. Asbestos fibers have been used to strengthen clay pots in Scandinavia. In addition, the Egyptians added straw fiber into the clay blocks used in the construction of the walls [2]. Natural fibers are mostly preferred in developing countries. Since natural fibers are not fully accepted as an alternative to synthetic fibers, the use of natural fibers in developed countries is still limited. Another disadvantage of natural fibers is that their long-term durability properties are not known exactly. [3]. Natural fibers absorb more water than synthetic fibers and its distribution in concrete can sometimes create a

*Corresponding author: gkaplan@atauni.edu.tr
[a] orcid.org/0000-0001-6067-7337; [b]orcid.org/0000-0003-0578-6965
DOI: http://dx.doi.org/10.17515/resm2020.242ma1222

problem. [1]. Unlike steel or synthetic fibers, natural cellulosic fibers contribute to a more sustainable structure. The environmental impact of natural fibers is less CO_2 emissions as they can be grown locally and require a low amount of energy for production. Besides, it is thought that natural fibers have negative carbon feature due to the photosynthesis of plants [1]. Mehta and Monteiro stated that natural fibers increase the tensile strength and bending toughness. [2]. It has also been observed that natural fibers improve the thermal insulation properties of concrete by reducing the thermal conductivity coefficient [4]. There are studies showing that natural fibers reduce the compressive strength because they cause adherence problems due to their superficial properties [5]. Hemp fibers, which are among natural fibers, have recently been used in the production of cement-based composites. Natural fibers must have appropriate physical and mechanical properties to be used in concrete. [6].

Usage of vegetable fibers such as hemp in terms of cost and performance was largely developed in Europe in the early 1990s and adopted by North American automakers in the late 1990s. [7]. Among the most important properties of hemp fiber, low cost and high tensile strength come to the forefront [6-8]. Hemp fibers vary in cylindrical and l/d (length/diameter) and they often have irregular surfaces. Average tensile strength of hemp fibers is 857 MPa, and E-Modulus is approximately 58 GPa [9]. In the study conducted by Sedan et al, E-Modulus decreased while flexural strength increased in optimum hemp fiber content. But, adherence of the fibers with the matrix was increased with the surface improvement realized with alkalis [10]. In the study they conducted, Elfordy et al improved mechanical and thermal properties of concrete blocks with hemp fiber in their study [11]. Ghalieh et al have obtained promising results regarding the use of polymer blends that are produced from hemp fiber for reinforcing reinforced concrete columns [4,12]. Siriluk et al. investigated the use of hemp fiber in the reinforcement phase of reinforced concrete beams. As a conclusion, they stated that it is more appropriate to apply hemp fiber to the beam in U shape (bottom surface+two side surfaces) [13]. Çomak et al showed that optimum ratio for hemp fiber with 12 mm length is 2-3% [14]. Ghosn et al used hemp fibers in concrete production and they observed improvements in bending toughness of concrete [15]. In the literature, there are studies [16-19] examining the contribution of hemp fiber to durability. Kremensas et al examined thermal and insulation properties of hemp fiber [20]. Besides, the microstructure properties of hemp fiber were also examined. [21-22].

In this study, physical and mechanical properties of mortars being produced from hemp fibers having different lengths and proportions have been investigated. In this regard, fresh and hardened mortar experiments have been carried out using 0.5, 1 and 2 cm long hemp fibers with ratios of 1, 2 and 3%.

2. Material and Method

2.1. Materials

CEM I 42.5R type cement being in accordance with TS EN 196-1 standard has been used in the preparation of the mixtures. Chemical and physical properties of cement are shown in Table 1.

Table 1. Chemical and physical properties of CEM I 42,5 R

Oxide (%)	CaO 64,08	SiO_2 19,03	Al_2O_3 4,15	Fe_2O_3 3,56	MgO 1,04	SO_3 3,01	Na_2O 0,45	K_2O 0,71	LOI 3,55
Specific gravity	3,13		Specific surface area (cm^2/g)		3230		Setting time-Initial/Final (Min.)		210/270

Limestone (limestone) having 0-4 mm sieve opening has been used as aggregate. Grain distribution of aggregate is shown in Figure 1. Specific gravity of aggregate has been determined to be 2.66 and the water absorption value has been determined as 2.6%. Chemical and physical properties of hemp fiber are given in Table 2.

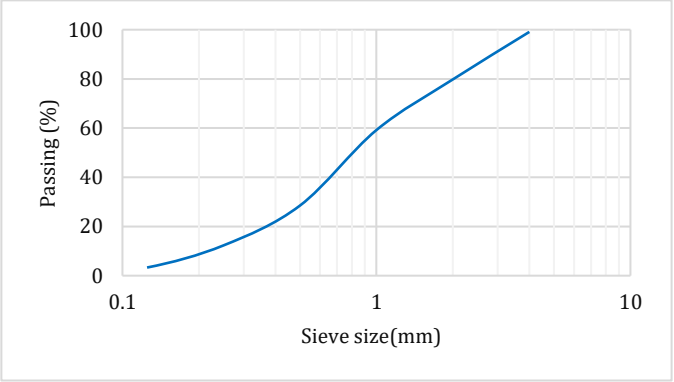

Fig.1 Particle distribution of limestone aggregate

Table 2. Technical properties of hemp fiber

Chemical properties		Physical properties	
Cellulose (%)	70-75	Specific gravity	1.47
Lignin (%)	3.5-6.0	Fiber length (cm)	0.5-2.0
Hemicellulose (%)	18-23	Moisture absorption (%)	~12
Pectin (%)	4-8	Tensile strength (MPa)	690
Wax (%)	1	Elongation at break (%)	3

No water reducing additives have been used in preparation of the mixtures and only potable water (Kastamonu city water) has been used. Hemp fibers were used in the lengths of 0.5, 1 and 2 cm. General view of hemp fibers is shown in Figure 2.

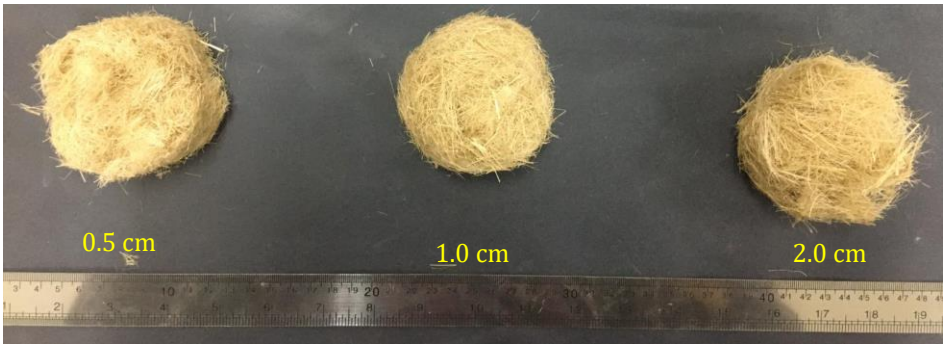

Fig. 2 General view of hemp fibers

2.2. Method

In the preparation of the mixtures, w/c (water/cement) ratio was selected as 0.50, while a/c (aggregate/cement) ratio was selected as 3. Amount of hemp fibers has been selected according to the cement amount. Fibers have been added to the mixture at the ratios of 1, 2 and 3% of the cement weight. Ratios and material quantities of mixtures have been presented in Table 3. Fibers have been added to the mixture in three different lengths and ratios. A total of 10 mixtures have been prepared, including 9 different fiber mixtures and 1 non-fiber mixture (reference). Hemp fibers were latest added to the mixture. After the aggregate, water and cement were mixed homogeneously, the fibers were added to the mixture. The fibrous mixture is mixed at a low speed of 1 minute and at a high speed of 1 minute.

Table 3. Mixing ratios and material quantities

Mixing ratio			Material quantities (g)			
Mix No.	Fiber length (cm)	Fiber raito (%)	Cement	Aggregate	Water	Fiber
1	0.5		450	1350	225	4,5
2	1,0	1	450	1350	225	4,5
3	2,0		450	1350	225	4,5
4	0.5		450	1350	225	9,0
5	1,0	2	450	1350	225	9,0
6	2,0		450	1350	225	9,0
7	0.5		450	1350	225	13,5
8	1,0	3	450	1350	225	13,5
9	2,0		450	1350	225	13,5
10 (Ref.)	-	-	450	1350	225	-

Flow diameters on the mortars have been determined first in accordance with the ASTM C 1437 standard. Mortars have been placed in the molds in two layers by applying vibration. Compressive and flexural strengths of 7 and 28 days have been carried out in accordance with ASTM C 349 and ASTM C 348 standards. For flexural strength test, prism samples of 40x40x160 mm have been used and compressive strength test has been carried out on the samples being divided into two at the end of the test. Capillarity properties of mortars have been determined in samples of 50x50x50 mm and in accordance with ASTM C 1585

standard. At the end of 28 days of curing, samples have been dried at 50 °C for 3 days and capillarity test was started. After water impermeability material has been applied to side surfaces of the samples, amount of water being absorbed by capillary way at 1th, 5th, 10th, 20th, 30th, 60th, 120th, 180th, 240th, 300th, 360th and 1440th minutes has been determined. Water absorption and porosity properties have been determined according to Archimedes' principle. Cube samples having size of 50x50x50 mm were used in relation to water absorption and porosity properties.

3. Results and Discussion

3.1. Fresh mortar properties

As a result of the experiment being performed according to ASTM C 1437 standard, the fresh state properties of some mortars (mixtures sufficient and poor in terms of workability) are shown in Figure 3. Flow diameters of mortars are shown in Figure 4.

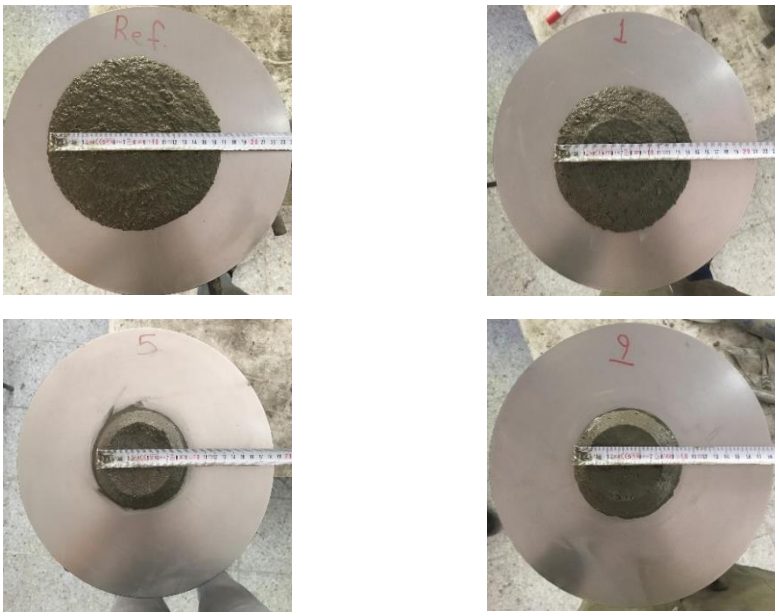

Fig. 3 Fresh properties of some mortars

As it is seen in Figure 4, as the fiber ratio and length increase, flow diameters of mortars get reduced. Flow diameters of mortars vary in the range of 14.4-9.4 cm. While the diffusion diameter of the reference mixture without fibers has been determined as 16.8 cm, the flow diameters of the mixtures with the addition of fiber has decreased below 15 cm. Spread diameter was generally 10 cm or below, especially when the fiber ratio was 2 or 3%. As a result of the increase in fiber length, the maximum processability loss has occurred at the ratio of 1% fiber. If the fiber length increased from 0.5 cm to 2 cm, flow diameter decreased by 29.8%. In the mixtures with 3% fiber, this ratio has been determined as 5%. Flow diameters of mixtures in which fiber with ratio of 2 and 3% has been used, showed similar properties. Usage of 2 cm long or 3% fiber affected the workability of the mortars negatively. Flow diameters of the fiber mixtures decreased by an average of 40% compared to the reference mixture.

As a result of the increase in fiber content and ratio, workability properties of mortars decrease. As a result of the increase in the fiber ratio, internal friction increases, hence decreasing the processability. If the fiber length increases, the fibers are not distributed homogeneously in the mixture and in this case it decreases the processability [23]. Similar results were observed in other studies in the literature [24-26].

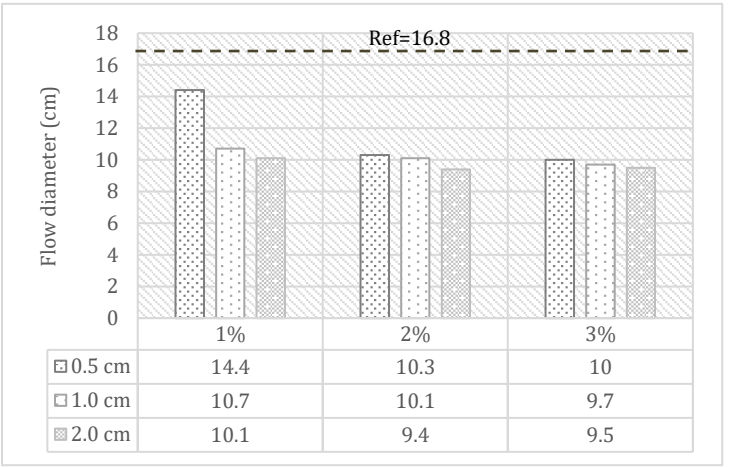

Fig. 4 Flow diameters of mortars with different fiber ratios and lengths

3.2. Dry Bulk Density (BD) and porosity properties of mortars

BD and visible porosity of the mortars are presented in Figure 5. BD values of fibrous mixtures vary in the range of 2037-2251 kg/m^3 (Figure 5a). BD value of the reference mixture without fiber is determined as 2116 kg/m^3. BD of the mixtures using only 3% fiber were lower than the reference mixture. This situation can be explained by the loss of workability. If 1 and 2% fiber is used, BD values are higher than the reference. When 1 and 2% fiber mixtures have been compared, the increase in fiber ratio increased the BD values of mortars. Reason for this effect can be explained by the particular that the mixing ratios are not volume-based and the proportions are fixed. Because as a result of the increase in the amount of fiber, BD values have increased. At 3% fiber content, the difficult placement of the mortars in the mold caused the formation of a hollow structure. When the fiber length is 1 or 2 cm, the BD values of mortars generally decrease. BD value exceeded 2250 kg/m^3 in the case of only 2% and 2 cm long fiber. Mixtures with a flow diameter of 10 cm and less, using 3% fiber, also have BD values below 2100 kg/m^3. Since the increase in fiber length prevents homogeneous distribution, it decreased the processability and as a result, the BD values generally decreased.

In Figure 5b, it is seen that the porosity values of fiber-based mixtures vary between 7.38-10.18%. As the fiber ratio in the mixtures increases, the apparent porosity values also increase. In addition, the increase in fiber length increased the apparent porosity values. Values closest to 7.88%, which is the porosity value of the reference mixture, were obtained in mixtures in which 1% fiber was used. Even the use of 0.5 and 1 cm long fibers made the porosity values come below the reference mixture. Mixtures produced from 0.5 cm long fibers were more homogeneous than other mixtures, as the spread diameter was 14.4 cm. This situation caused a decrease in porosity values. In addition, it has been stated in some studies that short fibers reduce porosity by acting as micro aggregates. The porosity values of the mixtures using 2 and 3% fiber are above 8%. (2037 kg/m^3) It is seen that the use of fiber with a length of 2 cm and 3% in mixtures provides the lowest BD value

and the porosity value exceeds 10%. In the study conducted by Olivito and Zuccarello, as the length of the steel fiber increases, the unit volume weight values decrease. However, this reduction is negligible. In addition, as the steel fiber ratio increased, the unit weight values of the mixtures increased [27]. In the study conducted by Asasutjarit et al, as the fiber length increased, the density of the composites decreased and the water absorption values increased. [28].

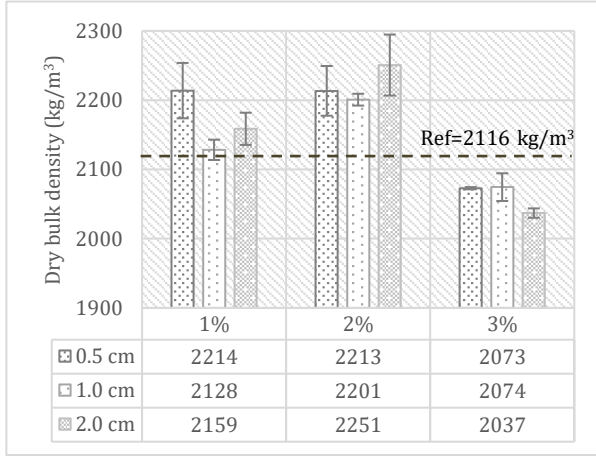

	1%	2%	3%
0.5 cm	2214	2213	2073
1.0 cm	2128	2201	2074
2.0 cm	2159	2251	2037

(a) Dry bulk density

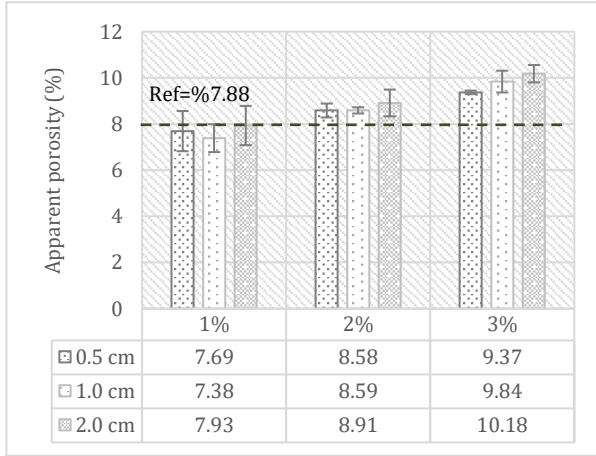

	1%	2%	3%
0.5 cm	7.69	8.58	9.37
1.0 cm	7.38	8.59	9.84
2.0 cm	7.93	8.91	10.18

(b) Apparent porosity

Fig. 5 Physical properties of fibrous and non-fibrous mortars

3.3. Mechanical properties of mortars

The 7 and 28 days flexural strength results of the mortars are given in Figure 6. As seen in Figure 6, it is seen that the 7 and 28 days flexural strength of the mortars do not show parallelism.

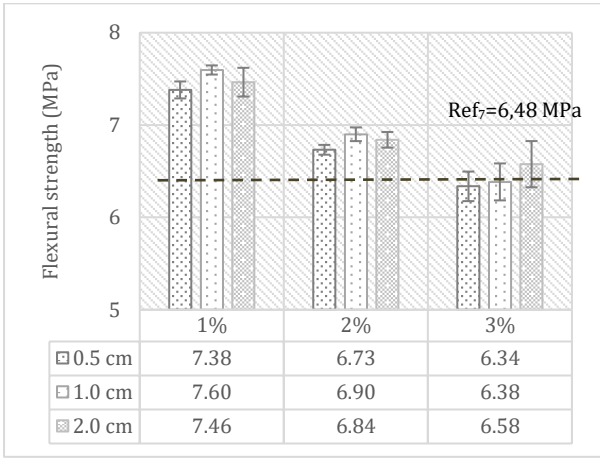

	1%	2%	3%
0.5 cm	7.38	6.73	6.34
1.0 cm	7.60	6.90	6.38
2.0 cm	7.46	6.84	6.58

(a) 7 days

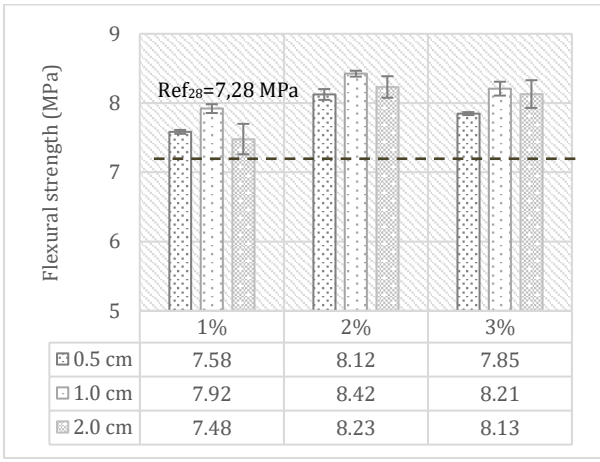

	1%	2%	3%
0.5 cm	7.58	8.12	7.85
1.0 cm	7.92	8.42	8.21
2.0 cm	7.48	8.23	8.13

(b) 28 days

Fig. 6 Flexural strength of mortars

Figure 6a shows that the bending strength of the fiber-free mixture is 6.48 MPa. When using 3% of 0.5 and 1 cm long fibers, the flexural strength was lower than the reference. This situation is thought to be caused by the loss of workability. Fiber length of 2 cm relatively increased flexural strength. In general, the increase in fiber length increases the bending strength. The highest bending strength was obtained when 1% fiber of 1 cm length was used. Flexural strength increased by 14.7% compared to the reference mixture. As a result of the increase in fiber ratio, their bending strength decreases. In particular, the use of 3% fiber has reduced the flexural strength to less than 6.50 MPa.

Figure 6b shows the 28-day flexural strength of the mortars. As a result of the increase in curing time, the flexural strength of the mortars has improved significantly. While the increase in fiber ratio in the 7-day bending strength caused a loss of strength, the opposite was observed in the 28-day blends. Especially, the strength of the mixture with a 7-day bending strength of 6.58 MPa, 2 cm long and containing 3% fiber, increased by 23.6% on the 28th day. On the 28th day, flexural strength of all mixtures is higher than the reference

mixture. Up to 2% fiber ratio, as the fiber length and ratio increases, the bending strength increases. Reductions in flexural strength were observed at 3% fiber content. It is understood that the ratio of 1 cm of the optimum fiber length is 2%. As a result of the increase in curing time, the fiber-matrix interface improved and resulted in an increase in flexural strength. It may be necessary to keep the curing period long for natural fibers such as hemp. It would be more appropriate to examine these findings with SEM analysis. Page et al. As the hemp fiber ratio increased, the bending strength increased. The increase in fiber length decreased the bending strength [29]. In addition, it was emphasized that the consistency of the mixture is effective in fiber orientation and that in this case it affects the bending strength. [30].

As seen in Figure 7a, the highest compressive strengths were obtained at 1% fiber content. As a result of the increase in fiber ratio, their 7-day compressive strength decreased. Using 1% of the 0.5 cm long fiber increased the compressive strength by 4.2% compared to the reference mixture. Fiber length of 1 cm generally increases compressive strength. It has been observed that blends produced from 0.5 and 2 cm long fibers have similar properties. If the fiber content was 3%, the compressive strength remained below the reference mixture. Figure 7b shows that the compressive strength increases as a result of the increase in curing time. All blends produced with 1% fiber provided higher compressive strength than the reference blend. However, as the fiber ratio increases, the compressive strength of the mortars decreases. Compressive strength of mixtures especially produced with 3% fiber is below 50 MPa. However, the fiber length being 1 cm generally increases the compressive strength. Page et al. Similar results were observed in the study conducted by [29]. Since the porosity values of the mixtures using fiber at 2 and 3% ratios are high, their compressive strength has decreased. However, an increase in bending strength was achieved at 2% fiber content. Although the porosity is high in these mixtures, the fibers act as reinforcement, preventing the crack propagation and increasing the bending strength.

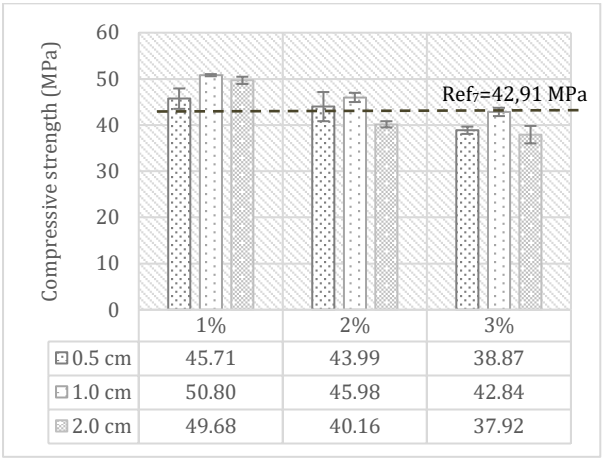

	1%	2%	3%
0.5 cm	45.71	43.99	38.87
1.0 cm	50.80	45.98	42.84
2.0 cm	49.68	40.16	37.92

(a) 7 days

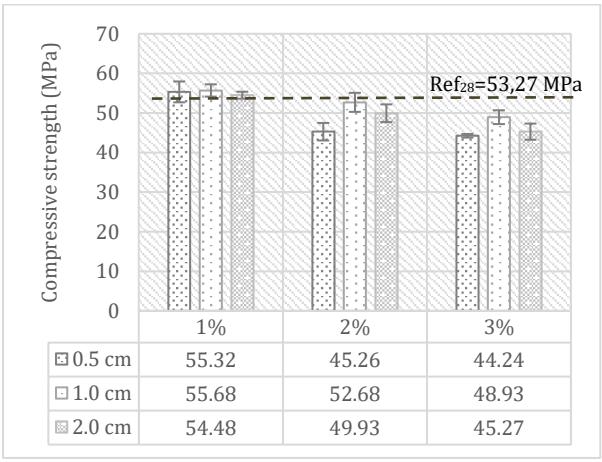

	1%	2%	3%
0.5 cm	55.32	45.26	44.24
1.0 cm	55.68	52.68	48.93
2.0 cm	54.48	49.93	45.27

(b) 28 days

Fig. 7 Compressive strength of mortars

3.4. Sorptivity properties of mortars

Sorptivity properties of mortars based on time are shown in Figure 8. With the increase in the fiber ratio, capillary coefficient of mortars also increased. Besides, the use of 1 cm long fiber reduces the capillarity coefficient, while the situation where fiber length is 2 cm negatively affects this. Capillarity coefficient of the reference mixture was measured to be 0.125 mm/min$^{0.5}$, and mixtures with 1% fiber ratio remained below this value. It was observed that the mixtures with 2% fiber content showed values close to the reference mixture. It is seen that capillarity and compressive strength show similar properties. It was observed that mortars with low capillarity coefficient showed higher compressive strength.

Taywood has made a quality classification for capillary properties of cement-based composites [31]. Classification is graded as good if the capillarity coefficient is less than 0.10 mm/min$^{0.5}$, it is graded as medium if it is between 0.1-0.2 mm/min$^{0.5}$, and it is graded as bad if it is greater than 0.2 mm/min$^{0.5}$. Using 1% of fibers of 1 and 2 cm long fibers

reduced the capillarity coefficient below 0.10 mm/min$^{0.5}$. The capillarity coefficient exceeded 0.20 mm/min $^{0.5}$ in the case of using 3% of 2 cm long fiber. It is observed that the mortars generally have a medium level of capillarity. In the study conducted by Nibudey et al, capillarity coefficient of the mixtures increased as the fiber ratio increased [32]. Similar results were found in the study conducted by Ramezanianpour et al. [33]. Rostami et al reported that fibers can also reduce the porosity of mixtures by closing gaps in some cases. [34].

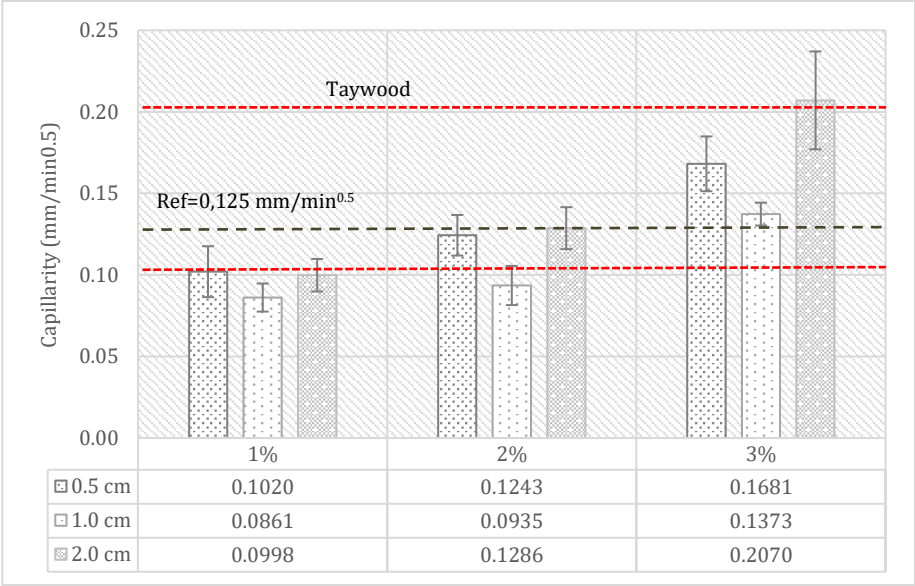

	1%	2%	3%
0.5 cm	0.1020	0.1243	0.1681
1.0 cm	0.0861	0.0935	0.1373
2.0 cm	0.0998	0.1286	0.2070

Fig. 8 Sorptivity properties of mortars

4. Conclusions

Increasing of fiber length and ratio has decreased the flow diameter of mortars. Especially if 3% fiber is used, flow diameters have decreased below 10 cm. Increasing of fiber length and ratio prevents homogeneous distribution of fibers.

Using 2% fiber increased the BD values of the mixtures. But with the fiber ratio being 3%, the BD values decreased depending on the processability. There is a difference of approximately 10% in the BD values between the mixtures. As the fiber length and ratio increase, porosity values of mixtures increase. Especially if 2 and 3% fiber was used, higher porosity value was obtained compared to the reference mixture.

As the fiber ratio increased in the 7-day mixtures, the flexural strength decreased. However, the increase in fiber length increased the flexural strength relatively. In 28-day mixtures, as the fiber ratio increased, the flexural strength increased. This is an indication of the improvement of the fiber-matrix interface with improved hydration. It has also been observed that 1 cm long fibers are more suitable in terms of flexural strength.

As the fiber ratio increases in 7- and 28-day mixtures, the compressive strength decreases. If the fiber length was 1 cm, the compressive strength increased, while the strength loss occurred at 2 cm fiber length. It has been observed that with 1% hemp fiber, compressive strengths of 50 MPa and above can be obtained.

Capillarity coefficients of mixtures produced with 3% fiber ratio were relatively higher. But the capillarity coefficients of the mixtures using 1% fiber are below 0.10 mm/min$^{0.5}$. Fiber length' being 2 cm significantly increased capillary coefficients. It was observed that the optimum fiber length in terms of capillarity is 1 cm.

As a conclusion, it was determined that the best performance in terms of fiber length should be 1 cm. Considering the flexural strength, it has been determined that the optimum fiber ratio should be 2%.

References

[1] Zhou X, Saini H, Kastiukas G. Engineering properties of treated natural hemp fiber-reinforced concrete. Front Built Environ. 2017. https://doi.org/10.3389/fbuil.2017.00033

[2] Mehta PK, Monteiro PJM. Third Edition Prentice- Hall, Inc., Englewood Cliffs, NJ. Concrete: microstructure, properties, and materials. 2006.

[3] Stevulova N, Cigasova J, Estokova A, Terpakova E, Geffert A, Kacik F, et al. Properties characterization of chemically modified hemp hurds. Materials (Basel). 2014. https://doi.org/10.3390/ma7128131

[4] Ghalieh L, Awwad E, Saad G, Khatib H, Mabsout M. A Study on the Behavior of Concrete Columns Wrapped with Hemp Fabrics. Mag Concr Res. 2020 Sep;1-35. https://doi.org/10.1680/jmacr.20.00103

[5] Bentur A, Mindess S. Fibre Reinforced Cementitious Composites. Fibre Reinforced Cementitious Composites. 2006. https://doi.org/10.1201/9781482267747

[6] Li Z, Wang L, Wang X. Compressive and flexural properties of hemp fiber reinforced concrete. Fibers Polym. 2004. https://doi.org/10.1007/BF02902998

[7] Ramadevi K, Deepa Shri S. Flexural behaviour of hemp fiber reinforced concrete beams. ARPN J Eng Appl Sci. 2015.

[8] Rai A, Joshi YP. Applications and Properties of Fibre Reinforced Concrete. J Eng Res Appl www.ijera.com ISSN. 2014.

[9] Pickering KL, Beckermann GW, Alam SN, Foreman NJ. Optimising industrial hemp fibre for composites. Compos Part A Appl Sci Manuf. 2007. https://doi.org/10.1016/j.compositesa.2006.02.020

[10] Sedan D, Pagnoux C, Smith A, Chotard T. Mechanical properties of hemp fibre reinforced cement: Influence of the fibre/matrix interaction. J Eur Ceram Soc. 2008; https://doi.org/10.1016/j.jeurceramsoc.2007.05.019

[11] Elfordy S, Lucas F, Tancret F, Scudeller Y, Goudet L. Mechanical and thermal properties of lime and hemp concrete ("hempcrete") manufactured by a projection process. Constr Build Mater. 2008. https://doi.org/10.1016/j.conbuildmat.2007.07.016

[12] Ghalieh L, Awwad E, Saad G, Khatib H, Mabsout M. Concrete Columns Wrapped with Hemp Fiber Reinforced Polymer - An Experimental Study. In: Procedia Engineering. 2017. https://doi.org/10.1016/j.proeng.2017.07.062

[13] Siriluk S, Hussin Q, Rattanapitikorn W, Pimanmas A. Behaviours Of RC deep beams strengthened in shear using hemp fiber reinforced polymer composites. Int J GEOMATE. 2018. https://doi.org/10.21660/2018.47.STR167

[14] Çomak B, Bideci A, Salli Bideci Ö. Effects of hemp fibers on characteristics of cement based mortar. Constr Build Mater. 2018. https://doi.org/10.1016/j.conbuildmat.2018.03.029

[15] Ghosn S, Cherkawi N, Hamad B. Studies on Hemp and Recycled Aggregate Concrete. Int J Concr Struct Mater. 2020 Dec;14(1):54. https://doi.org/10.1186/s40069-020-00429-6
[16] Kalpana K, Thamizhthendral K, Dhanalakshmi G. Investigation on the Performance and Durability of Hemp Concrete. Int Res J Eng Technol. 2018.
[17] Ramadan R, Saad G, Awwad E, Khatib H, Mabsout M. Short-Term Durability of Hemp Fibers. In: Procedia Engineering. 2017. https://doi.org/10.1016/j.proeng.2017.07.018
[18] Walker R, Pavia S, Mitchell R. Mechanical properties and durability of hemp-lime concretes. Constr Build Mater. 2014. https://doi.org/10.1016/j.conbuildmat.2014.02.065
[19] Ziane S, Khelifa M-R, Mezhoud S. A Study of the Durability of Concrete Reinforced with Hemp Fibers Exposed to External Sulfatic Attack. Civ Environ Eng Reports. 2020; https://doi.org/10.2478/ceer-2020-0025
[20] Kremensas A, Stapulioniene R, Vaitkus S, Kairyte A. Investigations on Physical-mechanical Properties of Effective Thermal Insulation Materials from Fibrous Hemp. In: Procedia Engineering. 2017. https://doi.org/10.1016/j.proeng.2017.02.069
[21] Hamzaoui R, Guessasma S, Mecheri B, Eshtiaghi AM, Bennabi A. Microstructure and mechanical performance of modified mortar using hemp fibres and carbon nanotubes. Mater Des. 2014. https://doi.org/10.1016/j.matdes.2013.10.084
[22] Mostefai N, Hamzaoui R, Guessasma S, Aw A, Nouri H. Microstructure and mechanical performance of modified hemp fibre and shiv mortars: Discovering the optimal formulation. Mater Des. 2015. https://doi.org/10.1016/j.matdes.2015.06.102
[23] Kasagani H, Rao CBK. Effect of graded fibers on stress strain behaviour of Glass Fiber Reinforced Concrete in tension. Constr Build Mater. 2018. https://doi.org/10.1016/j.conbuildmat.2018.06.193
[24 Ismail MA, Hashim H Bin. Palm oil fiber concrete. 3rd ACF Int Conf -ACF/VCA. 2008.
[25] Liu G, Cheng W, Chen L. Investigating and optimizing the mix proportion of pumping wet-mix shotcrete with polypropylene fiber. Constr Build Mater. 2017. https://doi.org/10.1016/j.conbuildmat.2017.05.169
[26] Salman GA. The effect of mineral additions and adding various types, length and volume of fibers on fresh properties of self compacting concrete. In: Rheology and processing of Construction Materials - 7th RILEM International Conference on Self-Compacting Concrete and 1st RILEM International Conference on Rheology and Processing of Construction Materials. 2013.
[27] Olivito RS, Zuccarello FA. An experimental study on the tensile strength of steel fiber reinforced concrete. Compos Part B Eng. 2010. https://doi.org/10.1016/j.compositesb.2009.12.003
[28] Asasutjarit C, Hirunlabh J, Khedari J, Charoenvai S, Zeghmati B, Shin UC. Development of coconut coir-based lightweight cement board. Constr Build Mater. 2007. https://doi.org/10.1016/j.conbuildmat.2005.08.028
[29 Page J, Khadraoui F, Boutouil M, Gomina M. Multi-physical properties of a structural concrete incorporating short flax fibers. Constr Build Mater. 2017. https://doi.org/10.1016/j.conbuildmat.2017.02.124
[30] Boulekbache B, Hamrat M, Chemrouk M, Amziane S. Flowability of fibre-reinforced concrete and its effect on the mechanical properties of the material. Constr Build Mater. 2010. https://doi.org/10.1016/j.conbuildmat.2010.02.025
[31] McLeish A. Structural assessment, manual for life cycle aspects of concrete in buildings and structures. Taywood Eng Limited, UK B. 1987.
[32] Nibudey RN, Nagarnaik PB, Parbat DK, Pande AM. Compressive Strength and Sorptivity Properties of Pet Fiber Reinforced Concrete. Int J Adv Eng Technol. 2014.
[33] Ramezanianpour AA, Esmaeili M, Ghahari SA, Najafi MH. Laboratory study on the effect of polypropylene fiber on durability, and physical and mechanical characteristic

of concrete for application in sleepers. Constr Build Mater. 2013. https://doi.org/10.1016/j.conbuildmat.2013.02.076

[34] Rostami V, Shao Y, Boyd AJ. Durability of concrete pipes subjected to combined steam and carbonation curing. Constr Build Mater. 2011. https://doi.org/10.1016/j.conbuildmat.2011.03.025

Research on Engineering Structures & Materials
journal homepage: http://jresm.org
MIM Research Group

Research Article

Development of ZnO sensors via succession ionic layer adsorption and reaction (SILAR) method for ppb level NO gas sensing

Irmak Karaduman Er

Department of Medical Services and Techniques, Eldivan Medical Services Vocational School, Çankırı Karatekin University, Çankırı, Turkey

Article Info

Article history:
Received 01 Sep 2020
Revised 18 Nov 2020
Accepted 27 Dec 2020

Keywords:
Gas Sensor;
NO Gas;
ppb Level

Abstract

In this work, the effects of Cd doping on the gas sensing properties of ZnO thin films were synthesized by SILAR method and studied gas sensing characteristics against NO, CO, ammonia, methanol and acetone, systematically. Whereas the operating temperature of NO gas was found 90 °C, CO and acetone were 150 °C and 170 °C. The response was not observed in methanol and ammonia gases. Especially, it was observed that the response continued to increase as the temperature increased for methanol gas. In addition, the 5% Cd doped ZnO sensor exhibits the excellent selectivity for NO compared to other test gases as ~12% at 0.01 ppm. NO gas sensing reactions are accelerated with Cd doping because Cd doping was created increasing oxygen vacancies surface chemisorbed oxygen species, and defects in the lattice.

1. Introduction

Widely used as gas sensing material, ZnO is known for its high electron mobility and thermal stability [1,2]. ZnO has an optical transmittance of about 80% -90% in the visible region and an electrical resistivity in the region of 10^{-3}-$10^{+2}\Omega$.cm. The simplicity of the fabrication of nanostructured ZnO makes it simple to adapt its surface with a high surface area. Besides, Morphology regulation is widely used in various fields, including transistors, sensors [3], electronic noses [4], and energy storage [5]. There are three different VO states in ZnO: neutral vacancy V_O^0 (V_{OX} in Kröger-Vink notation), singly ionized vacancy V_O^{1+} ($V_O^{\bullet}$), and ionized 2+ state V_O^{2+} ($V_O^{\bullet\bullet}$). They have different defect formation energies and electron states, which would result to the complex photoluminescence and electronic properties [5,6]. Therefore, gas sensing characteristcs can be improve with these defects. Especially, Different production methods can lead to different gas detection properties. The growth during the production methods, the dispersion to the surface, the structures that can be formed, the oxygen gaps, etc. features can change gas detection parameters.

Unlike other solution-based methods, SILAR technique is cheaper and practical, but also suitable for mass production [7-9]. SILAR technique is highly preferred in recent years due to its characteristics such as cheaper, simpler and less time spent during enlargement, since it does not require expensive equipment such as vacuum among semiconductor film growth methods [9]. SILAR is an aqueous solution technique involving a series of sequential reactions between substrate and solution, and is the immersion of the compound semiconductor to be grown on the material used as substrate into aqueous solutions containing ions of each type in a certain order [9]. In the SILAR method, it is possible to

Corresponding author: irmakkaradumaner@karatekin.edu.tr
orcid.org/0000-0003-3786-3865;
DOI: http://dx.doi.org/10.17515/resm2020.212ma0901

control the thickness of the material to be grown on the substrate by determining the number of SILAR cycles and this is one of the most important parameters in the SILAR thin film growth method. As the number of cycles increases, the film thickness increases and a more stable structure is obtained. However, it is not appropriate to have too many SILAR cycles. Because when the film thickness reaches a certain value, ions will start to accumulate on the surface in the form of residue, as a result, ruptures will become easier and the quality of the film will decrease.

The doping in ZnO can change the electrical and dielectric characteristics and speed up the development of its practical applications [10]. The doping process depends on the nature of the fabrication technique and also the characteristics properties of dopant elements. The doping process is a substantial method to increase the sensing property of semiconductor sensors because of adjust the parameters of the crystal cell and the band structures of ZnO nanocrystals [11]. Therefore, Cd is one of the important doping elements to improve the sensitivity of gas sensors. One of the excellent doping material is Cd. The oxygen adsorption of thin films can be enhanced with Cd atoms and this leads to increase gas reactions on the gas sensing surface. Therefore, The doping of Cd atom into ZnO has changed the electrical parameters of ZnO and increase its characteristics of the near-interface region [12-14].

As can be seen from Table 1, although the Cd doping is made for all studies, the sensing materials produced with different production methods can have different operating temperatures. Table 1 gives the different Cd doping gas sensing materials produced by different production methods.

Table 1. Different Cd doping gas sensing materials

Materials	Producing Method	Gas Concentration	Sensing Response	Operating Temperature	References
Cd-ZnO Thin Films	Spray Deposited	Acetone	87	325 °C	[15]
Cd-doped ZnO Nanoparticles	A Surfactant-Mediated Method	n-butanol	130	300°C	[16]
Cd-doped ZnO	Electrospinning Method	40 ppm CO	95	135°C	[17]
ZnO/CdO	Electrospinning Method	1.2 ppm NO	226	215°C	[18]
Cd-doped ZnO Thin Films	RF Magnetron Sputtered	50 ppm Methanol	130	50°C	[19]
ZnO:Cd Nanorods	Hydrothermal Method	500 ppm Hydrogen	1.67	80°C	[20]

In this work, the effects of Cd doping on the gas sensing properties of ZnO thin films were studied gas sensing characteristics against NO, CO, ammonia, methanol and acetone, systematically. The sensing characteristics of the as prepared samples were systematically measured. Fabricated sensors were tested against NO, CO, ammonia, methanol and acetone. In addition, the effect of the doping amount on gas sensing was investigated.

2. Experimental Procedure

To synthesize Cd doped ZnO thin films, aqueous zinc-ammonia complex ions ($[Zn(NH_3)_4]^{2+}$) and aqueous cadmium-ammonia complex ions ($[Cd(NH_3)_4]^{2+}$) were chosen for the cation precursors, in which analytical reagents of $ZnCl_2$ (%99) of 0.1M, $CdCl_2$ (%99) of 0.1 M and concentrated ammonia (NH_3) (25-28%) were used. The double distilled water was used as a solvent. The molar ratio 1:10 of Cd-Zn:NH_3 was obtained as a result of several experiments. The obtained $[Zn(NH_3)_4]^{2+}$ and $[Cd(NH_3)_4]^{2+}$ complexes were mixed in appropriate proportions. All the synthesis processing parameters by SILAR method were previously

reported by the same authors [21-23]. The thin films of 1, 3, 5 and 7 % Cd-doped ZnO were named as CZO1, CZO3, CZO5 and CZO7, respectively.

XRD measurements were done with Panalytical Empyrean X-ray Diffractometer (Cu Kαλ= 1.5405 radiation) and also SEM analysis were done the FEI Quanta FEG 450 model SEM with energy dispersive X-ray analysis (EDAX) attachment. Thickness of the films was measured by the gravimetric weight difference method using sensitive microbalance.

The gas detection performance of the sensors was tested with a gas detection measuring system. In our previous studies, detailed information about the gas detection measurement system is given [21,22]. The gas sensing measurements have been carried out at different concentrations and operating temperatures by monitoring the resistance changes. Dry air has been used as the carrier gas, which is 99.9% purity (dry air is the 'blank' gas used to purge the sensor). The flow rate of the dry air undergoing testing has been fixed at 500 cm3 min−1 during the measurements. Air flow rate, under the same conditions in order to observe the behaviour of different concentrations must be kept always constant. To ensure stable zero-level resistance in ambient air prior to exposure to gas the stabilization of the nanostructure resistance is important because it ensures stable zero level for gas sensing applications. For the corresponding operating temperature of the gas chamber, it is the prime requisite to stabilize the resistance in air atmosphere before ejecting the gas into the chamber. It indicates the resistance of nanostructure in air. The target gases and dry airflow rates have been controlled by computer controlled mass flow controllers (MKS series). The LakeShore 325 temperature controller with platinum resistance temperature detectors has been used to maintain a constant temperature. The sensor resistance has been continuously monitored with a computer controlled system using a Keithley 2400 source meter. The data have been collected in real-time using a computer with corresponding data acquisition hardware and software. Relative humidity has been kept constant (about 25%) for all measurements, monitored by the Honeywell HIH-4000 humidity sensor [21,22].

3. Results and Discussion

In this study, the growth mechanism can be explained as below reactions;

$$ZnCl_2 + 2NH_4OH \leftrightarrow Zn(OH)_2 + 2NH_4^+ + 2Cl^- \quad (1)$$

$$Zn(OH)_2 + 4NH^{4+} \leftrightarrow 2\,[Zn\,(NH_3)4]^{2+} + +2H_2O + 2H^+ \quad (2)$$

$$[Cd(NH_3)4]^{2+} + 4H_2O \rightarrow Cd(OH)_{2(S)} + 4NH_4^+ + 2OH^- \quad (3)$$

After that, The substrate is submerged in hot water, $Cd(OH)_2$ is formed;

$$Zn(OH)_{2(s)} \rightarrow ZnO_{(s)} + H_2O \quad (4)$$

As a result, ZnO thin film was grown on glass substrate by the SILAR method. A single cycle SILAR method is complete [24]. When the doping process is began, $Cd(OH)_2$ solution is added to the solution in desired doping ratios and doping process is made. The solution mechanism is still under investigation. CdO formation mechanism is as follows [21-25];

$$CdCl_2 + 2NH_4OH \leftrightarrow Cd(OH)_2 + 2NH_4^+ + 2Cl^- \quad (5)$$

$$Zn(OH)_2 + 4NH^{4+} \leftrightarrow 2\,[Zn\,(NH_3)4]^{2+} + +2H_2O + 2H^+ \quad (6)$$

Figure 1 shows the XRD spectra of undoped and Cd-doped ZnO thin films. All peaks demonstrate the JCPDS data belonging to the hexagonal ZnO structure (Card No. 36-1451) [26,27]. Cd peaks increase with increasing doping concentrations, on the other hand, film

quality decrease. This can be associated with the ionic radius, which Cd^{2+} (1.10Å) ion is greater than of the Zn^{2+} (0.74 Å) ion. The calculated dislocation density, microstrain, interplanar distance, crystallite size, and FWHM of the peak values of the film can be seen in Table 2.

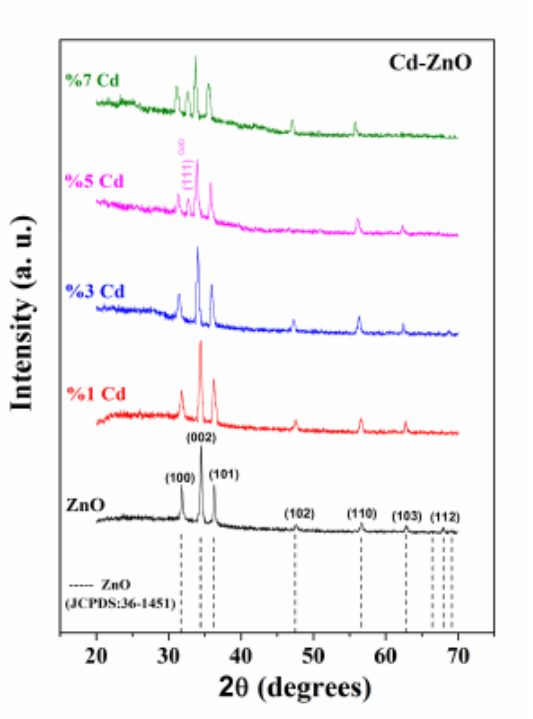

Fig 1. the XRD spectra of undoped and Cd-doped ZnO thin films

Table 2. The calculated dislocation density, microstrain, interplanar distance, crystallite size, and FWHM of the peak values of the films

Sample	(hkl)	2θ	D(nm)	FWHM	Interolanar Distance; d(Angstron)	Dislocation Density (δ) (10^{-4})	Microstrain (ε)
ZnO	(100)	31.85	64.30	0.2476	2.8066	2.4189	0.2160
	(002)	34.50		0.2508	2.5969		0.2019
	(101)	36.35		0.2648	2.4687		0.2016
1% Cd-doped	(100)	31.81	45.37	0.2810	2.8102	4.8590	0.2465
	(002)	36.30		0.3554	2.6004		0.3059
	(101)	36.30		0.4306	2.4719		0.3284
3% Cd-doped	(100)	31.49	47.28	0.2266	2.8376	4.4742	0.2064
	(002)	34.08		0.3407	2.6270		0.2779
	(101)	35.99		0.4033	2.4927		0.3298
5% Cd-doped	(100)	31.37	41.79	0.3045	2.8486	5.7273	0.2711
	(111)	32.69		0.3694	2.7363		0.3149
	(002)	34.04		0.3854	2.6306		0.3147
	(101)	35.84		0.3648	2.5028		0.2820
7% Cd-doped	(100)	31.16	41.92	0.3872	2.8672	5.6915	0.3471
	(111)	32.63		0.3541	2.7411		0.3024
	(002)	33.72		0.3838	2.6551		0.3166
	(101)	35.54		0.3202	2.5233		0.2497

It is seen that the crystallite-size is decreased with increase of Cd concentration. The crystalline size were calculated 64.30 nm, 45.37 nm, 47.28 nm, 41.79 nm and 41.92 nm for 1% at Cd, 3% at Cd, 5% at Cd, and 7% at Cd-doped ZnO films respectively. The difference in ionic radius between Cd2+ and Zn2+ leads the lattice distortion. Dislocation density (δ) can be thought of as a measure of crystallinity [28,29]. The best crystalline structure shows for undoped ZnO compared to doping ones. Thickness of the films was calculated by the gravimetric weight difference method in terms of deposited weight of all films on the glass substrate, per unit area (g/cm^2). Thickness of the films were found 90 nm, 95 nm, 82 nm and 102 nm for 1% at Cd, 3% at Cd, 5% at Cd, and 7% at Cd-doped ZnO films respectively. These results show that the thickest sample is 1 %, but the thinnest sample is 5% so Cd dopant effect to the growth of samples by SILAR method.

The SEM images of the thin films are shown in Figure 2. As a result of SEM analysis, information about the roughness, homogeneity, adhesion of the film and surface defects can be obtained. The images show a general view of the morphology of Cd-doped ZnO films. SEM images of (a) % 1 , (b) 3 % (c) 5 % and (d) 7 % Cd-doped ZnO thin films. The polycrystalline structure is revealed from the SEM micrographs. The films are porous as evident from absence of close packed morphology [30]. Such agglomeration makes it difficult to evaluate the grain size from SEM images. Figure 3 presents the EDAX analysis of Cd doped ZnO thin films. The EDAX analysis shows the presence of Zn, Sn and O elements in the films. The rates of Cd-doping are seen in EDAX analysis. Also, the presence of Si and Ca elements in the spectra may be caused by the substrate. It can be come from the glass substrate.

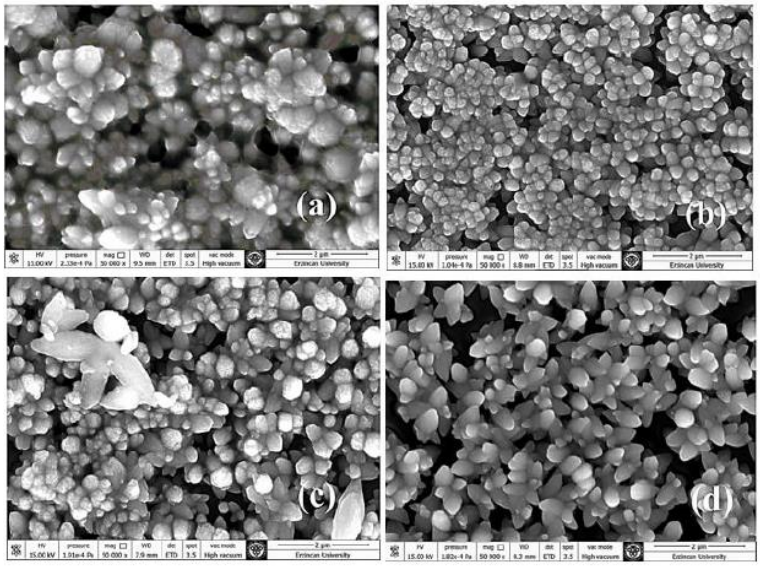

Fig 2. The SEM images of 1 % (a), 3 % (b), 5 % (c) and 7 % (d) Cd doped ZnO thin films

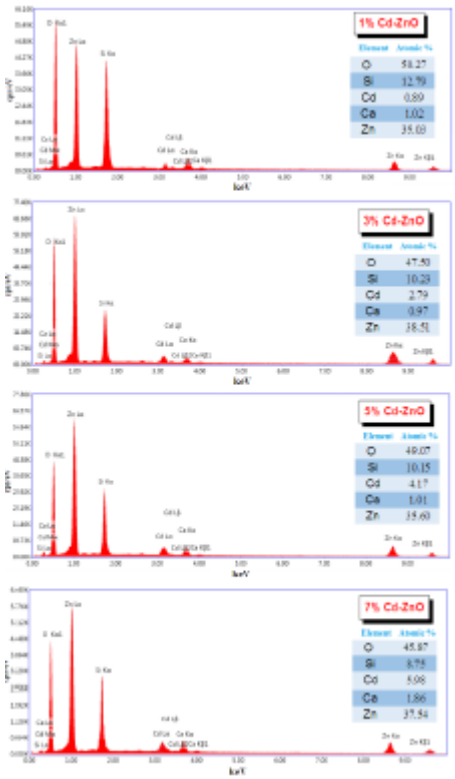

Fig 3. the EDAX analysis of Cd doped ZnO thin films

The optical absorption spectrum of the Cd-doped ZnO thin films was determined within the wavelength range of 300– 500 nm, as given in Figure 4. Except well-defined absorption peak related with wurtzite hexagonal phase ZnO, no other peak related with any impurity was observed which confirms that the synthesized Cd-doped ZnO multipods possess good optical properties. The optical absorbance spectra and the plots of $(\alpha h\nu)^2$ versus $(h\nu)$ of Cd doped ZnO thin films are given in Figure 4a. The direct bandgap values are calculated as 3.18, 3.11, and 3.08, 2.98 eV for 1% at Cd, 3% at Cd, 5% at Cd, and 7% at Cd-doped ZnO films respectively. When Cd doping was increased, there was a decrease was shown in the band gap values. the direct band gap of Cd is approximately 2.5eV which is lower than that of ZnO(~3.3eV) , however, they show low resistance due the defect of oxygen vacancies and Cadmium interstitials [31]. It can be seen in Figure 4.b.

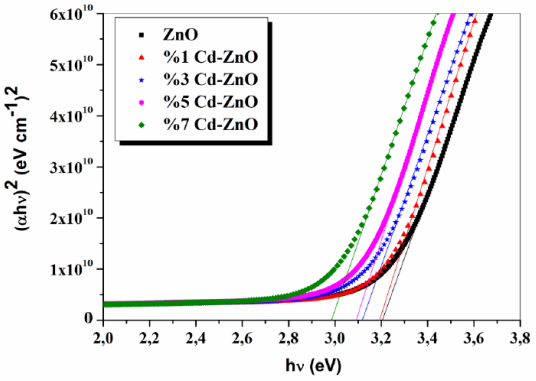

Fig 4a. The optical absorbance spectra and the plots of $(\alpha h\nu)^2$ versus $(h\nu)$ of Cd doped ZnO thin films

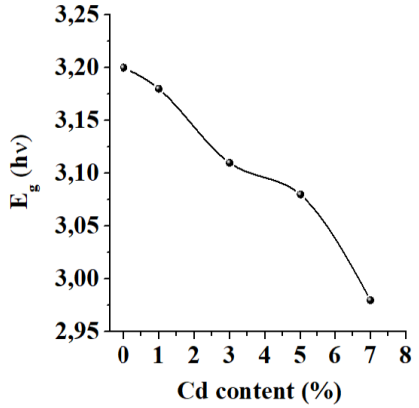

Fig 4.b. The direct bandgap values of Cd doped ZnO thin films

Figure 5 gives the resistance of Cd-doped thin films. The resistance values are decreased with increasing Cd doping concentrations. This shows the decrease in band gap upon Cd doping by suggesting the possibility of tuning of band gap with doping Cd. These values agree with the literature [32,33]. When examining the characteristics of gas sensors, the first parameter to be found is the operating temperature. The operating temperature of the

sensor may affect its lifetime as well as it may change depending on the target gas sent. It is given in the literature studies that each gas can have different operating temperatures. [33-35]. Therefore, the operating temperature of the sensor material produced by sending different gases was first found. In order to determine the optimum operating temperatures, the response of sensors to 100 ppm NO, CO,ammonia, methanol and acetone were tested as a function of operating temperature ranging from 30 °C to 250 °C, depicted in Figure 6. 5 % at Cd doped sensors exhibited the high response to NO as well as the high selectivity compared to other gases. The responses of 3% at Cd and 7% at Cd sensors were observed to be very close to each other. 1%, 3% and 7% at Cd doped ZnO sensors also exhibited high responses to acetone and CO apart from the NO gas. Whereas the operating temperature of NO gas was found 90 °C, CO and acetone were 150 °C and 170 °C. Response was not observed in methanol and ammonia gases. Especially in methanol gas, 250 °C is still increasing. The best responses were obtained for NO gas. NO is a type of radical and chemically active gas. Therefore, the other gas sensing characteristics were studied only NO gas. This can be explained by the fact that each gas has different binding energies. Thus, they show sensitivity at different working temperatures to break off the surface. In each sensor material produced in the gas sensor studies, it is seen that the target gases show different operating temperatures depending on the production method [33-36].

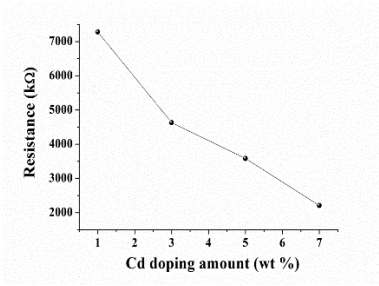

Fig 5. the resistance of Cd-doped thin films.

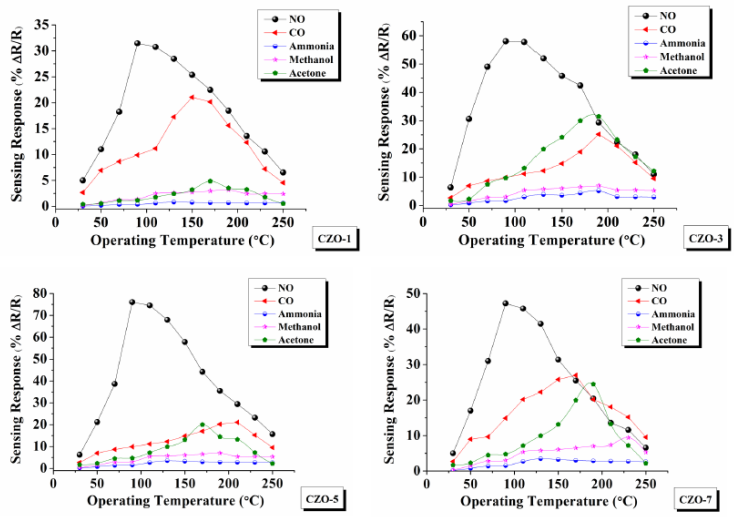

Fig 6. the response of sensors to 100 ppm NO, CO, ammonia, methanol and acetone were tested as a function of operating temperature

The NO gas concentrations from 0.01 ppm to 100 ppm were tested for all sensors. The response of 0.01 ppm were calculated 1%, 7% , 12% and 4 for 1%, 3%, 5 % and 7 % Cd-doped ZnO respectively, as shown in Figure 7. The response was increased with increasing NO gas concentration in all sensors. It was observed that the response of the sensors increased rapidly when all the sensors were exposed to the target molecules, and the response returned to the initial value [37] when the surface of the sensors was exposed to dry air after each dynamic measurement, as given in Figure 8.

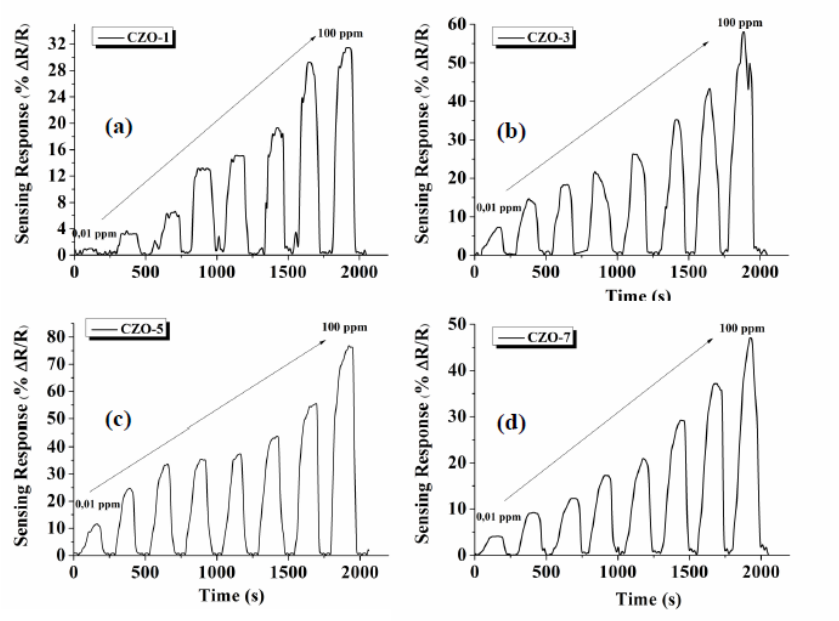

Fig 7. The response to NO gas concentrations from 0.01 ppm to 100 ppm

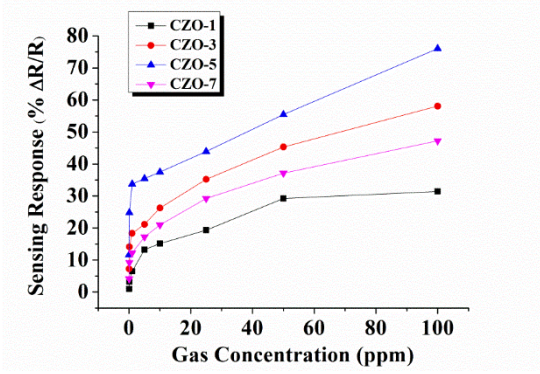

Fig 8. The response from 0.01 ppm to 100 ppm versus gas concentrations

Figure 9 depicts the response and recovery times of doped ZnO sensors. The response and recovery times of sensors were calculated for all NO gas concentrations at operating temperature of 90 °C. It was seen thst CZO5 sensor has the highest response and recovery times.

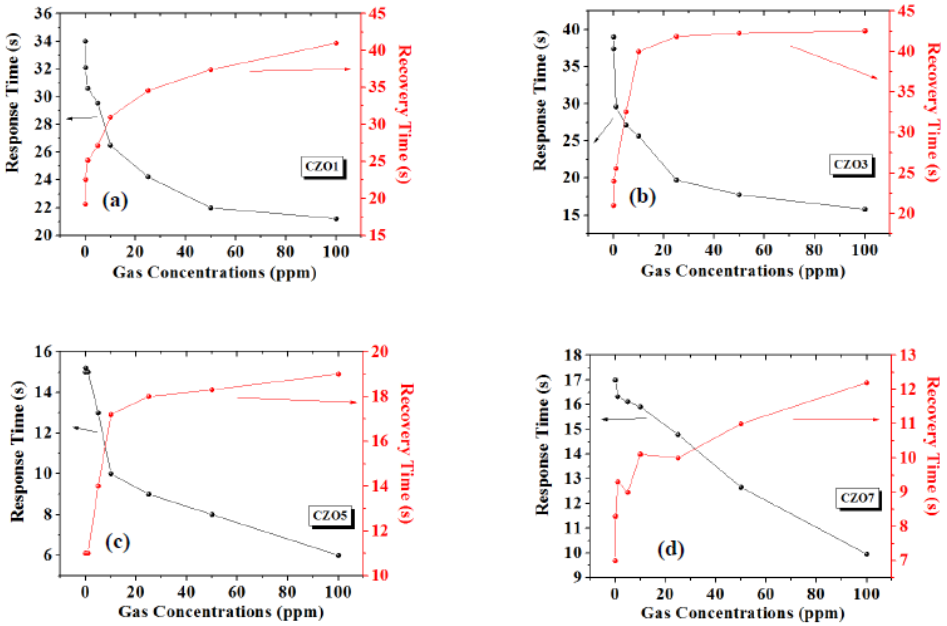

Fig 9. the response and recovery times of doped ZnO sensors

The detection limit of the sensor is calculated by using Signalto-Nosie approach and the root-mean-square. The root mean square noise (RMS_{noise}) can be obtained by the equations given above [38];

$$R_{X^2} = \sum (y_i - y)^2 \tag{7}$$

$$RMS_{noise} = \sqrt{\frac{R_{X^2}}{N}} \tag{8}$$

Where y_i is the response measured experimentally, y is the average response, and N is the number of experimental data point.

The sensor noise for 5% Cd-doped ZnO sensor is 0.01284. The detection limit can be thus calculated by the curve-fitting equation as given below [38]:

$$DL_{(ppm)} = 3\frac{RMS_{noise}}{slope} \tag{9}$$

The detection limit of the sensor to NO is then calculated to be 0.0089 ppm. The best results are given by the CZO5 sample. Therefore, other gas sensing parameters such as reproducibility and stability were made only for this sample. Figure 9 shows the reproducibility and stability of CZO5 sample for 0.01 ppm NO gas. Reproducibility measurements were done for 15 cycles. Slight shifts in sensitivity towards the end of the cyles were observed, as seen in Figure 10 (a). However, these are minor shifts that are negligible. The stability of CZO5 sensor was shown in Figure 10 (b). The measurements were carried out for 5 weeks. The sensor exhibited excellent stability.

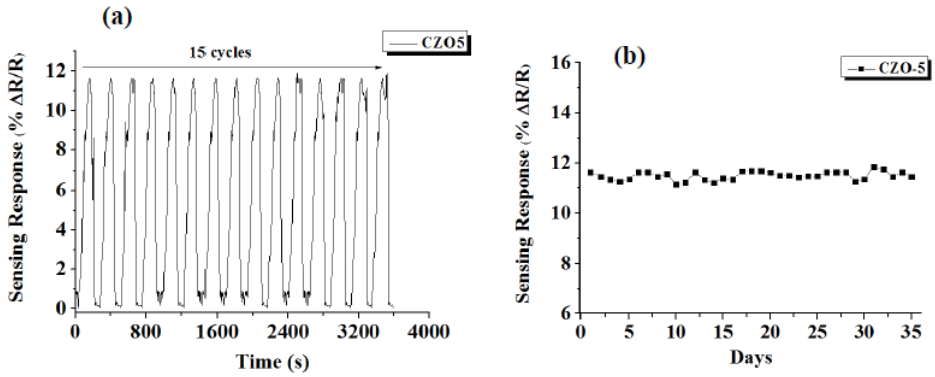

Fig10. Reproducibility measurements (a) The stability (b) of CZO5 sensor

The working principle of the thin film gas sensor can be explained as the change of the amount of carrier electrons on the surface according to the amount of gas in the environment and the measurement of the change in electrical characterization as a result. It is the determination of the change that occurs as a result of chemical or electronic interaction with semiconductor oxide and its surrounding oxide or reducing atmosphere [39]. The mentioned interactions create a change in electrical resistance on the semiconductor surface. In other words, the principle of operation of metal oxide gas sensors can be said to be based on the increase or decrease of electrical resistance as a result of surface reactions by the interaction of oxygen and target gas [40]. By measuring the changing electrical resistance, the concentration change of the target gas can be determined [41]. One of the important factor is doping effect. Cd doping increases the gas response and decreases the operating temperature. This can be associated with the differences in work-functions of Cd and ZnO: Φ(Cd) =4.08 eV and Φ(ZnO) =4 eV, which is assumed to induce electronic sensitization. Moreover, the rectifying Schottky junction at Cd-ZnO interfaces to improve electrical transport behavior. According the recent studies, it is seen that Cd^{2+} metal oxides can act as a kind of Lewis acid on the surface [42,43]. In addition, the presence of Lewis acid (Cd^{2+}) on the ZnO surface will significantly reduce the binding energy of another Lewis acid, which can inhibit NO adsorption on the surface, after finding the maximum doping concentration value. Thus, the response of the gas sensor to NO started to decrease after a certain Cd contribution [42-44]. Also, Cd^{2+}, Lewis acid domains can reduce adsorption of NO molecules to the surface, as well as improve the sensor's response response performance. The reduction of the binding energy of NO adsorbed to the surface by Cd^{2+} as the Lewis acid region facilitates the desorption of NO and improves the improved recovery performance of the gas sensor [45].

4. Conclusions

We proposed Cd doping on the gas sensing properties of ZnO thin films have been successfully synthesized by Succession Ionic Layer Adsorption and Reaction (SILAR) method. The response of 100 ppm NO gas were obtained 31.45 % , 58.08 % , 76.07 %, 47.23 % from 1 %, 3 %, 5 % and 7% Cd-doped ZnO sensors, respectively. In addition, the 5 % Cd-doped ZnO sensor gas sensing shows a high response of 76% at 100 ppm, and the detection limit is very low (10 ppb) at 90 °C. When tested with different gases (NO,CO, ammonia, acetone and methanol) for 5 % Cd-doped ZnO, the sensor exhibits a good selectivity for NO, excellent stability and repeatability. Overall, this sensor has great potential for developing high-performance gas sensors and can also be applied to the synthesis of many other devices.

Acknowledgement

The authors acknowledge that this study is supported by ÇAKU scientific research projects unit (BAP-project no: EYO080120B13).

References

[1] Madhaiyan G, Tung TW, Zan HW, Meng HF, Lu CJ, Ansari A, Chuang WT, Lin HC. (2020) Sensor. Actuator. 320, 128392. https://doi.org/10.1016/j.snb.2020.128392
[2] Tarwal NL, Patil AR, Harale NS, Rajgure AV, Suryavanshi SS, Bae WR, Patil PS, Kim JH, Jang JH. (2014) J. Alloys Compd., 598; 282-288. https://doi.org/10.1016/j.jallcom.2014.01.200
[3] Cai L, Li H, Zhang H, Fan W, Wang J, Wang Y, Wang X, Tang Y, Song Y. (2020).Mat Scı Semıcon Proc 118, 105196. https://doi.org/10.1016/j.mssp.2020.105196
[4] Singh P, Mangasa Simanjuntak F, Wu YC, Kumar A, Zan HW, Tseng TY. (2020) J Mater Sci 55:8850-8860. https://doi.org/10.1007/s10853-020-04659-7
[5] Zhu L, Zeng W. (2017) Sens Actuators A Phys 267:242-261. https://doi.org/10.1016/j.sna.2017.10.021
[6] Zhang SL, Lim JO, Huh JS, Lee W. (2012). IEEE Sens J 12:3143-3148. https://doi.org/10.1109/JSEN.2012.2211005
[7] Çorlu T, Karaduman I, Yildirim MA, Ateş A, Acar S. (2017). J Electron. Mater., 46;7, 3995-4002. https://doi.org/10.1007/s11664-017-5503-z
[8] Karaduman Er I, Çağırtekın AO, Çorlu T, Yıldırım MA, Ateş A, Acar S. (2019) Bull. Mater. Sci., 42, 32. https://doi.org/10.1007/s12034-018-1714-z
[9] Galioglu S, Karaduman I, Çorlu T, Akata B, Yıldırım MA, Ateş A, Acar S. (2018) J Mater Scı-Mater El. 29;2, 1356-1368. https://doi.org/10.1007/s10854-017-8042-8
[10] Erol A, Okur S, Comba B. (2010) Sensor. Actuators B 145:174-80. https://doi.org/10.1016/j.snb.2009.11.051
[11] Li G, Zhang H, Meng L, Sun Z, Chen Z, Huang X, Qin Y. Science Bulletin (Article in Press) (2020). https://doi.org/10.1016/j.scib.2020.05.027
[12] Zhao R, Zhang X, Peng S, Hong P, Zou T, Wang Z, Xing X, Yang Y, Wang Y. (2020) J. Alloys Compd.,813; 152170. https://doi.org/10.1016/j.jallcom.2019.152170
[13] Rouhani F, Morsali A. (2017) New J. Chem. 41; 15475-15484. https://doi.org/10.1039/C7NJ01509G
[14] Chen X, Wang S, Su C, Han Y, Zou C, Zeng M, Hu N, Su Y, Zhou Z, Yang Z. (2020) Sensor. Actuators: B. 305 , 127393. https://doi.org/10.1016/j.snb.2019.127393
[15] Tarwal NL, Patil AR, Harale NS, Rajgure AV, Suryavanshi S, Bae WR, Patil PS, Kim JH, Janga JH. (2014). J. Alloys Compd.,598; 282-288. https://doi.org/10.1016/j.jallcom.2014.01.200
[16] Zhao R, Li K, Wang Z, Xing X, Wang Y. (2018) J. Phys. Chem. Solids 112; 43-49. https://doi.org/10.1016/j.jpcs.2017.08.039

[17] Bai S, Chen S, Zhao Y, Guo T, Luo R, Li D, Chen A. (2014) J. Mater. Chem. A, 2;16697. https://doi.org/10.1039/C4TA03665D
[18] Naderi H, Hajati S, Ghaedi M, Espinos JP. (2019) Sens. Actuators B, 297; 126774. https://doi.org/10.1016/j.snb.2019.126774
[19] Vinoth E, Gowrishankar S, Gopalakrishnan N. (2017) Materials and Manufacturing Processes, 32, I4. https://doi.org/10.1080/10426914.2016.1244834
[20] Yang X, Wang W, Xiong J, Chen L, Ma Y. (2015) Int. J. Hydrog. Energy. 40; 12604-12609. https://doi.org/10.1016/j.ijhydene.2015.07.086
[21] Yıldırım MA, Tuna Yıldırım S, Ateş A. (2017) J. Alloys Compd., 701, 37-42. https://doi.org/10.1016/j.jallcom.2017.01.092
[22] Yıldırım MA, Ateş A, (2010) Opt. Commun. 283 1370-1377. https://doi.org/10.1016/j.optcom.2009.12.009
[23] Yıldırım MA, Ateş A, (2009) Sens. Actuators A 155 272-277. https://doi.org/10.1016/j.sna.2009.09.002
[24] Gujar TP, Shinde VR, Kim W, Jung KD, Lokhande CD, Joo OS. (2008) Appl. Surf. Sci., 254, 3813-3818. https://doi.org/10.1016/j.apsusc.2007.12.015
[25] Güney H, İskenderoğlu D. (2019) Physica B 552; 119-123. https://doi.org/10.1016/j.physb.2018.09.045
[26] https://www.webelements.com/periodicity/ionic_radius_2_tet/.
[27] Khalaf KA, Al-Rawas A, Gismelseed A, Al-Ruqeishi M, Al-Ani S, Al-Jubouri A, Al-Ryami K, Al-Jaddedi B. (2019) Advances in Materials 8(2): 70-93 doi: 10.11648/j.am.20190802.15. https://doi.org/10.11648/j.am.20190802.15
[28] Kamble LD, Harale NS, Patil VL, Patil PS, Kadam LD, (2017) Journal of Analytical and Applied Pyrolysis, 127; 38-46. https://doi.org/10.1016/j.jaap.2017.09.004
[29] Phuo PH, Hung CM, Toan NV, Duy NV, Hoa ND, Hieu NV. (2020) Sensor. Actuators A 303;111722. https://doi.org/10.1016/j.sna.2019.111722
[30] Cao PF, Ma SY, Xu XL, Wang BJ, Almamoun O, Han T, Xu XH, Pei ST, Zhang R, Zhang JL, Liu WW. (2020) Vacuum 177 109359. https://doi.org/10.1016/j.vacuum.2020.109359
[31] Ramamurthy M, Yuvaraj P. (2012) International Journal of Science and Research (IJSR), ISSN (Online): 2319-7064; 68-71.
[32] Sampath Kumar AG, Obulapathı L, Sofı Sarmash T, Jhansı Ranı D, Maddaıah M, Subba Rao T, Asokan K. JOM (2015) 67; 834-839. https://doi.org/10.1007/s11837-015-1344-5
[33] Rudra K, Prajapati YK. (2020) Ceram. Intern., 46;8,A; 10135-10141. https://doi.org/10.1016/j.ceramint.2020.01.004
[34] Roshanzamir Modaberi M, Rooydell R, Brahma S, Akande AA, Mwakikunga BW, Liu CP. (2018) Sensor. Actuator. B, 27310; 1278-1290. https://doi.org/10.1016/j.snb.2018.06.117
[35] Sankar Ganesh R, Durgadevi E, Navaneethan M, Patil VL, Ponnusamy S, Muthamizhchelvan C, Kawasaki S, Patil PS, Hayakaw Y. (2018) Sensor. Actuator. A, 269; 331-341. https://doi.org/10.1016/j.sna.2017.11.042
[36] Mirzaei A, Leonardi SG, Neri G. (2016), Ceram. Int. 42;15119-15141. https://doi.org/10.1016/j.ceramint.2016.06.145
[37] Niu G, Zhao C, Gong H, Yang Z, Leng X, Wang F. (2019), Microsyst Nanoeng.; 5: 21. https://doi.org/10.1038/s41378-019-0060-7
[38] Gu D, Wang X, Liu W, Li X, Lin S, Wang J, Rumyantsev MN, Gaskov AM, Akbar SA. (2020) Sensor. Actuator. B, ,305; 127455. https://doi.org/10.1016/j.snb.2019.127455
[39] Ahmad Naseem Z, Manzoor S, Talib M, Islam SS, Mishra P. (2020) Mater. Sci. Eng., B 255; 114528, https://doi.org/10.1016/j.mseb.2020.114528
[40] Yang CM, Chen TC, Yu-Cheng M, Meyyappan Y. (2019) RSC Adv. 9;23343-23351. https://doi.org/10.1039/C9RA01295H
[41] Chikkadi K, Muoth M, Roman C, Haluska M, Hierold C. (2014) Beilstein J. Nanotechnol. 5, 2179-2191. https://doi.org/10.3762/bjnano.5.227

[42] Chen X, Wang S, Su C, Han Y, Zou C, Zeng M, Hu N, Su Y, Zhou Z, Yang Z. (2020) Sensor. Actuator. B 305; 127393. https://doi.org/10.1016/j.snb.2019.127393
[43] Rouhani F, Morsali A. (2017) New J. Chem. 41; 15475-15484. https://doi.org/10.1039/C7NJ01509G
[44] Masoomi MY, Beheshti S, Morsali A. (2015) Cryst. Growth Des, 15, 2533-2538. https://doi.org/10.1021/acs.cgd.5b00304
[45] Hu JS, Shang YJ, Yao XQ, Qin L, Li YZ, Guo ZJ, Zheng HG, Xue ZL. (2010) Cryst. Growth Des, 10, 4135-4142. https://doi.org/10.1021/cg1008208

Research on Engineering Structures & Materials
journal homepage: http://jresm.org
Research Group

Research Article

Fabrication of semi-epitaxial Fe microdots on GaAs (100) substrates

Nilay Gunduz Akdogan

Faculty of Engineering, Piri Reis University, 34940 Istanbul, Turkey

Article Info

Article history:
Received 16 Nov 2020
Revised 05 Feb 2021
Accepted 25 Feb 2021

Keywords:
Fe/GaAs; micro-dots; magnetic anisotropy; MEMS

Abstract

Fe thin films and micro-dots were deposited onto Si (001) and GaAs (100) substrates by a combinatorial approach of lithography and e-beam deposition techniques. The base pressure in the evaporation chamber was $1x10^{-6}$ mbar. 50nm and 5 nm of Fe was deposited with a deposition rate of 0.1 nm/sec onto Si and GaAs, respectively. Continuous films and microdots were covered with 5 nm Cr to prevent oxidation. In-plane interfacial uniaxial magnetic anisotropy has been observed in micro-dots. Room temperature coercivity of 925 Oe has been observed in out-of-plane direction. Effects of strain and interfacial phases on in-plane uniaxial anisotropy are discussed. Synthesized micro-dots could be the building blocks for next-generation magnetoelectronic devices.

1. Introduction

Since the first observation of epitaxy in Fe films deposited on GaAs substrate, the system attracted quite a bit of attention from the research community. [1] This is due to the system's suitability to be used in spin-based magneto-electric device applications (spintronic). [2] Among the many hybrid Ferromagnetic/Semiconductor (FM/SC) systems, Fe and GaAs have special status not only due to their low lattice mismatch (η=1.4%) [3,4] but also due to the high curie temperature of Fe and widely known III-V SC substrate; GaAs. Some other possible SC substrate candidates are ZnSe, InAs, AlAs, Ge, etc.

Even though the spin injection efficiencies are reasonably lower compared to other SC devices [5], it has been shown that interface engineering could improve the spin injection efficiency of the Fe/GaAs system considerably. [6–8]

Several difficulties relating to the Fe/GaAs interface are known in the literature. A high-temperature deposition is necessary to increase the surface mobility but also causes the out-diffusion of substrate atoms into the thin film. Ergo, a wide range of deposition temperatures from -150 ^{o}C (9] to RT [1,10] and even to 580 ^{o}C [11] have been applied. It is widely known that out-diffusion of As (Even Ga) into the Fe film is a big problem since Fe atoms prefer bonding to As over Ga. [12] Even segregation of As has been observed on the surface of the Fe films. [13] Besides, it has been observed that the As segregation (surface diffusion) is possible at all temperatures (-15 ^{o}C to 175 ^{o}C) [10,14–16]

Filipe et al. [17] showed that the out-diffused As atoms form Fe-Ga-As (ferromagnetic, Hc:50 Oe, has a fraction of Fe's magnetic moment) and Fe_2As (antiferromagnetic) at the interface, thus leading to an epitaxial Fe/Reacted-phases/GaAs hybrid structure. Several

Corresponding author: ngakdogan@pirireis.edu.tr
orcid.org/0000-0001-7268-0605;
DOI: http://dx.doi.org/10.17515/resm2020.233na1116

groups tried to experiment with surface temperature, surface termination, and preventive buffer layers (Ag [18], Al [9], S [19] and Oxide [20]) to prevent the out-diffusion, but either the buffer layer did not prevent the diffusion or caused other problems such as shunting the magnetoelectric device or distorting epitaxy.

The main interest of this work and the subject of ongoing scientific speculations is the observed interplay between four-fold bulk like in-plane magnetic anisotropy and two-fold uniaxial in-plane magnetic anisotropy. While the latter is dominant in ultrathin Fe films, the former is governing the thicker and bulk dimensions. [2] In-plane uniaxial anisotropy is believed to be caused by the interfacial phases and/or magnetoelastic strain. Magnetic anisotropy will be discussed in detail later on.

In this study, 5 nm thick Fe micro-dots have been successfully deposited onto the GaAs substrate by using the combination of lithography and e-beam evaporation techniques and magnetic properties have been discussed. Such microdots could be used in future magnetoelectric devices and MEMS.

2. Experimental

Fe micro-dots were synthesized by the lift-off process. GaAs (100) and Si (001) wafers were used as substrates. Substrates were spin-coated at a speed of 4000 rpm for 45 sec. with Az5214e photoresist. The coated resist was baked to harden at 105 ^{o}C for 1 min. Next, substrates were subjected to a UV-light (4.5 sec.) through the prefabricated mask with a pattern of 100 μm diameter circles decorated 100 μm apart. (Midas/MDA-60MS Mask Aligner 4') UV lights weaken the links of the exposed parts of the resist coating, which was later removed by 726 MIF developer. The prepared array of circular holes was filled by depositing (Torr E-beam and Thermal Evaporator) 50 nm Fe (deposition rate:0.1 nm/sec) (5 nm on GaAs) and 5 nm Cr cover layer (to prevent oxidation). The base pressure in the evaporation chamber was 1x10^{-6} mbar. (Scheme 1)

2.1 Characterization:

Morphology analyses of the samples were performed using Jeol JSM 6010. Magnetic measurements at room temperature were made with a Quantum Design VSM-SQUID. Structural characterizations were performed using Bruker D8 X-ray diffractometer (XRD) using a monochromatic Cu Kα X-ray source.

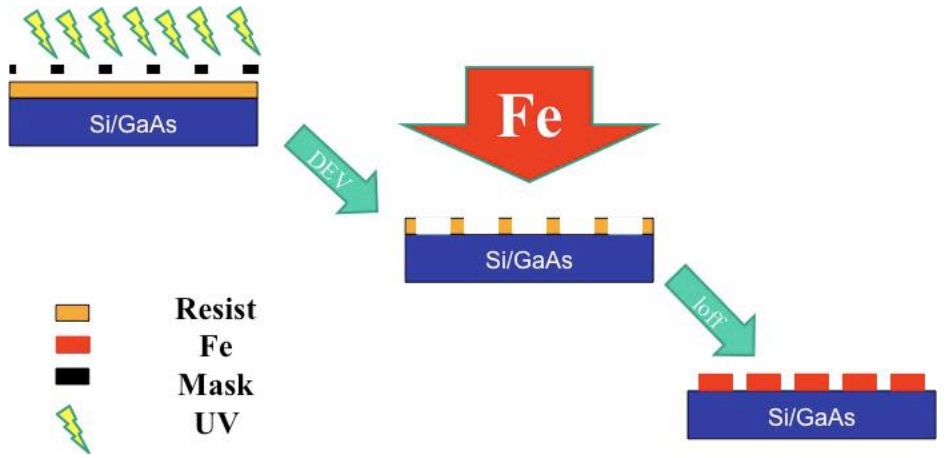

Scheme. 1 Schematic of the experimental process.

3. Results and Discussion

In order to have a base data for the films deposited on GaAs, Fe continuous thin film and microdots (100 nm in diameter) with a thickness of 50 nm have been deposited onto Si wafers. Indexing of Fe continuous thin film's on Si and microdots on GaAs XRD scan confirmed the presence of α-Fe BCC phase (ICSD 44863; space group I m3m)[21]. (Figure 1)

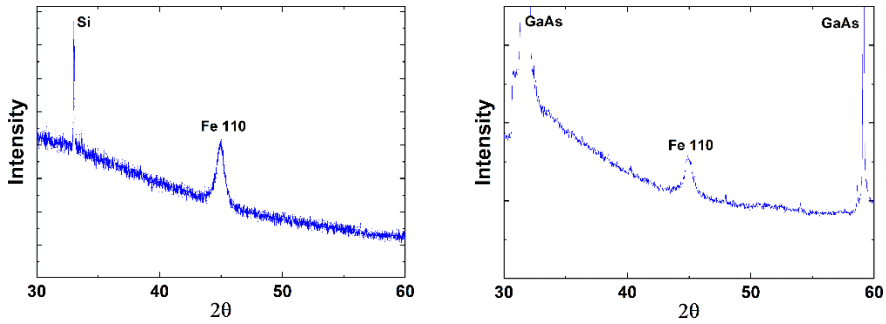

Fig. 1 XRD data of Fe continuous thin film on Si (left) and microdots GaAs (right).

Room temperature hysteresis loops (in-plane) of the Fe continuous films and microdots revealed a soft magnetic behaviour (as expected [22]). (Figure 2) Loops have a square shape, corresponding to the easy axis of the film. Minor room temperature coercivities of 85 Oe and 65 Oe were also observed for Fe continuous films and microdots, respectively. Large Mr/Ms ratio of 0.9 and 0.8 has been observed for Fe continuous films and microdots, respectively, which is quite important for high-density recording media applications. [23]

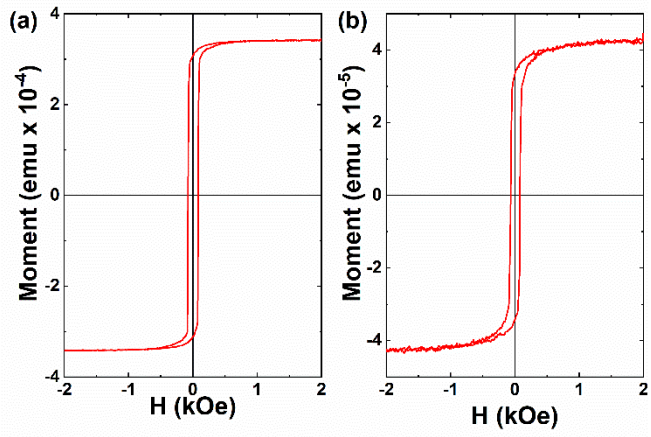

Fig. 2 Room temperature hysteresis loops (in-plane) of Fe (a) continuous film, (b) microdots deposited on Si wafer.

After confirming the data for the continuous and micro-dot Fe films on Si wafers, Fe microdots were synthesized on GaAs substrates. To reduce the mismatch between Fe and GaAs films and increase the quality of epitaxy, the thickness of the micro-dots was limited to 5 nm. [1] Scanning electron microscopy (SEM) image of the Fe micro-dots shows that the structures were successfully synthesized. (Figure 3)

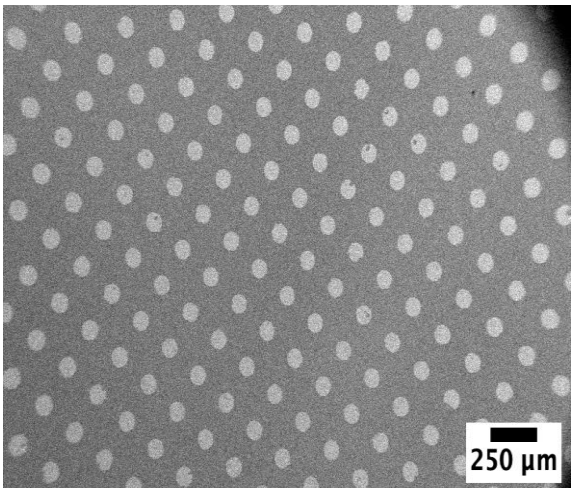

Fig. 3 SEM image of Fe micro-dots.

As it was stated earlier, the main focus of this work was toward seeing the effect of in-plane anisotropy in micro-dots. Ergo, both in-plane and out-of-plane hysteresis loops were taken at room temperature. While the loop taken in-plane has the characteristic of two-phase/magnetic anisotropies behaviour with soft and hard ferromagnetic contributions (RT H_C=300 Oe), the out-of-plane loop corresponds to the classical hard direction loop with a room temperature coercivity of 925 Oe. (Figure 4) The reason behind the shape of the in-plane loop is the interplay between the two types of magnetic anisotropies; magnetoelastic and magneto-crystalline interface anisotropy. Whilst the latter is of interfacial origin thus due to the bonding of the Fe atoms with As atoms and reconfiguration according to the uniaxial symmetry of the substrate surface (surface anisotropy, [24–26]), the former is due to the anisotropic strain relaxation throughout the volume (anisotropic in-plane strain) of the thin film starting from compressive stress on the interface due to mismatch and later transforms to tensile due to the interfacial phase formation (Fe-Ga-As). These two different anisotropy effects form the basis of the term uniaxial in-plane magnetic anisotropy, ergo the reason behind the behaviour observed in the in-plane hysteresis loop of the Fe microdots deposited on GaAs substrate. [2]

On contrary, the out-of-plane loop is due solely to cubic anisotropy. It should be noted that thin-film shape anisotropy forces the magnetization to lie in-plane thus out-of-plane direction is hard. [2] It should also be noted that M_R/M_S ratio lower than 0.5 on in-plane and out-of-plane loops could be an indication for uniaxial anisotropy contribution produced by internal strains. [27,28]

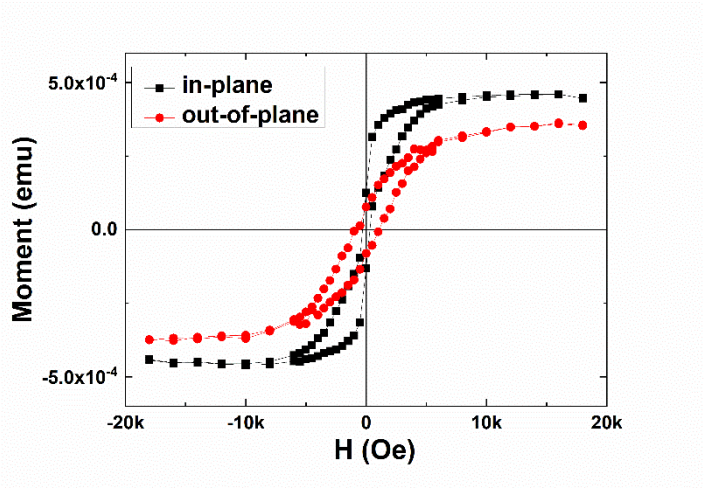

Fig. 4 Room temperature hysteresis loops of Fe microdots deposited on GaAs substrate.

5. Conclusions

Fe/GaAs hybrid micro-structures were successfully synthesized by a combinatorial approach of lithography and e-beam deposition techniques. 50 nm and 5 nm of Fe was deposited onto Si (001) and GaAs (100) substrates, respectively. Continuous films and microdots were covered with 5 nm Cr to prevent oxidation. XRD scan confirmed the presence of α-Fe BCC phase (ICSD 44863; space group I m3m) on Fe continuous films and microdots deposited on Si and GaAs substrates, respectively. SEM image showed that the microdots (100 μm diameter) were decorated throughout the wafer (100 μm in between the microdot disks). Large Mr/Ms ratio of 0.9 and 0.8 has been observed for Fe continuous films and microdots deposited on Si substrate, respectively, which is quite important for high-density recording media applications. Moreover, minor room temperature coercivities of 85 Oe and 65 Oe were also observed for Fe continuous films and microdots deposited on Si substrate, respectively. While the loop taken in-plane has the characteristic of two-phase/magnetic anisotropies behaviour with soft and hard ferromagnetic contributions (room temperature Hc=300 Oe), the out-of-plane loop corresponds to the classical hard direction loop with a room temperature coercivity of 925 Oe. In-plane uniaxial magnetic anisotropy was observed similar to the a priori observed effects on continuous films. The underlying reason for the in-plane uniaxial magnetic anisotropy is postulated to be interfacial origin due to the interfacial mixing of Fe atoms and out-diffused GaAs substrate atoms (mainly As). In addition to the interfacial effects, anisotropic strain distribution causes a uniaxial magnetoelastic anisotropy in-plane. Furthermore, MR/MS ratio lower than 0.5 on in-plane and out-of-plane loops could be an indication for uniaxial anisotropy contribution produced by internal strains. Fabricated semi epitaxial Fe micro-dots could be used in magnetoelectronic devices and micro electro mechanic systems by further improving the interface quality, thus increasing the spin incision efficiency.

Acknowledgement

Author would like to thank Ozan Akdogan for his helpful discussions. This work was supported by TUBITAK project: 217M322.

References

[1] Waldrop JR, Grant RW. Interface chemistry of metal-GaAs Schottky-barrier contacts. Appl Phys Lett. 1979;34(10):630-2. https://doi.org/10.1063/1.90642

[2] Wastlbauer G, Bland JAC. Structural and magnetic properties of ultrathin epitaxial Fe films on GaAs(001) and related semiconductor substrates. Adv Phys. 2005;54(2):137-219. https://doi.org/10.1080/00018730500112000

[3] Moodera JS, Kinder LR, Wong TM, Meservey R. Large magnetoresistance at room temperature in ferromagnetic thin film tunnel junctions. Phys Rev Lett. 1995; https://doi.org/10.1103/PhysRevLett.74.3273

[4] VAN DER MERWE JH. Epitaxial Interfaces. Treatise Mater Sci Technol. 1973 Jan;2:1-103. https://doi.org/10.1016/B978-0-12-341802-9.50007-8

[5] Hanbicki AT, van 't Erve OMJ, Magno R, Kioseoglou G, Li CH, Jonker BT, et al. Analysis of the transport process providing spin injection through an Fe/AlGaAs Schottky barrier. Appl Phys Lett. 2003 Jun;82(23):4092-4. https://doi.org/10.1063/1.1580631

[6] Taniyama T, Wastlbauer G, Ionescu A, Tselepi M, Bland C. Spin-selective transport through Fe/AlOx/GaAs(100) interfaces under optical spin orientation. Phys Rev B - Condens Matter Mater Phys. 2003; https://doi.org/10.1103/PhysRevB.68.134430

[7] Zega T, Yasar M, Zega T, Yasar M. Interface Effects on Spin Injection in Fe/AlGaAs spin-LEDs. APS. 2005;V10.008. https://doi.org/10.1017/S1431927604882850

[8] Hirohata A, Steinmueller SJ, Cho WS, Xu YB, Guertler CM, Wastlbauer G, et al. Ballistic spin filtering across ferromagnet/semiconductor interfaces at room temperature. Phys Rev B. 2002 Jul;66(3):035330. https://doi.org/10.1103/PhysRevB.66.035330

[9] Chye Y, Huard V, White ME, Petroff PM. Properties of a Fe/GaAs(001) hybrid structure grown by molecular-beam epitaxy. Appl Phys Lett. 2002 Jan;80(3):449-51. https://doi.org/10.1063/1.1434302

[10] Klaua M, Kirschner J, Urban R, Myrtle K. Magnetoresistance and magnetic properties of fe/cu/fe/gaas(100). Phys Rev B - Condens Matter Mater Phys. 1999 Oct;60(14):10242-51. https://doi.org/10.1103/PhysRevB.60.10242

[11] Hirose S, Haneda S, Yamaura M, Hara K, Munekata H. Electronic structure, growth, and structural and magnetic properties of magnetic semiconductor Fe/GaAs heterostructures. J Vac Sci Technol B Microelectron Nanom Struct. 2000 Jun;18(3):1397. https://doi.org/10.1116/1.591392

[12] Thibado P, Kneedler E, Jonker B, Bennett B, Shanabrook B, Whitman L. Nucleation and growth of Fe on GaAs(001)-(2×4) studied by scanning tunneling microscopy. Phys Rev B - Condens Matter Mater Phys. 1996;53(16):R10481-4. https://doi.org/10.1103/PhysRevB.53.R10481

[13] Chambers SA, Xu F, Chen HW, Vitomirov IM, Anderson SB, Weaver JH. Simultaneous epitaxy and substrate out-diffusion at a metal-semiconductor interface: Fe/GaAs(001)-c(8×2). Phys Rev B. 1986 Nov;34(10):6605-11. https://doi.org/10.1103/PhysRevB.34.6605

[14] Mirbt S, Sanyal B, Isheden C, Johansson B. First-principles calculations of Fe on GaAs(100). Phys Rev B - Condens Matter Mater Phys. 2003; https://doi.org/10.1103/PhysRevB.67.155421

[15] Schultz BD, Farrell HH, Evans MMR, Lüdge K, Palmstrøm CJ. ErAs interlayers for limiting interfacial reactions in Fe/GaAs(100) heterostructures. J Vac Sci Technol B Microelectron Nanom Struct. 2002 Aug;20(4):1600. https://doi.org/10.1116/1.1491994

[16] Sano K, Miyagawa T. Surface segregations during epitaxial growth of fe/au multilayers on gaas(Ool). Jpn J Appl Phys. 1991;30(7 R):1434-41. https://doi.org/10.1143/JJAP.30.1434

[17] Filipe A, Schuhl A, Galtier P. Structure and magnetism of the Fe/GaAs interface. Appl Phys Lett. 1997 Jan;70(1):129-31. https://doi.org/10.1063/1.119284
[18] Farrow RFC, Parkin SSP, Speriosu VS. New approaches to epitaxy of transition metals and rare earths: Heteroepitaxy on lattice-matched buffer films on semiconductors (invited). J Appl Phys. 1988; https://doi.org/10.1063/1.342404
[19] Anderson GW, Hanf MC, Norton PR. Growth and magnetic properties of epitaxial Fe(100) on S-passivated GaAs(100). Phys Rev Lett. 1995 Apr;74(14):2764-7. https://doi.org/10.1103/PhysRevLett.74.2764
[20] Filipe A, Schuhl A. Magnetism of Fe thin layers on GaAs (001). J Appl Phys. 1997; https://doi.org/10.1063/1.364821
[21] Bergerhoff G, Brown ID. Inorganic Crystal Structure Database. Acta Crystallogr Sect A Found Crystallogr. 1981; https://doi.org/10.1107/S0108767381089411
[22] Cullity BD, Graham CD. Introduction to Magnetic Materials. Introduction to Magnetic Materials. Hoboken, NJ, USA: John Wiley & Sons, Inc.; 2008. https://doi.org/10.1002/9780470386323
[23] Weller D, Doerner MF. Extremely high-density longitudinal magnetic recording media. Annu Rev Mater Sci. 2000 Aug;30(1):611-44. https://doi.org/10.1146/annurev.matsci.30.1.611
[24] Néel L. Anisotropie magnétique superficielle et surstructures d'orientation. J Phys le Radium. 1954; https://doi.org/10.1051/jphysrad:01954001504022500
[25] Krebs JJ, Jonker BT, Prinz GA. Properties of Fe single-crystal films grown on (100)GaAs by molecular-beam epitaxy. J Appl Phys. 1987; https://doi.org/10.1063/1.337886
[26] Jantz W, Rupp G, Smith RS, Wettling W, Bayreuther G. Investigation of single crystal fe films grown by MBE on GaAs substrates. IEEE Trans Magn. 1983;19(5):1859-61. https://doi.org/10.1109/TMAG.1983.1062649
[27] Bitar Z, El-Said Bakeer D, Awad R. Synthesis, characterization, and magnetic properties of nanosized Zn 0.5 Co 0.5 Er x Fe 2−x O 4 prepared by coprecipitation method. Turkish J Phys. 2019;43(1):80-92. https://doi.org/10.3906/fiz-1808-22
[28] Ammar S, Helfen A, Jouini N, Fièvet F, Rosenman I, Villain F, et al. Magnetic properties of ultrafine cobalt ferrite particles synthesized by hydrolysis in a polyol medium. J Mater Chem. 2001 Jan;11(1):186-92. https://doi.org/10.1039/b003193n

Research on Engineering Structures & Materials
journal homepage: http://jresm.org
MIM Research Group

Research Article

Temperature effects in deep drawing of advanced high strength steels

Kadir Akcan[1,a], Eren Billur*[2,b], H. İbrahim Saraç[3,c]

[1]*Ford Otosan A.Ş., Denizevler Mah. Ali Uçar Cad. No:53 41650 Gölcük, Kocaeli, TR*
[2]*Department of Automotive Engineering, Atılım University, Kızılcaşar Mah., 06830, Gölbaşı, Ankara, TR*
[3]*Department of Mechanical Engineering, Kocaeli University, Umuttepe Yerleşkesi, 41001, İzmit, Kocaeli, TR*

Article Info

Article history:
Received 4 Oct 2020
Revised 30 Dec 2020
Accepted 26 Jan 2021

Keywords:

Sheet metal forming; Finite element analysis; Thermomechanical modelling

Abstract

As advanced high strength steels (AHSS) find more use in automotive industry to meet crashworthiness and light weighting targets, concurrently. AHSS typically have higher strength, but lower formability; often limiting a part's dimensions and geometric complexity. Several studies have clearly shown that, in sheet metal forming, significant portion of the work done to overcome friction and to plastically deform a sheet is converted into heat. In this study, a thermomechanical finite element model has been developed to calculate the temperature rise in forming DP800 (AHSS). The model was validated with experiments from literature. A multi-cycle model is developed to find out possible problems due to tool heating. The process and material are selected to speed up the heating. Under different realistic press conditions, failures are observed after 20 to 80 hits.

1. Introduction

Automotive industry is pressured to reduce the emissions, while improving the crashworthiness. To achieve both targets automakers are forced to use either low density materials (such as aluminum alloys) or downgauging (reducing the thickness of the sheet) by using higher strength steels [1].

Conventional high strength steels (HSS) have been used in the automotive industry since late 1970's. In HSS, microstructure was ferritic and strengthening mechanisms were: (1) alloying with interstitials or (2) solid solution, (3) bake hardening effect (only valid for bake hardening steels in HSS), (4) carbide-forming and (5) grain refinement [2]. Conventionally, as the strength of the steel was increased, its formability would suffer. This is very well shown in the famous "banana-curve", in Figure 1.

In 1990's, automotive industry started using the multi-phase, so-called "advanced high strength steels" (AHSS). One of the first automotive applications was with the dual-phase (DP) steels (see the black dashed line in Figure 1). These steels consist of a soft ferrite matrix for formability and numerous martensitic islands for strength [3]. At similar yield strength levels, DP steels have higher elongation, compared to HSS, as seen in Figure 2.

DP steels are typically named after their tensile strength levels. For example, DP800 means a dual phase steel with approximately 800 MPa tensile strength. A recent study by Ford of Europe showed that replacing mild steel with DP800 could save 35% weight in crash components, as shown in Fig. 1. DP800 could be used both in axial crush regions (such as front or rear rails) and 3-point bending regions (such as rocker reinforcement and B-pillar) [4]. Since 2000's, the increase of DP steel usage in several Ford models is shown in Fig. 2.

*Corresponding author: eren.billur@atilim.edu.tr
[a] orcid.org/0000-0003-1454-3818; [b] orcid.org/0000-0001-9984-3697; [c] orcid.org/0000-0002-3414-3582
DOI: http://dx.doi.org/10.17515/resm2021.218me1004

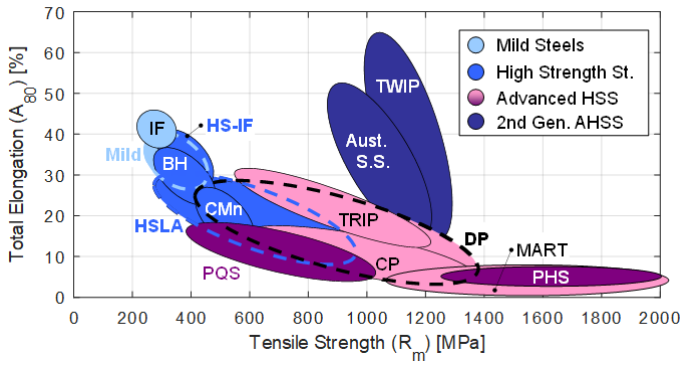

Fig. 1 Banana curve showing several automotive grades (3rd generation AHSS is omitted for better visibility)

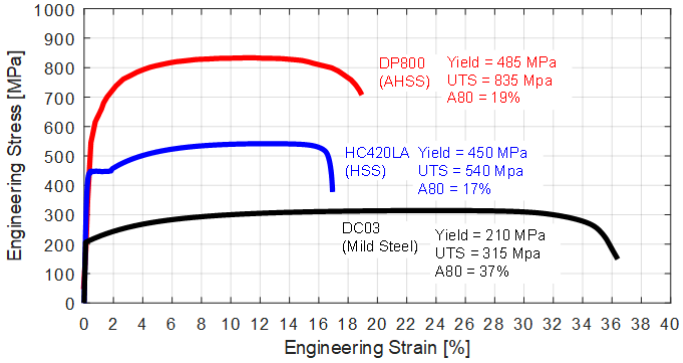

Fig. 2 Comparison of engineering stress-strain curves of DP800 with an HSS and mild steel.

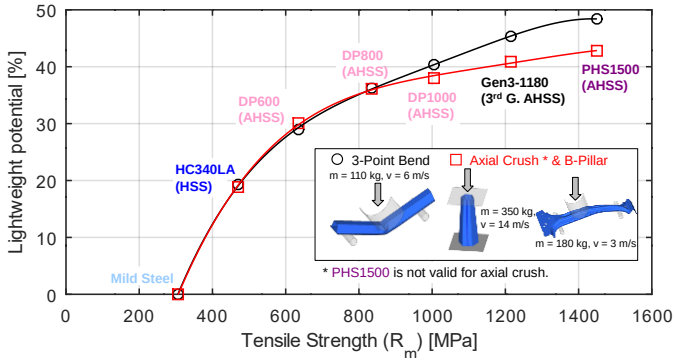

Fig. 1 Lightweight potential of several steel grades, compared to mild steel (re-created after [4])

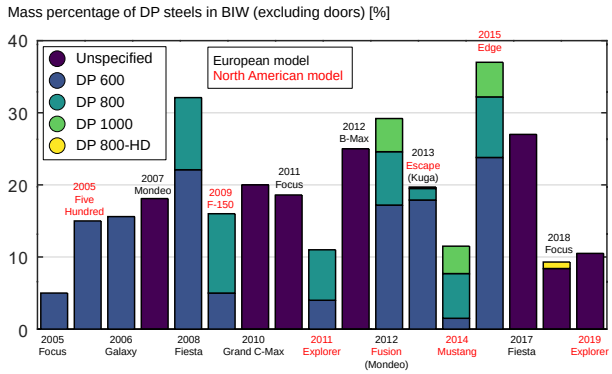

Fig. 2 Dual phase steel usage in several European and North American Ford Models

Although AHSS have higher formability (could be measured by total elongation, FLC_0, n-value at various intervals) compared to conventional HSS, as the strength level is increased, several forming challenges are still faced. These are [5]:

- Early fractures, especially due to local edge cracks
- Hard to control spring back
- Faster tool wear (shorter tool lives)
- Requirement of larger press capacities (both in force and energy)

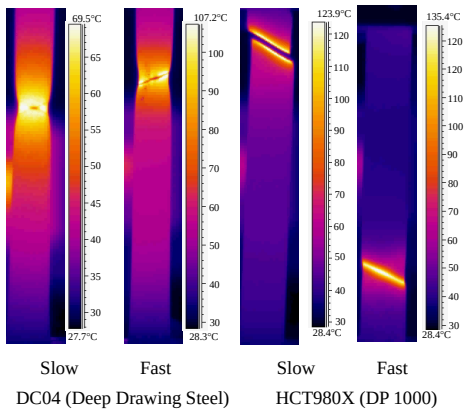

Fig. 3 Thermal images of tensile specimens just before fracture [7]

During press forming, significant amount of force (in the order of several hundreds of tons) is applied along the forming stroke (in the order of several hundreds of mm's). As a rule of thumb, 90% of the forming energy (integral of the force-stroke curve) is considered to be converted into heat [6]. Fig. 3 shows thermal camera images, captured at 50 frames per second. Two different materials were studied, a mild steel and an AHSS, DP1000. Two findings from this study could be: higher local maximum temperatures can be observed (1) when higher strength steels are deformed, and (2) when deformation is done faster. These thermal images show heat generation due to plastic deformation only [7].

In press forming, there would be heat generation due to plastic deformation and also, due to the friction between the blank and the tools. Local high temperatures would be observed with: (a) deeper draws, (b) higher strength materials and (c) high press speeds [8, 9]. When the speed of forming is increased – i.e., higher stroked per minute (SPM's), which are

favored in mass production, due to increased production volume – there would be less time for heat to dissipate and local temperatures may be even higher. Heat generation (or increased die temperatures) may affect the robustness of mass production of stamped components. A study at Volvo showed that in deep drawing of mild steels, even at 8 SPM, tool temperatures may increase by 10°C, causing splits in the drawn panel. The problem was initially solved by reducing the blankholder force after several strokes. Later, Volvo switched to a lower-friction coating (from GI to Zinc-Magnesium) [10]. Another solution, rather costly one, for high volume parts is to use an in-die cooling system, similar to hot stamping dies. Fig. 4, shows BMW's deep drawing tools for mild steels and AHSS. Cooling system was only used in high-volume AHSS applications [9].

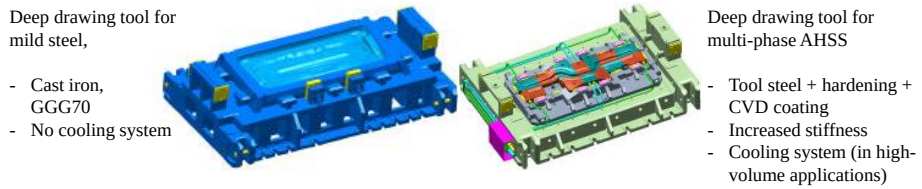

Fig. 4 Deep drawing tool design at BMW: (a) for mild steels, (b) for multi-phase AHSS (e.g., TRIP700) [9].

In this study, heat generation during deep drawing of DP800 is simulated, and the results are compared with the experiments in the literature.

2. Material Model

DP800 (sometimes also called as DP780) is selected, as this grade can be used in most applications in a car body (as shown in Fig. 1). There are several standards in Europe which defines chemical and mechanical properties of DP800. Table 1 summarizes the mechanical properties of DP800 equivalents in the European Norm EN 10338 [11], German Association of the Automotive Industry's VDA239-100 [12] and Ford's internal standard WSS-M1A368 [13]. It is important to note that these steels also have bake-hardening effect.

Table 1. DP800 material in different standards [11, 12, 13].

Standard	EN10338	VDA239-100	WSS-M1A368
Naming – Primary (Secondary)	HCT780X (1.0943)	CR440Y780T-DP (-)	CRDP800 (A14)
Proof strength ($R_{p0.2}$) [MPa]	440-550	440-550	420-550
Tensile strength (R_m) [MPa]	≥780	780-900	780-900
Total elongation (A_{80}) [%]	≥14	≥14	≥14
$n_{4\text{-}6}$ [-]	-	≥0.15	≥0.15
$n_{10\text{-}20/Ag}$ [-]	≥0.11	≥0.11	≥0.11
BH_2 [MPa]	≥30	≥30	≥30

To simulate a metal forming process, three key material data are required. These are:

1) Flow curve(s): true plastic strain-true stress curves for all conditions (i.e., if needed, at various temperature levels and strain rates).

2) Yield locus is used to calculate stress and strain tensors in multi-axial stress conditions.

3) Failure criterion: typically forming limit curve (FLC) is used, it is also possible to use thinning limit curve (TLC) or triaxial failure curve (TFC).

In this study, commercially available metal forming simulation software, AutoForm ® R8 with Thermo Plug-In was used for simulations. Material data was taken from AutoForm material library using Tata Steel's DP800 GI (Galvanized) Thermo model. There were 24 flow curves (4 temperature levels and a total of 6 strain rates), some of them are plotted in Fig. 5 [14].

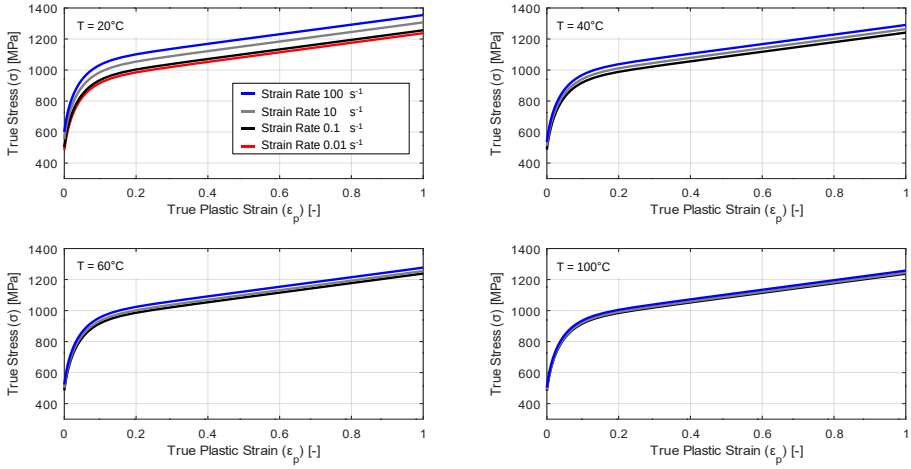

Fig. 5 Flow curves of all temperatures and some of the strain rates (re-created after [14])

In this study, Vegter 2006 (also known as Corus-Vegter or Vegter-Full) yield locus is used. To generate the yield locus, a total of 4 different experiments and 13 tests are required: (1) uniaxial tensile tests in 3 directions, with r-value determination, (2) shear test in 3 directions, (3) plane-strain test in 3 directions and (4) a biaxial test (preferably hydraulic bulge test) [15]. In this study, isotropic hardening is used [14].

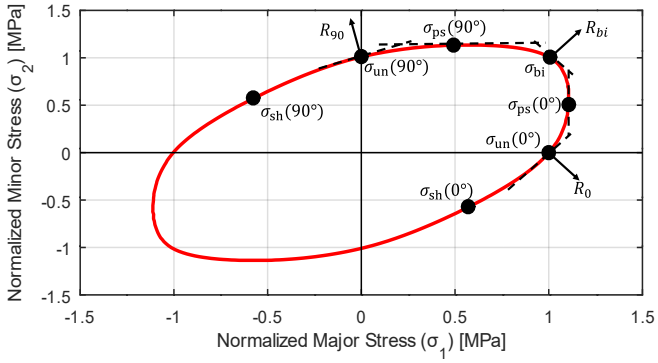

Fig. 6 Yield locus of DP800, using Vegter 2006 yield criterion (re-created after [14, 16])

Table 2. Parameters of Vegter yield locus at 20°C temperature and 0.01s^{-1} strain rate [14]

Parameter	Angle to rolling direction			Biaxial
	0°	45°	90°	
Uniaxial Yield Strength (σ_{un}) [MPa]	484	482	490	487
Normalized σ_{un} [-]	1	0.996	1.013	1.007
r-values	0.750	0.850	0.875	0.857
Shear Strength (σ_{sh}) [MPa]	279	276	276	-
Normalized σ_{sh} [-]	0.577	0.570	0.570	-
Plane-strain Strength (σ_{ps}) [MPa]	536	541	552	-
Normalized σ_{ps} [MPa]	1.107	1.117	1.140	-
Plane-strain Minor Stress (σ_{ps2}) [MPa]	247	250	238	-
Normalized (σ_{ps2}) [MPa]	0.511	0.516	0.492	-

Lastly for the Forming Limit Curve, Abspoel 2012 model is used – commonly referred to as Tata Steel model. In this model, r-values and total elongation (A_{80}) values for all 3 directions (0°, 45° and 90° to rolling direction) and thickness of the blank are required. The output will be similar to Marciniak FLC (i.e., FLC_0 coinciding with the y-axis) with only 4 data-points, as clearly indicated in Fig. 7 [17]. FLC is given for only 20°C. When the thickness is different than that of the FLC, Keeler approximation is used to calculate the new FLC.

In automotive industry, "failure criterion" is used when designing a die with simulation. For a given element, assume the maximum minor-major strain distribution during forming would be point A in Fig. 7. The failure criterion is the linear distance from origin to point A divided to the linear distance to the FLC. In Fig. 7, point A's failure criterion is approximately 0.5. In theory if failure criterion is equal to or over 1.0, the part would split. During die design process, failure criterion is typically kept around 0.7-0.8 to have a robust production.

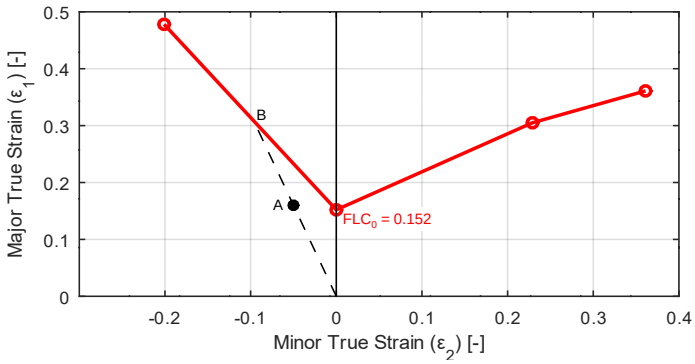

Fig. 7 Forming Limit Curve of 1.6 mm thick DP800 [14].

3. Simulations

In this study, a new deep drawing tool for DP800 has been developed, considering the heat generation effects. The thermomechanical finite element simulations were first validated with experiments in the literature.

3.1. Validation of Thermomechanical Model

To validate the predictions of the thermomechanical model, Pereira and Rolfe's experimental study [18] was replicated. The dimensions of the tools are given in Figure 10. Pereire and Rolfe studied a number of different sheet steels, in this study only 2.0 mm DP800 is replicated. Tools were considered to be uniformly 20°C before the forming process. Tools were modeled with 3D heat conduction, and a 100 mm tool height was added. Thus, the tools may heat up after stamping process. Simulation parameters are summarized in Table 3. In these simulations, mechanical press is simulated with a motion curve, developed by one of the co-authors.

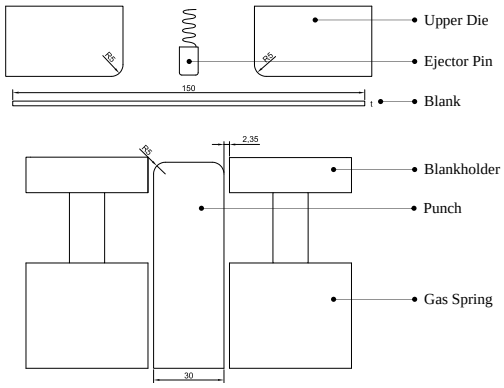

Fig. 10 Schematic view of the tools (re-created after [18])

Table 3. Simulation parameters

Friction coefficient [-]	0.15	
Blankholder force [kN]	27.2	
Draw depth [mm]	40	
Mechanical press stroke length [mm]	203.2	
Stroke rate [SPM]	1	
Thermal properties	Tools	Sheet
Initial Temperature [°C]	20	20
Heat Conductivity [W/m°K]	22	52
Volumetric Heat Capacity [mJ/mm³°K]	3.588	3.564

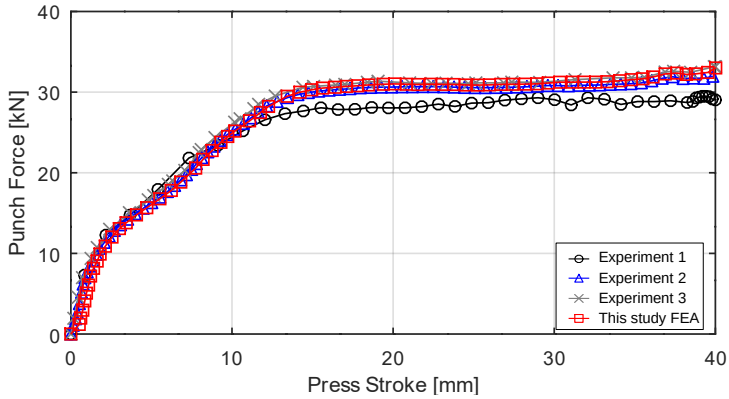

Fig. 8 Punch force vs. press stroke, experiments from [18].

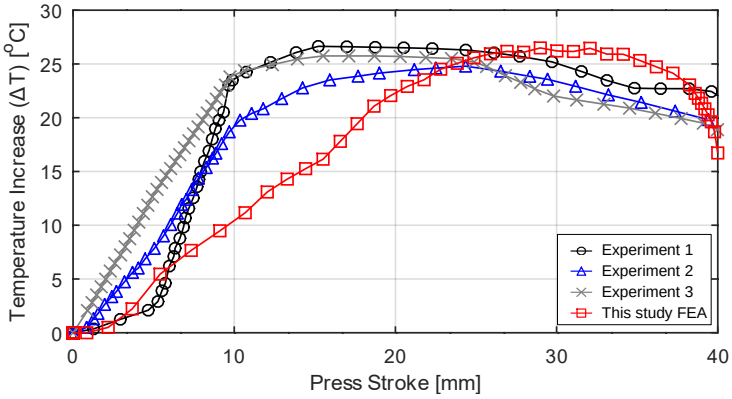

Fig. 9 Temperature increase in the blank, experiments from [18].

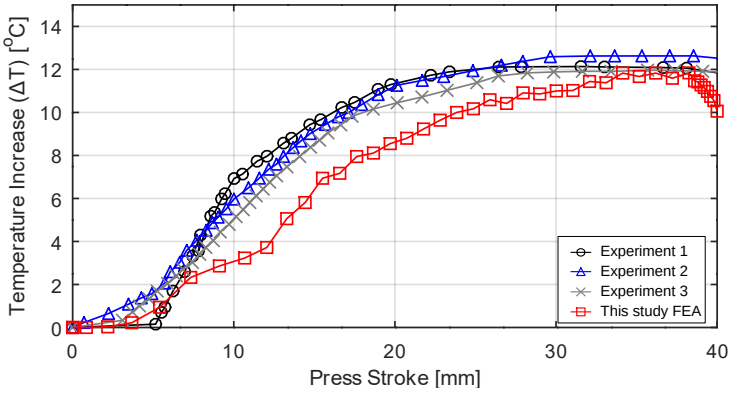

Fig. 10 Temperature increase of the tools (measured below upper die surface).

Pereira and Rolfe made all the experiments and measurements with five repetitions. In this study, we digitized three of them to compare our simulation results. By this method, the figures would be easier to read. The three data sets were selected as the highest values, lowest values and the average. The first comparison was done in punch force vs. stroke. As seen in Fig. 8, the curves were very close. The discrepancy at the bottom of the stroke may be due to the gas springs' compression. As the paper did not share the details of the gas springs, but assumed an average force of 27.2 kN, the effect of compression had to be neglected. The second comparison was done on the temperature of the blank. As seen Fig. 9, the peak temperature calculated in the simulation overestimated the experimental peak temperature by only 0.15-1.84°C. On the other hand, tool temperatures are slightly underestimated by 0.13-0.79°C. These can be explained by heat transfer coefficient between the blank and the tool, constant friction coefficient, variation of material properties between the material card and the experiments. Still, the results show the thermomechanical model has good correlation with the experiments.

3.2. Developing the DP800 Draw Die Model

In this study, the effect of tool temperature on deep drawability of DP800 is studied. In order to measure the effect of tool temperature, the cup draw test die set (i.e., only a draw ring, not a full die cavity) defined by Ju et al. [19] was slightly modified. Ju et al. used a punch with vertical wall. In most automotive applications, to facilitate drawing and ejecting the part, the punch typically has a positive wall angle. Although it may vary from part to part, a wall angle of 7° is quite common. The die set, shown in Figure 14, is designed for parts up to 170 mm depth.

Lubrication (or in simulation terms, friction) affects the deep drawability. In most studies, various oil or water-based lubricants are applied. In automotive industry, for environmental concerns, "dry press shops" are favored. In a so-called "dry press shop", the blanks are formed with the mill oil with no additional lubricant [20]. Mill oil is the oil film on the coil to avoid corrosion during shipping, typically between 1.0-2.0 g/m^2.

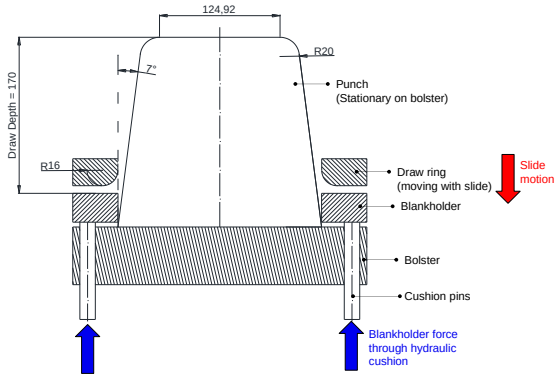

Fig. 14 Cup draw die set-up.

In this study, the simulations were run with only mill oil. The friction coefficient was not selected as a constant value throughout the part, but instead TriboForm Plug-in was used. 1.0 g/m^2 oil was selected and the Dual Phase GI friction model was imported from TriboForm library.

In industrial production, a link motion press is used for deep drawing. The press has frequency inverter speed control, adjustable from 8 to 22 strokes per minute (SPM). The

real stroke-time curves of the deep draw press at Otosan are shown with red color in Fig. 11. To study the effect of press speed, a mechanical press without link motion, but the same stroke length and SPM were also modeled. Black curves in Fig. 11 show this fictious mechanical press stroke-time profiles.

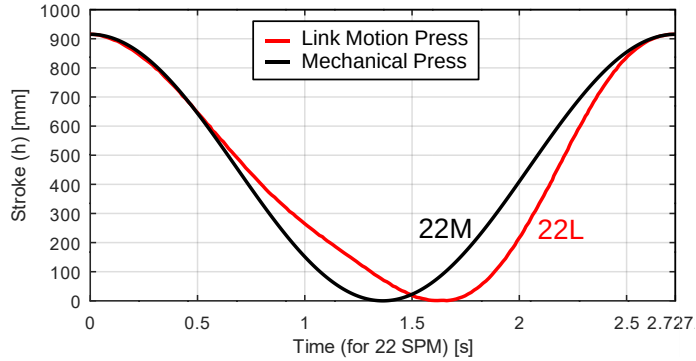

(a)

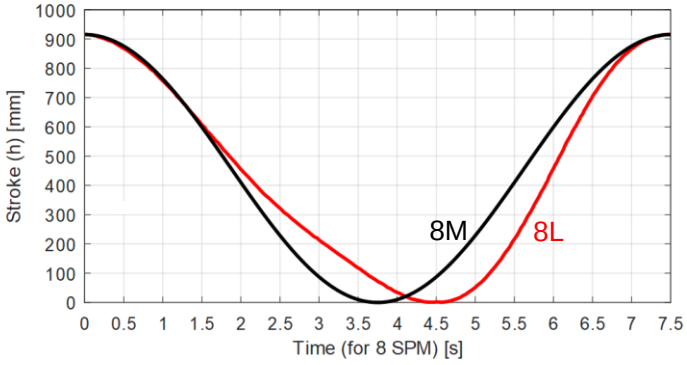

(b)

Fig. 11 Press stroke-time curves for link-motion and mechanical press with 916 mm stroke: (a) at maximum speed of the line (22 SPM) and (b) at minimum speed of the line (8 SPM).

Between 4 different models, several differences would be simulated:

1) Due to decreased press speed, at 8 SPM, flow stress would be slightly lower, due to lower strain rate;

2) Since TriboForm plug-in is used, as the velocity is decreased, friction coefficient will increase;

3) As Thermo plug-in is used, there would be heat generation in the blank (due to plastic deformation) and die-blank interface (due to friction). At high speeds, there would be less time to dissipate the heat. Higher local temperatures may occur, softening the steel; but increasing the friction.

Due to all these interacting effects of press speed (SPM and type), it was found that if the blankholder force would be kept constant between 4 different models, significant changes in formability would occur. Thus, to have comparable results, blankholder force was changed to keep the "failure criterion" (FC) as close as possible after the first hit. Table 4 shows the parameters and the FC values after first hit. Incoming blanks at each hit are assumed to be 20°C. The tools were uniformly at 20°C before the first hit, but are allowed to accumulate heat after each hit. Tools lose some of the heat to the environment through convection.

Table 4. Simulation parameters and failure criteria after first hit.

Short name	Press Speed (SPM)	Press Type	Blankholder Force (kN)	FC after first hit
8M	8	Mech.	78	0.677
8L	8	Link	77	0.675
22M	22	Mech.	80	0.676
22L	22	Link	87	0.679

4. Results

In the automotive industry, process is designed such that the FC value is kept under 0.7-0.8 – depending on the part complexity. In this study, the FC values after the first hit were kept very close to 0.7 intentionally. Then, more cycles are run until the FC value surpasses 1.0. In this case, the part is considered to have a split (failure). Figures 12 through 15 summarizes the change of FC values and tool temperature. Here, the local maximum temperature on any tool surface (punch, die or blankholder) is shown.

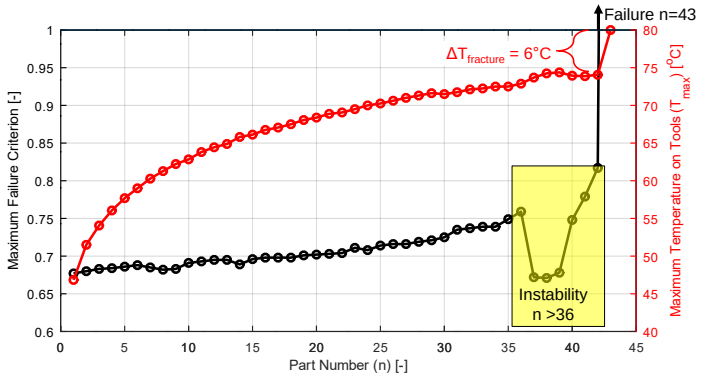

Fig. 12 Condition 8M: failure at 43rd part with over 74°C maximum tool temperature

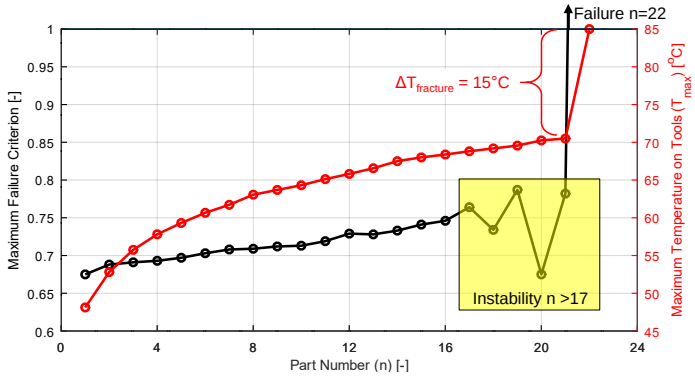

Fig. 13 Condition 8L: failure at 22nd part with over 70°C maximum tool temperature

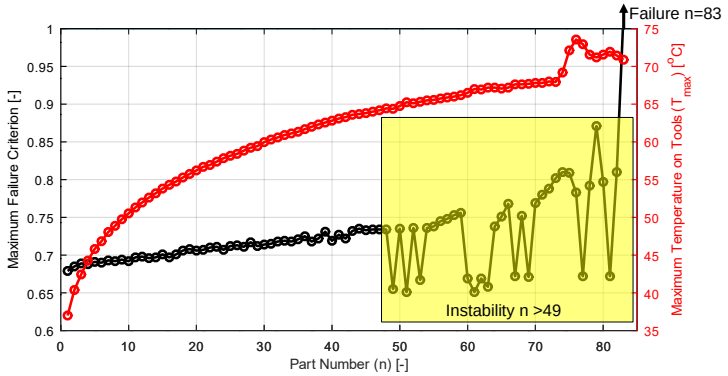

Fig. 14 Condition 22M: failure at 83rd part with over 71°C maximum tool temperature.

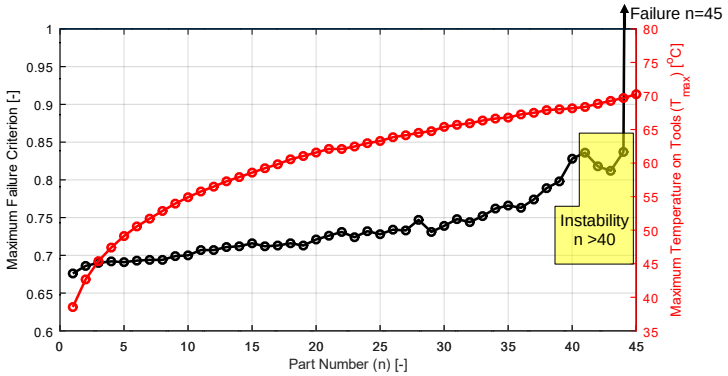

Fig. 15 Condition 22L: failure at 45th part with over 70°C maximum tool temperature.

In most stamping operations, the first hit has a much lower FC value, and it takes much longer to have a failure due to heating (over 300-500 hits [10, 21]). In this particular design, use of strong steel (DP800) with very deep draw (170 mm) may have accelerated the failure due to tool temperature. This was intentionally done to: (1) reduce the simulation time, and (2) keep the failure below 100 cycles, which was the limitation of the software.

In all conditions, a few hits before the failure, FC values are lowered. This is marked as "instability". This could be due to a glitch in the mathematical model and requires further investigation.

Overall, once the tool temperatures surpass 70°C, failure is observed. According to Waanders et al., friction coefficient may increase by 40% at temperatures over 60°C [21].

Contrary to expectations, link motion presses seemed to be disadvantageous in this study. This can be explained by the increased friction coefficient due to reduced slide velocity and reduced time to dissipate the heat energy in link motion presses. In reality, the lower shock at force build-up improves the lubrication condition. Another problem was the idle times: durations of final part (hot) and incoming blank (cold) sitting on the tools. Mathematical model could be improved by measuring real idle times on a press line.

Figure 16 shows the local maximum temperature of the blanks after each hit – excluding the fractured part. As expected, blank temperatures are higher at 22 SPM. At low SPM's, the blank drawn in a link motion press has lower temperature. Similar to FC-values, before fracture, the maximum temperatures seem to reduce in the last few hits. It is very critical to note that, the material card had flow curves only until 100°C (see Fig. 5). Over this temperature, extrapolation was used.

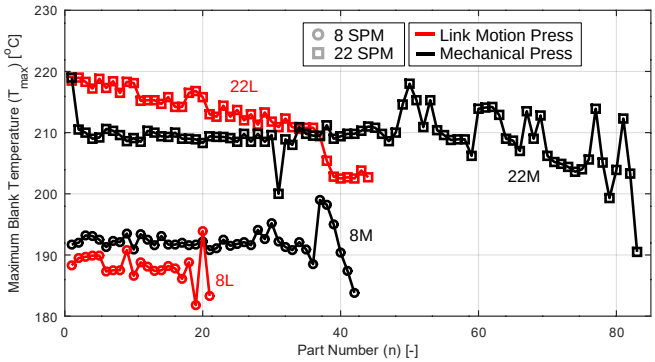

Figure 16 Maximum blank temperature in all 4 conditions.

5. Conclusions and Future Work

A mathematical model for heat generation has been developed and validated with experiments from literature. After the first hit, the temperature predictions were within ±2°C.

Once this model is validated, a multi-cycle model is generated. The die design and material selection were done to speed up the heat generation, such that, after only 22 to 83 hits failures were observed.

Several improvements could be done in the mathematical model, such as:

1) Temperature dependent FLC may be required to further improve FC-value predictions,
2) Higher temperature flow curves could reduce the error due to extrapolation,
3) Correction of idle times on the tools may change the tool temperatures,
4) Friction model requires further investigation.

After the proposed work done, it is possible to find the best possible process window to improve productivity (higher SPM) and reduce costs (due to scrapping of failed parts). A draw die with built-in cooling channels is planned for further experimental studies.

Acknowledgments

Authors would like to thank Dr. Alper Güner, AutoForm Engineering Deutschland GmbH, Mr. Nihat Kurtuluş from Grup Otomasyon, and Mr. Metehan Karaköse for their valuable input in this article.

References

[1] J. R. Fekete and J. N. Hall, "1 - Design of auto body: Materials perspective," in Automotive Steels, R. Rana and S. B. Singh, Eds., Woodhead Publishing, 2017, pp. 1-18. https://doi.org/10.1016/B978-0-08-100638-2.00001-8
[2] Posco, "Automotive Steel Data Book," 2016.
[3] T. B. Hilditch, T. de Souza and P. D. Hodgson, "2 - Properties and automotive applications of advanced high-strength steels (AHSS)," in Welding and Joining of Advanced High Strength Steels (AHSS), M. Shome and M. Tumuluru, Eds., Woodhead Publishing, 2015, pp. 9-28. https://doi.org/10.1016/B978-0-85709-436-0.00002-3
[4] F. Özkan and A. Bach, "Future trends and challenges in using AHSS in body structure," Presented at PHS Suppliers Forum, September 19, Troy, MI, 2019.
[5] E. Billur and T. Altan, "Challenges in forming advanced high strength steels," Proceedings of New Developments in Sheet Metal Forming, p. 285-304, 2010.
[6] A. Fallahiarezoodar, R. Peker and T. Altan, "Temperature Increase in Forming of Advanced High-Strength Steels Effect of Ram Speed Using a Servodrive Press," Journal of Manufacturing Science and Engineering, vol. 138, 7 2016. https://doi.org/10.1115/1.4033996
[7] E. Billur, "Heating helps cutting - Adiabatic cutting of high strength sheets," Metalforming Magazine, December 2020 Issue, p. 12-13, 2020.
[8] E. Ceron and N. Bay, "Testing and prediction of limits of lubrication in sheet metal forming," in iddrg 2012 incorporating SMF 2012: Lightweighting: Possibilities & Challenges, 2012.
[9] M. Pfestorf, "Manufacturing of high strength steel and aluminum for a mixed material body in white," in Advanced Materials Research, 2005. https://doi.org/10.4028/0-87849-972-5.109
[10] N. Kurtulus, "New Developments in Sheet Metal Forming Simulations," in Proceedings of the 2nd Metal Forming Technology Day (meftech2019), Istanbul, TR, 2019.
[11] EN 10338, "Hot and cold rolled non-coated flat products of multi-phase steels for cold forming - Technical delivery conditions," European Standard, 2015.
[12] Verband Der Automotbilindustrie E.V. (VDA), "Sheet Steel for Cold Forming," Material Specifications, 2016.
[13] Ford Global Technologies LLC, "WSS-M1-A368 - Engineering Material Specification," Company Standard, 2017.
[14] Tata Steel, «CR_DP800-GI_Vegter+thermo_1.2-1.6.mtb,» AutoForm Material Card, 2019.
[15] H. Vegter and A. H. van den Boogaard, "A plane stress yield function for anisotropic sheet material by interpolation of biaxial stress states," International Journal of Plasticity, vol. 22, pp. 557-580, 2006. https://doi.org/10.1016/j.ijplas.2005.04.009
[16] H. Vegter, C. ten Horn and M. Abspoel, "The corus-vegter lite material model: simplifying advanced material modelling," International Journal of Material Forming, vol. 2, p. 511, 15 12 2009. https://doi.org/10.1007/s12289-009-0640-4

[17] M. Abspoel, M. E. Scholting and J. M. M. Droog, "A new method for predicting Forming Limit Curves from mechanical properties," Journal of Materials Processing Technology, vol. 213, pp. 759-769, 2013. https://doi.org/10.1016/j.jmatprotec.2012.11.022

[18] M. P. Pereira and B. F. Rolfe, "Temperature conditions during 'cold' sheet metal stamping," Journal of Materials Processing Technology, vol. 214, pp. 1749-1758, 2014. https://doi.org/10.1016/j.jmatprotec.2014.03.020

[19] L. Ju, T. Mao, J. Malpica and T. Altan, "Evaluation of Lubricants for Stamping of Al 5182-O Aluminum Sheet Using Cup Drawing Test," Journal of Manufacturing Science and Engineering, vol. 137, 9 2015. https://doi.org/10.1115/1.4030750

[20] N. Asnafi, "Tooling and Technologies for Processing of Ultra High Strength Sheet Steels," Presented at Tool and Technologies for Processing Ultra High Strengh Materials, TTP2011, Graz, Austria, 2011.

[21] D. Waanders, J. H. Marangalou, M. Kott, S. Gastebois and J. Hol, "Temperature Dependent Friction Modelling: The Influence of Temperature on Product Quality," Procedia Manufacturing, vol. 47, pp. 535-540, 2020. https://doi.org/10.1016/j.promfg.2020.04.159

Research on Engineering Structures & Materials
journal homepage: http://jresm.org
Research Group

Research Article

Single edge crack fracture behavior of S2 glass/epoxy under different temperature, strain rate and crack length

Zafer Kaya[1,a], H Ersen Balcioglu[2,b], Halit Gün[2,c]

[1]*Graduate School of Natural and Applied Sciences, Uşak University, Uşak 64100, Turkey*
[2]*Department of Mechanical Engineering, Uşak University, Uşak 64100, Turkey*

Article Info

Article history:
Received 19 Feb 2021
Revised 09 Mar 2021
Accepted 30 Mar 2021

Keywords:

S-2 glass/epoxy;
Fracture toughness;
Strain energy release rate;
J-integral method;
Deformation rate;
Temperature effect;
Finite Element Method

Abstract

S-2 glass fiber draws attention because of its higher strength and elasticity module compared to other glass fiber types. When cracks occur on these structures, which have their distinctive strength properties, they may suddenly lose their physical life or in a shorter time than they should be. In this study, the fracture behaviors of S-2 glass fiber reinforced composite materials for different temperatures, deformation rate, and crack geometry were investigated. To investigate the effects of crack geometry on fracture behavior, cracks were formed on S-2 glass/epoxy composites in two different lengths (10mm and 15mm) and at two different angles (0° and 45°). Fracture tests were performed at two different environments impending cold (-20°C) and hot (80°C), and three different tensile strain rates (8.3×10^{-3}, 8.3×10^{-4}, and 8.3×10^{-5} s^{-1}). For these experimental conditions, opening mode (Mode I) and mixed-mode (Mode I/II) fracture toughness values (K_C) and strain energy release rates (G_C) were investigated experimentally and numerically. The $J_{integral}$ method was used to calculate numerical fracture toughness. Experimental results have shown that fracture toughness increases with increasing temperature and crack length in general. As the deformation rate increases, fracture toughness decreases. Also, identical expressions that define experimentally and numerically calculated fracture were found close to each other. $J_{integral}$ method was found to be a successful method to analyze the fracture behavior of fiber-reinforced composites.

1. Introduction

In fiber-reinforced composite materials, cracks may occur on them during their production or after external effects. Crack and following fracture damage can create situations that will result in serious losses in a structure. Crack negatively affects both the strength and physical life of the materials. The behavior of the crack should be analyzed to know the safe physical life and safe usage conditions of the composite materials that have brittle structure and crack. The geometry of the crack, environmental factors (such as temperature and humidity), and the magnitude of the load affecting the material are the main factors affecting the crack behavior. In a composite structure having cracks, the length of the crack directly affects the fracture toughness of the material and the crack propagation rate. Therefore, it is important to know the effects of crack length on the fracture behavior of the composite material.

In their study on the crack location and crack length, Yin et al.[1] have examined the opening distance at the crack bottom as a toughness assessment criterion for the model they created in their experimental and numerical studies. Healey et al.[2] have studied the fracture behavior between layers on carbon fiber prepreg composite structure test

*Corresponding author: ersenbalcioglu06@gmail.com
[a] orcid.org/0000-0002-5489-3997; [b] orcid.org/0000-0002-8579-5142; [c] orcid.org/0000-0001-8107-5036
DOI: http://dx.doi.org/10.17515/resm2021.263me0219

specimens with crack lengths between 20-40mm. Loutas et al. [3] studied Mod I fracture behavior in metal composites. They used 28mm, 34.5mm, 54.5mm, and 67.6mm anterior crack lengths in their studies. Andric and Curtin [4] modeled fractured specimens with a central crack ranging from 2mm to 15mm in their fracture studies. Bosbach et al. [5] measured the strain energy release rate between fiber and matrix at opening distances between 53mm and 78mm of the crack. Kaushik and Ghosh [6] evaluated the crack in terms of strain energy release rate and fracture toughness in crack expansions between 60mm and 110mm in polytetrafluoroethylene (PTFE) prepreg composite plates. Insausti et al.[7] have performed a numerical analysis for double cantilever beam test specimens to determine the crack length, the compliance, and the energy release rate.

The position of the crack or the angle of load that forces the crack to progress causes the development of different fracture damage modes such as opening mode (Mode I), in-plane shearing mode (Mode II), out-of-plane shearing mode (Mode III) or mixed mode. Mousavi et al.[8] Mode I, Mode II and Mod I/II; Aliha and Mousavi [9] Mod I and Mod I/II; Kaynan et al.[10] Mod I/II for carbon fiber prepregs; Li et al.[11] Mod I/II; Ravindran et al.[12] Mode II studied experimental specimens with different crack lengths in fracture modes. Shahani et al. [13] experimentally investigated the inter-laminar fracture behavior under Mode I loading in a glass/epoxy composite structure. Torabi et al. [14] studied Mod I/II fracture toughness in nanocomposites. They worked on experiment specimens with 1mm, 2mm, and 4mm length central cracks.

One of the factors affecting fracture damage is environmental factors such as temperature and humidity [15]. Although the effects of these factors have been an issue studied since the 1980s, there is still no standard test method. In the literature, the results of some studies on this subject showed that the fracture toughness increased with increasing temperature. Such that, fracture toughness investigation in a carbon epoxy laminated structure, the inter-laminar fracture toughness generally increases with the increase in temperature for Mode I crack tip opening status [16,17]. Foyouzat et al. [18] investigated the Mode I fracture toughness of shape memory polymers (SMP) between 20˚C and 100˚C temperatures. Arash Farshidi et al. [19] in their experiments in foam core sandwich composites -20˚C and room temperature (23˚C), they found a decrease in Mod I and Mod I/II fracture toughness as the temperature dropped. M. Fakhri et al. [20] performed crack analysis of hot mix asphalt at 5˚C, 15˚C, and 25˚C temperatures under Mod I, Mod II, and Mod I/II loading conditions. Khashaba et al.[21] performed some experiments to investigate the mechanical properties of Epocast 50-A1/epoxy at room temperature and 50˚C. Pan et al.[22] have investigated thermo-mechanical response and morphology of three-dimensional knitting carbon/epoxy composites under different environment temperatures such as 25˚C, 60˚C, 90˚C, and 120˚C. Pini et al. [23] examined the strain energy release rate at 0˚C and 60˚C temperature ranges for cracked test specimens of laminated carbon fiber composite. In another study, Rahmani et al. [24] determined in their experimental study, which performed at the temperature range of -80˚C to +22˚C, that a reduction in the fracture energy absorption capacity of the composite structure at very low temperature occurred.

Another factor affecting the fracture behavior of the composite structure is the strain rate effect. Aktaş et al. [25] investigated the mechanical behavior properties of glass/epoxy laminated composite plates at different deformation rates of 0.005 s^{-1}, 0.0005 $s^{-1,}$ and 0.00005 s^{-1}. Also, Jia et al. [26] investigated Mode I fracture toughness of polyurethane adhesive at 0.5mm/min, 50mm/min, 500mm/min loading speeds.

S-2 glass/epoxy laminated composite structures are frequently used as reinforcement materials in composite applications that require high strength. Sometimes these composite structures can be used in a body material of cold storage tank. Also, due to its lightness, it

is used as a building material in wind turbines working in a hot environment. Therefore, it is important to know the fracture behavior of S-2 glass fiber reinforced composite having different crack geometry under cold and hot environments and at different deformation rates. In this context, S-2 glass/epoxy laminated composites having single edge crack length (10 mm and 15 mm) were tested in two different temperatures (-20˚C and 80˚C) and three different deformation rates (8.3×10^{-3}, 8.3×10^{-4}, and 8.3×10^{-5} s^{-1}) for Mode I and Mode I/II crack tip opening status. Also, the fracture behavior of S-2 glass/epoxy laminated composites was modeled using the ANSYS finite element program and fracture toughness and J integral values were calculated for each experimental parameter. When the accessible literature was examined, it was seen that the fracture behavior of S-2 glass reinforced composite structures was not investigated depending on the temperature and deformation rate changes. The response of different crack lengths to these variables has been the main research subject of the study. The combination of experimental and finite element studies will contribute to the literature.

2. Material and Methods

2.1. Production of Composite Materials

Vacuum resin transfer molding method (VARTM) was used to the manufacturing of composite plates having 8 laminas. The reinforcement material is woven S-2 glass fabric has 190 g/m^2 weight, and 130 μm thickness. Two-component resin consisting of epoxy (Hexion MGS L285) and hardener (Hexion H287) was used as the matrix material. Technical specifications of reinforcement material and the matrix material are shown in Table 1.

Table 1. The material properties of fiber material and epoxy resin

Material Properties	Fibre Material (S-2 Glass) [27]	Matrix Material (Hexion Epoxy Resin) [28]
Young's modulus (E) in GPa	86-93	3.2
Shear Modulus (G) in GPa	35-39	1.18
Poisson's ratio (υ)	0.21	0.36
Tensile Strength in MPa	4700-4800	70-80
Compressive Strength in MPa	4000-5000	120-140

During the tests, load-displacement curves were saved for each specimen utilizing the computer-controlled tensile test machine. The displacement values for specimens under load were observed using a video extensometer capable of recording bidirectional deformation. Before the fracture tests, the test specimens were kept at the relevant test temperature and ensured to reach an equal temperature with the environment. Each experiment was repeated three times and the averages of these three experiments were used in the study.

Linear Elastic Fracture Mechanics (LEFM) is the whole of analytical expressions used in the study of fracture mechanics and developed based on the principle that all behaviors in the material remain within elastic limits. The basic principle of this method is to express the stresses formed at the crack tip depending on the stress applied to the part, the length and direction of the crack. The principles of LEFM was used to examine the fracture behavior of fiber-reinforced composite material [4,13,32].

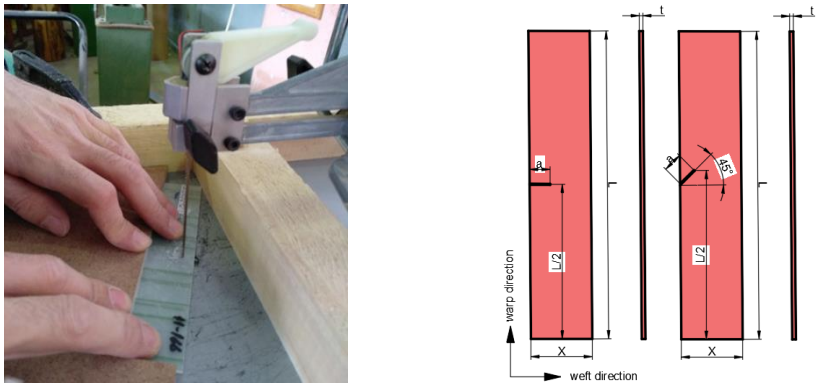

(a) (b)

Fig. 1 Single edge crack test specimen (a) crack creation (b) test sample sizes

The produced S-2 glass/epoxy composite plates were cut in the warp direction with the dimensions L=150 mm and X=30 mm. Then cracks of a=10mm and a=15mm length on the fracture test specimens were created from the single edge of the specimen with a jigsaw at 0˚ and 45˚ angles according to the weft axis as shown in Figure 1. The thickness of each crack is 0.5 mm [8,29–31].

2.2. Fracture Tests

The fracture tests were carried out in the Shimadzu AG-X model tensile testing device having the thermostatic chamber. The loading capacity of the test machine is 100kN. The hot and cold environments required for fracture tests were created inside the thermostatic chamber of the test device. Fracture tests performed in cold and hot environments in 5 repetitions have enabled the polymer-built composite material to determine ductile and brittle deformation behavior. Thanks to the electrical heater of the thermostatic chamber the environment was heated to 80°C, and to obtain a cold environment (-20°C) Nitrogen gas was used (Figure 2). Fracture tests were performed three different strain rates of 8.3×10^{-3} s^{-1}, 8.3×10^{-4} $s^{-1,}$ and 8.3×10^{-5} s^{-1}. To obtain strain rates of 8.3×10^{-3} s^{-1}, 8.3×10^{-4} $s^{-1,}$ and 8.3×10^{-5} s^{-1}, test specimens were subjected to tensile testing at jaw feed rates of 50 mm/min, 5 mm/min and 0.5 mm/min, respectively.

Fig. 2 Shimadzu AG-X 100 kN universal test device

The critical stress intensity factor is determined by the fracture test. This factor is calculated according to the damage condition of the crack opening (Mode I), sliding (Mode II), opening sliding (Mode I/II). The critical stress intensity factor (K_c) for the test specimen with a single edge crack is calculated according to the following Eq.1.

$$K_c = \frac{P_{app}\sqrt{\pi a}}{Xt} y(\frac{a}{X}) \quad (1)$$

In this formula, P_{app}, represents the applied load, a crack length, X specimen width, t specimen thickness, $y(\frac{a}{X})$ geometric factor [33–35].

2.3. Mod I Fracture Toughness

In the Mode I crack tip opening status, the normal component of the stress influence vertical to the crack surface. This stress forces to damage by only the opening of the crack tip. Since the Mode I damage type is the most critical damage type among brittle composite materials, it is the most widely studied case in fracture mechanics studies. In Mode I, where the crack tip is forced to open (crack angle α=0˚), it is called Fracture Toughness (K_{IC}) when the stress intensity factor reaches the critical value. Expressed in K_{IC} (Eq. 2).

$$K_{ıc} = \frac{P_{cr}\sqrt{\pi a}}{Xt} y_ı \left(\frac{a}{X}\right) \quad (2)$$

Unlike from Eq. 1, in the formula; P_{cr} represents the damage load and $y_ı \left(\frac{a}{X}\right)$ represents the geometric factor for the opening mode. $y_ı \left(\frac{a}{X}\right)$ geometric factor values depend on crack length, temperature, and deformation rate. These values were calculated by using the finite element method. For this aim, single edge cracked test models were created in the finite element program ANSYS according to the experimental fracture test dimensions of specimens. The following steps have been applied to calculate the $y_I \left(\frac{a}{X}\right)$ geometric factor value.

- A randomly selected load of P=1000 N was applied to these models created for each test condition.
- The value of $(K_{IC})_{Num}$ for Mode I obtained by using the "Fracture Tool" of the program.
- Then, the geometric factor value $y_I \left(\frac{a}{X}\right)$ was calculated by substituting the obtained fracture toughness value in Eq. 3 [35,36].

$$y_I \left(\frac{a}{X}\right) = \frac{(K_{IC})_{Num}.wt}{P.cos\alpha\sqrt{\pi a}} \quad (3)$$

In the case of Mode I for each experiment parameters, $y_ı \left(\frac{a}{X}\right)$ values are obtained as in Table 2.

Table 2. Geometric dimension factor values obtained from ANSYS finite element program for Mode I (opening mode).

Deformation Rate (s^{-1})	a=10 mm		a=15 mm	
	-20°C	80°C	-20°C	80°C
8.3×10^{-3}	1.9821	2.1788	3.1289	3.4570
8.3×10^{-4}	1.8628	2.3603	3.3696	3.7612
8.3×10^{-5}	2.2449	2.5211	3.5655	4.0238

2.4. Mod I/II Fracture Toughness

If the direction of the applied load is parallel to the crack, occurred stress at crack tip force the crack by shearing and this condition is called pure shearing mode (Mode II). In some cases, the crack tip is forced to both open and shear. The state where the effects of Mode I and Mode II are seen together is called mixed mode, namely Mode I/II. In this case, two stress intensity factor components are formed at the crack tip. The stress intensity factor value reaches the critical value as soon as the specimen breaks and the fracture toughness value is expressed in K_{mix} [37–39]. K_I and K_{II} toughness values given in Eq. 4 and 5 are the opening and shearing components of K_{mix} toughness value given in Eq. 6 [34]. Mod Mode I/II fracture behavior of S-2 glass/epoxy composites was investigated for the crack angle of α=45°.

$$K_I = \frac{P_{cr} cos45^o \sqrt{\pi a}}{Xt} y_{mI}\left(\frac{a}{X}\right) \tag{4}$$

$$K_{II} = \frac{P_{cr} sin45^o \sqrt{\pi a}}{Xt} y_{mII}\left(\frac{a}{X}\right) \tag{5}$$

$$K_{mix} = \sqrt{K_I^2 + K_{II}^2} \tag{6}$$

For Mode I/II, $y_{mI}\left(\frac{a}{X}\right)$ and $y_{mII}\left(\frac{a}{X}\right)$ are a function of geometric dimension factor values, crack length, crack angle (α), temperature, and deformation rate. The $y_{mI}\left(\frac{a}{X}\right)$ and $y_{mII}\left(\frac{a}{X}\right)$ geometrical factor value required to calculate the Mode I/II fracture toughness value was calculated by following the same procedure. The geometric factor values for the opening ($f_{mI}\left(\frac{a}{w}\right)$) and shearing ($f_{mII}\left(\frac{a}{w}\right)$) directions were calculated by substituting the obtained fracture toughness values in places of Eqs. 7-8, respectively [35,36].

$$f_{mI}\left(\frac{a}{w}\right) = \frac{(K_I)_{Num}.wt}{P.cos\alpha\sqrt{\pi a}} \tag{7}$$

$$f_{mII}\left(\frac{a}{w}\right) = \frac{(K_{II})_{Num}.wt}{P.sin\alpha\sqrt{\pi a}} \tag{8}$$

The geometric factors ($y_{mI}\left(\frac{a}{X}\right)$ and $y_{mII}\left(\frac{a}{X}\right)$)for the Mod I/II crack tip opening status were given in Table 3.

Table 3. Geometric factor values obtained from ANSYS finite element program for Mode I/II

Deformation Rate (s^{-1})	$y_{mI}\left(\frac{a}{X}\right)$				$y_{mII}\left(\frac{a}{X}\right)$			
	a=10 mm		a=15 mm		a=10 mm		a=15 mm	
	-20˚C	80˚C	-20˚C	80˚C	-20˚C	80˚C	-20˚C	80˚C
8.3×10^{-3}	1.4063	1.5344	1.8463	2.0208	0.7970	0.8949	1.0142	1.1512
8.3×10^{-4}	1.5020	1.6553	1.9847	2.2078	0.8653	0.9808	1.1152	1.2851
8.3×10^{-5}	1.5747	1.7523	2.0912	2.3509	0.9319	1.0708	1.2109	1.4145

As seen in Tables 2 and 3, the geometric factor value is affected by the mechanical properties of the material, ambient temperature, crack position and length, and deformation rate values. Geometric factor values are a concept that directly changes the fracture toughness and strain energy release rate studied experimentally. Therefore, when examining the fracture behavior of laminated composites, geometric dimension factor value should be calculated for each test parameter.

2.5. Determination of Strain Energy Release Rate

Another parameter used to express the elastic behavior of the crack tip is the strain energy release rate (G_C). The G_C value can also be expressed as the energy used up as the crack proceeds as much as a unit area. For the orthotropic material, in the plane stress state, in the warp direction and the weft direction, the value of strain energy release rate is calculated by Equation 9-10 [9,40,41].

$$G_{IC} = \frac{K_{IC}^2}{E_I} \tag{9}$$

$$G_{IIC} = \frac{K_{IIC}^2}{E_{II}} \tag{10}$$

The mixed-mode (Mode I/II) strain energy release rate (G_{mix}) is calculated using Equation 11. K_{Ic} and K_{IIc} toughness values are opening and sliding components of fracture toughness in the case of Mod I/II. For the S-2 glass/epoxy composite, E_I warp direction and E_{II} weft direction are the modulus of elasticity.

$$G_{mix} = G_{Ic} + G_{IIc} \tag{11}$$

Similar to the mixed fracture toughness formula, here G_{Ic} and G_{IIc} are components of the mixed-mode strain energy release rate value in the opening and shearing direction [42].

2.6. Finite Element Analyses

Using Ansys Workbench V19, different models were created for each experiment condition and finite element analysis was made, fracture toughness and J Integral data were calculated. In the finite element model, the same as in experimental studies, the geometric model fixed from the bottom side, and the tensile load was applied from the upper side. The models (Mod I and Mod I/II) were created using 6981 nodes and 3346 triangular elements. The mesh structure around the crack tip was rearranged so that the smallest element size was about 0.05 mm. The singularity of the stress/strain area was analyzed using single type elements around the first ring of the crack tip elements (Figure 3).

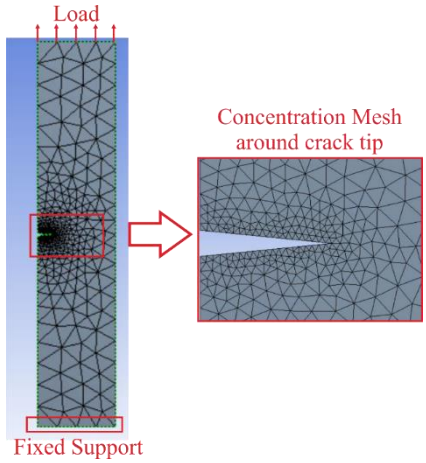

Fig. 3 Geometric model of single edge cracked specimens

Table 4. Mechanical properties of S-2 glass/epoxy laminated composite material in two temperature conditions

Temperature (°C)		-20°C			80°C		
Deformation rate (s^{-1})		8.3×10^{-3}	8.3×10^{-4}	8.3×10^{-5}	8.3×10^{-3}	8.3×10^{-4}	8.3×10^{-5}
Mechanical Properties	E_I (GPa)	18.59	18.58	18.62	16.18	16.29	16.34
	E_{II} (GPa)	19.53	19.68	21.19	15.41	15.66	17.24
	G (GPa)	2.08	2.57	3.20	1.32	1.67	2.05
	Y_T (MPa)	382.92	386.89	392.49	277.24	310.47	341.81
	X_T (MPa)	341.71	354.36	355.71	256.69	287.07	291.36
	Y_C (MPa)	299.69	305.14	311.56	192.90	219.16	244.64
	X_C (MPa)	287.67	301.65	316.69	185.27	216.71	264.91

Mechanical experiments were conducted according to ASTM D3039, ASTM D3410, and ASTM D3518M test standards to determine the mechanical behavior of S-2 glass/epoxy laminated composites under tensile, compression and shear loads, respectively. Weft direction elasticity module (E_l), warp direction elasticity module (E_{ll}), shear modulus (G), warp direction tensile strength (Y_t), weft direction tensile strength (X_t), warp direction compressive strength (Y_c) and weft direction compressive strength (X_c) was found. The determined mechanical properties were given in Table 4. In addition, Poisson ratios were assumed as v_{xy}=0.11, v_{yx}=0.18 and v_{yz}=0.18 [43,44].

In the finite element analysis, the numerical fracture toughness and J integral value at different temperatures and strain rates were calculated. J integral represents the amount of energy per unit opening at the crack tip of the composite material [40,45].

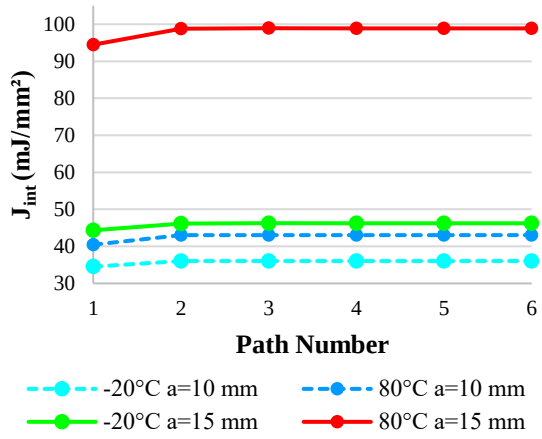

(a)

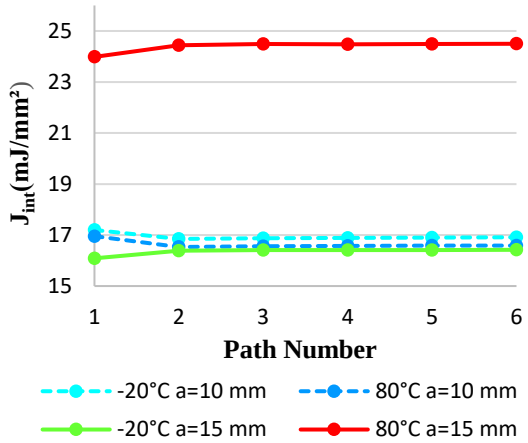

(b)

Fig. 4 J integral change from the crack tip (a) Mode I status and (b) Mode I/II status

During modeling, six paths were created in line with the crack tip onset direction starting from the crack tip. In Figure 4, J integral value changes of the samples, which were tested at different temperatures and 5mm/min deformation speed (8.3×10^{-4} s^{-1}), were given starting from the crack tip. Since a similar curve behavior occurs in other deformation rates, a single deformation rate is given. When the J integral change curves are given for the opening mode (Mode I) in Figure 4(a) are examined, it is seen that the J integral value of 15 mm crack length is higher. This is believed to be due to the increased energy absorption capacity of the polymer matrix, which becomes ductile with high temperatures.

In the case of mixed mode (Mode I/II) in Figure 4(b), the highest value of the J integral value is observed in the crack length of 15 mm and in the hottest experimental conditions. In other experimental conditions, J integral values very close to each other are seen. In the case of Mode I/II, S-2 glass/epoxy shows a more complex behavior. The reason for this situation is the effect of the energy released from the fibers in the direction of sliding while opening the crack mouth. For both crack tip opening mode conditions, when the J integral

value in each path is examined, as they move in the direction of the displacement vector increases a little and then follow a course close to the horizontal [46–48].

3.Results and Discussion

3.1. Fracture Toughness Results

In Figure 5, the load-displacement curves obtained from the fracture tests for Mod I and Mode I/II crack tip opening status were given. Test results have shown that the S-2 glass/epoxy laminated composite has a brittle fracture behavior in a cold environment. For two different crack opening status and 10 mm crack length, at -20˚C high tensile strength was obtained. When the crack length was 15 mm, it was more effective to brittleness at -20˚C. And according to the 80˚C temperature, the fracture occurred at much lower forces. The deformation ability of this material is higher at low temperatures in all deformation rates, crack length, and loading modes. Generally, under the same conditions, the fracture load (P_{cr}) in the Mode I/II crack tip opening status is higher than in the Mode I status. This is because, in the case of Mod I/II, the shearing effects force the crack mouth to open in different directions. A similar situation is seen in other studies [49,50].

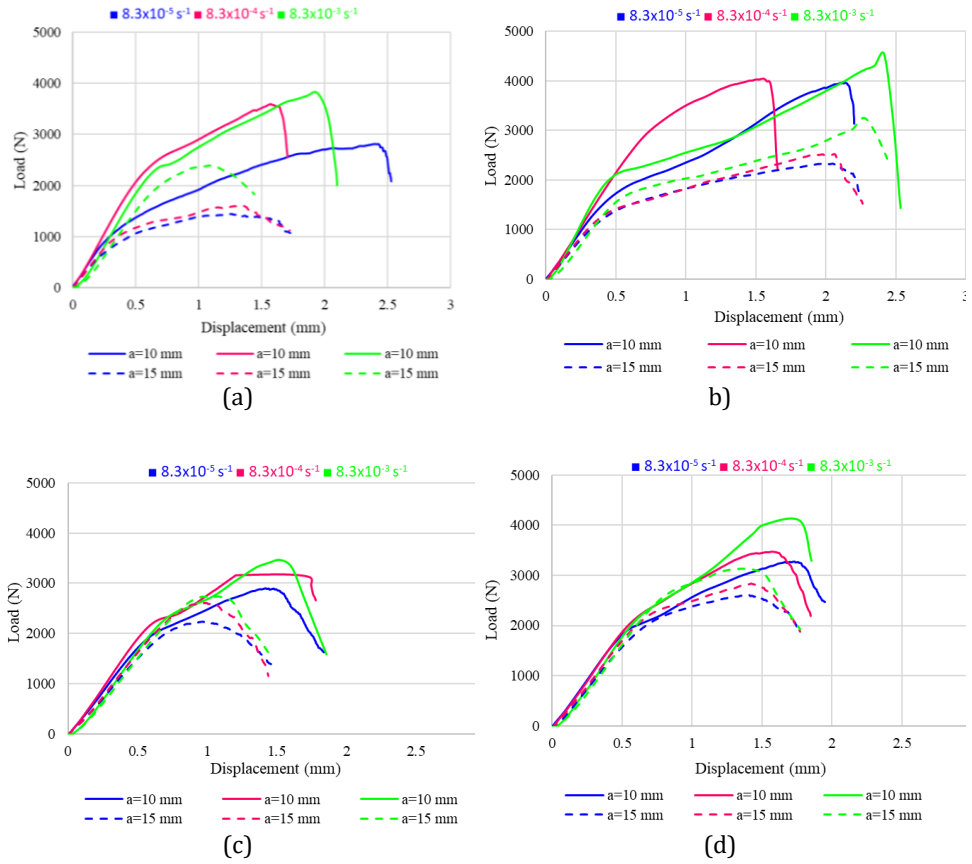

Fig. 5 Load-displacement curves, (a) Mode I at -20˚C, (b) Mode I/II at -20˚C, (c) Mode I at 80˚C and (d) Mode I/II at 80˚C

The fracture damage load, obtained from the load-displacement curve was used to calculate the toughness values obtained from the experimental and FEM analysis. Experimental and FEM fracture toughness values were compared for Mod I and Mod I/II crack tip opening in Table 5 and Table 6, respectively.

Table 5. Experimental and FEM fracture toughness values in Mode I opening case

Deformation Rate (s^{-1})	a=10 mm							
	-20˚C				80˚C			
	Standard deviation	$K_{IC(exp)}$ ($MPam^{1/2}$)	$K_{IC(num)}$ ($MPam^{1/2}$)	% Error	Standard deviation	$K_{IC(exp)}$ ($MPam^{1/2}$)	$K_{IC(num)}$ ($MPam^{1/2}$)	% Error
8.3×10^{-3}	27,6	851,77	858,53	0,8	25,7	879,54	884,31	0,5
8.3×10^{-4}	36,4	847,37	848,98	0,2	11,9	870,16	872,26	0,2
8.3×10^{-5}	25,9	825,54	828,77	0,4	40,9	859,85	866,45	0,8
Deformation Rate (s^{-1})	a=15 mm							
	-20˚C				80˚C			
	Standard deviation	$K_{IC(exp)}$ ($MPam^{1/2}$)	$K_{IC(num)}$ ($MPam^{1/2}$)	% Error	Standard deviation	$K_{IC(exp)}$ ($MPam^{1/2}$)	$K_{IC(num)}$ ($MPam^{1/2}$)	% Error
8.3×10^{-3}	24,1	991,59	963,47	2,8	25	1333,32	1351,7	1,4
8.3×10^{-4}	45,1	959,36	958,79	0,1	22,2	1332,53	1344	0,9
8.3×10^{-5}	117	956,63	957,63	0,1	54,7	1312,77	1320,9	0,6

The maximum experimental fracture toughness in Mode I was found to be 1333.32 $MPam^{1/2}$. This value was obtained from the parameters of 80˚C, 15 mm crack length, and 8.3×10^{-3} s^{-1} strain rate. The minimum experimental fracture toughness was found as 825.54 $MPam^{1/2}$ as a result of experiments at -20˚C temperature, in 10 mm crack length, and 8.3×10^{-5} s^{-1} strain rate. When crack length increased from 10mm to 15mm for the same strain rates a maximum increase of 14.1% was observed in Mod I fracture toughness at -20˚C. If the same compression was made for 80˚C temperature it seen that the increased value was at 34.69%. When the fracture toughness values were evaluated in terms of strain rate, there is a trend towards increasing the experimental fracture toughness value as the strain rate increases in both cold and hot temperatures. When the same temperature and the same crack lengths were evaluated, as a result of the experiments, while the strain rate increased from the lowest to the highest, the fracture toughness value increased by a maximum of 3.65%. When experimental and numerical fracture toughness is compared, there is a maximum difference of around 3% between the results.

Table 6. Experimental and FEM fracture toughness values in mixed mode (Mode I/II)

Deformation Rate (s^{-1})	a=10 mm							
	-20°C				80°C			
	Standard deviation	$K_{mix(exp)}$ ($MPam^{1/2}$)	$K_{mix(num)}$ ($MPam^{1/2}$)	% Error	Standard deviation	$K_{mix(exp)}$ ($MPam^{1/2}$)	$K_{mix(num)}$ ($MPam^{1/2}$)	% Error
8.3×10^{-3}	27.7	570.17	572.7	0.4	23.3	549.75	552	0.4
8.3×10^{-4}	27.6	567.17	572.69	1	12.5	536.5	540.28	0.7
8.3×10^{-5}	48.1	564.46	567.5	0.5	23.4	504.02	508.87	1
Deformation Rate (s^{-1})	a=15 mm							
	-20°C				80°C			
	Standard deviation	$K_{mix(exp)}$ ($MPam^{1/2}$)	$K_{mix(num)}$ ($MPam^{1/2}$)	% Error	Standard deviation	$K_{mix(exp)}$ ($MPam^{1/2}$)	$K_{mix(num)}$ ($MPam^{1/2}$)	% Error
8.3×10^{-3}	40.7	578.49	580.47	0.3	44.8	684.14	694.14	1.4
8.3×10^{-4}	21.3	569.62	574.4	0.8	24	668.47	675.54	1
8.3×10^{-5}	32.1	567.8	572.96	0.9	34.5	632.59	637.22	0.7

In the Mode I/II crack tip opening status, the crack is exposed simultaneously to both the opening and shearing effect. Therefore, the fracture toughness values are smaller than the Mod I status. Thus, the maximum fracture toughness value (684.14 $MPam^{1/2}$) was found under 80°C temperature, 15 mm crack length, and 8.3×10^{-3} s^{-1} deformation rate parameters. The Minimum fracture toughness (504.02 $MPam^{1/2}$) was found under 80°C temperature, 10 mm crack length, and at the 8.3×10^{-5} s^{-1} deformation rate. For samples, which were tested at -20°C and the same deformation rate, when the crack length increased from 10mm to 15mm, a maximum 1.43% increase in mixed-mode fracture toughness was observed. When a similar comparison was made for 80°C, this increase in fracture toughness was found to be 20.32%. In the case of Mode I/II, when the fracture toughness values were evaluated in terms of deformation rate, the fracture toughness increased by a maximum of 9.07% as the deformation rate increased for the same temperature. For Mode I/II, when the toughness values obtained from the experimental and FEM analysis were compared, a maximum difference of 1.4% was observed between them.

3.2. Fracture Energy Results

In linear elastic fracture mechanics, another parameter that expresses fracture is energy. The J integral value is equal to the potential energy release rate for a virtual crack extension at any point along the crack front [51]. The equivalent of the experimentally calculated strain energy release rate (G) value is the J integral value in the analysis of FEM [52]. The strain energy release rates and J integral values obtained by experimental and FEM method were given for Mode I in Table 7 and Mode I/II in Table 8.

The maximum strain energy release rate (109 mJ/mm^2) obtained experimentally in the case of Mod I was at 15 mm crack length, 80°C, and 8.3×10^{-4} s^{-1} deformation rate. The lowest strain energy release rate (36.66 mJ/mm^2) was found at -20°C temperature, 10 mm crack length, and the lowest deformation rate under experimental conditions. Suitable with

similar studies in the literature, the energy value is higher in the hot environment for the same deformation rate[23,53,54]. When the same deformation rate and temperatures are evaluated, the strain energy release rate depending on the two crack lengths varies by up to 26.22% at -20˚C temperature, while this change at 80˚C temperature is 57.35%. As the deformation rate increases in specimens tested under the same temperature and crack length, the energy value increased by a maximum of 7.27%. When experimental and FEM energy values are compared, the highest error percentage is around 13%.

Table 7. Comparison of strain energy release rate and J integral values for opening (Mode I) status.

Deformation Rate (s^{-1})	a=10 mm					
	-20˚C			80˚C		
	G_{IC} (mJ/mm^2)	J_{int} (mJ/mm^2)	% Error	G_{IC} (mJ/mm^2)	J_{int} (mJ/mm^2)	% Error
8.3×10^{-3}	38.96	38.38	1.5	47.34	45.29	4.3
8.3×10^{-4}	38.65	36.60	5.3	46.48	43.05	7.4
8.3×10^{-5}	36.66	34.57	5.7	45.70	41.43	9.3
Deformation Rate (s^{-1})	a=15 mm					
	-20˚C			80˚C		
	G_{IC} (mJ/mm^2)	J_{int} (mJ/mm^2)	% Error	G_{IC} (mJ/mm^2)	J_{int} (mJ/mm^2)	% Error
8.3×10^{-3}	52.81	47.78	9.5	108.80	103.35	5.0
8.3×10^{-4}	49.54	46.25	6.6	109.00	98.84	9.3
8.3×10^{-5}	49.23	44.95	8.7	106.51	92.67	13.0

Table 8. Comparison of strain energy release rate and J integral values for mixed-mode (Mode I/II) state

Deformation Rate (s^{-1})	a=10 mm					
	-20˚C			80˚C		
	$G_{IC\text{-}mix}$ (mJ/mm^2)	J_{int} (mJ/mm^2)	% Error	$G_{IC\text{-}mix}$ (mJ/mm^2)	J_{int} (mJ/mm^2)	% Error
8.3×10^{-3}	16.94	17.13	1.1	18.25	17.71	3.0
8.3×10^{-4}	17.07	16.91	0.9	17.85	16.59	7.1
8.3×10^{-5}	16.93	16.27	3.9	15.91	14.36	9.7
Deformation Rate (s^{-1})	a=15 mm					
	-20˚C			80˚C		
	$G_{IC\text{-}mix}$ (mJ/mm^2)	J_{int} (mJ/mm^2)	% Error	$G_{IC\text{-}mix}$ (mJ/mm^2)	J_{int} (mJ/mm^2)	% Error
8.3×10^{-3}	17.47	17.25	1.3	28.28	26.90	4.9
8.3×10^{-4}	17.23	16.42	4.7	27.71	24.50	11.6
8.3×10^{-5}	17.13	15.83	7.6	25.06	21.01	16.2

In the Mode I/II, the maximum strain energy release rate was observed as 28.28 mJ/mm^2. This value was obtained in a hot environment (80˚C), the highest deformation rate (8.3×10^{-3} s^{-1}) and 15 mm crack length tests. The minimum strain energy release rate was found to be 15.91 mJ/mm^2 in experiments where the crack length was 10 mm under hot conditions and the lowest deformation rate. For tests performed at the same temperature and the same crack length, the energy value increased up to a maximum rate of 14.7% as the deformation rate increased. When the crack length increased from 10 mm to 15 mm at the

same temperature and the same deformation rate, the strain energy release rate maximum increased up to 3.03% at -20˚C and 36.52% at 80˚C. In the case of Mode I/II, when comparing the energy values in experimental and FEM analyses, there is a maximum of 16.2% difference between them.

4. Conclusions

The effect of crack length, temperature and deformation rate on fracture behavior in S-2 glass/epoxy laminated composite plates have been investigated experimentally and numerically. The results of this study, which examined the changes in fracture toughness and fracture energy values to crack tip opening status of Mode I and Mode I/II, can be summarized as follows.

- Mode I is the most sensitive opening mode for two crack lengths with a 50% difference between them. The change in crack length, especially at 80˚C temperature, is seriously felt in fracture toughness and energy values.
- For both Mode I and Mode I/II, fracture toughness is also seen to increase with the increase of deformation rate. Change in deformation rate at 80°C temperature in Mod I/II state is more effective than in Mod I state.
- S-2 glass/epoxy laminated composite structure is brittle in a cold environment and more ductile in a hot environment has a structure. It shows higher fracture toughness at 80˚C due to its ductile structure. In Mod I there is a maximum 59% fracture toughness difference between the two temperatures.
- In Mode I/II, the fracture toughness varied at most by 19.98% between the cold and hot temperature values. Indicates that a 45˚ angle crack on S-2 glass/epoxy laminated composite to be used in cold and hot environments will be less affected by the change in temperature, crack length, and deformation rates.
- For the same temperature and crack length parameters, the strain energy release rate increases as the deformation rate increases. This trend applies to both Mod I and Mod I/II.
- As the temperature increases, the ductile material releases more energy. In Mode I, when the ambient temperature reaches from -20˚C to 80˚C, the energy release rate value increases (maximum 190.53%). This also applies to Mod I/II, although there is less variation (maximum 66.94%).
- As a result of experiments, where crack length, temperature, and deformation rates are the same, the fracture toughness obtained of the Mode I is a maximum of 107.52% greater than the fracture toughness in the Mode I/II status. This ratio is 325.02% in terms of the strain energy release rate. These differences were found at 80˚C experimental conditions. This result shows that the cracked S-2 glass/epoxy laminated composite structure is more sensitive to both Mode I opening mode and temperature.
- S-2 glass fiber reinforcement material is a type of material used especially in the aviation industry and also in outdoor environments. Experimentally and numerically, this study examined the S-2 glass/epoxy laminated composite structure at two different temperatures, such as -20˚C (for example, a cold climate zone winter temperature) and 80˚C (for example, the conservation box of a heat source machine). If this material has different crack lengths and fracture modes, this study can be used as a reference source to predict fracture damage mechanisms by loaded with different deformation rates.

Acknowledgment

This study was supported by Usak University Scientific Research Agency. Project Number: 2018/MF003 scientific research project.

References

[1] Yin S, Gong Y, Li W, Zhao L, Zhang J, Hu N. A novel four-linear cohesive law for the delamination simulation in composite DCB laminates. Compos Part B Eng 2020;180:107526. https://doi.org/10.1016/j.compositesb.2019.107526

[2] Healey R, Chowdhury NM, Chiu WK, Wang J. Experimental and numerical determination of mode II fracture toughness of woven composites verified through unidirectional composite test data. Polym Polym Compos 2019;27:557-66. https://doi.org/10.1177/0967391119853736

[3] Loutas T, Tsokanas P, Kostopoulos V, Nijhuis P, van den Brink WM. Mode I fracture toughness of asymmetric metal-composite adhesive joints. Mater Today Proc 2020. https://doi.org/10.1016/j.matpr.2020.03.075

[4] Andric P, Curtin WA. Atomistic modeling of fracture. Model Simul Mater Sci Eng 2019;27:013001. https://doi.org/10.1088/1361-651X/aae40c

[5] Bosbach B, Ohle C, Fiedler B. Structural health monitoring of fibre metal laminates under mode I and II loading. Compos Part A Appl Sci Manuf 2018;107:471-8. https://doi.org/10.1016/j.compositesa.2018.01.008

[6] Kaushik V, Ghosh A. Experimental and numerical characterization of Mode I fracture in unidirectional CFRP laminated composite using XIGA-CZM approach. Eng Fract Mech 2019;211:221-43. https://doi.org/10.1016/j.engfracmech.2019.01.038

[7] Insausti N, Adarraga I, De Gracia J, Arrese A, Mujika F. Numerical assessment of an experimental procedure applied to DCB tests. Polym Test 2020;82:106288. https://doi.org/10.1016/j.polymertesting.2019.106288

[8] Mousavi A, Aliha MRM, Imani DM. Effects of biocompatible Nanofillers on mixed-mode I and II fracture toughness of PMMA base dentures. J Mech Behav Biomed Mater 2020;103:103566. https://doi.org/10.1016/j.jmbbm.2019.103566

[9] Aliha MRM, Mousavi SS. Sub-sized short bend beam configuration for the study of mixed-mode fracture. Eng Fract Mech 2020;225:106830. https://doi.org/10.1016/j.engfracmech.2019.106830

[10] Kaynan O, Atescan Y, Ozden-Yenigun E, Cebeci H. Mixed Mode delamination in carbon nanotube/nanofiber interlayered composites. Compos Part B Eng 2018;154:186-94. https://doi.org/10.1016/j.compositesb.2018.07.032

[11] Li JG, Liu PF, Chu JK. Finite Element Analysis of Delamination Behaviors of Composite Laminates under Hygrothermal Environment Using Virtual Crack Closure Technique. J Fail Anal Prev 2019;19:147-53. https://doi.org/10.1007/s11668-019-00582-5

[12] Ravindran AR, Ladani RB, Wang CH, Mouritz AP. Synergistic mode II delamination toughening of composites using multi-scale carbon-based reinforcements. Compos Part A Appl Sci Manuf 2019;117:103-15. https://doi.org/10.1016/j.compositesa.2018.11.011

[13] Shahani AR, Abolfathitabar R, Shooshtar H. On the validity of LEFM methods to investigate the fracture behavior of angle-ply laminates. Compos Part B Eng 2019;160:249-53. https://doi.org/10.1016/j.compositesb.2018.10.013

[14] Torabi AR, Rahimi AS, Ayatollahi MR. Mixed mode I/II fracture prediction of blunt V-notched nanocomposite specimens with nonlinear behavior by means of the Equivalent Material Concept. Compos Part B Eng 2018;154:363-73. https://doi.org/10.1016/j.compositesb.2018.09.025

[15] Torabi AR, Majidi HR, Cicero S, Ibáñez-Gutiérrez FT, Fuentes JD. Experimental verification of the Fictitious Material Concept for tensile fracture in short glass fibre

reinforced polyamide 6 notched specimens with variable moisture. Eng Fract Mech 2019;212:95-105. https://doi.org/10.1016/j.engfracmech.2019.03.026
[16] Duin V, Pinheiro DC, Hyun M. Josefson, Lennart; van Duin, Stephen; de Carvalho Pinheiro, Bianca; Yang, Nana; Luo, Yu; Zamarin, Albert; Remes, Heikki; Roland, Frank; Gaiotti, Marco; Naoki , Osawa; Horn, Agnes M.; Kim, Myung Hyun; Mishra, Brajendra Committee V.3: Materials and fabricat. 2018. https://doi.org/10.3233/978-1-61499-864-8-143
[17] Brunner AJ. Fracture mechanics of polymer composites in aerospace applications. Elsevier Ltd; 2020. https://doi.org/10.1016/B978-0-08-102679-3.00008-3
[18] Foyouzat A, Bayesteh H, Mohammadi S. A brittle to ductile phase transition fracture analysis of shape memory polymers. Eng Fract Mech 2020;224:106751. https://doi.org/10.1016/j.engfracmech.2019.106751
[19] Farshidi A, Berggreen C, Carlsson LA. Low temperature mixed-mode debond fracture and fatigue characterisation of foam core sandwich. J Sandw Struct Mater 2018. https://doi.org/10.1177/1099636218779420
[20] Fakhri M, Haghighat Kharrazi E, Aliha MRM. Mixed mode tensile - In plane shear fracture energy determination for hot mix asphalt mixtures under intermediate temperature conditions. Eng Fract Mech 2018;192:98-113. https://doi.org/10.1016/j.engfracmech.2018.02.007
[21] Khashaba UA, Othman R, Najjar IMR. Development and characterization of structural adhesives for aerospace industry with alumina nanoparticles under shear and thermo-mechanical impact loads. Proc Inst Mech Eng Part G J Aerosp Eng 2020;234:490-507. https://doi.org/10.1177/0954410019875557
[22] Pan Z, Wu X, Wu L. Temperature rise caused by adiabatic shear failure in 3D braided composite tube subjected to axial impact compression. J Compos Mater 2019. https://doi.org/10.1177/0021998319877558
[23] Pini T, Briatico-Vangosa F, Frassine R, Rink M. Matrix toughness transfer and fibre bridging laws in acrylic resin based CF composites. Eng Fract Mech 2018;203:115-25. https://doi.org/10.1016/j.engfracmech.2018.03.026
[24] Rahmani A, Choupani N, Kurtaran H. Thermo-fracture analysis of composite-aluminum bonded joints at low temperatures: Experimental and numerical analyses. Int J Adhes Adhes 2019;95:102422. https://doi.org/10.1016/j.ijadhadh.2019.102422
[25] Aktas M, Balcioglu HE, Külahli G. Strain rate effects on tensile and compressive behaviour of woven-knitting glass/epoxy composites. Adv Compos Lett 2013;22:13-9. https://doi.org/10.1177/096369351302200103
[26] Jia Z, Yuan G, Hui D, Feng X, Zou Y. Effect of high loading rate and low temperature on mode I fracture toughness of ductile polyurethane adhesive. J Adhes Sci Technol 2019;33:79-92. https://doi.org/10.1080/01694243.2018.1546364
[27] AZO Materials. S-Glass Fibre 2001:1-3. https://www.azom.com/properties.aspx?ArticleID=769 (accessed July 23, 2019).
[28] HEXION® Specialty Chemicals. Laminating Resin MGS® L 285 Hardeners MGS® 285-287 Technical Data Sheet n.d. https://www.hexion.com/en-US/search?id=30303 (accessed July 23, 2019).
[29] Chabchoub M, Vieille B, Moutou Pitti R. Numerical estimation of the mode I strain energy release rate in woven-ply thermoplastic-based composites at high temperature based on G θ method. Theor Appl Fract Mech 2019;101:169-77. https://doi.org/10.1016/j.tafmec.2019.02.018
[30] Satyanarayana A, Gattu M. Effect of displacement loading rates on mode-I fracture toughness of fiber glass-epoxy composite laminates. Eng Fract Mech 2019;218:106535. https://doi.org/10.1016/j.engfracmech.2019.106535
[31] Siddique A, Abid S, Shafiq F, Nawab Y, Wang H, Shi B, et al. Mode I fracture toughness of fiber-reinforced polymer composites: A review. J Ind Text 2019. https://doi.org/10.1177/1528083719858767

[32] Torabi AR, Pirhadi E. Failure analysis of round-tip V-notched laminated composite plates under mixed mode I/II loading. Theor Appl Fract Mech 2019;104:102342. https://doi.org/10.1016/j.tafmec.2019.102342
[33] Vieille B, Gonzalez JD, Bouvet C. Fracture mechan ics of hybrid composites with ductile matrix and brittle fibers: Influence of temperature and constraint effect. J Compos Mater 2019;53:1361-76. https://doi.org/10.1177/0021998318802613
[34] Jamali J, Fan Y, Wood JT. The mixed-mode fracture behavior of epoxy by the compact tension shear test. Int J Adhes Adhes 2015;63:79-86. https://doi.org/10.1016/j.ijadhadh.2015.08.006
[35] Choupani N. Experimental and numerical investigation of the mixed-mode delamination in Arcan laminated specimens. Mater Sci Eng A 2008;478:229-42. https://doi.org/10.1016/j.msea.2007.05.103
[36] Aliha MRM, Shaker S, Keymanesh MR. Low temperature fracture toughness study for bitumen under mixed mode I + II loading condition. Eng Fract Mech 2019;206:297-309. https://doi.org/10.1016/j.engfracmech.2018.11.037
[37] Kaman MO. Stress Intensity Factor Analysis of Antisymmetrically Carbon / Epoxy Laminated Composite Plates with Different. Turkish J Sci Technol 2011;6:61-74.
[38] Kaman MO. Effect of fiber orientation on fracture toughness of laminated composite plates [0°/θ°]s. Eng Fract Mech 2011;78:2521-34. https://doi.org/10.1016/j.engfracmech.2011.06.005
[39] Arasan Ş, Aktaş M, Balcıoğlu HE. Fracture toughness of woven glass and carbon reinforced hybrid and non-hybrid composite plates. Polym Compos 2018;39:783-93. https://doi.org/10.1002/pc.23999
[40] Fu, Shao-Yun_ Lauke, Bernd_ Mai Y-W. Science and engineering of short fibre-reinforced polymer composites (2019, WP). Matthew Deans; 2019. https://doi.org/10.1016/B978-0-08-102623-6.00005-6
[41] Hossein Abadi R, Refah Torun A, Mohammadali Zadeh Fard A, Choupani N. Fracture characteristics of mixed-mode toughness of dissimilar adherends (cohesive and interfacial fracture). J Adhes Sci Technol 2020;34:599-615. https://doi.org/10.1080/01694243.2019.1674102
[42] Balcioglu HE, Yalcin D. The Determination of Fracture Characterization of Knitted Fabric Reinforced Composites Using Arcan Test. Fibers Polym 2020;21:849-63. https://doi.org/10.1007/s12221-020-9619-z
[43] Manzella AF, Gama BA, Gillespie JW. Effect of punch and specimen dimensions on the confined compression behavior of S-2 glass/epoxy composites. Compos Struct 2011;93:1726-37. https://doi.org/10.1016/j.compstruct.2010.11.006
[44] Kaya Z, Ersen H, Halit B. The strain rate and temperature effects on the static and dynamic properties of S2 glass / epoxy composites. Appl Phys A 2020;126:1-15. https://doi.org/10.1007/s00339-020-03855-1
[45] Albiter NL. On the fracture behavior of ductile polymer films : notch quality, essential work of fracture, J-integral, and crack tip opening displacement. Universitat Politècnica de Catalunya-BarcelonaTech, 2018. https://doi.org/10.1016/j.engfracmech.2017.01.019
[46] Kim JH, Paulino GH. Mixed-mode J-integral formulation and implementation using graded elements for fracture analysis of nonhomogeneous orthotropic materials. Mech Mater 2003;35:107-28. https://doi.org/10.1016/S0167-6636(02)00159-X
[47] Zou G, Chen H. Path-dependent J-integrals under mixed-mode loads of mode I and mode II. Theor Appl Fract Mech 2018;96:380-6. https://doi.org/10.1016/j.tafmec.2018.05.014
[48] Balcıoğlu HE. Fracture Behaviors of SiC Particle Filled and Jute Fiber Reinforced Natural Composites. J Nat Fibers 2020;00:1-18. https://doi.org/10.1080/15440478.2020.1811186

[49] Rocha AVM, Akhavan-Safar A, Carbas R, Marques EAS, Goyal R, El-zein M, et al. Fatigue crack growth analysis of different adhesive systems: Effects of mode mixity and load level. Fatigue Fract Eng Mater Struct 2020;43:330-41. https://doi.org/10.1111/ffe.13145

[50] Zeinedini A. A novel fixture for mixed mode I/II/III fracture testing of brittle materials. Fatigue Fract Eng Mater Struct 2019;42:838-53. https://doi.org/10.1111/ffe.12955

[51] Hein J, Kuna M. A generalized J-integral for thermal shock analyses of 3D surface cracks in spatially and temperature dependent materials. Theor Appl Fract Mech 2017;92:318-30. https://doi.org/10.1016/j.tafmec.2017.04.013

[52] Vieille B, Chabchoub M, Gautrelet C. Influence of matrix ductility and toughness on strain energy release rate and failure behavior of woven-ply reinforced thermoplastic structures at high temperature. Compos Part B Eng 2018;132:125-40. https://doi.org/10.1016/j.compositesb.2017.08.011

[53] Coronado P, Viña JA, Argüelles A, Sánchez S. Fractographic Analysis of the Temperature Influence in the Mode I Fatigue Delamination of Carbon/Epoxy Composites. Proceedings 2018;2:1477. https://doi.org/10.3390/proceedings2231477

[54] Sales R de CM, Gusmão SR, Gouvêa RF, Chu T, Marlet JMF, Cândido GM, et al. The temperature effects on the fracture toughness of carbon fiber/RTM-6 laminates processed by VARTM. J Compos Mater 2017;51:1729-41. https://doi.org/10.1177/0021998316679499

Research on Engineering Structures & Materials
journal homepage: http://jresm.org
Research Group

Research Article

Influence of interventions on the seismic performance of URM buildings designed according to pre-modern codes

Neritan Shkodrani [1, a], Huseyin Bilgin*[2, b], Marjo Hysenlliu [1, c]

[1]*Department of Civil Engineering, Polytechnic University of Tirana, Albania*
[2]*Department of Civil Engineering, EPOKA University, Tirana, Albania*

Article Info

Article history:
Received: 31 May 2020
Revised: 20 Apr 2021
Accepted: 16 May 2021

Keywords:

URM buildings;
Pushover analysis;
2019 Albania Earthquake;
Template projects.

Abstract

On November 26,2019, an earthquake of magnitude 6.4 hit Durres city, Albania. After the earthquake, the inspection carried out by the authors in the region has provided relevant findings regarding the methods of construction, quality of the materials and the performance of structures. The dominant building types in the Albanian building stock comprise unreinforced masonry (URM) structures with load-bearing masonry walls. These units suffered the worst damage. Dynamic response of masonry is highly nonlinear, and generally shows high vulnerability to seismic loading. Moreover, many buildings of these type have undergone structural interventions like adding floors, or wall openings, especially in the first floors of the buildings, which are parallel to the main roads, because of great demand for shops and stores. This paper aims at making seismic performance assessment of the intervened buildings based on macro-element modeling approach. Due to its efficiency, this approach is becoming popular among the practitioners and field experts in this area and allows simulating the non-linear behavior of masonry buildings. This method is applied to two old masonry buildings from the Albanian construction practice that are representatives of mid-size residential buildings with and without interventions. It must be said that in Albania, masonry buildings have been built using templates all over the country, so both models with and without intervention are common. Capacity curves of the investigated buildings are derived to assess the most probable seismic response of the investigated housing construction in the region as well as to evaluate the seismic performance of the tested structures.

1. Introduction

The recent seismic activities that affected many areas of Albania in 2019 clearly showed how much attention should be taken of existing masonry building stock and its preservation. Evaluating the earthquake damage potential of a masonry building may be a challenging task to achieve, considering how peculiar these structures are, necessitating advanced and computationally rigorous numerical models to have an accurate estimation of their dynamical behavior to seismic actions. Recent Albanian earthquakes (Durres 2019 Seismic sequences) caused irreparable damages to many masonry structures all over the country [1-2].

Understanding the historical earthquake activity of any place is essential to recognize the possibility that an earthquake can affect the territory again and to consider the extent of possible damage. While the second is a function of the vulnerability, the first warns us of the main hazard.

*Corresponding author: hbilgin@epoka.edu.al
[a] orcid.org/0000-0002-8638-9664; [b] orcid.org/0000-0002-5261-3939; [c] orcid.org/0000-0002-0863-2112
DOI: http://dx.doi.org/10.17515/resm2020.197ea0331

Throughout the history, earthquakes in Albania, like in many earthquake-prone countries in the region, have seriously affected built environment causing numerous human casualties and economic loses [3-9]. In this regard, buildings' vulnerability is a key concept to focus on to mitigate the consequences of seismic events. Generally, URM buildings present a poorer seismic performance as compared to reinforced concrete buildings due to the low ductility, strength, and rigidity of their inherent components. Consequently, modern seismic guidelines include recommendations and commentaries aimed at reducing their seismic vulnerability. However, a significant part of existing masonry building stock has been built per pre-modern codes, thus considering unrestrictive conditions [10-11].

The dominant building types in the Albanian territory consist of URM structures with load-bearing masonry walls and buildings with RC framing system and infill baked clay and/or concrete walls. Most of them have been designed according to the KTPs–Albanian Technical Codes, which were first issued and implemented as a legal provision in 1963 and last amended in 1989 and still in force. Majority of the existing masonry buildings in the country, like in many other European countries were designed considering earlier seismic codes [12-14]. Nevertheless, its compliance requirements were not as explicit as those established by recent modern seismic codes like Eurocode 6 [15] and Eurocode 8 [16] from European practice. This led to a lack of seismic considerations in building's design process.

The URM structures with the load-bearing masonry walls suffered the most by the November 26, 2019 Durrës Earthquake sequences due to reasons including poor quality of construction, aging, climatological effects, poor workmanship, interventions made by people, the design code of the time, lack of preservation and insufficient repair after former damaging seismic events. URM buildings suffered not only non-structural but also structural damage including partial or total collapse of the load-bearing masonry walls.

The seismic response of masonry buildings is affected by the presence of openings on the load bearing walls. Even though most of the existing masonry buildings satisfy the regularity criteria according to seismic regulations, they may have structural systems composed of irregular walls with openings. Such irregularities can arise from the lack of conceptual seismic design or even due to the creation / closure of openings influenced by architectural or structural reasons. These geometric irregularities can significantly affect the earthquake response of masonry walls by causing not only a nonuniform distribution of gravity loads on masonry panels but also a concentration of displacement demands in some parts of the walls. In Albania, many URM buildings have undergone structural interventions like adding floors, or wall openings, especially in the first floors of the buildings, which are parallel to the main roads, because of great demand for shops and stores. The seismic response of such masonry buildings can only be effectively modeled with a good knowledge of the inelastic response of individual walls with openings.

This study aims at investigating the influence of wall openings on the first floor of the selected URM buildings. In order to make a comparative assessment, two URM buildings with and without interventions, having the same initial architectural and structural design were selected and modelled by using the TREMURI [17]. Structural features such as member dimensions, material types and loading conditions of the buildings were determined from their architectural and structural designs projects and field investigations on investigated buildings. Mechanical features were determined experimentally and adopted for mathematical modeling. Pushover analyses have been deployed to obtain the seismic capacities, the performance points and the damage level states according to Eurocode 8 by using 3Muri software package [17].

2. Seismicity of Albanian Territory

Balkan neighborhood is in a complicated seismotectonic region and prone to earthquakes. A high frequency of earthquakes has been experienced, resulting in loss of life and property destruction in the region [18-19]. Faulting zones in Eastern part of the Albania are typically defined by the influence of normal faults [20]. The western fault regions are characterized by reverse faulting– at the range of 40-50% extending along the coastal shore, while the appearance of strike-slip faults is in range of 15% of whole tectonic activity. The influence of normal faulting style ranges from 30-40% in this case very close to the major directivity of trust-fault type.

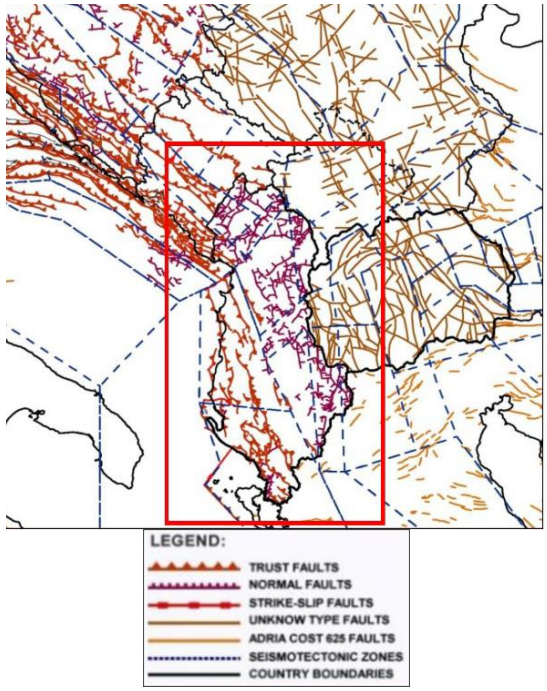

Fig. 1 Types of faults affecting the region [20]

Two transverse and three longitudinal active fault zones are evidenced into the Albanian orogen (Fig. 1). It has been concluded that the major seismic activity is located along the following seismic belts [21]:

- The NW up to nearly NNW trending Ionian-Adriatic thrust fault zone,
- The NW trending Shkodra-Mati-Librazhd graben fault zone,
- The N-S trending Peshkopi-Korça graben fault zone,
- The NE trending Shkodra-Tropoja normal fault zone,
- The NE trending Elbasan-Dibra normal fault zone.

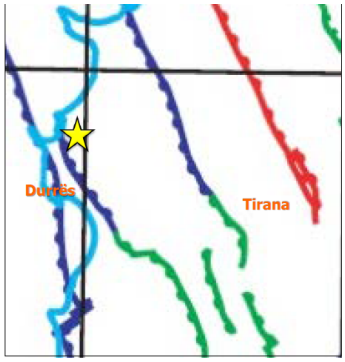

Fig. 2 Active fault zones and faults of the November 26, 2019 affected area

The 2019 earthquake affected area is dominated by NW-SE striking reverse active faults. Blue lines correspond to faults triggered during Middle Pleistocene-Holocene, the green lines to faults triggered during Pliocene-Lower Pleistocene and the red lines to faults activated during Pre-Pliocene period (Fig. 2). The star corresponds to the epicenter of the Mw 6.4 Durrës earthquake occurred on November 26, 2019.

2.1 November 26, 2019 Earthquake and Seismic Hazard Maps of Albania

An earthquake hit the central western part of Albanian territory on November 26, 2019. It was evaluated as Mw 6.4 (Fig. 3). Its focal depth was about 10 km [USGS, 2019]. According to the several seismological institutes and observations, the main shock was caused by the activation of a NW-SE striking reverse fault. The main shock was felt in the neighboring countries.

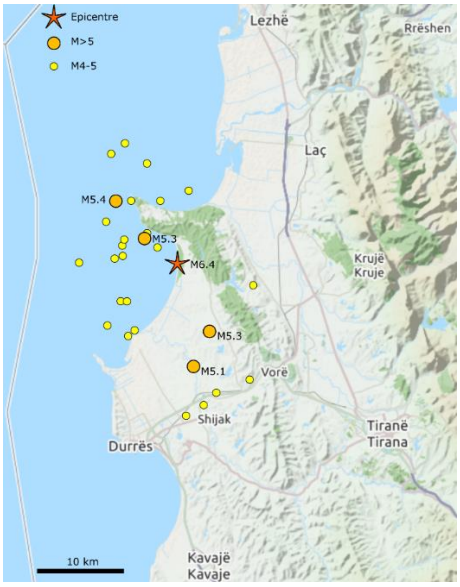

Fig. 3 The epicenter and location of aftershocks in the first month of the 26 November 2019 earthquake

The main shock and the aftershocks caused damage to buildings of Durrës, Tirana and several settlements of the wider area. Building damage was distributed along an elliptical

region (Fig. 4). This area coincides with the strike of the seismogenic fault as it is derived from the fault plane solutions provided by several seismological institutes and observatories [INGV, 2019 and USGS, 2019]. This area could be characterized as macroseismic epicenters as the result of the interaction between the seismotectonic setting and the local soil conditions and as the result of several reflections, refractions, directivity phenomena of seismic waves and resonance resulting in destruction in the earthquake-affected regions.

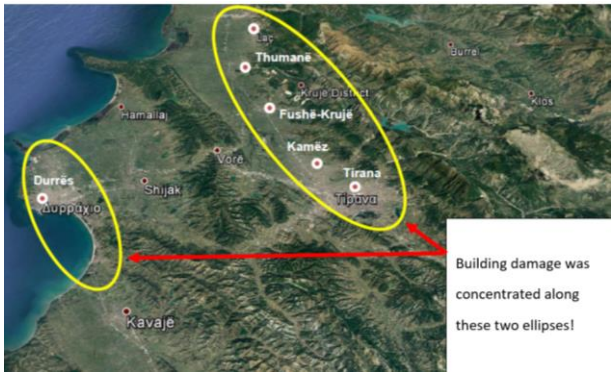

Fig. 4 Earthquake-affected region of 2019 Durres (Albania) earthquake

Based on the seismic map of Albania, published by Ministry of Construction (1989), it can be observed that the resulted intensities from this earthquake, are within the boundaries suggested in the Seismic Zonation Map (Fig. 5)

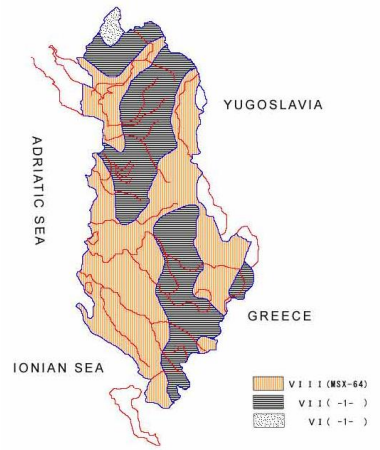

Fig. 5 Seismic intensity zonation map of Albania [22]

3. Description of the Case Study Buildings

Masonry building stock in Albania are mostly composed of template designs of low to mid-rise buildings. The structure is principally comprised of stiff walls with several openings and the diaphragms constructed by RC slabs. For the scope of this study, a typified URM mid-rise building is selected as a representative in the region. The masonry building, which has been analyzed, has five stories in its original design. However, by time due to the

demand in line with the increment in population and needs for several purposes, this template has been modified by opening some new spaces on the ground floor keeping the architectural features same above this floor.

The main dimensions of the load bearing system of the building blocks were determined with in-situ site investigations. Analyses was carried out according to the prepared load bearing system dimensions. Since the buildings under investigation are old ones, limited number of architectural drawings or details of the initial conditions of the building were reached. Therefore, a detailed inspection of the existing structures was extracted. In these plans, the location and dimensions of the walls, windows and doors were determined. Based on the measurements obtained, structural floor plans of the existing structures were prepared, and structural models were developed accordingly for seismic analysis.

This template is of year 1972, referred as 72/1 in the manual of Albanian Construction Institute. This building has plan dimensions of (18.32x12.43) m. It has 5 story high with 285cm height for each story. The load bearing walls are built with clay bricks M75 (strength 7.5 MPa). The mortar is M25 of strength 2.5MPa. The wall thickness is 38cm in the first and second floor, then 25cm on the remaining. The partition walls are with hollow clay bricks. The concrete corner columns and slabs are constructed with M150 concrete. There are two buildings of this template, 5 floors each but in one intervention is done on the first floor (Fig. 6-7). In one side of the first story, walls are replaced with reinforced concrete frames, with 5 openings as shown (Fig. 7). Columns are of reinforced concrete C20/25 with dimensions of (40x40) cm2 and steel reinforcement B400 with $A_s = A'_s = 12.56\ cm^2$ and stirrups φ8 every 15 cm. Beams are also of reinforced concrete C20/25 with dimensions of (30x50) cm2 and steel reinforcement B400 with $A_s = A'_s = 3.14 cm^2$ and stirrups φ8 every 20cm.

In order to characterize the strength and structural integrity of the structure, mechanical characteristics of the masonry material are assessed from the experimental tests. It consists of strength tests on brick units and mortar samples, as well as tests on small masonry assemblages, such as compression and shear tests on triplets. The clay bricks were tested in compression according to EN 772-1 (2000) [23]. The flexural and compressive strength of the mortar were defined according to the prescriptions of EN 1015-11 [24]. These tests allowed the determination of the compressive strength of masonry (f_m). Specimens of masonry were also subjected to the shear test for the determination of the initial shear strength (f_{v0}) and the friction coefficient (μ), according to the guidelines given by EN 1052-3 [25]. According to the test results, clay bricks and the mortar inherent characteristics are given as follows:

Brick tests: $f_b = 7.3MPa$ $f_{bt} = 1.9MPa$ $\rho_b = 1705\ kg/m^3$

Mortar tests: $f_m = 2.4MPa$ $f_{mt} = 0.62MPa$

Masonry tests: $f_k = 1.97\ MPa$ $f_{vk} = 0.35$ $f_{vk0} = 0.18$

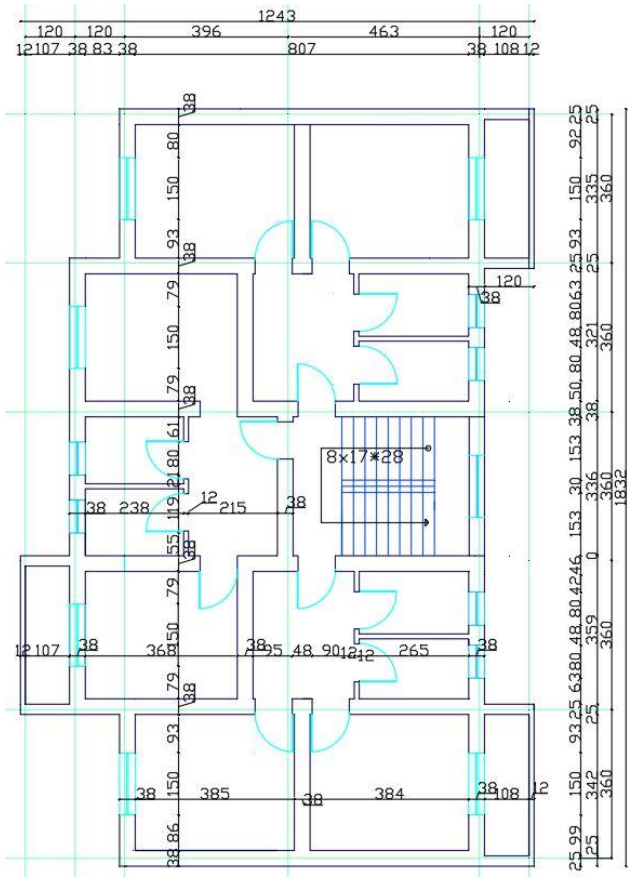

Fig. 6 Typical plan view of the selected masonry building before intervention

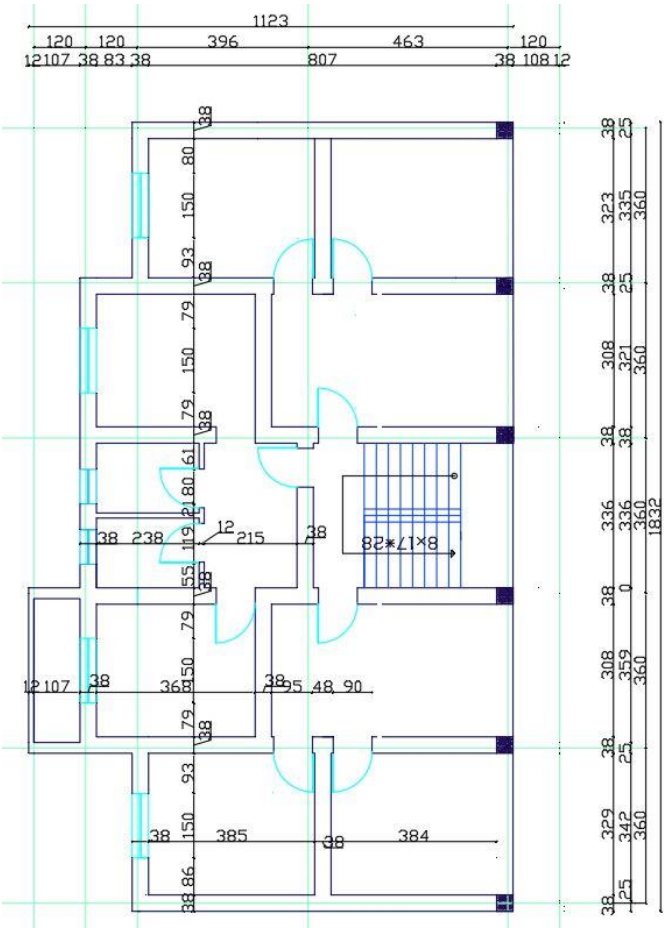

Fig. 7 Typical plan view of the selected masonry building after intervention in the 1st story

3. Mathematical Modeling

Masonry bricks units and the mortar are the two main units of the masonry structures. Mechanical properties of this heterogeneous materials depend on the inherent characteristics of its constituents. Its behavior can be quite complex under simple static loadings. To simulate the response of URM structures, numerous theories are developed, and numerical models are proposed in the literature [26]. The adopted model in this paper is macro-modelling approach. In this approach, each wall is characterized by discretized components that have the same properties. TREMURI [17] is used to perform the numerical analysis. The nonlinear macro-element method, suggested by Gambarotta and Lagomarsino [27], allows with a partial number of degrees of freedom, to characterize the two main in-plane failure modes, shear-sliding and bending-rocking mechanisms.

The conventional macro-element used for nonlinear static analyses is sketched with the kinematic model depicted in Fig. 8a. The 3D model of the examined masonry buildings, where it is apparent that masonry walls are modelled through a mesh of masonry piers and spandrels, is depicted in Fig. 8b.

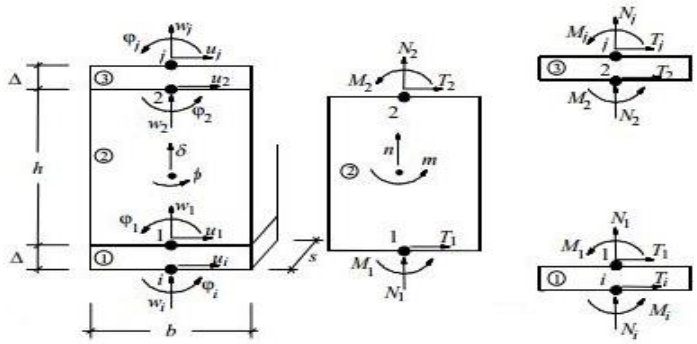

(a)

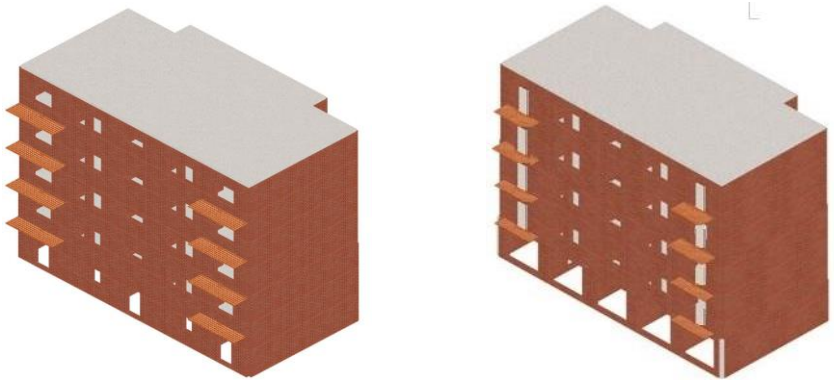

(b)

Fig. 8 a) The macro-element kinematic model; b) the 3D building model with (right) and without (left) interventions setup through the TREMURI software.

Seismic capacity of both buildings is obtained by nonlinear static analyses.

5. Results

5.1 Dynamic Characteristics

The modal analysis was performed for both building models and the results were presented for first three modes of vibrations. The results of the linear modal dynamic analyses were synthesized in Table 1.

Table 1. Modal Analyses results for the first 3 modes of vibration

Building Type	Mode	Period (sec)	M_x (%)	M_y (%)	M_z (%)
Original Building	1	0.244	0.01	72.74	0.03
	2	0.230	75.60	0.01	0.00
	3	0.190	0.41	0.05	0.00
Building with intervention	1	0.235	76.92	1.62	0.00
	2	0.223	1.83	70.57	0.07
	3	0.190	0.71	0.06	0.00

5.1 Seismic Capacity Assessment

There are several useful structural analysis parameters to determine earthquake risk [28-29]. Pushover analyses are useful tools for the assessment of URM wall capacities. The seismic response has been analyzed by using pushover analysis; under the constant gravity load and a monotonically increasing horizontal loads. Based on this methodology, the influence of the earthquake loads has been assessed by applying two systems of lateral forces orthogonal to each other. The behavior of the building is characterized by capacity curve which usually describes the relation between the base-shear force and roof displacement. It could be also plotted in acceleration displacement response spectrum format together with the response spectrum curve and estimate the top story displacement under the design earthquake to obtain the performance point of the building.

In the TREMURI, two load patterns are deployed: proportional with the 1st mode shape, based on the fundamental mode shape of the building, and a uniform load distribution to all stories. The two are performed in two orthogonal directions x- and y- and with positive and negative values. So, in total eight analysis: +x MF1, +x uniform, -x MF1, -x uniform, +y MF1, +y uniform, -y MF1, -y uniform (Fig. 9). These analyses are repeated for each combination. Without eccentricity of gravity load and with eccentricity of two different levels. For both simulations representing the original and intervened building are computed 24 analyses, for all load combinations, earthquake direction, with and without eccentricity. The numbers shown in the legend of capacity curves (Fig. 10-11) represents the eccentricity of the load application point.

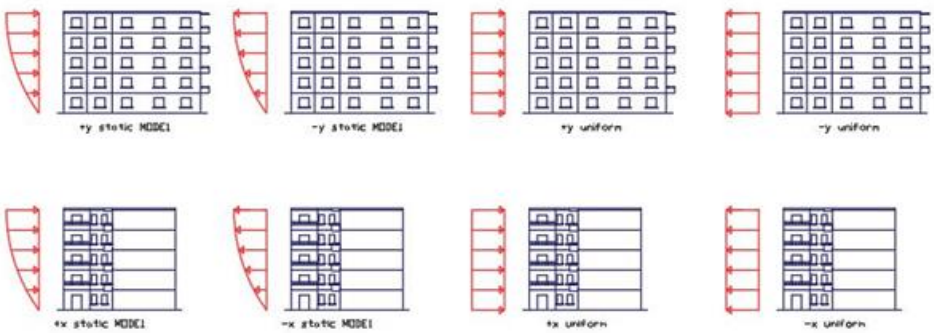

Fig. 9 Load patterns used of pushover analyses

Upon finishing the modeling, the capacity curves of both buildings were estimated by carrying out nonlinear static analysis in TREMURI (Fig. 10-11). Gravity load of the buildings were evaluated by considering the combination of Dead and Live loads.

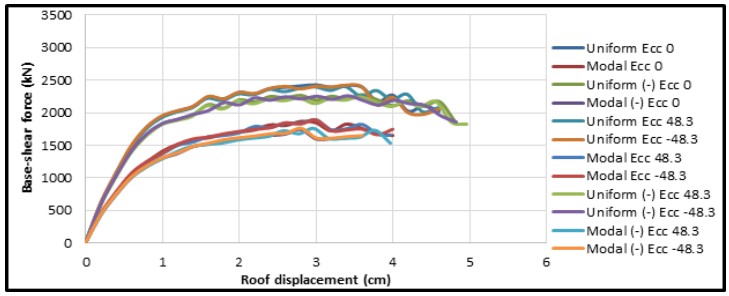

a) *x*- direction

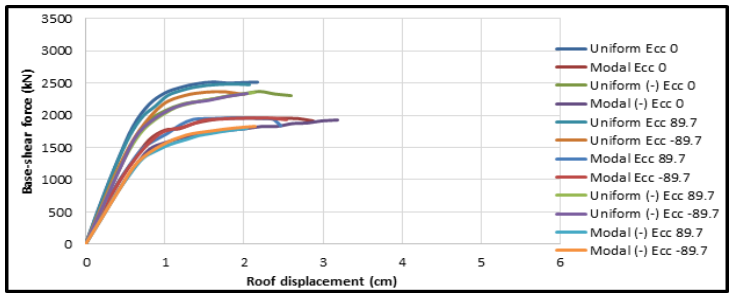

b) *y*- direction

Fig. 10 Capacity curves of the URM building without intervention

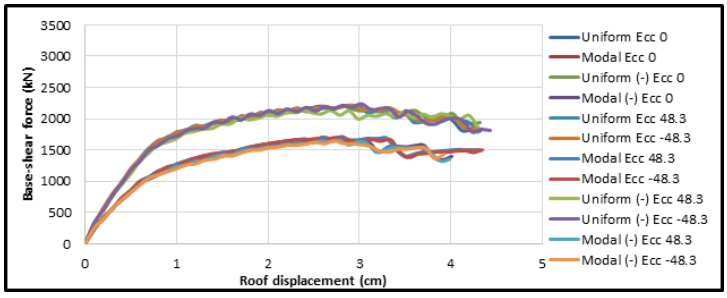

a) *x*- direction

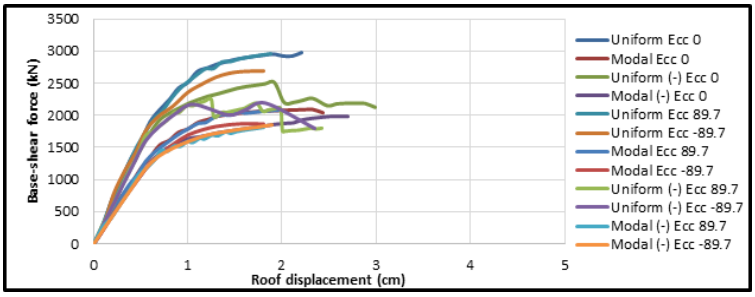

b) *y*- direction

Fig. 11 Capacity curves of the URM building with intervention

The worst cases were taken as the representative pushover curves for both x- and y-directions of the buildings. Normalized values of bilinear capacity curves are shown below (Fig. 12).

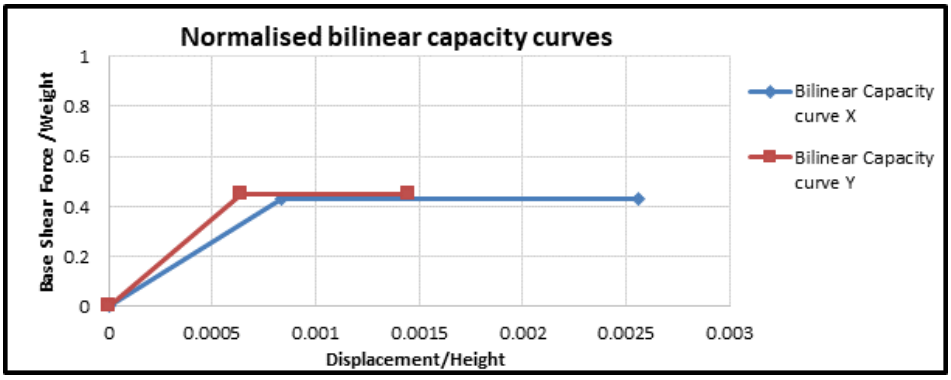

a)

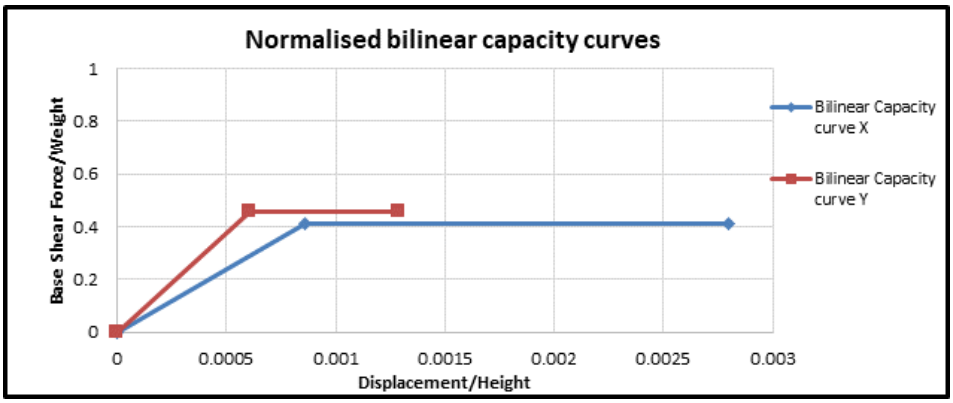

b)

Fig. 12 Normalized bilinear capacity curves; a) Original building, b) Building with intervention

Then, damage limit states of both buildings were evaluated using the criteria in Eurocode 8-3, and seismic capacities were estimated. The capacity assessment of the investigated buildings was performed using Eurocode 8, Part 3 [30]. Three limit states levels, i.e, "Damage Limitation (DL)", "Significant Damage (SD)" and "Near Collapse (NC)" are defined for performance evaluation.

In this study, performance evaluation of the buildings is done considering the soil Type-C with a moderate seismicity (*0.20g*) according to Eurocode 8 [30] and its corresponding spectra considering Soil category II and medium seismicity in KTP-N2-89 [14]. For both buildings, these limit states were estimated, and maximum "a_g" values were compared for each limit states.

Table 2. Global drift capacities and seismic spectral acceleration capacities of studied buildings

Building	Direction	Global Drift (mm)			Spectral acceleration "ag" (m/s2)		
		DL	SD	NC	DL	SD	NC
Original Building	x	8.1	26.9	35.9	1.098	2.239	2.901
	y	6.2	15.2	20.3	1.160	1.699	2.134
Building with intervention	x	8.6	29.4	39.2	1.039	2.250	2.933
	y	5.7	13.6	18.1	1.179	1.656	2.063

The two structures in this study show different levels of seismic response. As can be seen from Table 2-3, the PGA (a_g) that can be sustained for the *NC* state for the original building is near 0.22g meanwhile for building with intervention is near 0.2g.

Table 3. Performance levels and their corresponding PGAs for the studied buildings

Building	0.12g	0.14g	0.16g	0.18g	0.2g	0.22g
Original Building	DL		SD			NC
Building with intervention	DL		SD		NC	

5.2 Discussion of the Results

From the comparison of the pushover curves of both buildings, in the *x*- direction is viewed a decrease in stiffness and max base shear force, but a slight increase in displacement and ductility (Table 4). It must be said that this value is close, and the difference is at levels of 8.35% for stiffness, 5.1% for max force, and 6% in ductility. Since the demolished walls were in this direction, the load bearing capacity has slightly decreased. Meanwhile, in y-direction happens the opposite. Since the walls in this direction are the same, but also columns had been added in first floor, the stiffness and maximum force, slightly increases, while ductility levels remain almost the same, with some little decrease. The values of initial stiffness change at a ratio of 6.6%, the values of max force change at a ratio of 2.1% and the value of ductility at a ratio of 5.9%.

Table 4. Comparison of the parameters before and after intervention of the selected URM building

	Yield Force (kN)	Yield shear Force/Weight	Yield Disp. (cm)	Max Disp. (cm)	Ductility
URM-x	1617	0.433	1.17	3.59	3.07
URM-x +int	1520	0.411	1.20	3.92	3.27
URM-y	1670	0.447	0.90	2.03	2.26
URM-y +int	1689	0.456	0.85	1.81	2.13

6. Conclusion

Recent earthquakes have revealed that URM structures built of masonry walls including openings have been shown to have poor seismic capacity. This paper presents the seismic capacity comparison of two typical mid-rise existing masonry buildings with and without interventions. In order to make a comparative assessment, two URM buildings having the same initial architectural and structural design were selected and modelled by using the TREMURI. The first building was constructed by using a template design and the second one was intervened by removing the first story walls and replaced them with RC frames in that direction. Member dimensions, material types and loading conditions of both

buildings were determined from their architectural and structural designs projects and field investigations on considered buildings. Three dimensional structural models were simulated, and general properties of the members and material characteristics were determined based on experimental tests. The seismic capacities of the buildings were estimated by using a structural model which uses macro modelling approach for the load bearing masonry walls using TREMURI software package.

In this study, the influence of the removal of first floor load bearing walls on a typical URM building response has been investigated. The models are investigated using pushover analyses. The findings, expressed in terms of shear distributions and displacements, are compared with each other. The seismic demand has been defined by the response spectrum suggested by the EC 8 and the corresponding Albanian seismic codes. Based on the test results, the URM building was made of solid bricks with 7.3 MPa compressive strength and mortar with 2.4 MPa.

Damage levels were estimated according to Eurocode 8. The performance points were obtained and comparatively evaluated. The in-plane seismic capacity was found to be affected by the wall openings. Based on the analysis results, capacity curves obtained by pushover analyses reveal that URM building with intervention showed a slightly poor performance where the load bearing walls were removed and replaced by RC columns. On the other side, performance of the buildings was slightly increased due to the favorable effect of added columns on other direction. It does also show a higher shear capacity and lower ductile response.

Openings can decrease the stiffness of masonry walls and even alter the failure mechanisms of the masonry walls. Such irregular layout of openings may induce not only a non-uniform distribution of gravity loads between masonry panels but also may cause a concentration of seismic strength and drift demands in some parts of the wall. Accordingly, these interventions can lead to unfavorable damage concentrations increasing the seismic vulnerability of the entire wall, as shown by past earthquake inspections, i.e 2002 Molise, Italy earthquake [31].

This study shows that openings in load bearing walls can have a notable effect on the in-plane seismic capacity of the URM structures. Based on the findings of this study, the authors suggest including geometrical irregularities within capacity models of URM walls with openings. Further research is needed to evaluate the influence of various number of openings on seismic capacity assessment of URM buildings. Moreover, one can investigate the effects of complex irregularity patterns on seismic capacity.

References

[1] Bilgin, H. and Hysenlliu, M. (2020). Comparison of near and far-fault ground motion effects on low and mid-rise masonry buildings, Journal of Building Engineering, Volume 30, 2020, 101248, ISSN 2352-7102. https://doi.org/10.1016/j.jobe.2020.101248

[2] Hysenlliu M, Bidaj A, Bilgin H. Influence of material properties on the seismic response of masonry buildings. Res. Eng. Struct. Mater., 2020; 6(4): 425-437. https://doi.org/10.17515/resm2020.177st0120

[3] Isik, E, Aydin MC, Buyuksarac A. (2020). 24 January 2020 Sivrice (Elazığ) earthquake damages and determination of earthquake parameters in the region. Earthquakes and Structures, 19 (2), 145-156. https://doi.org/10.1007/s10518-020-01018-4

[4] Ademović N, Hadzima-Nyarko M, Zagora N. Seismic vulnerability assessment of masonry buildings in Banja Luka and Sarajevo (Bosnia and Herzegovina) using the macroseismic model. Bull Earthquake Eng 18, 3897-3933 (2020). https://doi.org/10.1007/s10518-020-00846-8

[5] Ozmen HB. A view on how to mitigate earthquake damages in Turkey from a civil engineering perspective. Res. Eng. Struct. Mater., 2021; 7(1): 1-11. http://dx.doi.org/10.17515/resm2020.231ea1113ed
[6] Milani G, Shehu R. Valente M. (2017). Seismic Vulnerability Mitigation of a Masonry Church by Means of CFRP Retrofitting. Procedia Engineering. Vol:195, 40-47. https://doi.org/10.1016/j.proeng.2017.04.521
[7] Hadzima-Nyarko M, Pavić G, Lešić M. Seismic vulnerability of old confined masonry buildings in Osijek, Croatia. Earthquakes and Structures. 2016,11(4):629-648. https://doi.org/10.12989/eas.2016.11.4.629
[8] Penna A, Morandi P, Rota M. et al. Performance of masonry buildings during the Emilia 2012 earthquake. Bull Earthquake Engineering. 2014(12):2255-2273. https://doi.org/10.1007/s10518-013-9496-6
[9] Yılmaz S, Tama YS, Bilgin H. Seismic performance evaluation of unreinforced masonry school buildings in Turkey. Journal of Vibration and Control. 2013,19(16):2421-2433. https://doi.org/10.1177/1077546312453190
[10] Pavić G, Hadzima-Nyarko M, Plaščak I, Pavić S. Seismic vulnerability assessment of historical unreinforced masonry buildings in Osijek using capacity spectrum method. Acta Physica Polonica. A, 135 (2019), 5; 1138-1141. https://doi.org/10.12693/APhysPolA.135.1138
[11] Kalman Šipoš T, Hadzima-Nyarko M. Seismic Risk of Croatian Cities Based on Building's Vulnerability. Tehnički vjesnik, 25 (2018), 4; 1088-1094. https://doi.org/10.17559/TV-20170708190145
[12] KTP-1963, Albanian masonry design code. (1963), (In Albanian).
[13] KTP-9-78, Albanian masonry design code. (1978), (In Albanian).
[14] KTP-N2-89, Albanian seismic design code. (1989), (In Albanian).
[15] EN 1996-1-1 (2005): Eurocode 6: Design of masonry structures - Part 1-1: General rules for reinforced and unreinforced masonry structures [Authority: The European Union Per Regulation 305/2011, Directive 98/34/EC, Directive 2004/18/EC].
[16] EN 1998-1 (2004), Eurocode 8: Design of Structures for Earthquake Resistance - Part 1: General Rules, Seismic Actions and Rules for Buildings, The European Union Per Regulation 305/2011, Directive 98/34/EC, Directive 2004/18/EC.
[17] Lagomarsino S, Penna A, Galasco A, Cattari S. TREMURI program: an equivalent frame model for the nonlinear seismic analysis of masonry buildings. Eng Struct. 2013(56):1787-99. https://doi.org/10.1016/j.engstruct.2013.08.002
[18] Ademović N, Kalman Šipoš T, Hadzima- Nyarko M. Rapid assessment of earthquake risk for Bosnia and Herzegovina. Bulletin of earthquake engineering, 18 (2020), 1835-1863. https://doi.org/10.1007/s10518-019-00775-1
[19] Kalman Šipoš T, Hadzima-Nyarko M. Rapid Seismic Risk Assessment. International Journal of Disaster Risk Reduction, 24 (2017), 348-360. https://doi.org/10.1016/j.ijdrr.2017.06.025
[20] Nato Sfp - 983054 (2007-2010). Harmonization of Seismic Hazard Maps for The Western Balkan Countries (Bshap).
[21] Aliaj S, Kociu S, Muco B, Sulstarova E. (2010). Seismicity, Seismo-tectonics and Seismic Hazard Assessment in Albania. The Academy of Sciences of Albania. ISBN: 978-99956-10-26, Albania.
[22] Sulstarova E, Kociaj S, Aliaj Sh. (1980) "Seismic Regionalization of PSR of Albania." Publishing House of "8 Nentori" Tirana, 1980; 1-297.
[23] EN 772-1 (2000) European Standard: Methods of test for masonry units - Part 1: Determination of compressive strength, CEN, Brussels.
[24] EN 1015-11 (1999) European Standard: Methods of test for mortar for masonry - Part 11: Determination of flexural and compressive strength of hardened mortar, CEN, Brussels.

[25] EN 1052-1, -3, -5 (1998) European Standard: Methods of test for masonry, CEN, Brussels.
[26] Lourenço PB. Computations on historic masonry structures. Progress in Structural Engineering and Materials. 2002,4(3):301-319. https://doi.org/10.1002/pse.120
[27] Gambarotta L, Lagomarsino S. On dynamic response of masonry panels. Proceedings of the national conference on 'Masonry mechanics between theory and practice', Messina, Italy, 1996.
[28] Pavić G, Hadzima-Nyarko M, Bulajić B. A Contribution to a UHS-Based Seismic Risk Assessment in Croatia-A Case Study for the City of Osijek. Sustainability, 12 (2020), 5; 1796, 24. https://doi.org/10.3390/su12051796
[29] Ademović N, Hadzima-Nyarko M, Zagora N. Seismic vulnerability assessment of masonry buildings in Banja Luka and Sarajevo (Bosnia and Herzegovina) using the macroseismic model. Bulletin of earthquake engineering, 18 (2020), 8; 3897-3933. https://doi.org/10.1007/s10518-020-00846-8
[30] EN 1998-1. European seismic design code. (2004). "Design of structures for earthquake resistance. Part 1: General rules, seismic actions and rules for buildings".
[31] Augenti N, Cosenza E, Dolce M, Manfredi G, Masi A, Samela L. Performance of school buildings during the 2002 Molise, Italy, earthquake. Earthquake Spectra 2004; 20(S1): S257-270. https://doi.org/10.1193/1.1769374

Research on
Engineering Structures & Materials

CONTENT

In This Issue

Research Group